Quantification of Lower Hybrid wave absorption in the edge of the Alcator C-Mod tokamak

by

Ian Charles Faust

Nuclear Engineering and Radiological Sciences (2009)
University of Michigan - Ann Arbor

Submitted to the Department of Nuclear Science and Engineering
in partial fulfillment of the requirements for the degree of

Doctor of Philosophy in Nuclear Science and Engineering

at the

MASSACHUSETTS INSTITUTE OF TECHNOLOGY

September 2016

Author . . . .
Department of Nuclear Science and Engineering
August 25, 2016

Certified by. . . . .
Ronald R. Parker
Professor Emeritus, Department of Nuclear Science and Engineering
and Electrical Engineering and Computer Science
Thesis Supervisor

Certified by. . . . .
Dennis G. Whyte
Hitachi America Professor of Engineering
Head of the Department of Nuclear Science and Engineering
Director, Plasma Science and Fusion Center
Thesis Supervisor

Certified by. . . . .
Brian LaBombard
Senior Research Scientist, MIT Plasma Science and Fusion Center
Thesis Reader

Accepted by . . . .
Ju Li
Battelle Energy Alliance Professor of Nuclear Engineering
Professor of Materials Science and Engineering
Chair, Department Committee on Graduate Students

Quantification of Lower Hybrid wave absorption in the edge
of the Alcator C-Mod tokamak

by

Ian Charles Faust

Submitted to the Department of Nuclear Science and Engineering
on August 25, 2016, in partial fulfillment of the
requirements for the degree of
Doctor of Philosophy in Nuclear Science and Engineering

Abstract

A 1 MW Lower Hybrid Current drive (LHCD) radiofrequency system is used to replace inductive drive on the Alcator C-Mod tokamak. It was designed to test Advanced Tokamak (AT) scenarios for future steady-state diverted, high field tokamaks. However, at reactor-relevant densities ($\bar{n}_e > 1 \cdot 10^{20}$ m^{-3}), an anomalous current drive loss is observed. This loss, known as the LHCD density limit, occurs in diverted plasmas and is correlated with the plasma current and plasma density. Several mechanisms have been implicated in the loss of current drive, with both experimental and theoretical results suggesting edge power loss.

Power modulation is a standard technique used for characterizing power sources and plasma power balance. In this case, the Lower Hybrid radiofrequency (LHRF) power is modulated in time in a set of plasmas across the density range from efficient to negligible current drive. This data is used to characterize the absorption of LHRF power through the calculation of the LHRF power balance within 15%, typical of power balance studies. This power balance is used to derive characteristics of the cause behind the LHCD density limit.

The immediate nature of LHRF-induced conducted and radiated power losses confirm that LHRF power is absorbed in the edge plasma, even at the lowest densities. The edge losses increase to balance the reduced current drive, indicating that the observed power in the scrape-off-layer (SOL) limits the available power for current drive and the edge losses represent a parasitic mechanism. Unlike edge losses of other radiofrequency systems, this absorption occurs with a high degree of toroidal symmetry near the plasma separatrix. This indicates absorption occurs just inside the separatrix, or just outside the separatrix over multiple SOL traversals.

Measurements of the poloidal distribution of ionization and recombination in the edge were made using a specially designed Ly$_\alpha$ pinhole camera. It utilizes a MgF$_2$ filter and AXUV diode array to measure Ly$_\alpha$ emission from the lower to upper divertor. Edge deposited LHRF power was found to promptly ionize the active divertor plasma in all diverted topologies. This result highlights the power flow and importance of the divertor plasma in the LHCD density limit.

Three independent characteristics indicate the thermal absorption of LHRF power. First, in-/out balance of radiated and conducted LHRF power change with the reversal of the tokamak magnetic fields. Second, comparisons of the conducted heat via Langmuir probes and IR thermography are similar with and without LHRF power. Lastly, the Langmuir probe ratio of V_{fl}/T_e does not significantly modulate with modulated LHRF.

A second experiment utilized a high strike-point diverted discharge to determine the edge loss of fast electrons. The high strike point could be observed using the hard X-ray camera, which can compare core and edge X-ray emission. The measured count rates from thick-target bremsstrahlung were interpreted into fast electron fluxes using the `Win X-ray` code. Theoretical treatments of the fast-electron confinement time were also calculated for Alcator C-Mod. In all

cases the fast-electron edge losses are minimal and will be unimportant for future tokamaks due to the small fast electron diffusivity and their large size.

The loss of current drive in high density diverted plasmas correlates with high edge plasma collisionality. The newly derived characteristics set stringent requirements in $n_\parallel$ for electron Landau damping to cause the edge absorption of LHRF power. Several observed attributes, namely high frequency modulation and low density absorption do not correlate with Landau damping characteristics. However, parasitic collisional absorption in the divertor plasma yields the necessary plasma current, topology, symmetry, thermal, and ionization characteristics. High divertor plasma collisionality is expected if not required for future tokamaks. LHRF systems of future tokamaks must must avoid propagation through collisional regions, even on the first traversal through the SOL.

Thesis Supervisor: Ronald R. Parker
Professor Emeritus, Department of Nuclear Science and Engineering
and Electrical Engineering and Computer Science

Thesis Supervisor: Dennis G. Whyte
Hitachi America Professor of Engineering
Head of the Department of Nuclear Science and Engineering
Director, Plasma Science and Fusion Center

Thesis Reader: Brian LaBombard
Senior Research Scientist, MIT Plasma Science and Fusion Center

- For my friends and family -

ACKNOWLEDGMENTS

This thesis is the hardest thing I have ever done in my life. It was not just the research or the impending close of C-Mod, but that daily deep pit of dispair that comes with well-laid plans gone awry. However, things in life always change. Friends and family have convinced me that when God closes a door, he opens a window. Just as no man is an island, these other people made this body of work possible. With all the love I have to give, I cannot thank you all enough.

To my thesis advisors, professors Ron Parker and Dennis Whyte, and my reader Brian LaBombard. Thank you for putting up with my stubborn, uncouth, belated, and frenetic approach to plasma physics. You gave me a chance and walked me along the path to becoming a competitent scientist. Sometimes tough love is the right medicine for success.

To the scientists, students and staff of the PSFC: every measurement and every bit of analysis shown in this thesis was assisted by your amazing capabilities and knowledge. This includes people from the LHRF group like Greg Wallace, Syun'ichi Shiraiwa, Seung-Gyou Baek and Atma Kanojia. This work had the influnce of the scientists associated with C-Mod: Jerry Hughes, Luis Delgado-Aparicio, Matt Reinke, Eric Edlund, John Rice, Theodore Golfinopoulos, Robert Mumgaard, Jim Terry, Dan Brunner, Cornwall Lau, Amanda Hubbard, Catherine Fiore, Robert Granetz, Steve Wolfe, Professor Anne White, Professor Jeffrey Freidberg, Steve Wukitch, Yijun Lin, Martin Greenwald, and Earl Marmar. The awesome C-Mod staff also played a large part including Rui Vieira, Dave Terry, Bill Parkin, Josh Stillerman, Tom Toland, George McKay, Ron Rosati, Dave Tracey, Maria Silveira, Ed Fitzgerald, and Sam Pierson. Of course, the students which make the backbone of this place including Mark Chilenski, Leigh Ann Kesler, Adam Kuang and Alex Tinguely. This list of your names does not do justice for the immense work and care you have given me, I worry I will never repay this debt.

I also thank my friends that have helped me maintain my sanity. To Evan Davis, you see me as I truly am even at my worst. To Matt Bailey, thank you for always being honest, your opinion is worth its weight in gold. To John Walk, for being my partner in crime at the office. To Harold Barnard, for inspiring me in science and showing me true friendship. To Alfred Eng, you are the person we all aspire to be. Thank you for putting up with me, I owe each of you so much.

To Sejal Vyas, for seeing through the machismo and giving back unconditional kindness. Thank you for showing me order from the

chaos, without you I was truly lost. I cannot begin to state how important you are.

To the friends I've made in Cambridge. The great years living on Beast in East Campus, you have opened my eyes to so much more. I will be there for each of you, always. To the staff of the Muddy Charles, the BU Law crowd, John Paul, Kathleen and others for so many fun times. Thank you to the Harvard-Epworth United Methodist church, for reminding me to always do the right thing.

To my friends elsewhere: Chris Worley, Jason Singh, Brian Caldwell and Tim Knuston, I have so many good memories of home because of you all. From the University of Michigan I really thank the G-House crew (Dan and Elise Kechele, Kevin and Stephanie Hsu, Dan Son, David Yang, Cam Stewart, Le Nguyen and Vania Kurikesu), the NERS people (Eric Miller and Diana Li, Sam Falvo, Hamdi Fariz and Jessica Odish), Sarah Zelenak and Kim Seidel. Ben and Song Betzler, you guys are like family to me. Each of you has played some role in my life that has led me to this point and for that I am eternally grateful.

Thank you to my family for being the foundation of my life. My parents Carol and George, you are the best mother and father I could have ever imagined. I try to honor you in all that I do. Adam, you are the pioneer and leader of this ramshackle group; in most things I only wanted to be like you. Jacob, you are my other half not only in body but in mind, you are resolute when I am weak, fair when I am biased and you are so very kind. To the ever increasing number of ladies in the Faust family, Lauren, Megan and Claire, I love you all so much. I also thank my extended family (the Welborns, Hawkins, Fausts, Todds and Riechmanns) for spurring me on through this.

This document is in honor of each of you. I can only hope this demarcation in my life matches similar positive points in your own. I am not perfect and neither is this thesis; thank you for accepting me for who I am and I hope you enjoy this nonetheless. Take this document and read it, it is a labor of love meant for you.

CONTENTS

LIST OF FIGURES

LIST OF TABLES

OVERVIEW OF CURRENT DRIVE LOSS IN TOKAMAKS

Current drive in tokamaks is vital for steady-state operation. While effects like the bootstrap current[1] can reduce the need for non-inductive current generators, it is unlikely that self-generated current can sustain and control a fusion-reactor grade plasma. Off-axis current drive can tailor current profiles to enhance performance in the creation of Advanced Tokamak (AT) scenarios. Lower Hybrid Current Drive (LHCD) is the most efficient non-inductive current source available in tokamaks through the use of Landau damping in the toroidal direction.

The theory of current drive via electron Landau damping properly represents the experimental trends in LHCD observed in diverted tokamaks. However, in some cases an unexpected loss of current drive has been observed. On Alcator C-Mod, an abrupt loss of current drive occurs with an increase in line-averaged density ($\bar{n}_e$), known as the LHCD density limit. This unexpected loss of current drive in diverted plasmas could be an important issue for future tokamaks. In particular this limit is found at $\bar{n}_e \sim 1 \cdot 10^{20}$ m^{-3} in Alcator C-Mod which is in the lower range of density operation expected based on Lawson criterion and power density requirements. Characterizing this effect is key for avoiding the loss of current drive on current and future diverted tokamaks.

Several theoretical mechanisms have been proposed as a cause of LHCD efficiency loss. These loss mechanisms fit into three categories, large edge losses, edge electron Landau damping, and collisional absorption. Each of these categories has a different effect on the plasma, and possibly can be separated from one another. These characteristics can be used to isolate a cause or set of causes behind the loss of current drive in Alcator C-Mod diverted, high density plasmas.

In this chapter, the efficiency of LHCD is defined. Various current drive loss mechanisms are discussed theoretically with previous observations on other tokamaks. Finally, the observed current drive loss on Alcator C-Mod is described detailing evidence and attributes of the LHCD density limit. These other results are the foundation for the experimentation of this thesis.

ANOMALOUS LOSS OF LHCD EFFICIENCY

Expected current drive efficiency

Pioneering work by Fisch[2] laid the framework for generating current through asymmetric Landau damping in plasmas. The imparted energy from radiofrequency waves affects the population in one direction. This causes a shift in the first moment of the distribution function leading to a current. Generally this current is formed with the electrons due to their higher mobility.

Further work by Fisch and Boozer[3] found that the current is generated due to two distinct phenomena. First, the waves can directly impart momentum to the electrons. A second and more dominant effect derives from the asymmetric modification in resistivity caused by the higher electron energies. As a consequence, methods of heating which impart momentum perpendicular to the magnetic field (such as electron cyclotron radiofrequency heating) can also generate current. The current drive efficiency depends on the method of heating and energy of electrons which absorb the radiofrequency power.

Current drive efficiency is defined as the normalized current density generated for a given volumetric deposited power ($\frac{j}{P_d}$). It is normalized to the electron thermal current $em_e v_{th}$ and the collisional power loss $\nu m_e v_{th}^2/2$. The deposited power counteracts the slowing down and momentum destruction caused by collisions and can be modeled by a collision frequency ν. In the high energy limit, the Fokker-Planck collision operator yields a slowing-down and pitch angle scattering collision frequency ν which can be used to derive $\frac{j}{P_d}$.

$$\nu = \frac{\nu_0(5 + Z_i)}{2v^3} \tag{1.1}$$

Where Z_i is the ion charge, and v is the electron velocity and ν_0 is defined in the following equation.

$$\nu_0 = \frac{n_0 e^4 \ln \Lambda}{4\pi \epsilon_0^2 m_e^2} \tag{1.2}$$

The expected current drive efficiency can be derived for current carrying particles at two velocities. The evolution of the current for a kick in energy from state 1 to 2 is given by $\Delta E = (E_2 - E_1)\delta f$. The current in the direction $\hat{s}$ evolves from the difference in the collision frequency for a change in the distribution function δf where $J = q\delta f \hat{s} \cdot (\vec{v}_2 e^{-\nu_2 t} - \vec{v}_1 e^{-\nu_1 t})$. When the kick in energy is evaluated over time Δt, the power deposited is generated $P_d = \Delta E/\Delta t$. The average current for time Δt is shown in equation 1.3 for long times as the current decays more slowly for higher velocity electrons. This

equation and the definition for P_d and ΔE yield the current efficiency for moving a charged particle from E_1 to E_2 given in equation 1.4.

$$\langle j \rangle = \hat{s} \cdot \frac{q \delta f}{\Delta t} \left(\frac{\vec{v}_2}{v_2} - \frac{\vec{v}_1}{v_1} \right) \tag{1.3}$$

$$\frac{\langle j \rangle}{P_d} = \hat{s} \cdot q \frac{\vec{v}_2 / v_2 - \vec{v}_1 / v_1}{E_2 - E_1} \tag{1.4}$$

When taken to the limit of $v_1 \sim v_2$ the differences can be converted into gradients in velocity and energy. The definition given in equation 1.1 is combined with several normalizations to give the normalized current drive efficiency in equation 1.5. The previously defined normalizations for $\frac{j}{P_d}$ are applied and the velocity is normalized to the thermal velocity $\vec{u} = \vec{v}/v_{th}$ with $w = \hat{s} \cdot \vec{u}$.

$$\frac{j}{P_d} = \frac{4}{5 + Z_i} \frac{\hat{s} \cdot \nabla(wu^3)}{\hat{s} \cdot \nabla u^2} \tag{1.5}$$

This equation is derived more rigorously using Langevin equations in Fisch, 1987[4]. While the derivation of j/P_d is not straightforward, several simple characteristics can be derived. First, the current drive efficiency increases significantly with higher electron energies due to the reduced effect of collisions. Current drive is also more efficient for deposited power which increases electron energy parallel to the desired direction of current $\hat{s}$. Third, the current drive is inversely dependent on v_0 (which has been included in the P_d term through the normalization). As a consequence, the current drive efficiency scales inversely with density.

Lower Hybrid current drive (LHCD) is the most efficient method for generating non-inductive current due to its damping characteristics. The electrostatic wave damps on high energy electrons parallel to the magnetic-field and plasma current. The launched $n_\parallel$ ($n_\parallel = ck_\parallel/\omega$) evolves to higher values in the Alcator C-Mod tokamak[5] (known as upshift). These waves are then are absorbed effectively on electrons which satisfy the phase velocity matching criterion by Landau damping. Future tokamaks will have sufficiently high electron temperatures that negligible wave upshifts are necessary for significant damping. However, lower $n_\parallel$ values correlate with higher energy electrons and greater current drive efficiency. For Landau damping on Maxwellian electron velocity distributions, the rule-of-thumb is $n_{parallel} \approx c/3v_{th}$. The diffusion of electrons in energy space leads to a plateau of electrons in one direction which carries the current. Higher launched $n_\parallel$ are generally absorbed at lower velocities and lower temperatures.

Figure 1.1: The JT-60 scaling of current drive efficiency with core temperature matches results from a number of diverted tokamaks. This plot was taken from the ITER physics basis[12], which shows efficient current drive is possible on ITER. The significant reduction in current drive on Alcator C-Mod correlated with $\bar{n}_e$ and is matched with an approximate 50% change in $\langle T_e \rangle$. The change in current drive efficiency on Alcator C-Mod is more extreme than what the JT-60 scaling predicts.
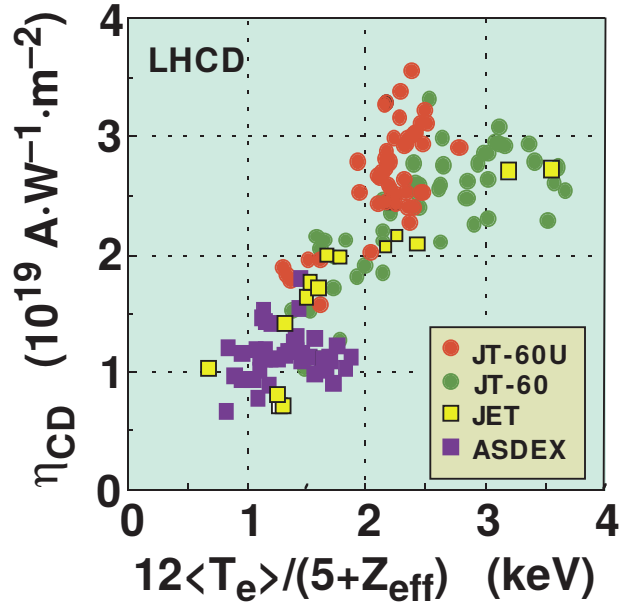
In practice a figure of merit different from j/P_d is used as an unbiased comparison between various current drive sources. For tokamaks, it is the average current density for a given power per particle defined as η_{20}[6, 7]. The average current density j can be generated by dividing the plasma current by the cross sectional area of the plasma A.

$$j = \frac{I_p}{A} \tag{1.6}$$

The power per particle is roughly the power per electron. This assumes that the density profile is flat, and can be represented by the line-averaged density $\bar{n}_e$.

$$\frac{P}{V n_e} = \frac{P}{2\pi R A \bar{n}_e} \tag{1.7}$$

Using these equations, η_{20} can be defined.

$$\eta_{20} = \frac{I_p/A}{P/V n_e} \approx \frac{R \bar{n}_e I_p}{P} \tag{1.8}$$

η_{20} has units of A m^{-2} W^{-1}, with the density in units of 10^{20} m^{-3}. These values are typically near .1-.4 for LHCD systems, and $< .1$ for other methods of current drive[6, 7]. Previous results from Alcator C-Mod found η_{20} to be approximately .25[8]. This matches results from various tokamaks [9] and fits with expectations derived from computer modeling[10, 11].

The 'JT-60 scaling'[13] of η_{20} finds that several tokamak LHCD efficiencies correlate strongly with the average core electron temperature $\langle T_e \rangle$. The LHCD efficiency was found to be in the range of .1-.4 η_{20} in these diverted tokamaks. However, this trend highlights a temperature dependence of the current drive efficiency. If absorption occurs at higher T_e, LHCD will increase the energy of higher energy electrons and the bulk electrons will be less collisional. These less collisional electrons are more efficient in sustaining current.

The T_e and n_e dependence of current drive efficiency indicates a covariance of plasma parameters in global LHCD efficiency. For the same input power and plasma equilibrium (*i.e* shape, magnetic field and plasma current), the stored energy stays relatively constant. Higher core densities are balanced by reduced core temperatures. Experimental trends of LHCD efficiency versus the plasma density masks a temperature dependence that exists.

A more useful metric for understanding current drive efficiency of LHCD which includes this T_e dependence can be derived from j/P_d. Instead of finding the current density related to the power per particle, the current density and input power are normalized to the thermal conditions of the plasma defined as $\tilde{j}/P_d$. The normalized current, $\tilde{j} = I_p/(e n_e v_{th} A)$, is the current density divided by the thermal current, and $P_d = P/(2\pi R A n_e m_e v_{th}^2 \nu^\dagger)$ is the normalized deposited power. $\nu^\dagger$ is defined as equal to $\nu(v_t h/v)^3$ where ν is given in equation 1.1 and yields the $(5 + Z_{eff})$ of the JT-60 scaling. This metric is similar to what is derived in a report by Tonon[14] and in thesis work by Wallace[15]. It suggests the JT-60 scaling is a consequence of improved current drive due to changing thermal conditions in the plasma.

$$\frac{\tilde{j}}{P_d} = \frac{I_p/(e n_e v_{th} A)}{P/(2\pi R A n_e m_e v_{th}^2 \nu^\dagger)} = \frac{m_e v_{th} \nu^\dagger}{e} \frac{2\pi R I_P}{P} \approx \frac{n_e I_p R}{P T_e} \propto \frac{\eta_{20}}{T_e} \quad (1.9)$$

Metrics for current drive efficiency highlight the importance of core plasma conditions and the radiofrequency wave characteristics. The plasma temperature and density can greatly impact the current drive efficiency through changes in collisionality and damping. The direction and energy of the affected electrons strongly dictate the efficiency. LHCD generates current through wave absorption by high energy electrons in the direction of the current. As a consequence, it is the most efficient method of current drive and is likely to be used in future steady-state tokamaks and fusion power plants like ARC[16] and ARIES-AT[17].

Overview of paths to LH efficiency loss

The generation of current through Landau damping requires multiple steps from launching to absorption. At each step, deviation from the expected will cause unexpected changes in the current drive. In many cases it can reduce the driven current and causes a reduction in the LHCD efficiency. Improved understanding of the missing physics leads to better implementations of LHCD and greater confidence in its extrapolation to future tokamaks.

Launched LHCD power models on Alcator C-Mod usually couple full-wave[18, 19] or ray-tracing codes[20, 21, 22] with Fokker-Planck[23, 24] solvers to determine the damping and propagation of LHRF waves. These codes model the wave propagation which leads to the necessary $n_\parallel$ upshift for electron Landau damping in the modest T_e cores of present experiments, such as ohmically heated Alcator C-Mod shots. An example of ray propagation is shown in figure 1.2. This complicated ray traversal through the Alcator C-Mod plasma highlights several conditions which may be improperly estimated. Incorrect estimates of propagation and absorption can reduce the LHCD efficiency outside the expected dependencies described in the previous section.

First, the propagation of waves or diffusion of particles may differ from what is expected. When LHRF waves create significant current near the edge it can be lost to the scrape-off-layer (SOL). Fullwave effects can cause significant upshifts in the wave $n_\parallel$ leading to unexpected changes in its spectrum. These both indicate that loss of current near the edge can occur due to misinterpreted upshifts and radial absorption profiles.

Second, nonlinear effects in the edge can significantly upshift the LHRF wave $n_\parallel$. Unexpected increases in $n_\parallel$ to 15 or greater can lead to electron Landau damping at the edge. Mechanisms such as scattering from density fluctuations or parametric decay instabilities (PDI) can upshift the LHRF waves over short distances. This edge damping can reduce the current thereby reducing LHCD efficiency.

Third, the inclusion of friction may lead to significant edge absorption. The cold tokamak SOL plasma separates the core plasma from the wall and is used in diverted plasmas to control power exhaust. Electromagnetic and electrostatic waves which propagate through very collisional plasma regions can be frictionally absorbed by the plasma response to the wave electric field. The high magnetic fields and high-densities of Alcator C-Mod have very collisional divertor plasmas which could absorb LHRF wave power.

Each of the three described categories will exhibit distinct effects in tokamak plasmas, with each illustrated in figure 1.3. Collisional absorption will be observed in the divertor with thermal changes in the plasma. Edge losses will be nonthermal in nature, indicated by fast-

Figure 1.2: An example GENRAY/CQL3D model generated by Dr. Syun'ichi Shiraiwa is shown. It models the Lower Hybrid ray propagation in an upper-single-null discharge on Alcator C-Mod with a realistic SOL and collisional absorption. The ray energy is given by the colorbar underneath as a fraction of the initial energy. The last closed flux surface (LCFS) is in gray, and the vacuum vessel and limiters are in black. The collisionality of the plasma is also colored, with the scrape-off-layer (SOL) being the most collisional. The Lower Hybrid waves traverse through the edge and core several times before being absorbed. In this case, significant power can be lost via collisions in the cold SOL plasma. The complicated propagation and absorption of LHRF waves on Alcator C-Mod can lead to unexpected changes in the current drive efficiency.
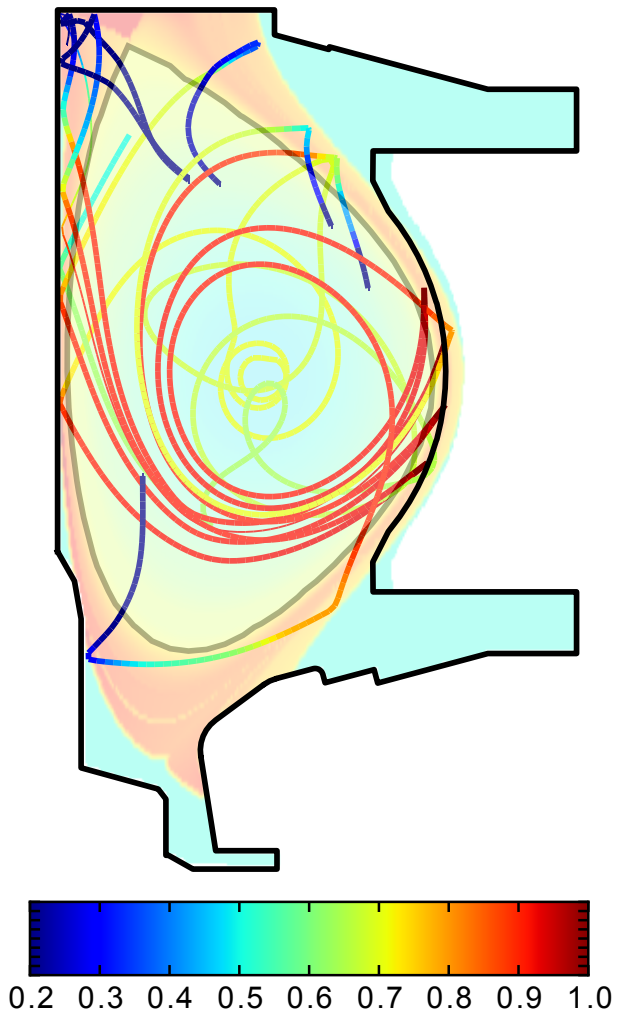
electrons in the SOL. Large $n_\parallel$ upshifts from nonlinear effects like PDI or density fluctuations will create epithermal electron populations in the edge and SOL. These effects (*i.e* edge electron Landau damping, edge nonthermal electron losses, and collisional absorption) implicate the edge as important in the loss of current drive efficiency.

This thesis attempts to recover and characterize the impact of these three effects in the edge plasma of Alcator C-Mod. In the following section, several example mechanisms implicated on C-Mod are discussed in detail. Characterizing each of these possible changes in the LHRF wave improves the understanding of wave propagation and damping which then can be used for designing LHCD systems for future steady-state tokamaks.

Figure 1.3: Unexpected current drive loss can be characterized into three categories. Three example rays come from the LHCD antenna on right and propagate into the plasma with the separatrix shown in red. The blue ray from the LHCD launcher shows a difference in ray propagation and absorption indicated in a. These effects can cause nonthermal populations in the edge. The ray in purple indicates nonlinear effects changing in the wave $\vec{k}$. This can lead to high $n_\parallel$ damping at the edge indicated by b. The wave can be frictionally absorbed by collisions indicated by the ray traveling into the cold, collisional divertor at c. Several mechanisms cause the same effect on the plasma and can be categorized together.
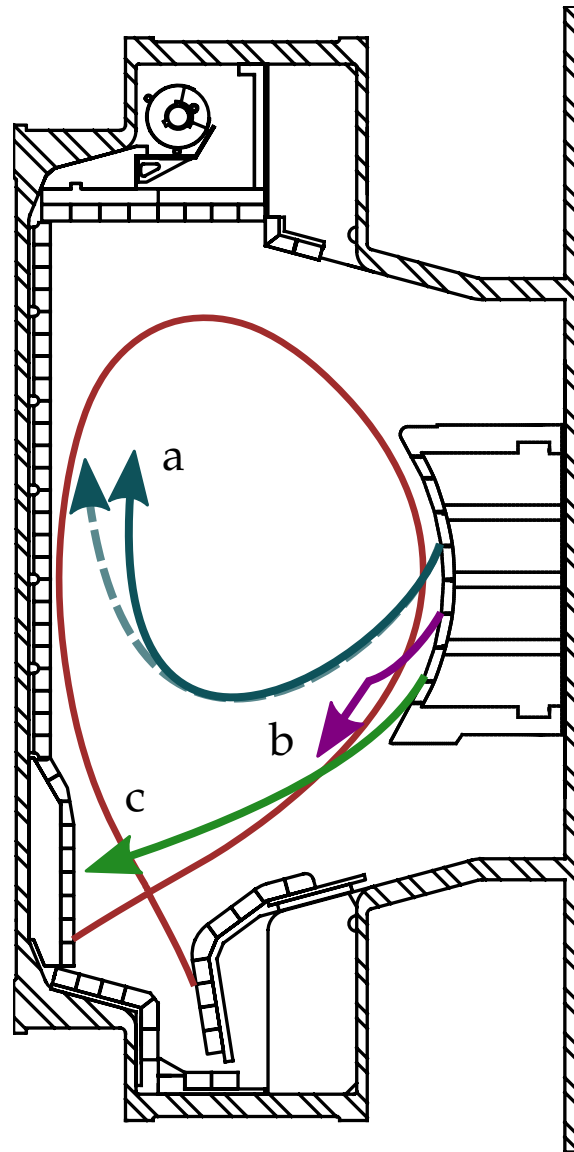
THEORETICAL LOSS MECHANISMS AND EXPERIMENTAL OBSERVATIONS

Collisional Absorption/Inverse Bremsstrahlung

Inverse bremsstrahlung describes the process of electromagnetic radiation energy absorption by charged particle collisions; it represents a possible cause of LHCD efficiency loss. The collisional absorption of power is a parasitic mechanism, reducing the available power driving current. Inverse bremsstrahlung for wave absorption has been used to great effect in inertial confinement fusion and laser plasmas due to their high plasma densities. Their applicability to lower density tokamak plasmas have been discussed theoretically by Catto and Myra[25].

The simplest model for collisional absorption begins by adding a frictional term to the classical electron force balance. The new electron-ion collision friction force is added with the oscillatory electromagnetic terms, shown in equation 1.10

$$m_e \frac{d\vec{v}}{dt} = \sum_i F_i - m_e \nu_{ei} \vec{v} \tag{1.10}$$

Using a Fourier representation of the electron motion ($\frac{d}{dt} \rightarrow i\omega$), the standard cold plasma dispersion relation can derive the effects of friction. This can be simply derived by converting the electron mass into a complex representation ($m_e^* = m_e(1 - i\frac{\nu_{ei}}{\omega})$). The use of ν_{ei} in the force balance is representative of the frictional effects between ions and electrons. This absorption mechanism will be observed thermally across the electron distribution function due to the v^{-3} dependence of electron-ion collisions.

A phase-space derivation of collisional absorption [26, 27] has been accomplished for electrostatic plasma oscillations induced by radiation. These derivations are in the 'weak-field' limit, shown by equation 1.11. It relates the average energy of an electron due to the oscillation to the average thermal energy of an electron. The increase in energy due to the electric field can change the collisional properties of the plasma, thereby making the absorption nonlinearly dependent on the electric field. This is analogous to BGK modes or ponderomotive forces, where the electric field can cause nonlinear effects in the plasma response. The relation of the electron kinetic energy induced by the wave to the plasma energy is key in determining the effect of collisional absorption. The electron kinetic energy is dependent on the peak electric field E_0, wave frequency ω, and is shown in equation 1.11.

$$\frac{3}{2} T_e > \frac{e^2 E_o^2}{2\omega^2 m_e} \tag{1.11}$$

Collisional absorption of LHRF waves in Alcator C-Mod is distinctly in the weak-field limit. For conditions in the Alcator C-Mod divertor with the LHRF ($T_e \sim 10eV$) at 4.6GHz, the electric field must exceed 10^{13} V/m to be in the strong-field limit. Except in circumstances with caustics, the peak electric field is roughly the electric field just in front of the launcher. The peak electric field observed at the front of the grill was $\sim 10^5$ to $\sim 10^7$ V/m[28]. The plasma changes from collisional absorption will be thermal in nature.

In addition, other nonlinear effects can impact the strength of collisional absorption. Tokamak plasmas are weakly coupled preventing the need of extensive advanced quantum-mechanical analysis necessary in high density laser plasmas[29]. In Alcator C-Mod the absorp-

tion of power in the weak-field electrostatic limit is given in equation 1.12. k_I is the imaginary part of the dispersion relation, representing the spatial coefficient for energy absorption.

$$k_I = \frac{Z^2 n_e n_i e^6 \ln \Lambda}{3c\omega^2 (2\pi^5)^{1/2} (m_e T_e)^{3/2} (1 - \omega_p^2/\omega^2)^{1/2}} \tag{1.12}$$

However, this collisional absorption derivation neglects the three-dimensional birefringent qualities of magnetized plasma near Lower Hybrid wave frequencies. Instead the calculation of k_{im} is numerically evaluated in ray-tracing or full-wave codes using the complex electron mass m_e^* during propagation. The dependence of absorption on n_e and T_e means that collisions become more important in regions where the cold plasma dispersion relation sufficiently describes wave dynamics. Due to the weak-field limit, ν_{ei} is determined from electron-ion momentum collision frequency defined in equation 1.13 [30]. In the weak-field limit ν_{ei} is unaffected by the oscillating field, but is instead modified by the deposited power absorbed through the collisions.

$$\nu_{ei} = \frac{2^{1/2} Z_{eff} n_e e^4 \ln \Lambda}{16 \epsilon_0^2 m_e^{1/2} T_e^{3/2}} \tag{1.13}$$

Trends in LHRF wave absorption by collisions can be derived from the cold plasma dispersion relation using the complex electron mass. A quadratic equation with respect to $n_\perp^2$ can be generated from the cold plasma dispersion relation, as shown in equation 1.14 defined with the standard representation of S, P and D.

$$0 = An_\perp^4 + Bn_\perp^2 + C \tag{1.14}$$

$$A = S$$

$$B = (n_\parallel^2 - S)(P + S) + D^2$$

$$C = P((n_\parallel^2 - S)^2 - D^2)$$

For the Lower Hybrid slow wave assuming $B^2 \gg 4AC$, $n_\perp^2$ can be simply defined. This ordering for LHRF waves assumes $\omega_{ci} \ll \omega \ll \omega_{ce}$, where $P > D \gg S \sim 1$.

$$n_\perp^2 \approx \frac{-P(n_\parallel^2 - S) - D^2}{S} = Q_R + iQ_I \tag{1.15}$$

The right hand side of the equation is complex due to the complex electron mass. In the case for LHRF waves, $P \sim -\frac{\omega_{pe}^{*2}}{\omega^2} = -\frac{\omega_{pe}^2}{\nu^2 + \omega^2}(1 + i\frac{\nu}{\omega})$

Figure 1.4: The absorption of LHRF waves by electron-ion friction can be analytically determined for Alcator C-Mod parameters. $k_{\perp I}$ is determined from the full cold-plasma dispersion relation for slow LHRF waves with contours in blue. The contours are for 4.6GHz waves at 5.4T with an $n_\parallel$ of 3 which replicates C-Mod LHRF parameters. The contours have units in m^{-1} with typical Alcator C-Mod divertor $k_{\perp I}$ values approaching 10^2 m^{-1}. A simplified expression for absorption given by equation 1.18 reproduces similar values as the full dispersion relation and is shown in red. It is only near the mode conversion layer that large differences develop. Inaccessible plasma conditions are shown in gray.
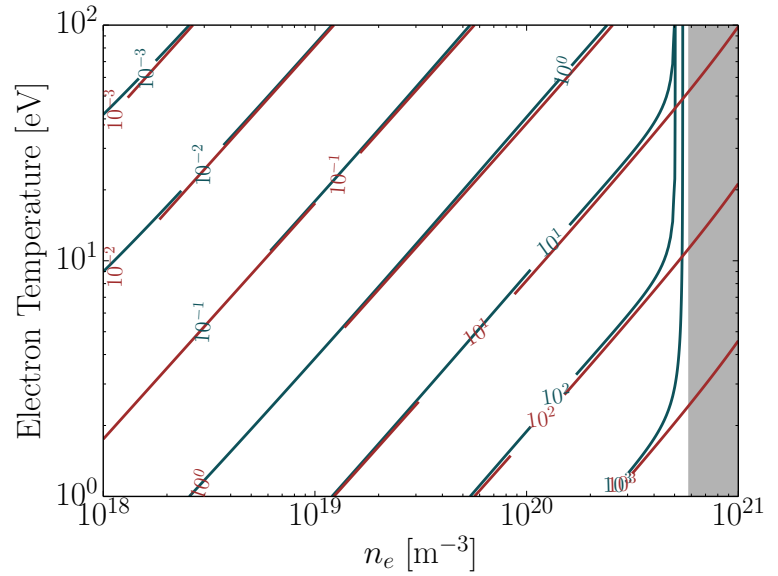
and $D \sim -\frac{\omega_{pe}^{*2}}{\omega\omega_{ce}^{*}}$. For LHRF waves, P is complex and D is purely real. Thus $n_\perp = n_{\perp,R} + in_{\perp,I}$, which can be solved using the following relation assuming a physically relevant solution.

$$n_{\perp,I} = -\frac{1}{\sqrt{2}}\sqrt{\sqrt{Q_R^2 + Q_I^2} - Q_R} \qquad (1.16)$$

Using the defined P,D and S for the LHRF wave, the new dispersion relation with complex components is given in equation 1.17

$$n_\perp^2 = \omega_{pe}^2\left(\frac{n_\parallel^2 - 1}{\nu^2 + \omega^2} - \frac{\omega_{pe}^2}{\omega_{ce}^2\omega^2}\right) + i\frac{\nu}{\omega}\frac{\omega_{pe}^2(n_\parallel^2 - 1)}{\nu^2 + \omega^2} \qquad (1.17)$$

$n_\perp$ is approximately proportional to $Q_I^{1/2}$ and weakly proportional to $Q_R^{1/2}$. Both Q_R and Q_I roughly maximize $n_{\perp,I}$ when $\nu = \omega$. For $n_e = 1 \cdot 10^{20}$ m^{-3} and $T_e = 10$ eV ν/ω is of order 10^{-3}. Further simplifications can be used for C-Mod conditions where $\nu \ll \omega$ which leads to $Q_I \ll Q_R$.

$$n_{\perp,I} \approx -\frac{1}{2}\left|\frac{Q_I}{\sqrt{Q_R}}\right| = -\frac{\nu\omega_{pe}}{2\omega^2}\sqrt{\left|\frac{n_\parallel^2 - 1}{1 - \frac{\omega_{pe}^2}{\omega_{ce}^2(n_\parallel^2-1)}}\right|} \approx -\frac{\nu\omega_{pe}n_\parallel}{2\omega^2} \quad (1.18)$$

This simplification is accurate for most Alcator C-Mod divertor conditions shown in figure 1.4. Only near the mode conversion layer does this simplified expression diverge from values given in the cold-plasma dispersion relation. The absorption is roughly proportional to $(n_e/T_e)^{3/2}$ which is highest in the active divertor SOL plasma. The

dependence on $n_\parallel$ and ω indicates that launching lower $n_\parallel$ at higher frequencies can reduce the collisional absorption.

In the regime where $v/\omega \ll 1$ the length scale of LHRF wave absorption $k_{\perp,I}$ is inversely proportional to the launched frequency and scales with the collision frequency. High SOL collisionality in C-Mod plasmas could lead to significant edge absorption. This parasitic mechanism absorbs thermally in the distribution and can decrease the efficiency of current drive. It should be observed on Alcator C-Mod at the most collisional regions of the plasma causing thermal changes to the boundary.

Parametric decay instabilities (PDI)

Parametric decay instabilities (PDI) can change the $n_\parallel$ of LHRF waves leading to substantial electron Landau damping in the edge[31]. This complicated and nonlinear phenomenon has been observed a range of LHCD experiments and is known to cause significant current drive loss. *Parametric* indicates a wave interaction driven by a time-dependent parameter usually of a different frequency. The time-dependent parameter is often an oscillation known as the *pump*. In this case, the pump is the original LHRF wave at 4.6 GHz in Alcator C-Mod. *Decay Instability* indicates that a set of lower frequency waves are driven by the pump. The output waves (or daughter waves) are a scattered electromagnetic wave (otherwise known as the *sideband*) and an electrostatic wave[32]. PDI for LHRF waves arises from the frequency-dependent ponderomotive force which can drive oscillations at other frequencies. Ponderomotive effects imply that PDI is inherently a function of the local LHRF power density.

Two different PDI modes are known to occur in tokamak plasmas. First is the decay of the Lower hybrid wave via the ion-sound quasi-mode, and the other is decay via the ion-cyclotron quasi-mode. A *Quasi-mode* is a plasma mode which can only occur in cases of non-linear drive. Each of these modes cause different frequency daughter waves to be generated with respect to the LHRF wave. In any case, all parametric decay instabilities are required to meet the three-wave frequency and wave vector conditions given in equations 1.19 and 1.20. ω_0 is the original Lower Hybrid wave, ω_2 is the quasi-mode, and ω_1 is the downshifted LHRF wave.

$$\omega_0 = \omega_1 + \omega_2 \tag{1.19}$$

$$\vec{k}_0 = \vec{k}_1 \pm \vec{k}_2 \tag{1.20}$$

The flow of power can be derived from the Manley-Rowe relations, with the low frequencies of the quasi-modes containing a small fraction of the LHRF power. PDI effectively scatters the LHRF wave with a subtle reduction in the frequency.

The ion-sound quasi-mode has a frequency $\omega_1 \approx k_\parallel v_{th,i}$, typically on the order of MHz. It develops from the interaction of LHRF waves with ion-acoustic modes. This loss mechanism has been suspected to cause significant LHCD losses on FT and FTU[33, 34] and was responsible for frequency broadening on Alcator A[35] and C[31]. Theoretical work suggests that these ion-sound modes are suppressed by collisional absorption in the edge[36].

Ion-cylcotron quasi-modes have frequencies which are harmonics of the local ion cyclotron frequency ω_{ci}. PDI creates sidebands that are offset from the Alcator C-Mod LHRF frequency by 10's of MHz, depending on the major radius. Downshifted electromagnetic waves generated from ion-cyclotron quasi-modes have been observed on Alcator C-Mod at the low field side and the high field side[37, 38, 39]. Some losses in LHRF power must occur due to this effect.

Growth rates γ of these modes can be determined from their respective dispersion relations and has been derived for both expected quasi-modes[40]. The linearized parametric dispersion relation takes the general form given in equation 1.21, where upshifted sideband contribution has been neglected.

$$\varepsilon\varepsilon_1 + \frac{(1+\chi_i)\chi_e}{4}(\mu^-)^2 = 0 \tag{1.21}$$

A far more complete derivation is available by several sources, with a very accessible derivation by Baek[41]. χ_e is the electron susceptibility, and χ_i is the ion susceptibility, where $\varepsilon = 1 + \chi_e + \chi_i$ is the dielectric function for low frequency ion modes. ε_1 is the LHRF sideband dielectric function. μ^- is the coupling coefficient which takes the form in equation 1.22.

$$(\mu^-)^2 \approx \frac{e^2 k^2}{m^2 k_1^2}\left(\frac{[(\vec{E}_{0\perp} \times \vec{k}_{1\perp}) \cdot \hat{B}]^2}{\omega_{ce}^2 \omega_0^2} + \frac{k_{1\parallel}^2 E_{0\parallel}^2}{\omega_0^4}\right) \tag{1.22}$$

The two terms inside the bracket are the perpendicular and parallel coupling terms. Each of the terms are dependent on the plasma and wave attributes, leading to differences in the coupling. The perpendicular and parallel coupling terms determine the growth rate and character of the sidebands, which is key for determining the edge damping of LHRF in Alcator C-Mod.

While these modes are absorbed via Landau damping they intensify through a process known as convective growth. The convective growth is limited by geometrical constraints of the growth region, and

Figure 1.5: The convective growth region is larger for the parallel coupling of LHRF waves. The top illustration represents the limited perpendicular growth region defined by the size of the launching grill $\Delta \vec{x}$ in the $\hat{Z}$ direction. The resonance cones are represented by the shaded regions for $\vec{v}_{g,pump}$ in blue and $\vec{v}_{g,sideband}$ in green, with propagation primarily in the parallel direction $\hat{\phi}$. This allows for larger regions of growth for parallel coupled PDI, highlighted by the illustration on bottom. The cylindrical coordinate system uses typical tokamak conventions of R, ϕ, Z. The growth of PDI requires knowing the three dimensional structure of $\vec{E}, n_e, T_e$ and $\vec{k}$ and thus is difficult to experimentally characterize and theoretically model.
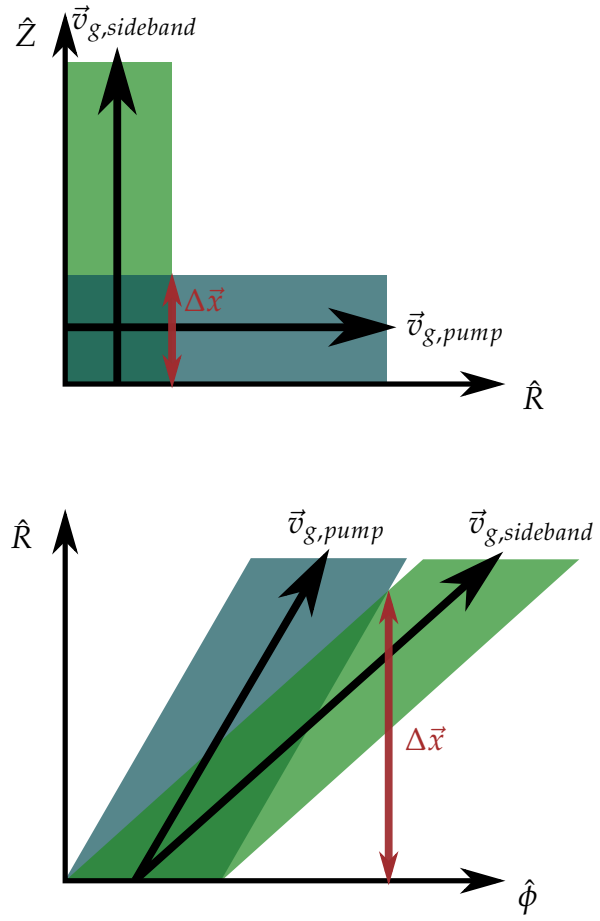
is related to the perpendicular and parallel coupling and differences in the wave's group velocities. These geometrical constraints lead to parallel PDI coupling to have larger regions of growth. PDI can only increase in magnitude for quasi-modes in the presence of the pump wave. The pump LHRF wave is generally limited to the resonance cones with a large toroidal (parallel) extent, meaning that a finite spatial extent exists for the growth of PDI given by $\Delta \vec{x}$. The scattered sideband grows in this region and convects outward due to the difference in $\vec{v}_g$, while the lower frequency quasi-mode is quickly damped. Differences in $\Delta \vec{x}$ for LHRF waves in tokamaks lead to a preferential coupling and is highlighted in figure 1.5. Work by Baek[41] finds that the spatial extent allowable for PDI convective growth occurs due to parallel coupling. The time available for a sideband to grow ($\sim e^{\Delta t \gamma}$) depends on the geometric limitations $\Delta \vec{x}$ and the sideband group velocity $\vec{v}_g$. This relation is given in equation 1.23.

$$\Delta t = \frac{|\Delta \vec{x}|}{|\vec{x} \cdot \vec{v}_g|} \tag{1.23}$$

Models of PDI have maximum growth rates near the LCFS[39] on Alcator C-Mod and is reproduced in figure 1.6. A large sideband cor-

Figure 1.6: Ion cyclotron quasi-mode PDI growth rate (γ/ω_{ci}) is highest near the LCFS for perpendicular coupling in red. This predicted dependence assumes $f_0 = 4.6$GHz, $n_\parallel = 2$ with an output $n_\parallel = 7$ for $P_{LHRF} = 100$kW. This figure is taken from Baek[39, 41]. The dominant ion-cyclotron quasi-mode harmonic is given in black ω/ω_{ci}. These values are derived from midplane density and temperature profiles ofa high density USN edge plasma.
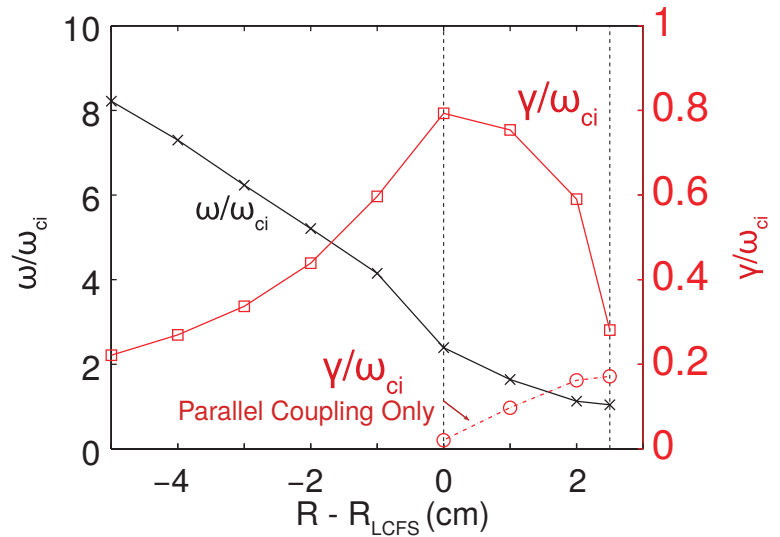
related with the reduction in current drive is observed on Alcator C-Mod [38] near the LHRF frequency reduced by the fundamental ion cyclotron frequency. Other higher ion cyclotron harmonics are also observed with similar characteristics, at lower powers than the fundamental sideband. Models have a maximum PDI growth rate near $n_\parallel$ of 30 for the 3rd ion-cyclotron harmonic, this $n_\parallel$ damps in plasmas with at least 90 eV electron temperatures. These results indicate that PDI can cause strong absorption of LHRF power in the edge plasma through electron Landau damping.

Significant electron Landau damping in the edge plasma can be observed as epithermal or high energy electrons depending on the scattered $n_\parallel$. While evidence exists for PDI on Alcator C-Mod, its quantitative importance in causing the loss of current drive can be determined by the location, magnitude, and nature of the associated Landau damping. Measurements of the edge $n_\parallel$ have been made for certain ranges on Alcator C-Mod [42]. However, this nonlinear effect is a function of many parameters such as the LHRF electric field, the input $n_\parallel$, the daughter $n_\parallel$, the plasma conditions and the physical geometry. Each of these parameters are independently difficult to determine on Alcator C-Mod, making modeling of PDI-induced absorption extremely difficult.

PDI damping in Alcator C-Mod depends on the generated $n_\parallel$. High $n_\parallel$ waves ($n_\parallel > 30$) generated by PDI damp immediately in the edge creating epithermal electrons in the SOL. $n_\parallel$ waves between 17 and 30 will create epithermal electrons just inside the separatrix. Low $n_\parallel$ waves will continue to propagate similarly to the launched waves through the core. Without fully characterizing the three-dimensional electric field structure of the LHRF wave, the input $n_\parallel$ and the background plasma conditions, it is difficult to determine the expected effect on the edge.

Density fluctuation scattering

Plasma density strongly influences the propagation of electromagnetic waves in plasmas. Fluctuations in density can greatly affect the nearly electrostatic nature of LHRF waves in Alcator C-Mod, leading to unexpected deviation in the ray trajectories through the plasma. Density fluctuations can be included into the cold plasma dispersion relation by replacing n with $n + \delta n$. A new cold plasma dispersion relation for electromagnetic waves which separates the fluctuation δn term was described by Bonoli and Ott[43] and is shown in equation 1.24. The change in the propagation due to fluctuations is dependent on the magnitude of the fluctuation $\delta n/n$ and its coherence[44]. ε is the cold-plasma dielectric tensor using a Fourier representation of $\vec{E}$ with wavenumber $\vec{k}$ and oscillation angular frequency ω.

$$D \cdot \vec{E}_k = \vec{k} \times \vec{k} \times \vec{E}_k - \frac{\omega^2}{c^2} \varepsilon \cdot \vec{E}_k = -\frac{\omega}{c^2} \sum_{k'} \frac{\delta n_{\vec{k}-\vec{k}'}}{n} (\varepsilon - \mathbf{I}) \cdot \vec{E}_{k'} \quad (1.24)$$

Mode coupling between the fluctuation and wave can be derived by first defining a direction $\hat{e}_k^*$ where $\hat{e}_k^* \cdot D \cdot \vec{E}_k = 0$ and then by expanding D to yield a complex portion where $D \approx D + i\frac{\partial D}{\partial \omega}\frac{\partial}{\partial t}$. The expansion assumes that the electric field changes in time slowly with respect to the LHRF frequency $\omega_k \gg i\partial/\partial t$. The mode coupling equation for waves with density perturbations is described in equations 1.25, 1.26, and 1.27, where $C(\vec{k}) = \sqrt{u(\vec{k})}$ and $M = c^2/(2\omega_k)\frac{\partial D}{\partial \omega}$.

$$u(\vec{k}) = \frac{\omega_k}{8\pi} \hat{e}_k^* \cdot \frac{\partial D}{\partial \omega} \cdot \vec{E}_k |\vec{E}_k| \quad (1.25)$$

$$i\frac{\partial}{\partial t}C(\vec{k}) = \sum_{k'} V(\vec{k}, \vec{k}', \omega_k) \frac{\delta n_{\vec{k}-\vec{k}'}}{n} C(\vec{k}') \quad (1.26)$$

$$V(\vec{k}, \vec{k}', \omega_k) = -\left(\frac{\omega_k}{2}\sqrt{\frac{|\vec{E}_k|}{|\vec{E}_{k'}|}}\right) \frac{\hat{e}_k^* \cdot (\epsilon - \mathbf{I}) \cdot \vec{E}_{k'}}{\sqrt{\hat{e}_k^* \cdot M \cdot \vec{E}_k}\sqrt{\hat{e}_{k'}^* \cdot M \cdot \vec{E}_{k'}}} \quad (1.27)$$

These complicated equations can be evaluated using a wave coupling code with known forms of $\delta n/n$. In tokamaks, the long parallel distance of $\delta n/n$ fluctuations only change $\vec{k}$ of LHRF waves perpendicular to the magnetic field thereby preserving the $n_\parallel$ value. The low frequencies of the density perturbations ($\sim$ 1MHz) also minimally change ω. The LHRF wave interaction with density perturbations on tokamaks is defined as perpendicular scattering due to the preservation of ω and $k_\parallel$. Equation 1.27 defines the coupling coefficient V,

which can be used to determine the probability for wave scattering for a given time[45].

The scattering can lead to changes in direction and magnitude of $k_\perp$. These effects tends to broaden of the radial wave damping profile on Alcator C-Mod as determined by modeling[46]. Different $k_\perp$ values can lead to a randomization of the wave propagation and has been theorized to fill the spectral gap[5]. Further propagation after scattering is required to evolve $n_\parallel$ for absorption. A reduction in current drive efficiency can occur if the evolution of $n_\parallel$ leads to significant damping in the edge.

The change in $k_\perp$ is converted into a change in $k_\parallel$ through the magnetic shear and through toroidicity effects. This will lead to a different absorption location which may occur in a region where the absorption leads to edge losses, high $n_\parallel$ edge damping or collisional absorption. Work by Bertelli[46] found that scattering effects do not enhance the level of collisional absorption in Alcator C-Mod. The conversion of the scattered waves to high enough $n_\parallel$ values for edge damping require scattering in cooler regions. This must occur in the SOL for edge absorption as the high core temperatures ($T_e > 1$ keV) in Alcator C-Mod will readily absorb high $n_\parallel$ waves. The change in $n_\parallel$ can also lead to damping nearer to the edge, where fast electrons may diffuse out of the plasma. The loss of current drive due to density fluctuation scattering can be observed in each of the distinct observable loss categories with various likelihoods, as edge loss of fast electrons, as epithermal electrons in the SOL, and thermal changes in the SOL.

Fast electron edge loss

The passing fast electrons generated by LHRF follow the functionally endless field lines constrained to the plasma flux surfaces. The electrons forward momentum and associated current is dissipated via collisions and is balanced by the applied LHRF power which maintains the plateau in velocity space and the generated plasma current. In the case that electrons diffuse onto field lines of finite length, their momentum can be absorbed instead by solid surfaces.

The effect of fast-electron edge losses on current drive efficiency were initially derived by Luckhardt [47]. The derived model assumes that the loss of fast electrons in phase space is dictated by a characteristic time τ_D known as the fast electron confinement time. The change in the distribution function due to edge losses are defined in equation 1.28.

$$\left.\frac{\partial f_1}{\partial t}\right|_{loss} = -\frac{f_1}{\tau_D(u,w)} \tag{1.28}$$

The influence of this additional loss term in the current drive efficiency is shown in equation 1.29. This equation uses the same representations and normalizations described in equation 1.5. When taken to the limit of $\tau_D \approx \infty$, the solution given in equation 1.5 is recovered.

$$\frac{J}{P_d} = \frac{4}{\hat{s} \cdot \nabla u^2} \hat{s} \cdot \nabla \left(\frac{w}{u^{2+z_i}} \int_0^u u'^{4+z_i} e^{2 \int_u^{u'} u''^2 / \tau_D du''} du' \right) \qquad (1.29)$$

The exponential integral with τ_D serves to reduce the current drive efficiency when compared to the ideal case. Lower confinement times correspond to reduced efficiency, and becomes increasingly important with the longer slowing-down times.

Calculating the value of τ_D is extremely difficult in practice. Similar to the calculation of the energy confinement time, the energy confinement of fast electrons can be determined from the ratio of the fast electron stored energy to the fast electron edge loss power. Both of these metrics are difficult to characterize, leaving to the experimental calculation of τ_D to a small set of cases [48].

In reality the deposition and loss of fast electrons is dependent on the diffusivity and deposition of LHCD. The radial phase space effects of diffusivity were derived by Rax and Moreau [49], showing that the redistribution in phase space by radial effects could also impact efficiency and not just edge losses. Proper modeling of LHCD in tokamak plasmas requires evaluating the radial profile of deposition with diffusion [50, 51].

The edge loss of fast electrons has been experimentally observed on JT-60U by Ushigusa [52]. Increases in edge X-ray emission from the strike point correlated with the application of LHCD in low density plasmas. A rise in the conducted heat on the divertor was found to contain $\sim 10\%$ of the LHRF power as measured by IR thermography. This edge loss decreases with increasing density and increasing $n_\parallel$.

Similar effects were observed on the WT-3 tokamak[53], but in a majority of larger devices such effects are minimal. Calculation of τ_D on ASDEX found edge loss to be an insignificant effect[48]. Most experiments focused on deriving the anomalous diffusivity D for radial modeling purposes [54, 55, 56, 57]. In most cases, edge loss is expected to inversely scale with the machine size as $\tau_D \propto a^2 / D$.

If the deposition of LHRF occurs in an unexpected location such as near the periphery, the distance needed to diffuse out of the tokamak becomes short. It becomes increasingly likely that edge losses occur and with shorter fast-electron confinement times. This loss should be observed as a large flux of fast electrons in the edge, leading to a large amount of thick-target bremsstrahlung. This bremsstrahlung source should become increasingly dominant with the loss of current drive. The effects of edge fast electron diffusion are analyzed in chapter 5. The impact of edge fast electrons on the SOL and first wall are

discussed and a relation of D to τ_D is evaluated. Finally, the impact of edge fast electron loss for C-Mod and other machines is evaluated.

Fullwave effects

Fullwave modeling of LHRF wave propagation in Alcator C-Mod captures diffraction, interference and focusing effects that are otherwise lost in ray tracing models. These are referred to as 'fullwave effects' and can affect the damping characteristics of LHRF wave power. Previous work[58] has implicated strong upshifts and spectral broadening after wall reflection for causing the reduction in efficiency. The strong upshift from wall reflection generates minimal current due to significant electron Landau damping in the edge plasma.

It is theorized that the broadening and upshift in $n_\parallel$ caused by the reflection cannot form the necessary plateau in the electron distribution function. This lack of a 'tail' begins with the low velocity electrons which absorb the LHRF power. The LHRF power density is insufficient in overcoming the collisional nature of these electrons. The power is thermalized or lost to the edge before a plateau can be formed, generating a minimal amount of current.

Results from Meneghini[58] suggest significant damping for $.8 < \rho < .9$ (Figures 7-6 and 7-14) on Alcator C-Mod, with significant power unable to form a tail. This mechanism should be observed with an increased electron temperature near the edge plasma (for $> .8\rho$) and an epithermal or fast-electron population in the SOL. However, the fullwave analysis did not have sufficient resolution to calculate the spectral content for $n_\parallel > 15$, preventing the calculation of electron Landau damping in the SOL and immediate edge. As a consequence, it is unknown what fullwave effects may cause in this region.

EFFICIENCY LOSS ON ALCATOR C-MOD

Divertor dependence of current drive efficiency

A large difference in current drive efficiency with plasma topology is observed on Alcator C-Mod. Previous research on Alcator C and C-Mod found limited discharges had significant current drive at reactor relevant densities $n_e > 1 \cdot 10^{20} \mathrm{m}^{-3}$. However, the addition of an X-point and divertor to the plasma correlates with a substantial decrease in the current drive efficiency.

First found by Wallace [59, 60], it has since prevented the use of LHCD for line-averaged plasma densities ($\bar{n}_e$) greater than $\sim 1 \cdot 10^{20} \mathrm{m}^{-3}$. These density conditions are normal to H-modes[61] and I-modes[62] on Alcator C-Mod, greatly limiting its applicability to these high-performance plasmas. While LHRF power has been applied to H-modes and I-modes, it is inconclusive if any current is driven. Mea-
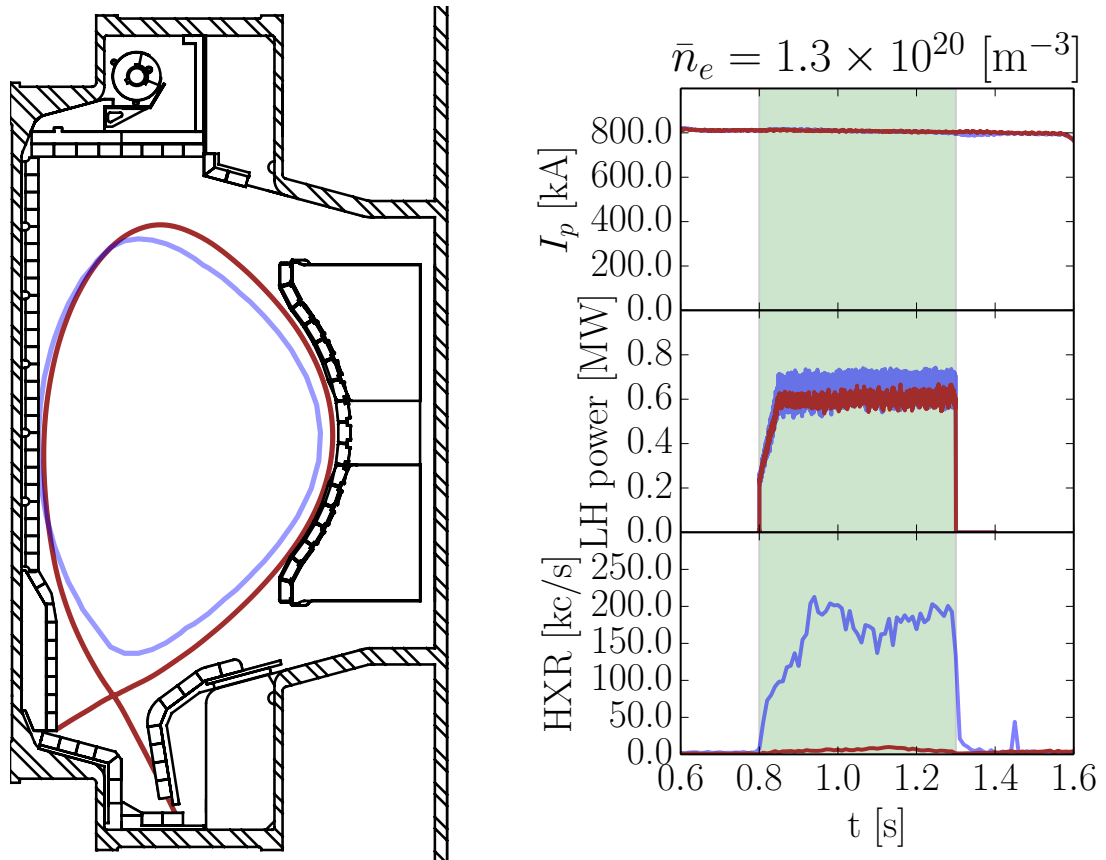
Figure 1.7: Similar 5.4T, 800kA discharges with similar densities and applied LHRF powers exhibit significantly different fast electron populations. On left are the two plasma equilibria, with the LCFS color matching the measurements on right. Measurements of core hard X-ray bremsstrahlung shown on right is used as a proxy for LHCD-driven fast electron population. Inner Wall Limited (IWL) discharges have orders of magnitude greater X-ray emission than diverted discharges. Current drive for 800kA diverted discharges is negligible above $1.4 \cdot 10^{20}$ m^{-3}, but is measurable in IWL plasmas. The addition of an X-point correlates with the loss of current drive.

surements of nonthermals (either by nonthermal electron cyclotron emission or by hard X-ray bremsstrahlung) are influenced by fast changes in temperature and neutron rates making their results questionable in high-performance plasmas. Changes in the loop voltage were also not observed and are strongly dependent on the background plasma electron temperature. Regardless, the cause of this current drive loss is vital for future steady state diverted tokamaks and steady-state fusion power.

In plasmas with low neutron rates, measurements of high-energy bremsstrahlung as hard X-rays (HXR) are used as a proxy for the LHCD-driven fast electrons. In similar plasma conditions (*i.e* similar densities, magnetic fields and plasma currents), diverted plasmas have a several order of magnitude reduction in HXR count rate compared to inner wall limited plasmas. Reduction in the loop voltage from LHCD occurs in inner wall limited plasmas at high $\bar{n}_e$, but are significantly reduced in diverted plasmas. This difference is shown in figure 1.7.

Figure 1.8: Exponential trends nonthermal emission (described in detail in chapter 3 and 5) indicates a significant loss of current drive correlated with $\bar{n}_e$. Nonthermal ECE is measured by an ECE channel with its resonance in the far-SOL where ECE emission is non-opaque and the signal is thus due to upshifted nonthermal emission. Both the nonthermal ECE and HXR bremsstrahlung are used as a proxy for the nonthermal population and are normalized to both the LHRF power and maximum value at low density. The decay rate is the same for both nonthermal measurements. This data is generated from modulated LHRF power described in chapter 3 from runday 1140822.
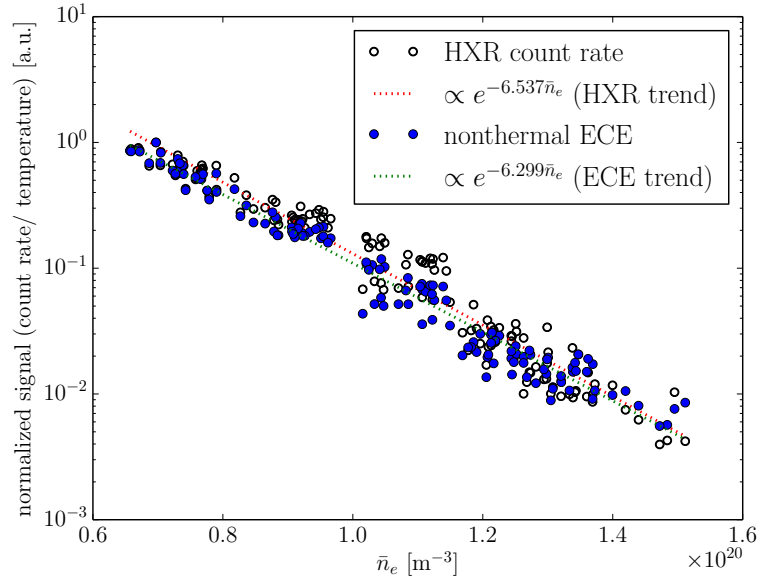
The power placed into plasma no longer absorbs via Landau damping on the high energy core electron distribution. This unexpected loss of current drive indicates a significant modification of the plasma or wave physics caused by the addition of an active X-point and divertor.

Current drive 'density limit'

LHCD efficiency on Alcator should trend similarly to the JT-60 scaling, as it reflects the scaling of core collisionality in the normalizations in j/P_d. j/P_d is proportional to $\langle T_e \rangle / (5 + Z_{eff}) \langle n_e \rangle$. For a constant core plasma pressure ($T_e \propto n_e^{-1}$), the current drive efficiency should scale as n_e^{-2}. Instead, measurements of nonthermal ECE (described in chapter 3) and hard X-rays (described in chapter 5) decrease at an exponential rate. This is shown in figure 1.8, where both measurements trend $\sim e^{-6\bar{n}_e}$ in diverted 700 kA plasmas.

This strong dependence of the fast electron population and LHCD efficiency on $\bar{n}_e$ is colloquially known as the 'LHCD density limit'. A small change in density $\Delta\bar{n}_e \sim 3 \cdot 10^{19}$ m^{-3} halves the LHCD efficiency and reduces the intensity of nonthermal emission by an order of magnitude. While some small level of current drive exists for densities $\sim 1.2 - 1.5 \cdot 10^{20}$ m^{-3}, the LHCD current generally is less than 10% of the total. This small amount of current has little impact on the core plasma.

The loss of core fast electrons implicates some form of edge absorption in causing the loss of current drive[59, 60, 63]. Thermoelectric currents were observed on some Langmuir probe measurements in the SOL with high density LHRF power. Ion-cyclotron quasi-mode PDI is observed with the onset of the density limit [37, 38, 39]. Improve-

ments in H-mode confinement due to changes in the edge plasma
are observed with LHRF power [64, 65]. Without a core population of
fast electrons the impact on other core and edge populations must be
evaluated to determine absorption of LHRF power and the dominant
loss mechanism.

Current drive efficiency versus $n_\parallel$

The current drive efficiency on Alcator C-Mod has been rigorously
observed to be weakly influenced by the launched $n_\parallel$[66]. Current
drive on Alcator C-Mod is in the weak-damping regime where the
waves bounce through the periphery of the plasma several times be-
fore damping in the core. The launched $n_\parallel$ does not impact the scaling
or nature of the observed density limit in diverted discharges. The re-
flection coefficient for the LHRF antenna is a function of launched $n_\parallel$,
thus the coupled LHRF power is also a function of the $n_\parallel$. As a result,
this thesis uses the same launched $n_\parallel$ for all of the experimentation
($n_\parallel = 1.9$).

I_p dependence of current drive efficiency

Figure 1.9: The loss of current drive is
correlated with the plasma current.
This figure, reproduced from Baek[39],
shows that a fast-electron population
is maintained for higher densities at
higher currents in diverted plasmas.
Some improvement in current drive
efficiency is expected with higher core
T_e due to the higher I_p. However, the
difference in emission exceeds two
orders of magnitude. Thus, changes in
the SOL due to I_p (such as a shorter
SOL width[67]) are the likely the
cause for the improved efficiency.
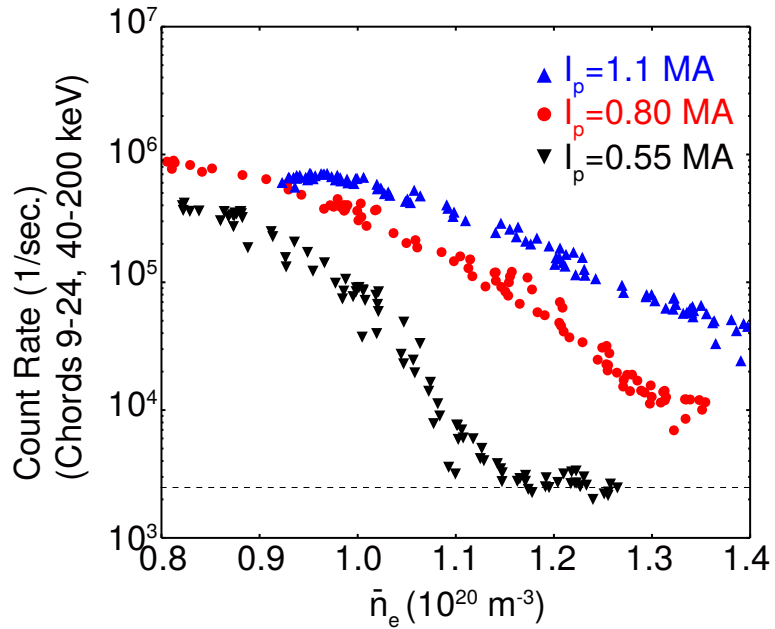
Results by Baek[39] found that the nonthermal emission is a strong
function of the plasma current I_p. At low densities, LHCD efficiency
improves with higher I_p[66] and has also been observed on Tore
Supra[68]. The higher plasma current improves the energy confine-
ment and increases the input ohmic power, each of these effects causes
a higher core T_e. However, the improvement with plasma current ex-

ceeds the expectations of j/P_d given by the JT-60 scaling, suggesting changes in the edge due to I_p influence the current drive efficiency.

The SOL of tokamaks has characteristic heat flux, density and temperature widths that scale inversely with I_p[67]. The SOL profiles of temperature and density correlate strongly with the Greenwald fraction $\bar{n}_e/n_G$[69]. Higher currents minimize the region that is vastly different from limit discharges (*i.e.* smaller SOL widths). Several important phenomena follow this trend, for instance the appearance of MARFEs[70] (which are regions of extremely high localized collisionality due to a radiation instability) and the empirical Greenwald density limit[71], which increases as I_p and has been associated with radial collisional transport near the LCFS. The divertor is influenced by the narrowing of the heat heat channel and the distance that LHRF waves travel through the cold plasma edge is reduced.

SUMMARY AND DISCUSSION

A range of possible mechanisms can explain the loss of current drive observed in diverted Alcator C-Mod discharges. The loss of current drive is associated with edge effects including measured ion-cyclotron quasi-mode PDI, thermoelectric currents[59], H-mode quality [64, 65] and a plasma current dependence[38]. Theoretical losses implicate changes in the edge plasma in causing the LHCD density limit. However, many of these mechanisms are hard to quantify with models due to the complicated three-dimensional nature of LHRF wave propagation and absorption in tokamak plasmas.

Similarly, direct quantifiable observation of a specific mechanism is difficult and unlikely. The large number of plausible mechanisms makes it more advantageous to first reduce this set by elimination. However this experimental methodology comes at a cost, as it is unable to definitively prove a particular mechanism. As was shown in this chapter, these mechanisms can be categorized into three observable current drive loss effects.

Separating these effects requires finding more characteristics of the LHCD power at high densities. The additional power into the tokamak does not develop a fast-electron plateau and must be observed in some other population or region of plasma. Calculating the power balance validates the expectation of edge loss in the loss efficiency. The effects which derive from the power balance can then be used to categorize the loss mechanism. This thesis attempts to reduce the set of possible mechanisms through the use of modulation for power balance. This work is also characterizes SOL fast-electrons and their relation to the density limit. The previous evidence and theory discussed in this chapter is synthesized with new data and analysis. From these observations, evidence is derived for a most-likely cause to the loss of current drive.

[1] C.E. Kessel. Bootstrap current in a tokamak. *Nuclear Fusion*, 34(9):1221, 1994.

[2] Nathaniel J. Fisch. Confining a tokamak plasma with rf-driven currents. *Phys. Rev. Lett.*, 41:873–876, Sep 1978.

[3] N. J. Fisch and A. H. Boozer. Creating an asymmetric plasma resistivity with waves. *Phys. Rev. Lett.*, 45:720–722, Sep 1980.

[4] Nathaniel J. Fisch. Theory of current drive in plasmas. *Rev. Mod. Phys.*, 59:175–234, Jan 1987.

[5] Paul T. Bonoli and Edward Ott. Toroidal and scattering effects on lower-hybrid wave propagation. *Physics of Fluids*, 25(2):359–375, 1982.

[6] C Gormezano. Summary of the europhysics topical conference on radiofrequency heating and current drive of fusion devices. *Plasma Physics and Controlled Fusion*, 35(SA):A239, 1993.

[7] A.S. Kaye and G. O'Connor. High frequency heating and current drive in next step steady state tokamaks. *Fusion Engineering and Design*, 56–57(0):47 – 57, 2001.

[8] J.R. Wilson, R. Parker, M. Bitter, P.T. Bonoli, C. Fiore et al. Lower hybrid heating and current drive on the Alcator C-Mod tokamak. *Nuclear Fusion*, 49(11):115015, 2009.

[9] G Tonon. Heating and current drive by LH-waves on toroidal plasmas: problems and perspectives. *Plasma Physics and Controlled Fusion*, 26(1A):145, 1984.

[10] Yu.F. Baranov, A. Ekedahl, P. Froissard, C. Gormezano, M. Lennholm et al. Modelling of lower hybrid current drive and comparison with experimental results in JET. *Nuclear Fusion*, 36(8):1031, 1996.

[11] Y Peysson, the TORE SUPRA Team and Y Peysson. Progress towards high-power lower hybrid current drive in tore supra. *Plasma Physics and Controlled Fusion*, 42(12B):B87, 2000.

[12] Heating ITER Physics Expert Group on Energetic Particles, Current Drive and ITER Physics Basis Editors. Chapter 6: Plasma auxiliary heating and current drive. *Nuclear Fusion*, 39(12):2495, 1999.

[13] K. Ushigusa, T. Imai, Y. Ikeda, O. Naito, K. Uehara et al. Lower hybrid current drive efficiency in the JT-60 tokamak. *Nuclear Fusion*, 29(6):1052, 1989.

[14] G. Tonon. Current drive efficiency requirements for an attractive steady-state reactor. Technical Report EUR-CEA-FC–1526, Association Euratom-CEA, Centre d'Etudes Nucleaires de Cadarache, 13 - Saint-Paul-lez-Durance (France). Dept. de Recherches sur la Fusion Controlee, August 1994.

[15] Gregory M Wallace. *Behavior of lower hybrid waves in the scrape off layer of a diverted tokamak*. PhD thesis, Massachusetts Institute of Technology, February 2010.

[16] B.N. Sorbom, J. Ball, T.R. Palmer, F.J. Mangiarotti, J.M. Sierchio et al. ARC: A compact, high-field, fusion nuclear science facility and demonstration power plant with demountable magnets. *Fusion Engineering and Design*, 100:378 – 405, 2015.

[17] Farrokh Najmabadi, A. Abdou, L. Bromberg, T. Brown, V.C. Chan et al. The ARIES-AT advanced tokamak, advanced technology fusion power plant. *Fusion Engineering and Design*, 80(1–4):3 – 23, 2006. Aries - {AT} Special Issue.

[18] J. C. Wright, P. T. Bonoli, A. E. Schmidt, C. K. Phillips, E. J. Valeo et al. An assessment of full wave effects on the propagation and absorption of lower hybrid waves. *Physics of Plasmas*, 16(7), 2009.

[19] O. Meneghini, S. Shiraiwa and R. Parker. Full wave simulation of lower hybrid waves in maxwellian plasma based on the finite element method. *Physics of Plasmas*, 16(9), 2009.

[20] Paul T. Bonoli and Ronald C. Englade. Simulation model for lower hybrid current drive. *Physics of Fluids*, 29(9):2937–2950, 1986.

[21] Yves Peysson, Robert Arslanbekov, Vincent Basiuk, Joël Carrasco, Xavier Litaudon et al. Magnetic ripple and the modeling of lower-hybrid current drive in tokamaks. *Physics of Plasmas*, 3(10):3668–3688, 1996.

[22] A.P. Smirnov, R.W. Harvey and K. Kupfer. A general ray tracing code GENRAY. In *Bulletin of American Physical Society*, volume 39, page 1626. American Physical Society, 1994.

[23] R. W. Harvey and M. McCoy. The CQL3D code. In F. Zacek, J. Stoeckel, J. Badalec, L. Dvoracek, K. Jakubka et al, editors, *Proceedings of the IAEA Technical Committee Meeting on Simulation and Modeling of Thermonuclear Plasmas*, pages 489–526, International Atomic Energy Agency, Vienna, 1992.

[24] S. Shiraiwa, O. Meneghini, R. Parker, P. Bonoli, M. Garrett et al. Plasma wave simulation based on a versatile finite element method solver. *Physics of Plasmas*, 17(5), 2010.

[25] Peter J. Catto and J. R. Myra. A quiver-kinetic formulation of radio-frequency heating and confinement in collisional edge plasmas. *Physics of Fluids B*, 1(6):1193–1204, 1989.

[26] Tudor Wyatt Johnston and John M. Dawson. Correct values for high-frequency power absorption by inverse bremsstrahlung in plasmas. *Physics of Fluids*, 16(5):722–722, 1973.

[27] John Dawson and Carl Oberman. High-frequency conductivity and the emission and absorption coefficients of a fully ionized plasma. *Physics of Fluids*, 5(5):517–524, 1962.

[28] S. Shiraiwa, O. Meneghini, R.R. Parker, G. Wallace, J. Wilson et al. Design, and initial experiment results of a novel lh launcher on Alcator C-Mod. *Nuclear Fusion*, 51(10):103024, 2011.

[29] John F. Seely and Edward G. Harris. Heating of a plasma by multiphoton inverse bremsstrahlung. *Phys. Rev. A*, 7:1064–1067, Mar 1973.

[30] P. Helander and D.J. Sigmar. *Collisional Transport in Magnetized Plasmas*. Cambridge Monographs on Plasma Physics. Cambridge University Press, 2005.

[31] Yuichi Takase and Miklos Porkolab. Parametric excitation of ion-sound quasimodes during lower-hybrid heating experiments in tokamaks. *Physics of Fluids*, 26(10):2992–3003, 1983.

[32] C.S. Liu and V.K. Tripathi. Parametric instabilities in a magnetized plasma. *Physics Reports*, 130(3):143 – 216, 1986.

[33] R. Cesario and A. Cardinali. Parametric instabilities excited by ion sound and ion cyclotron quasi-modes during lower hybrid heating of tokamak plasmas. *Nuclear Fusion*, 29(10):1709, 1989.

[34] R. Cesario, A. Cardinali, C. Castaldo, F. Paoletti, W. Fundamenski et al. Spectral broadening of lower hybrid waves produced by parametric instability in current drive experiments of tokamak plasmas. *Nuclear Fusion*, 46(4):462, 2006.

[35] J.J. Schuss, M. Porkolab, Y. Takase, D. Cope, S. Fairfax et al. Lower hybrid heating in the Alcator A tokamak. *Nuclear Fusion*, 21(4):427, 1981.

[36] C. Castaldo, A. Di Siena, R. Fedele, F. Napoli, L. Amicucci et al. Influence of collisions on parametric instabilities induced by lower hybrid waves in tokamak plasmas. *Nuclear Fusion*, 56(1):016003, 2016.

[37] S G Baek, R R Parker, S Shiraiwa, G M Wallace, P T Bonoli et al. Measurements of ion cyclotron parametric decay of lower hybrid waves at the high-field side of Alcator C-Mod. *Plasma Physics and Controlled Fusion*, 55(5):052001, 2013.

[38] S. G. Baek, R. R. Parker, S. Shiraiwa, G. M. Wallace, P. T. Bonoli et al. Characterization of the onset of ion cyclotron parametric decay instability of lower hybrid waves in a diverted tokamak. *Physics of Plasmas*, 21(6):–, 2014.

[39] S.G. Baek, R.R. Parker, P.T. Bonoli, S. Shiraiwa, G.M. Wallace et al. High density LHRF experiments in alcator C-Mod and implications for reactor scale devices. *Nuclear Fusion*, 55(4):043009, 2015.

[40] Miklos Porkolab. Parametric instabilities due to lower-hybrid radio frequency heating of tokamak plasmas. *Physics of Fluids*, 20(12):2058–2075, 1977.

[41] Seung Gyou Baek. *Detection of lower hybrid waves at the plasma edge of a diverted tokamak*. PhD thesis, Massachusetts Institute of Technology, February 2014.

[42] S. G. Baek, G. M. Wallace, T. Shinya, R. R. Parker, S. Shiraiwa et al. Measurements of the parallel wavenumber of lower hybrid waves in the scrape-off layer of a high-density tokamak. *Physics of Plasmas*, 23(5), 2016.

[43] Paul T. Bonoli and Edward Ott. Accessibility and energy depositon of Lower-Hybrid Waves in a Tokamak with Density Fluctuations. *Phys. Rev. Lett.*, 46:424–427, Feb 1981.

[44] P. L. Andrews and F. W. Perkins. Scattering of lower-hybrid waves by drift-wave density fluctuations: Solutions of the radiative transfer equation. *Physics of Fluids*, 26(9):2537–2545, 1983.

[45] Edward Ott. Lower hybrid wave scattering by density fluctuations. *Physics of Fluids*, 22(9):1732–1736, 1979.

[46] N Bertelli, G Wallace, P T Bonoli, R W Harvey, A P Smirnov et al. The effects of the scattering by edge plasma density fluctuations on lower hybrid wave propagation. *Plasma Physics and Controlled Fusion*, 55(7):074003, 2013.

[47] S.C. Luckhardt. The efficiency of rf current drive in the presence of fast particle losses. *Nuclear Fusion*, 27(11):1914, 1987.

[48] R Bartiromo. Transport properties of current driven tokamak plasmas. *Plasma Physics and Controlled Fusion*, 35(SA):A167, 1993.

[49] J.M. Rax and D. Moreau. Non-local current response in wave driven tokamaks. *Nuclear Fusion*, 29(10):1751, 1989.

[50] M.R. O'Brien, M. Cox and J.S. McKenzie. Effects of radial trans-port on current drive in tokamaks. *Nuclear Fusion*, 31(3):583, 1991.

[51] R.A. Cairns, V. Fuchs, C. Cote and Y. Demers. Spatial diffusion of fast particles in lower hybrid current drive. *Nuclear Fusion*, 35(11):1413, 1995.

[52] K. Ushigusa, T. Kondoh, O. Naito, Y. Ikeda, S. Ide et al. Direct loss of energetic electrons during lower hybrid current drive in JT-60U. *Nuclear Fusion*, 32(11):1977, 1992.

[53] T. Maekawa, M. Nakamura, T. Komatsu, T. Kishino, Y. Kishigami et al. Heat flux of fast electrons to the limiter in lower hybrid current drive plasma on WT-3. *Nuclear Fusion*, 32(10):1755, 1992.

[54] Y Peysson. Transport of fast electrons during LHCD in TS, JET, and ASDEX. *Plasma Physics and Controlled Fusion*, 35(SB):B253, 1993.

[55] A. Schmidt, P. T. Bonoli, O. Meneghini, R. R. Parker, M. Porko-lab et al. Investigation of lower hybrid physics through power modulation experiments on Alcator C-Mod. *Physics of Plasmas (1994-present)*, 18(5):–, 2011.

[56] S. Knowlton, M. Porkolab and Y. Takase. Experimental studies of the radial diffusion of energetic electrons in lower-hybrid wave heated plasmas in the Alcator-C tokamak. *Physics of Plasmas*, 1(4):891–900, 1994.

[57] S. E. Jones, J. Kesner, S. Luckhardt, F. Paoletti, S. von Goeler et al. Fast electron transport and lower hybrid absorbed power pro-files from hard x-ray imaging in the Princeton Beta Experiment-Modified. *Physics of Plasmas*, 2(5):1548–1560, 1995.

[58] Orso (Orso-Maria Cornelio) Meneghini. *Full-wave modeling of lower hybrid waves on Alcator C-Mod*. PhD thesis, Massachusetts Institute of Technology, February 2012.

[59] G. M. Wallace, R. R. Parker, P. T. Bonoli, A. E. Hubbard, J. W. Hughes et al. Absorption of lower hybrid waves in the scrape off layer of a diverted tokamak. *Physics of Plasmas (1994-present)*, 17(8):–, 2010.

[60] G.M. Wallace, A.E. Hubbard, P.T. Bonoli, I.C. Faust, R.W. Harvey et al. Lower hybrid current drive at high density in Alcator C-Mod. *Nuclear Fusion*, 51(8):083032, 2011.

[61] M. Greenwald, R.L. Boivin, F. Bombarda, P.T. Bonoli, C.L. Fiore et al. H mode confinement in Alcator C-Mod. *Nuclear Fusion*, 37(6):793, 1997.

[62] D.G. Whyte, A.E. Hubbard, J.W. Hughes, B. Lipschultz, J.E. Rice et al. I-mode: an H-mode energy confinement regime with L-mode particle transport in Alcator C-Mod. *Nuclear Fusion*, 50(10):105005, 2010.

[63] G. M. Wallace, I. C. Faust, O. Meneghini, R. R. Parker, S. Shiraiwa et al. Lower hybrid current drive at high density in the multi-pass regime. *Physics of Plasmas*, 19(6):–, 2012.

[64] J.W. Hughes, A.E. Hubbard, G. Wallace, M. Greenwald, B. LaBombard et al. Modification of H-mode pedestal structure with lower hybrid waves on Alcator C-Mod. *Nuclear Fusion*, 50(6):064001, 2010.

[65] J. L. Terry, M. L. Reinke, J. W. Hughes, B. LaBombard, C. Theiler et al. Improved confinement in high-density H-modes via modification of the plasma boundary with lower hybrid waves. *Physics of Plasmas*, 22(5):–, 2015.

[66] Robert Thomas Mumgaard. *Lower Hybrid Current Drive on Alcator C-Mod : measurements with an upgraded MSE diagnostic and comparisons to simulation*. PhD thesis, Massachusetts Institute of Technology, June 2015.

[67] T. Eich, B. Sieglin, A. Scarabosio, W. Fundamenski, R. J. Goldston et al. Inter-ELM power decay length for JET and ASDEX upgrade: Measurement and comparison with heuristic drift-based model. *Phys. Rev. Lett.*, 107:215001, Nov 2011.

[68] M. Goniche, J. F. Artaud, V. Basiuk, Y. Peysson, T. Aniel et al. Lower hybrid current drive efficiency on Tore Supra and JET. *AIP Conference Proceedings*, 787(1):307–310, 2005.

[69] B. LaBombard, J.W. Hughes, D. Mossessian, M. Greenwald, B. Lipschultz et al. Evidence for electromagnetic fluid drift turbulence controlling the edge plasma state in the Alcator C-Mod tokamak. *Nuclear Fusion*, 45(12):1658, 2005.

[70] B. Lipschultz, B. LaBombard, E.S. Marmar, M.M. Pickrell, J.L. Terry et al. Marfe: an edge plasma phenomenon. *Nuclear Fusion*, 24(8):977, 1984.

[71] M. Greenwald, J.L. Terry, S.M. Wolfe, S. Ejima, M.G. Bell et al. A new look at density limits in tokamaks. *Nuclear Fusion*, 28(12):2199, 1988.

ALCATOR C-MOD AND LYMAN-ALPHA INSTRUMENTATION

Alcator C-Mod and its associated LHCD system are used to test the physics of Advanced Tokamak scenarios in reactor-relevant plasmas[1]. The high densities and magnetic fields available on Alcator C-Mod are in the range of parameters expected for high power-density diverted plasmas on future devices[2, 3]. LHRF testing on C-Mod is directly relevant for conditions of a steady-state tokamak fusion power plant. The physics tested in this thesis are dependent on plasmas utilizing these systems.

The importance of LHRF power edge losses described in the following chapters has required further instrumentation. Ly_α emission is directly related to the neutral/plasma interface that exists in the edge of tokamak plasmas[4]. The physical characteristics of the transition from the n=2 excited state to the ground state is ideal for localized measurements of the edge. These measurements can observe changes occurring to the edge plasma due to edge-deposited LHRF power.

The theory and implementation of pinhole Ly_α cameras are described. The vacuum ultraviolet (VUV) Ly_α light is difficult to measure as the pinhole system must be under vacuum. VUV pinhole cameras must also utilize special VUV-capable filters and diode arrays to discern changes in emitted power. These cameras have been used on a range of tokamaks for tomographic reconstruction of tokamak edge fueling[5, 6, 7].

The B-port Lyman-α (BPLY) camera radiometrically measures a near complete poloidal slice of the plasma using 22 sightlines. It can discern changes in ionization and recombination local to the main chamber and divertor. Because it has only one pinhole it cannot be used for tomographic reconstruction. However it can provide important information on the poloidal distribution of edge recycling light, which is a very close proxy for ionization intensity. Ly_{alpha} measurements have three principal advantages: it is very fast due to the large intensity of Ly_{alpha}, the minimal reflection from internal surfaces and the insensitivity of emission to T_e-determined rate coefficients. The high time resolution and relative sensitivity to edge changes are useful for a multitude of physics which includes edge LHRF deposition.

The BPLY camera has been vital in edge LHRF power characterization. Results shown in chapters 3 and 4 rely on the local measurements provided by this camera. The relation of the camera's measurements to ionization has been used to discover LHRF-induced ionization of the active divertor.

THE ALCATOR C-MOD TOKAMAK AND LHCD SYSTEM

Alcator C-Mod

Alcator C-Mod is a tokamak fusion device used for understanding physics related to reactor-relevant tokamak parameters such as high density, high magnetic field, diverted plasmas. It uses an innovative sliding-joint magnet design which allows for a majority of the magnetic field forces to be supported by a surrounding superstructure. As a consequence, it has the highest magnetic field of any operational tokamak with a divertor, capable of operating up to 9T. While smaller than most other major tokamaks, it accesses tokamak parameter values previously unavailable such as, but not limited to density, collisionality and heat flux. The wide range of operation and unique experimental capability is directly relevant for next step tokamaks.
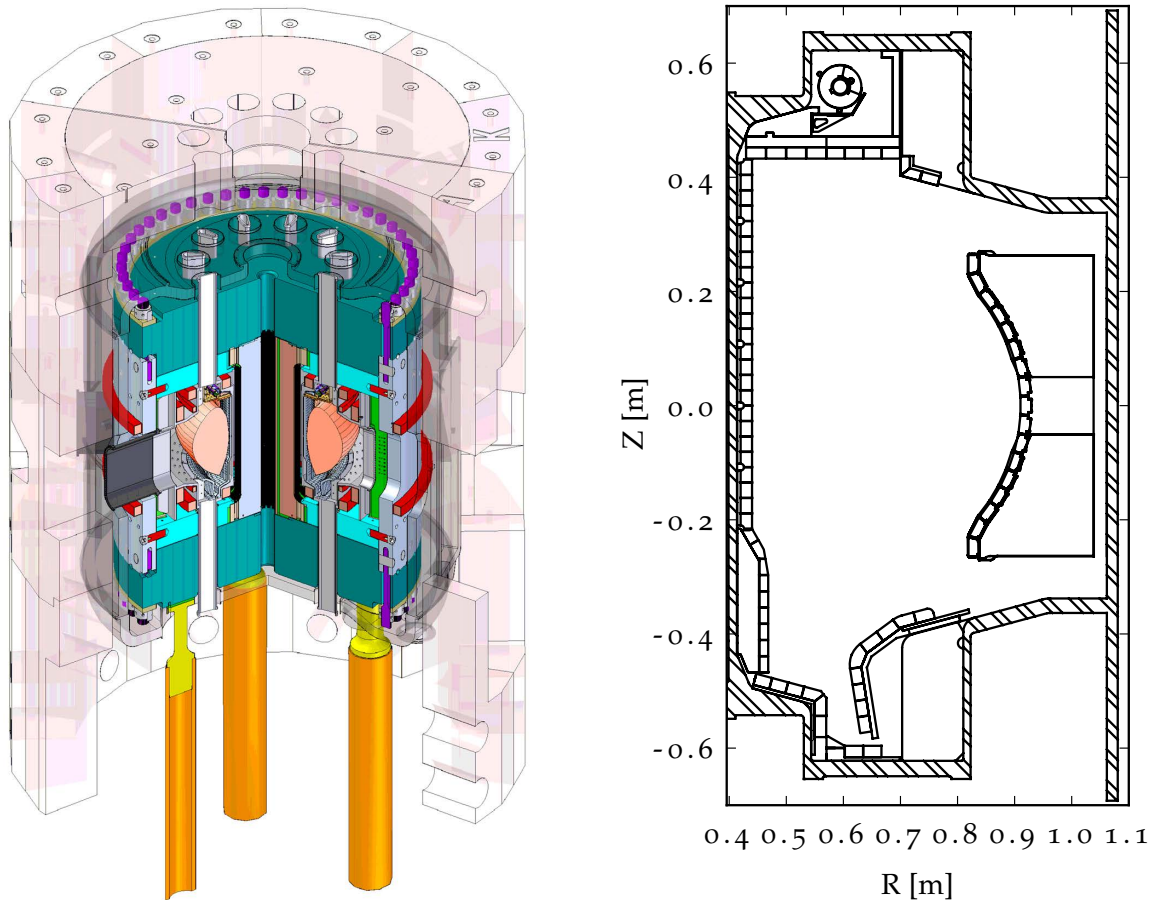
Figure 2.1: Alcator C-Mod is a high magnetic field, high plasma current diverted tokamak. The structure, neutron shielding, vacuum vessel, magnets and example plasma are shown on left. On right is the axisymmetric poloidal view of the vacuum vessel with the G-H limiter. The lower divertor has an optimized closed shape for heat handling. The upper divertor has an associated cryopump used for density control. The outer limiter is not axisymmetric, with various diagnostics and heating antennas placed about the outer midplane. The shown outboard limiter is closest to the plasma at the outboard.

A majority of Alcator C-Mod plasma discharges have toroidal magnetic fields of 5.4T with a range of plasma currents from 450kA to 1.2MA. Additional magnetic coils are used to create lower single null (LSN), upper single null (USN), double null (DN) and inner-wall limited (IWL) equilibria[8]. Development of plasma diagnostics on Alcator C-Mod has also occurred for over twenty years; the large collection of measurements characterize a range of parameters at many locations in the plasma[9]. These attributes combine into a versatile, unique and well-diagnosed tokamak which can address a wide range of physics questions important for tokamak fusion energy.

Auxiliary power sources on Alcator C-Mod are focused on radiofrequency heating and current drive. Three separate ion-cyclotron radiofrequency (ICRF) antennas are capable of heating tokamak plasmas to electron temperatures of 10 keV with 5MW of net power. Fully non-inductive plasmas can also be generated using the 1.2MW of LHCD power. When combined, these two systems are meant to be used to create 'Advanced Tokamak' (AT) scenarios which improve tokamak performance[1].

Major Radius	R	.666	m
Minor Radius	a	.21	m
Toroidal Field	B_T	9	T
Plasma Current	I_P	3	MA
Elongation	κ	1.8	-
Triangularity	δ	.4	-
Flat Top-duration	(@5T)	7	s
Flat Top-duration	(@9T)	1	s
Inductive Volt-s	-	7.5	Wb
Required Energy	-	500	MJ

Table 2.1: The upper bound of parameters of Alcator C-Mod as designed, reproduced from Fairfax[10]. Typical operation is either at 5.4T or 8T, with a range of currents from 450kA to 2MA. 5.4T operation minimizes the impact on felt-metal contacts in the magnet joints. A large superstructure supports the large magnetic forces created by the cryogenically-cooled copper magnets (using liquid nitrogen). A large flywheel supplies the necessary energy to generate the high-field plasmas.

AT scenarios utilize current profile control and high bootstrap fractions to create non-inductive discharges with internal transport barriers. These attributes generate long pulse plasmas with higher pressures which are both vital for tokamak fusion energy. The current generated in the plasma using LHCD expands the tokamak parameter space available for steady state, high performance operation of AT scenarios. Understanding LHCD physics on Alcator C-Mod is key for generating AT scenarios and extrapolating LHCD performance to future steady state tokamaks.

Lower Hybrid current drive on Alcator C-Mod

Lower Hybrid current drive is the most efficient method for generating non-inductive current in tokamak plasmas[11]. Through electron Landau damping, it generates an asymmetric non-thermal tail of high energy electrons[12]. The high energy (fast) electrons carry significant momentum and asymmetrically modifies the collisionality[13]. It is used on C-Mod to change the current profile and replace the inductive drive[1].

The Alcator C-Mod LHCD system utilizes ten klystrons each operating up to 250kW of 4.6 GHz radiofrequency power[14]. The power is generated in the Alcator C-Mod cell and is transported to the LHCD launcher via WR-187 waveguides. With the waveguide losses, the forward LHRF power into the plasma is limited to less than 1.2 MW[15]. This power is routed into what is known as the Lower Hybrid launcher, an end-fire phased waveguide array[16].

The current launcher is the second version with a four row by sixteen column grill of waveguides. The power of each klystron is split vertically to four individual waveguides in a column[15]. In order to power the 16 columns of waveguides, one klystron may supply the power to two columns. Klystron-to-klystron phasing is used to vary the column to column phasing, save for those columns supplied by the same klystron (which have a phase offset of $\sim 90°$).

Frequency	4.6	GHz
Waveguide rows	4	-
Waveguide columns	16	-
Waveguide Height	60	mm
Waveguide Width	7	mm
Waveguide Mode	TE01	-
Septum thickness	1.5	mm
Peak $n_{\parallel}$ upper limit	2.8	-
Peak $n_{\parallel}$ lower limit	1.5	-
Total Klystron Power	2.5	MW
Net Launched power	< 1.2	MW
Pulse length	$> .5$	s

Table 2.2: Parameters of the LH2 LHRF launcher on the Alcator C-Mod tokamak. It is used to create an asymmetric electron distribution for the creation of current in Alcator C-Mod. This can non-inductively create the necessary plasma current[15]. A wide range of launched $n_{\parallel}$ and P_{LH} are used in various plasma conditions.

The waveguide grill and wave phase control are used to generate a nearly electrostatic wave in the plasma with various $n_{\parallel}$. The main lobe of $n_{\parallel}$ can vary between 1.5-2.8 by changing column-to-column phasing. Some ($\sim 20\%$) of the power exists at high negative $n_{\parallel}$, re-

Figure 2.2: In vessel photograph from B-port towards the LH launcher at C-port. The phased waveguide array ('grill') has a 4x16 set of waveguides which can couple < 1.2 MW of 4.6 GHz power to the plasma from the outer midplane. The launcher can be moved radially to improve the coupling. The grill structure is used as an end-fire array to generate a nearly electrostatic wave in the plasma. This wave is evanescent in vacuum and must penetrate to the cutoff layer in the plasma. Each column of four waveguides are fed by the same kylstron, this design insures the purity of the coupled spectrum as axisymmetry will cause the column to column impedances to be similar. The power is redistributed poloidally, not toroidally. The column to column phase offset is generally 90°. The main lobe spectrum can vary, with a range from $1.5 < n_{\parallel} < 2.2$. Some power ($\sim$ 20%) is also launched at higher $n_{\parallel}$ in the reverse direction.
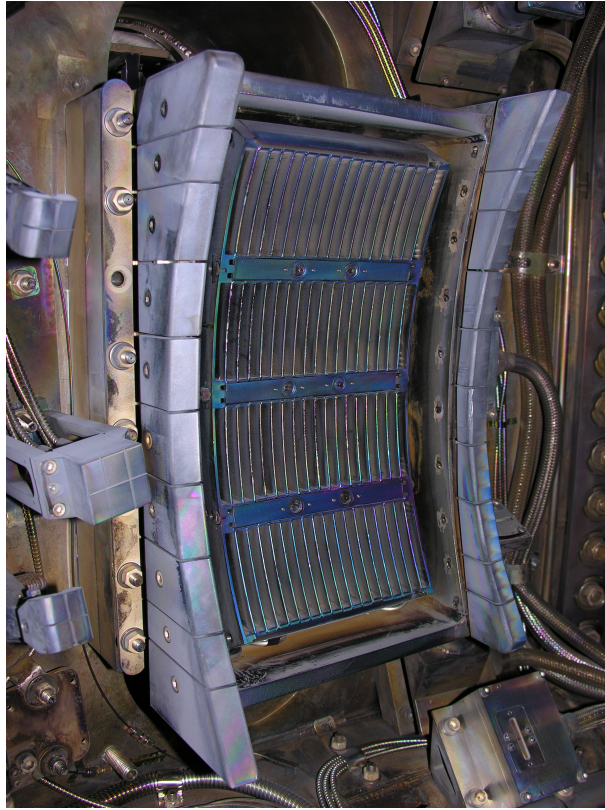
ferred to as 'reversed $n_{\parallel}$'. The choice of launched $n_{\parallel}$ strongly dictates the coupling as the wave must penetrate through the vacuum in front of the grill.

The launcher can be moved in and out radially to reduce this vacuum gap and maximize coupling. It is also instrumented with Langmuir probes, thermocouples, and a reflectometer[17] to characterize the plasma and grill. The control system allows for extended operation of the LHRF launcher which are limited by the cathode heating in the klystron (.5s of full beam current)[18]. Together this system is used to drive current in the Alcator C-Mod tokamak.

The Alcator C-Mod LHCD system is capable of driving fully non-inductive plasmas. It can reduce or remove sawtoothing behavior and can generate internal transport barriers[19]. While this system has been effective for low $\bar{n}_e$ cases, its utility in high $\bar{n}_e$ cases has been extremely limited. This work explores and quantifies the edge deposition of LHRF power theorized and observed at high densities.

LYMAN-α PHYSICS AND RADIOMETRY

Ly_{α} emission and its relation to the plasma boundary

Nearly every ion and electron in the plasma is generated from the ionization of atoms near the boundary of the tokamak. It is diffi-

cult to model or characterize the edge plasma particle source due to the complicated interaction of ionization, excitation, recombination, charge-exchange and transport of particles in the two dimensional, narrow boundary plasma. The intensity and spectrum of edge light corresponds to the background SOL parameters but are influenced by atomic characteristics of the particles. Atomic physics databases provide rate coefficients which allow the translation of edge photon emission to parameters of interest, such as ionization rates and power loss[4]. For fueling to impurity generation, the observed light can then be translated in various SOL attributes using these coefficients.

Tokamak experiments use wall materials that reflect significant amounts of visible radiation. The reflections from metallic wall materials like refractory metals (*e.g* Tungsten and Molybdenum) can deleteriously impact the interpretation of edge measurements. The additional light sources can create spatial features which requires analysis to remove which vary in time and space making interpretation difficult.

Hydrogenic Lyman-α, known as Ly_α through the thesis, is the light is emitted from the transition from the $2p$ state to the ground $1s$ state. The wavelength is 121.53 nm for deuterium and 121.56 for hydrogen, but are indistinguishable in BPLY measurements. This line emission has characteristics which are more ideal for characterizing the neutral/plasma boundary. Ly_α light is closely linked to the neutral particle background due to the transition to the ground state. The Einstein coefficient $A_{2,1}$ (for Ly_α) is $4.69 \cdot 10^8$ s^{-1} is the largest for all hydrogenic transitions and is an order of magnitude greater than $A_{3,2}$ ($H_\alpha = 4.41 \cdot 10^7$ s^{-1})[20]. Einstein coefficients plays a role in relativistic measurements[21] which make Ly_α ideal, but are unimportant at low temperatures in edge plasmas. The reflection of Ly_α light is minimal due to its vacuum ultraviolet (VUV) nature[6]. Ly_α is especially bright due to the lack of other radiative transitions for the $n = 2$ excited state and its inherent relation to the ground state. These attributes allow for a more precise estimation of the background plasma attributes and neutral fueling conditions. The close relation to the ground state is observed in the coefficients which relate emission to plasma conditions.

One such example of the close relation between Ly_α emission and ionization is the S/XB coefficient. This value is used to turn absolute measurements of line radiation into fluxes of neutrals undergoing ionization for a given background electron density and temperature. *S* is the ionization rate, *X* is the excitation rate and *B* is the branching ratio, this coefficient is defined using a collisional-radiative model. For Ly_α emission in the edge of tokamak plasmas, this value is relatively constant near unity. This is shown in figure 2.3 for the range of 5eV $< T_e <$ 100 eV. A value of 1 signifies that one ionization corresponds to one Ly_α photon. The relatively flat value of S/XB ($.4 < S/XB < 1.6$)

Figure 2.3: The Ly$_\alpha$ S/XB coefficient relates the observed fluence of photons to hydrogen ionizations[22]. *S* is the ionization rate, *X* is the excitation rate and *B* is the branching ratio. It is typically used for characterizing impurity and main-ion influxes from surfaces. The flat value near unity for typical SOL conditions indicates the close relation of Ly$_\alpha$ emission to ionization in tokamaks. These attributes make Ly$_\alpha$ measurements useful in understanding the edge particle/plasma interface.
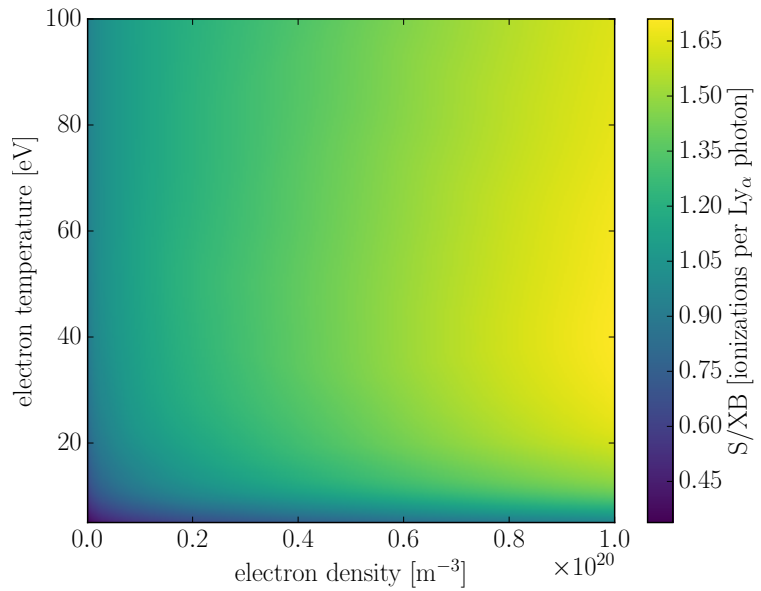
means that the intensity of emission is proportional to the ionization for all C-Mod SOLs.

In some very high neutral densities, the optical depth (attenuation scale length) is short enough for Ly$_\alpha$ light to be reabsorbed (trapped)[23]. This has been observed in the Alcator C-Mod divertor near detachment but is not the case in the plasma conditions used in the following chapters. This effect highlights the highly absorptive nature of Ly$_\alpha$ emission and its strong relation to the edge neutral conditions.

While the physics behind the generation of Ly$_\alpha$ light is favorable for understanding the plasma, its use in measurement has been very limited. The high energy of the emitted photons (10.2 eV) requires diagnostic implementations similar to measurements of the EUV and SXR light in tokamaks. The following sections describe the implementation of a Ly$_\alpha$ camera called the BPLY camera on Alcator C-Mod. It uses this close relation to ionization for understanding the effect of edge deposited LHRF power.

Introduction to Ly$_\alpha$ pinhole cameras

Vacuum ultraviolet light (100-200 nm) is significantly attenuated in air and cannot propagate through any known vacuum window material. VUV light is also rapidly attenuated in most detector materials (*i.e.* silicon), which makes measurement of the light very difficult. As a consequence, all measurements of this wavelength band of light must occur under vacuum. Its measurement requires specially designed vacuum-capable diodes with thin passivation layers so that the photons can be properly observed.

VUV light cannot be collimated with standard optics and must be measured using a pinhole camera. These cameras significantly reduce the photon fluence in exchange for generating an image plane. The 'pinhole' is a small opening with a small but finite area which allows light to pass through. The pinhole and a point on the image plane creates a line where only photons emitted along that line are observed. This line is known as a sightline or chord. The BPLY (B-Port LYman-alpha) camera is a pinhole camera under vacuum which utilizes a pinhole system with twenty-two sightlines. Each sightline is defined by a measurement diode and the pinhole.

Unlike typical visible optics, pinhole cameras have infinite focus meaning that the focal plane at any distance is accurately resolved at the image plane. The magnification is set by the pinhole-diode geometry with the spreading of sightlines indicating reduced magnification. In other words the distance of the focal plane to the pinhole sets the magnification, with larger images observed at greater distances. This is ideal for optically thin plasmas where the main goal is volumetric radiometry without a distinct focal plane.

However, each sightline has a finite pinhole area and a finite diode area. The total incident power onto a detector for an optically thin media is defined in equation 2.1. The emissivity per unit steradian ($W/m^3/sr$) is defined as $d\varepsilon/d\Omega$, and is integrated over volume V. The diode only measures some solid angle of this emission (Ω) and depends on the emission location $\vec{r}$.

$$P = \int_v \int_\Omega \frac{d\varepsilon}{d\Omega} d\Omega d^3\vec{r} \qquad (2.1)$$

A viewing volume can be interpreted an integral over a set of rays or paths with differential cross-sectional areas, together these are known as beams. For pinhole cameras, a single chord is defined by the integral $\vec{r}$ which is set by the sightline generated by the pinhole and diode. The length along the sightline is s and has a differential cross sectional area defined as $dxdy = dA$ ($d^3\vec{r} = dsdxdy = dsdA$). dA is proportional to s^2 due to the spherical Jacobian ($dA = s^2 dA'$). The differential solid angle along s is proportional to s^{-2} as the detector subtends a reduced solid angle with increasing distances ($d\Omega = s^{-2}d\Omega'$ also generated from the spherical Jacobian). These simplifications generate equation 2.2 with parameter $G = dA'd\Omega'$.

$$P = \int_v \int_\Omega \frac{d\varepsilon}{d\Omega} dxdyd\Omega ds = \int_v \int_\Omega \frac{d\varepsilon}{d\Omega} Gds \qquad (2.2)$$

G is a constant along s due to the interplay of the area and solid angle with the spherical Jacobian (*e.g.* s^2 from the increase in area balances s^{-2} from the decrease in solid angle). This is illustrated graph-

Figure 2.4: In Hamiltonian optics, the étendue is an invariant for the cross sectional area and solid angle phase space of a ray or line of sight. Two cases with the same étendue on right show the balance of area to solid angle for a pinhole sightline. A larger cross-sectional area is balanced by a reduced solid angle, and vice versa. The integrated area and solid angles are shown by the solid blue regions on the plots of x, y and Ω respectively. A cartoon representation is given by dx, dy and $d\Omega$. The étendue is defined for the differential area and solid angle, which pinhole optics approximate.
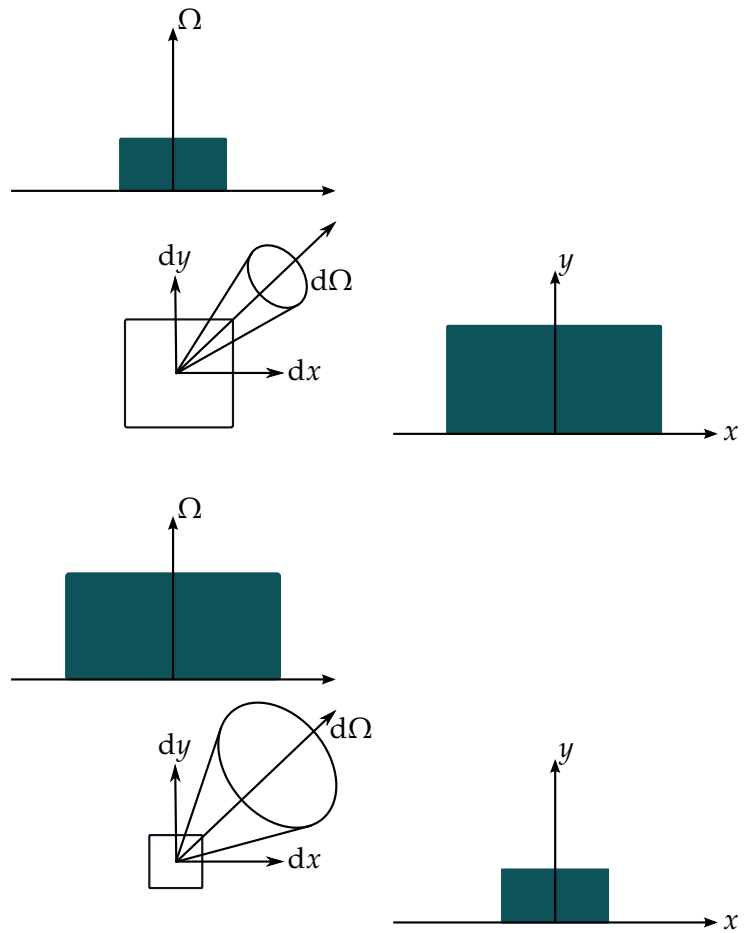
ically in figure 2.4. G is known as the étendue, has units of m^{2}sr and is used widely in the field of Hamiltonian optics. The étendue varies from beam to beam and is still a function of position and angle. It is only constant along one ray or sightline trajectory. In the case of an isotropic source, and a constant value G the integrals given in 2.2 can be further simplified to an integral over ds as is shown in equation 2.3.

$$P = \int_s \varepsilon(s) \frac{G}{4\pi} ds \tag{2.3}$$

Both the area and solid angle do not vary significantly across the cross-sectional area for a pinhole camera by definition. Thus, dA' and $d\Omega'$ can be numerically determined given the geometry of the pinhole and detector. This gives a single value for G along the idealized singular sightline. At the pinhole, the solid angle of the detector is $d\Omega' = A_{det}/d^2$ where d is the distance from pinhole to the detector along s. The area is simply $dA' = A_p$ at the pinhole. The étendue is $A_{det}A_p/d^2$ for a single chord in a pinhole geometry.
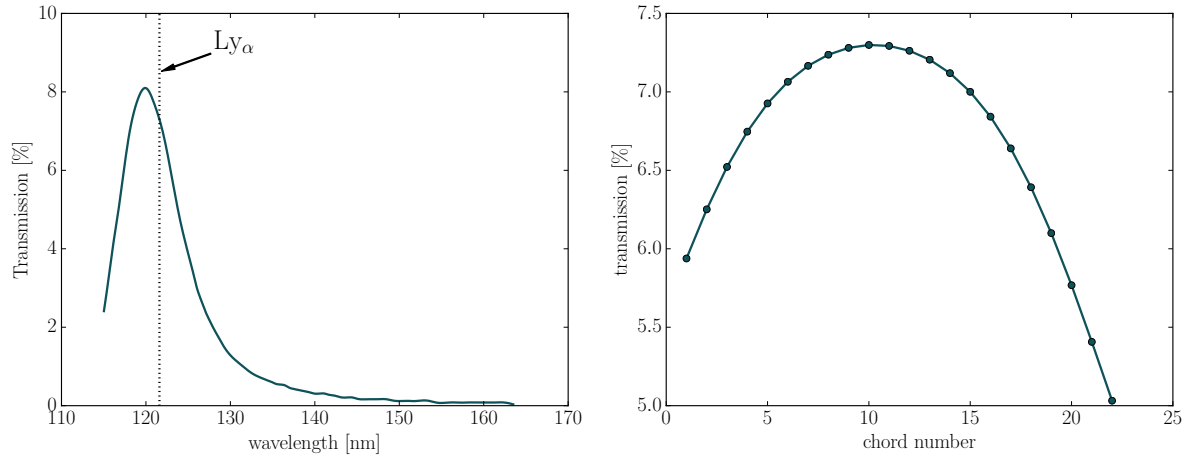
Figure 2.5: The BPLY camera uses a MgF$_2$ transmission interference filter for isolating Ly$_\alpha$. Manufactured by Acton Optics, the filter function blue-shifts with off-axis incidence and is described in equation 2.4. The normal-incidence filter function for the BPLY is shown on left. Off-axis light incidence reduces the transmission of the filter for chords viewing the upper and lower divertors (*i.e.* on the ends of the diode array) as shown in the figure on right. This loss in transmission does not account for increased attenuation due to the increased path-length through the filter.

The value $4\pi P/G$ is known as the brightness and is extensively used in the field of tomography. Brightnesses allow for rough chord-to-chord comparisons as vignetting across the image plane is removed. Uses of pinhole cameras in this work utilize brightnesses for this reason (except in the case of the HXR camera where the detector signal is given as a count rate of discrete high-energy photons.).

The measured power, and by extension the brightness, is also a function of any attenuation in the sightline. Attenuation in the plasma is neglected in optically thin media like tokamak plasmas. However, the addition of a filter can reduce the power onto the detector. Radiometric measurements of Ly$_\alpha$ power require accounting for the transmission of the filter.

The filters used in pinhole Ly$_\alpha$ cameras were developed by Acton Optics near the wavelength limit of transmission interference filters. The MgF$_2$ interference filters have a 120 nm peak with a FWHM of 8.6nm and are generally placed between the diode and pinhole to minimize plasma exposure. The transmission characteristics versus wavelength for the BPLY filter is given in figure 2.5. Interference filter transmission is a function of the light incidence angle as the layer spacing appears larger. For the BPLY filter, the transmission characteristics are defined at normal (90°) incidence.

The change in the effective layer spacing can be characterized using equation 2.4 with a known index of refraction of the filter n_f and of the surrounding medium n_0 (vacuum). The filter transmission at wavelength λ_0 will be the transmission at wavelength λ for angle θ. The value of transmission for various chords can be solved by find-

ing the corresponding λ_0 value. Overall, the filter function blue-shifts with increasing off-normal incidence.

$$\lambda(\theta) = \lambda_0 \sqrt{1 - \left(\frac{n_0 \sin\theta}{n_f}\right)^2} \tag{2.4}$$

The impact on the measurements is also shown for each of the BPLY chords in figure 2.5. Outer chords of the BPLY will have a 30% reduction in the measured power due to off-normal incidence. However, this calculation does not include the additional attenuation from the increased path-length through the filter. This reduction in the transmission is not accounted for in the BPLY, but likely makes a minimal change in the filter transmission (likely $< 15\%$).

The use of filters and pinhole optics under vacuum allows for the radiometric measurement of VUV Ly$_\alpha$ light. The data and analysis of Ly$_\alpha$ measurements relies on multiple measured brightnesses and their comparison. The line-integrated signals can be used for tomography and poloidal localization of ionization in the SOL plasma. The absolute measurement of power relies on properly characterizing all attenuation and geometrical effects.

Design goals of the BPLY camera

The BPLY camera is designed to look at poloidal asymmetries in the edge Ly$_\alpha$ emission along field lines connected and not connected to the LHRF launcher. The diagnostic is located close to the launcher at B-port to view field lines connected to the LHRF launcher that are otherwise intercepted by the AB limiter. This limited the available space to install the camera to a midplane port previously used for Lithium pellet injection[24]. As with all C-Mod diagnostics, it must meet the necessary vacuum, electrical, and radiation requirements in a small size.

Its capabilities match the expected attributes of the Alcator C-Mod SOL. Reasonable diagnostic time resolution ($\sim$ 1ms) is necessary to accurately characterize the rapidly varying SOL conditions. The edge plasma exhibits a short confinement time of energy and particles in the edge. Also, a large pinhole size is used to maximize the étendue and throughput while also giving reasonable spatial resolution. The toroidal extent of measurement extends nearly $\pi/12$ at the inner wall, as can be roughly observed in figure 2.9. The large light fluence reduces the necessary gain and maximizes signal-to-noise of the digitize signal. Together the strong signal and fast time resolution accurately measure the varying spatial conditions of the neutral/plasma interface.

Figure 2.6: The twenty-two sightlines of the pinhole BPLY camera (in blue). The camera nearly views the entirety of the vacuum vessel with some limitation in the upper divertor and the outer strike point. Located at B-port, the camera measures on fieldlines connected and not connected to the launcher. The separatrix of shot 1140822011 at 1.0s is given in red, with internal flux surfaces with dashed lines. This equilibrium represents the plasmas used in chapters 3 and 4. The wide view gives measure in the polodial character of the neutral/plasma interface, but does not allow for effective tomography of this emission.
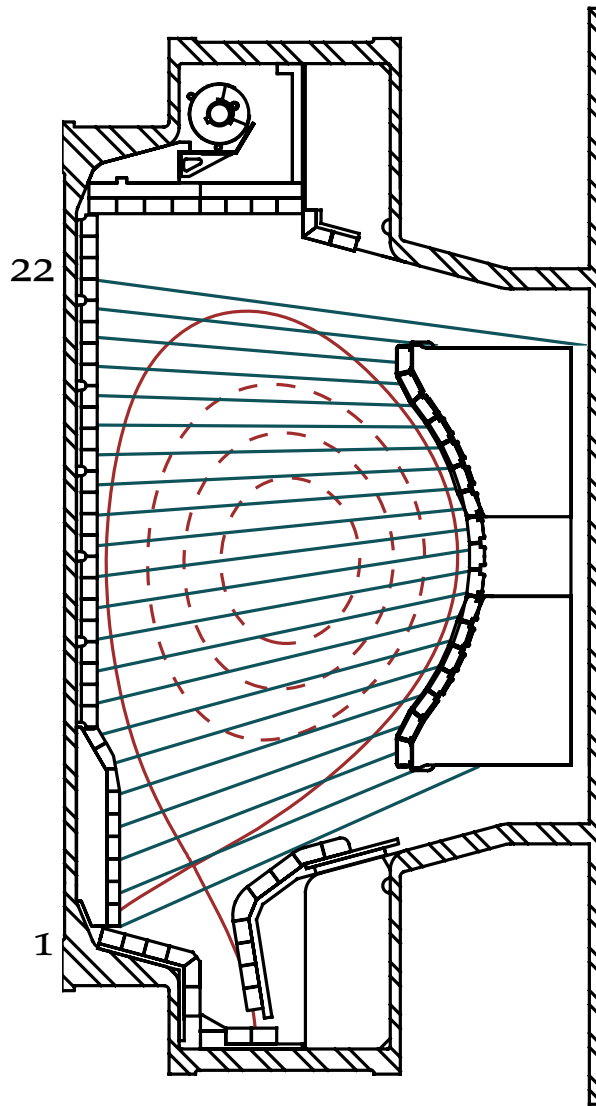
An AXUV array was used due to the low cost and spatial limitations of the view, limiting the camera to twenty-two chords. This limits the spatial resolution and removes the possibility of tomographic reconstruction. Other similar Ly_α pinhole cameras were used for this purpose with example data shown in figure 4.3. However, the twenty-two chords are capable of sufficiently determining the polodial character of Ly_α emission.

The wide view of the camera is shown in figure 2.6. It observes the emission from the lower to the upper divertor which is limited by the vertical extent of the port nearest the plasma. This viewing geometry allows for all plasma topologies to be characterized. The plasmas used in the following chapters have the entire plasma volume within the BPLY field of view except the outer leg of the lower divertor. However, the radially inward view cannot separate in/out

difference in Ly$_\alpha$ emission, requiring correlation with other diagnostics.

In order to minimize cost and development time, previous similar bolometer and Ly$_\alpha$ camera components were reused. The filters were designed for a smaller AXUV diode array, limiting the filter distance from the pinhole. The electronics are the same as those used on other AXUV systems on Alcator C-Mod[25, 26]. Digitization of the output voltage was made using available channels previously used for the other AXUV systems at 250kHz.

The BPLY meets the necessary geometric constraints to measure the LHRF-induced SOL changes both near and far from the launcher. Electronics, diodes, filters, and other components meet the stringent requirements necessary to measure Ly$_\alpha$ emission under vacuum. Unfortunately, the geometry is incapable of determining the in/out variation of emission. In the following sections the method for interpreting the BPLY will be explained.

Mechanical Design of the BPLY camera

The BPLY camera was designed to create the necessary pinhole geometry, to minimize stray light, and to operate under vacuum, all at minimum cost. BPLY's design contained some innovation necessary to achieve these goals within the prescribed constraints. This is highlighted in the filter placement and simplicity in construction. The associated mechanical design builds from a heritage of similar systems on the Alcator C-Mod tokamak[6, 25, 27].

The pinhole-diode distance, vital for the geometry of the fan of sightlines, is generated using three components which minimizes the manufacturing-induced geometric errors. The pinhole mounts to a circular plate of set thickness which connect to two pylons. The pylons are the main components which attach the camera to the flange. The AXUV diode is mounted to a plate which connects to these pylons. These three components are connected via screws, with the distance error dependent on the AXUV plate and pinhole thickness and the placement of the AXUV mount holes. Notches in the pylons fit the filter and diode mounts and constrain their rotation as they are not controlled by the side mount screws. The filter and diode mounts slide in between the pylons at the notches. These notches are not shown in figure 2.7 as they are mating surfaces.

This structure also mounts the filter and external shroud, completing the invessel components of the BPLY camera. The two flange screws are covered with shim stock and spot welded to prevent them from becoming loose. Components inside the shroud are all independently too large to fall into the vacuum vessel. The only other screws which can cause catastrophic failure, the outer screws of the shroud, are also shim-stock covered to keep them in place.

Figure 2.7: The mechanical design focuses around setting the proper diode-pinhole distance (the diode is in green and pinhole in blue) while also allowing for the use of the small MgF_2 filter. A custom copper gasket (in orange) is compressed in order to insure a light-tight seal around the filter. The entire system is attached to the 4-5/8" flange via two screws. The diodes are fed through the flange via a d-sub connector, with a short in vacuum cable run. The vacuum flange attaches to B-port via an added extension. The camera angle and location is the same as the previously implemented Lithium pellet injector[24].
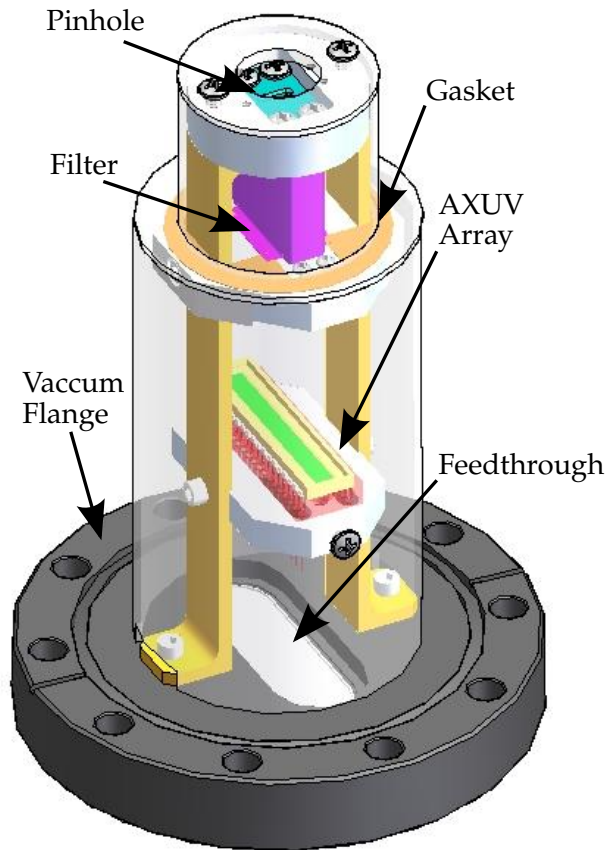
The used AXUV diodes can measure light from the near infrared to soft X-rays. Various sources of light other than filtered Ly_α photons must be reduced as much as possible. This is accomplished two ways in the BPLY, first through its geometry and secondly by passivation. For stray light to reach the AXUV diodes, several reflection are required on surfaces which minimally reflect.

The BPLY camera is placed within a 2-7/8" ID tube, which is recessed from the B-port flange face. The camera shroud shown in figure 2.8 fits closely within the tube (with a difference in radius of .25"). This exterior surface fits closely to the flange and covers the camera from the flange to the pinhole. The small difference in diameters is not significantly impede the flow of background particles necessary for fast vacuum pumping. All metallic components are passivated to minimize reflection, except for the filter gasket and screws. The passivation absorbs light across the visible to UV spectrum. Stray light which reflects from the flange must interact with the shroud at least once, and is geometrically limited by the vacuum extension and shroud design.

The shroud and filter mount also limit the stray light through the pinhole. Rather than shroud the AXUV diode array closely with the filter, the small filter (meant for the smaller AXUV-20ELG) had to be moved closer to pinhole to meet the geometric constraints. The filter

Figure 2.8: All major mechanical pieces of the BPLY camera were manufactured in-house and are capable of handling the in-vessel temperature, vacuum, and radiation constraints. All mechanical components were passivated in order to minimize in-camera light reflection. Stray light requires a minimum of two reflections to be observed on the AXUV diode array.

mount is made of three components and is designed to be removed for bench-top calibrations without disturbing the pinhole-diode geometry. The filter is mounted on a single piece which slides between the pylons, with two other pieces which mount on either side of the pylons. A set of screws combine all three filter mount pieces with the pylons. A custom thin copper gasket is placed over the filter plate so that stray light cannot travel through the contact surfaces of the three filter components.

The filter gasket is compressed between the shroud and the compound filter plate. This seal separates the pinhole and filter region from the filter and diode region. Other Ly_α designs have been noted to locate their filters too close to the pinhole and have had boron coatings from boronizations. The location of BPLY camera and the pinhole-filter distance are both sufficiently large to minimize the effects of boronization[28].

The pinhole was cut into a small stamp-like piece using electrical discharge machining. Through this process a precise 3mm by 4mm pinhole was made for use on the BPLY, several stamps with different pinhole locations were also made which can subtly change the view. Its movement is constrained by the machined surface in the circular pinhole mount and the four mounting screws.

The volumetric view of this camera in the Alcator C-Mod tokamak is shown in figure 2.9. Some chord-to-chord view overlap is due to the large pinhole size. The larger view reduces the BPLY poloidal precision but is balanced by a larger signal-to-noise from the increased throughput. In the following section, the impact of the increased

chord	étendue [10^{-3} mm^{2}sr]	filter incidence angle
1	6.646	72.36°
2	6.850	73.78°
3	7.044	75.22°
4	7.226	76.68°
5	7.394	78.15°
6	7.547	79.65°
7	7.682	81.15°
8	7.799	82.67°
9	7.895	84.20°
10	7.970	85.74°
11	8.023	87.29°
12	8.052	88.84°
13	8.058	89.61°
14	8.040	88.06°
15	8.000	86.51°
16	7.936	84.97°
17	7.850	83.44°
18	7.743	81.91°
19	7.617	80.40°
20	7.472	78.90°
21	7.311	77.41°
22	7.136	75.94°

Table 2.3: The pinhole-diode geometric characteristics of the BPLY camera. These values dictate the filter transmission and chord étendue for each diode. Together they set the throughput and sensitivity of each measurement and are defined in the pinhole coordinate system. The BPLY diagnostic is designed to maximize Ly_α photon throughput through a wide toroidal pinhole extent.

throughput is apparent in the electrical circuity used for this measurement.

Transimpedance amplifiers and electronic design of the BPLY camera

The Ly_α light is measured using a 22 diode AXUV-22EL array. AXUV diodes, manufactured by IRD inc. (now Opto-Diode Corp), are meant for measuring light across a wide spectrum. They come in a wide assortment of shapes, sizes, and arrays. This family of silicon diodes has a specially designed thin (~ 8 Å) passivation layer to allow for VUV photons to reach the p-n junction. These photons can then generate current proportional to the photon flux which can be measured.
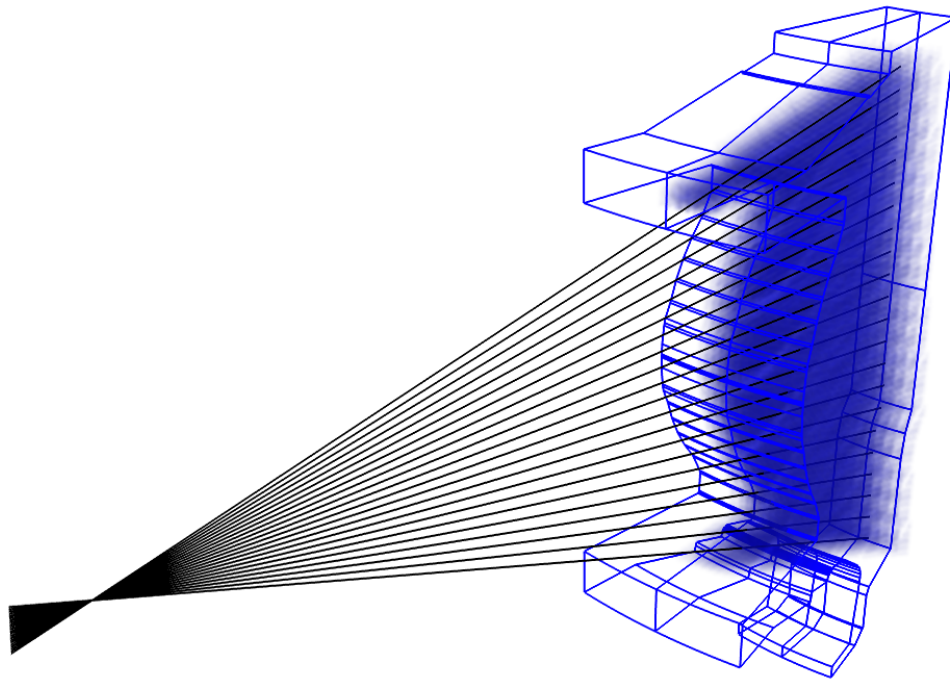
Figure 2.9: A 3D isometric representation of the BPLY camera on Alcator C-Mod. The idealized sightlines for the 22 chords are shown in black. The sightlines intersect at the pinhole in B-port far from the plasma.The wireframe blue outline is a $\pi/12$ segment of the Alcator C-Mod first wall and vacuum vessel. The translucent blue cloud is a 3D rendering of the volumetric measurement of the BPLY camera. It shows a consistent chord-to-chord overlap. The chords extend $\sim \pi/12$ toroidally around the vessel to maximize throughput.

Shown in figure 2.10, the responsivitiy (or current per watt of photons) is .108 A/W at 121.6 nm.

Each diode anode is connected via a common ground at each corner of the diode array using wire bonds. The cathodes and common grounds travel through the flange using a 25 pin D-subminiature feedthrough into the amplifier boards. The small travel distance in the vessel ($\sim$ 1.5") minimizes the current induced in the circuit by toroidal and poloidal magnetic flux. The amplifier boards convert the current into a voltage for measurement.

An inverting transimpedance amplifier is used to convert the diode current into voltage, shown in figure 2.11. Voltage gains are set by the feedback resistor of the operation amplifier. Feedback resistances of 10^6 Ω generate sufficient voltages with reasonable signal-to-noise ratios. This is set by the value of R_f in figure 2.11, with the capacitor C_f used to prevent ringing in the circuit. Lower gains allow for higher signal bandwidth, improving the time resolution. As a consequence of the significant photon throughput and reasonable signal-to-noise, no voltage bias is used to improve the signal bandwidth.

The transimpedance amplifiers are located at B-port on a two meter cable from the vacuum feedthrough. Signal measurements from the
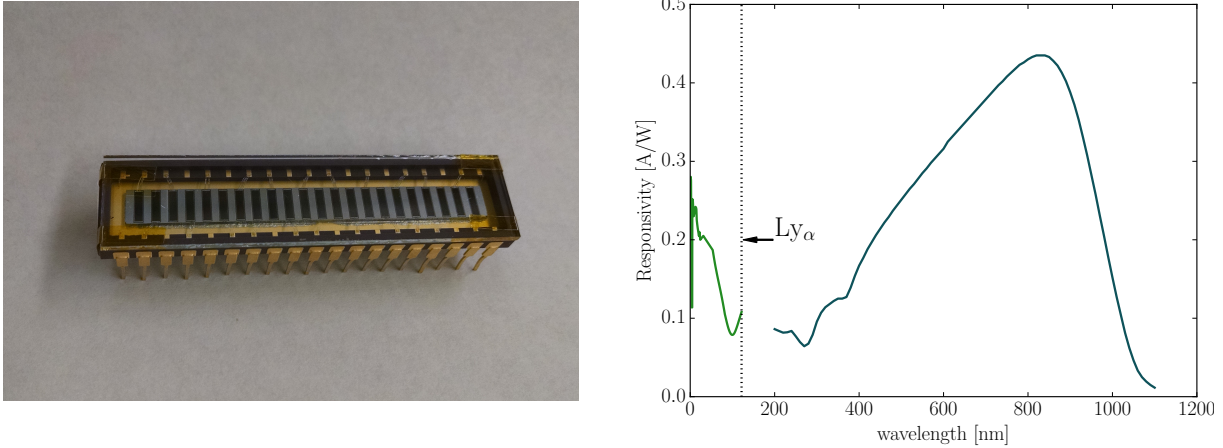
Figure 2.10: On left, an example AXUV-22EL of the same model used in the BPLY camera with protective glass cover. This silicon-diode array has a thin passivation layer in order to measure vacuum ultraviolet (VUV) radiation. The sensitivity versus wavelength is given on right, with a vertical line at hydrogenic Ly_α transition (121.6 nm). The sensitivity of AXUV diodes is .108 A/W at 121.6nm. The two separate trends represents two separate measurements of sensitivty for different wavelength ranges. Wire-bonds connect the four corner grounds and diodes to the The lack of a flat response limits these diodes use in bolometric measurements, but are well-suited for VUV measurements under vacuum.

cathodes of AXUV diodes have been known to be photoemissive especially in the 70-140 nm range. While this effect has not been observed on other C-Mod AXUV systems, any significant negative voltages are likely due to this effect.

The common ground of the amplifier circuit and diode is grounded at a single point on the B-port flange. This minimizes the possible ground loops which are known to create significant noise due to the tokamak driven changes in magnetic flux. The digitizer measures differentially even though it operates using a separate power supply and ground. However, no noticeable increase in noise occurs during a discharge, indicating that it is properly isolated.

The voltage output is measured using a DTACQ 196 with 250 kS/s sampling rate at J-port. Each signal shares a common ground from the amplifier, which is split to the various digitizer channels near the digitizer. The high impedance of the DTACQ 196 (20 $k\Omega$) means that for a 1V signal the amplifier drives .05 mA. This circuit does not require the use of buffers to supply the necessary current to drive the circuit.

Together, the BPLY electronics are capable of measuring the power of Ly_α photons using photodiodes and transimpedance amplifiers. The circuity converts currents into voltages at time-scales sufficient for edge measurements up to 10kHz. Single-point grounding and extensive shielding minimize the induced noise from diode to digitizer. The simple but effective electronics are sufficient for measurements on Alcator C-Mod.

Figure 2.11: The current generated by the AXUV diodes are converted to a voltage signal using a transimpedance amplifier. The linear response of the circuit to the diode current is due to large input impedance of the op-amp. A majority of the current flows through R_F which sets the current to voltage gain. The high gains necessary for the low Ly_α fluence require additional capacitance (C_F) to provide circuit stability (as the AXUV diodes have some inherent capacitance). A bias voltage can reduce the capacitance which can improve the circuit bandwidth, instead no bias is used on the BPLY. Gains of $2 \cdot 10^6$ are used outside the lower divertor (Chords 6-22) with reduced gain ($1 \cdot 10^6$) for the other channels.
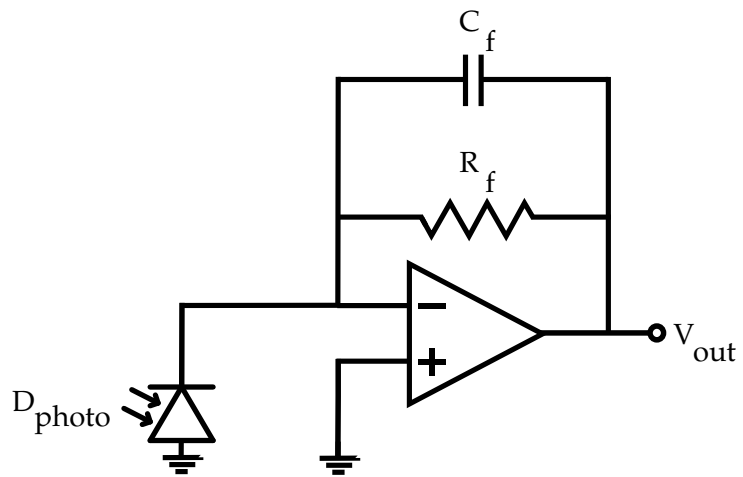
Performance and limitations of the BPLY camera

The inverting transimpedance amplifiers generate negative voltages on the digitizer. Digital signal smoothing on the sampled data is used to reduce high frequency fluctuations in the signal. Fluctuations in the signal are similar in time channel to channel. It is recommended in future iterations that one diode be covered so that these fluctuations can be removed in amplifier circuit. This can improve the time resolution significantly.

An example signal time trace is highlighted in figure 2.12. The signal can still recover 1kHz features in the signal, with 101 point smoothing being sufficient to remove this noise. Typically signals are multiplied by -1 and then smoothed for analysis. The shown work in future chapters utilize this approach in the analysis of BPLY chords.

Several channels have damaged connections on the vacuum side of the BPLY camera. Chord 4 has an intermittent connection and is typically not utilized. Other channels (such as chords 11 and 12) have similar effects at a reduced level. With sufficient smoothing, these chords can also be used in analysis.

Photoemission from the diode (which causes an unexpected negative measured power) occurs in specific cases on specific channels. This is due to the transimpedance amplifier measuring the current from the cathode. This is especially evident in cases with extremely large LHRF powers with significant current drive on chords which view the edge of the plasma. It is likely that high energy photons are able to penetrate through the filter into the diode and liberate electrons and photons.

Channels outside the divertor tend to have signal levels on the order of .1V. Divertor channels often approach 1V, showing the signifi-

Figure 2.12: Analysis of BPLY signals requires first inverting (multiply by -1) then smoothing the data. Shown on right is a raw (green) and smoothed (black) voltage trace from Chord 3 on 1160722014 which views the lower divertor. Voltage levels are typically less than 1V, and are smoothed to a ~ 1 kHz Nyquist frequency.
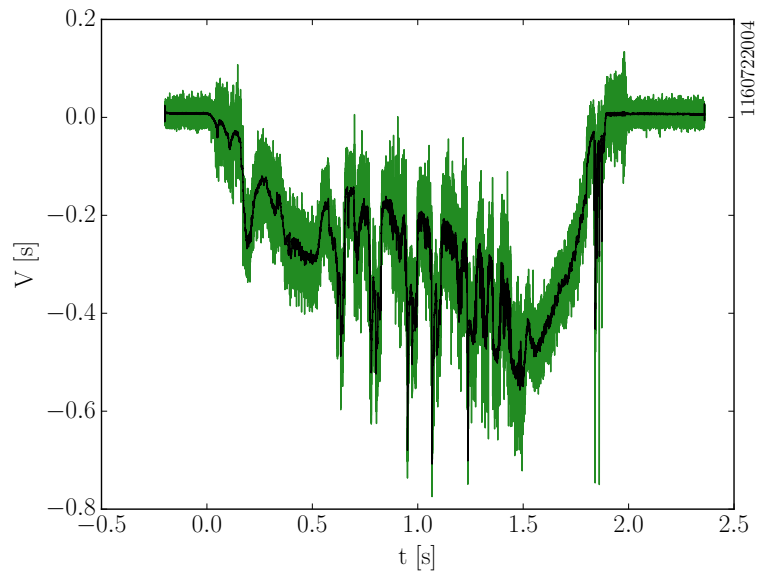
cant poloidal difference in ionization and recombination in diverted plasmas. Together the electronics and design of the BPLY camera yields sufficient data for analyzing edge effects on Alcator C-Mod.

SUMMARY AND DISCUSSION

The unique capabilities of Alcator C-Mod and its LHCD system are key for understanding current drive for future tokamaks. The 4.6 GHz kylstrons and phased waveguide array are used as a system capable of driving the entire current of an Alcator C-Mod discharge. Together these systems can be used to address and test a wide range of physics necessary for tokamak fusion reactors including AT scenarios. The experimental framework of C-Mod and its LHCD system lay the foundation for the experiments of this thesis.

A Ly_α camera was designed and implemented on the Alcator C-Mod tokamak at B-port. It is meant to observe edge effects due to LHRF at high electron densities on field lines which connect to the LHRF launcher due to its location. However, it can also measure field lines which do not intercept the antenna. While Ly_α light is closely related to the edge neutral/plasma interface, it is difficult to measure. The BPLY Ly_α camera accomplishes this through the use of a pinhole with special silicon diodes, all of which are under vacuum.

While some limitations due exist in the implementation, the mechanical and electrical design of the BPLY can be used for other vacuum compatible pinhole cameras on C-Mod and elsewhere. The simple mechanical design is effective for minimizing stray light while also meeting the extreme invessel conditions. It designed for simple bench-top calibration and maximizing photon throughput. The electrical design utilizes the same electronics of other similar AXUV systems. When combined, the electrical and mechanical attributes of the

BPLY yielded accurate local measurements of ionization and recombination on Alcator C-Mod.

While some limitations in the use of AXUV diode arrays do exist, the system is capable of providing accurate measurements of the invessel Ly_α conditions. Digital smoothing can recover useful, unambiguous changes in the edge plasma under various conditions. While under certain rare conditions the array responds unusually, in a majority of circumstances it operates as expected. This robust system is useful for a range of edge physics and is vital to the characterization of edge losses of LHRF power. The experimentation highlighted in the following chapters utilizes these measurements to great effect in both time and space.

BIBLIOGRAPHY

[1] P.T. Bonoli, R.R. Parker, M. Porkolab, J.J. Ramos, S.J. Wukitch et al. Modelling of advanced tokamak scenarios with LHCD in Alcator C-Mod. *Nuclear Fusion*, 40(6):1251, 2000.

[2] Farrokh Najmabadi, A. Abdou, L. Bromberg, T. Brown, V.C. Chan et al. The ARIES-AT advanced tokamak, advanced technology fusion power plant. *Fusion Engineering and Design*, 80(1–4):3 – 23, 2006. Aries - {AT} Special Issue.

[3] B.N. Sorbom, J. Ball, T.R. Palmer, F.J. Mangiarotti, J.M. Sierchio et al. ARC: A compact, high-field, fusion nuclear science facility and demonstration power plant with demountable magnets. *Fusion Engineering and Design*, 100:378 – 405, 2015.

[4] H. P. Summers. *The ADAS User Manual*. University of Strathclyde, 2004.

[5] A. W. Degeling, H. Weisen, A. Zabolotsky, B. P. Duval, R. A. Pitts et al. AXUV bolometer and Lyman-α camera systems on the TCV tokamak. *Review of Scientific Instruments*, 75(10):4139–4141, 2004.

[6] R. L. Boivin, J. W. Hughes, B. LaBombard, D. Mossessian and J. L. Terry. High resolution measurements of neutral density and ionization rate in the Alcator C-Mod tokamak. *Review of Scientific Instruments*, 72(1):961–964, 2001.

[7] V. A. Soukhanovskii, A. L. Roquemore, R. E. Bell, R. Kaita and H. W. Kugel. Spectroscopic diagnostics for liquid lithium divertor studies on National Spherical Torus Experiment. *Review of Scientific Instruments*, 81(10), 2010.

[8] Ian H. Hutchinson, Steve F. Horne, Gerasimos Tinios, Stephen M. Wolfe and Robert S. Granetz. Plasma shape control: A general approach and its application to Alcator C-Mod. *Fusion Science and Technology*, 30(2):137–150, November 1996.

[9] N. P. Basse, A. Dominguez, E. M. Edlund, C. L. Fiore, R. S. Granetz et al. Diagnostic systems on Alcator C-Mod. *Fusion Science and Technology*, 51(3):476–507, April 2007.

[10] S. Fairfax. Alcator C-MOD. In *Fusion Engineering, 1991. Proceedings., 14th IEEE/NPSS Symposium on*, pages 656–661 vol.2, Sep 1991.

[11] A.S. Kaye and G. O'Connor. High frequency heating and current drive in next step steady state tokamaks. *Fusion Engineering and Design*, 56–57(0):47 – 57, 2001.

[12] Nathaniel J. Fisch. Confining a tokamak plasma with rf-driven currents. *Phys. Rev. Lett.*, 41:873–876, Sep 1978.

[13] N. J. Fisch and A. H. Boozer. Creating an asymmetric plasma resistivity with waves. *Phys. Rev. Lett.*, 45:720–722, Sep 1980.

[14] M. Grimes, D. Gwinn, R. Parker, D. Terry and J. Alex. The Alcator C-Mod lower hybrid current drive experiment transmitter and power system. In *Fusion Engineering, 2002. 19th Symposium on*, pages 16–19, 2002.

[15] S. Shiraiwa, O. Meneghini, R.R. Parker, G. Wallace, J. Wilson et al. Design, and initial experiment results of a novel lh launcher on Alcator C-Mod. *Nuclear Fusion*, 51(10):103024, 2011.

[16] M. Brambilla. Slow-wave launching at the lower hybrid frequency using a phased waveguide array. *Nuclear Fusion*, 16(1):47, 1976.

[17] C. Lau, G. Hanson, Y. Lin, J. Wilgen, S. Wukitch et al. First results of the SOL reflectometer on Alcator C-Mod. *Review of Scientific Instruments*, 83(10):–, 2012.

[18] G.M. Wallace, S. Shiraiwa, J. Hillairet, M. Preynas, W. Beck et al. Advances in lower hybrid current drive technology on Alcator C-Mod. *Nuclear Fusion*, 53(7):073012, 2013.

[19] S. Shiraiwa, G. Baek, P.T. Bonoli, I.C. Faust, A.E. Hubbard et al. Progress towards steady-state regimes in Alcator C-Mod. *Nuclear Fusion*, 53(11):113028, 2013.

[20] W. L. Wiese and J. R. Fuhr. Accurate atomic transition probabilities for hydrogen, helium, and lithium. *Journal of Physical and Chemical Reference Data*, 38(3):565–720, 2009.

[21] G. R. McKee, R. J. Fonck, C. Fenzi and B. P. Leslie. A Lyman-alpha-based (VUV) plasma density fluctuation diagnostic design. *Review of Scientific Instruments*, 72(1):992–995, 2001.

[22] K Behringer, H P Summers, B Denne, M Forrest and M Stamp. Spectroscopic determination of impurity influx from localized surfaces. *Plasma Physics and Controlled Fusion*, 31(14):2059, 1989.

[23] J. L. Terry, B. Lipschultz, A. Yu. Pigarov, S. I. Krasheninnikov, B. LaBombard et al. Volume recombination and opacity in Alcator C-Mod divertor plasmas. *Physics of Plasmas*, 5(5):1759–1766, 1998.

[24] Darren Thomas Garnier. *Lithium pellet injection experiments on the Alcator C-Mod Tokamak*. PhD thesis, Massachusetts Institute of Technology, June 1996.

[25] M. L. Reinke and I. H. Hutchinson. Two dimensional radiated power diagnostics on Alcator C-Mod. *Review of Scientific Instruments*, 79(10), 2008.

[26] M.L. Reinke, J.E. Rice, I.H. Hutchinson, M. Greenwald, N.T. Howard et al. Non-neoclassical up/down asymmetry of impurity emission on Alcator C-Mod. *Nuclear Fusion*, 53(4):043006, 2013.

[27] R.S. Granetz and L. Wang. Design of the X-ray tomography system on Alcator C-Mod. In P.E. Stott, D.K. Akulina, G. Gorini and E. Sindoni, editors, *International School of Plasma Physics*, pages 425–437. Editrice Compositori Bologna, 1991.

[28] J Winter. Wall conditioning in fusion devices and its influence on plasma performance. *Plasma Physics and Controlled Fusion*, 38(9):1503, 1996.

MODULATION TECHNIQUES FOR THE POWER BALANCE OF LOWER HYBRID WAVES

A tokamak plasma's power balance links power losses to associated power inputs and changes in energy confinement. In the same way, the power balance of LHRF waves correlates variations in the plasma losses to the input LHRF power. The loss of current drive indicates changes in wave absorption in the plasma and will lead to differences in the power losses. Attributes of lost power derived from the power balance can then be used to discover additional characteristics of the LHCD density limit. Through an isolated power balance via LHRF modulation, the nature of high density LHRF wave absorption can be investigated.

Determining the power balance in a plasma can be difficult due to the varied nature of the plasma's inputs and loss mechanisms. This complicated problem requires separate measurement of each mechanism in order to fully characterize the power flow. As each input and loss are dependent on one another, it can be difficult to determine the effect of an individual auxiliary power source's deposition. This inverse problem (*i.e.* understanding the power source through changes in the plasma) requires correlating the input power to changes in the each of the other power sources and sinks.

In most cases auxiliary power must be isolated from the background ohmic heating. Ohmic heating is provided by the current and the finite resistance of the plasma. This power depends on the plasma's inductive timescales and cannot be changed rapidly due to the long L/R values, while the resistance of the plasma $\propto T^{-3/2}$[1] and changes on global energy confinement times. This quasi-continuous power source provides both stability and the baseline power for the plasma's sustainment. Rapid variation of the auxiliary power separates the effects of auxiliary power from ohmic power. The power source changes in the core pressure and losses independently in a quantifiable way to yield the power source's effect. This methodology will be used for understanding the LHCD density limit and help isolate the power deposition characteristics of LHCD at high density.

Power modulation is an effective method for determining radiofrequency power deposition in tokamak plasmas. However, stringent requirements exist on the modulation character due to the plasma's response. When properly used, the time delay and power quantities observed in the core and SOL can determine the nature and magnitude of deposition in the different regions of the plasma. The chosen increment in LHRF power represented a $> 50\%$ change in the

total input power and the delay between steps was longer than an energy confinement time. This LHRF modulation was used in several time-invariant (*i.e.* constant parameter) plasmas to determine core and edge deposition across the density range where current drive loss occurs.

At the highest densities no discernible effect was observed in the core electron temperature during LHRF pulses. Changes in the core density and neutron rate were due to ionization effects in the edge (which are discussed in the following chapter). The minimal changes in the core simplify the RF power balance and focuses the current drive efficiency loss investigation to the edge plasma.

A nearly instantaneous change in both SOL heat conduction to the divertor plates and edge radiation were observed with applied LHRF power at high density. The edge loss magnitude increases with density, thus decreasing efficiency and leading to an increasing power fraction parasitically absorbed in the edge. These results support previous theories suggesting significant edge plasma deposition at high density. This edge absorption parasitically reduces the power available for current drive.

REVIEW OF MODULATION TECHNIQUES FOR RADIOFREQUENCY WAVES IN TOKAMAK PLASMAS

Power balance under the influence of auxiliary power in tokamaks

Power balance is used for describing the flow of power in a tokamak plasma. In steady-state conditions an equilibrium develops where the power into the device is balanced by losses. The transformation of the power into the plasma into losses is determined by the absorption qualities of the plasma, the absorption attributes also dictates the plasma performance. This balance allows for the loss mechanisms and the core plasma performance to describe the effects of an input power source.

Current drive efficiency loss highlights an unexpected change in the LHRF wave power deposition in Alcator C-Mod plasmas. While direct LH wave detection methods have been used to understand this change[2, 3, 4], the location and interpretation of these measurements are limited by the complex three-dimensional nature of wave propagation and damping. A large suite of measurements is available for characterizing the plasma power flow on C-Mod[5] and can be used inversely to study the propagation and deposition of LHRF waves. Differences in the plasma power balance provides important evidence regarding the source of the LHCD efficiency loss.

It is necessary to totally quantify the applied LHRF wave power in the current drive loss. Each observed LHRF effect has an associated value and importance dictated by the fraction of LHRF power
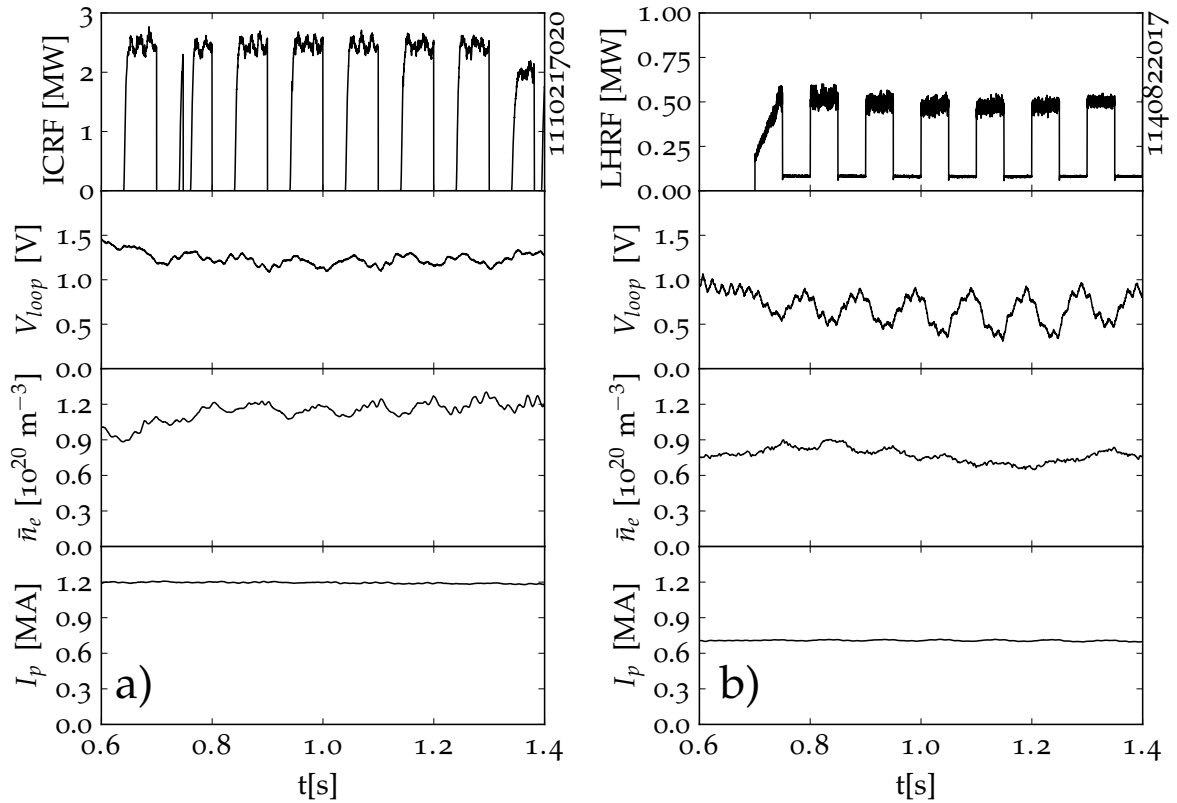
Figure 3.1: LHCD and other auxiliary sources impact the inductive ohmic input power on Alcator C-Mod. On left (figure a), ion cyclotron RF power (ICRF) heats the bulk plasma reducing its collisionality and resistivity (minimal changes in current and density are observed). The voltage necessary to drive the same current is reduced, shown by a subtle variation in the loop voltage with the modulation. The ohmic power deposited in the plasma is reduced by the ICRF. On right (figure b), LHCD replaces inductive current and has a much larger effect on the loop voltage. In both cases the ohmic power is reduced with applied auxiliary power.

which causes it. Power balance verification is necessary in order to link plasma losses to absorption of LHRF power. This connection can then be used to understand the cause of current drive loss. This process begins with the non-trivial isolation of the auxiliary power from the background input power.

Tokamaks have an input ohmic power source associated with an induced toroidal current. Some form of toroidal current is necessary for stability of tokamaks, usually the controlled loop voltage varies to in order fix the induced current regardless of the plasma conditions. The deposited ohmic power depends on the plasma's resistivity and can be inferred using equation 3.1. The surface loop voltage (V_{loop}) drives both a resistive and inductive load (defined with normalized internal inductance, l_i), where the resistive load is the ohmic heating

in the plasma. The ohmic power supplied by the central solenoid can be inferred from plasma equilibrium reconstructions.

$$P_{OH} = (V_{loop} - \frac{\pi \mu_0 R_0}{2} l_i \frac{\partial I_P}{\partial t}) I_p \qquad (3.1)$$

Theoretically, the neoclassically-corrected Spitzer resistivity[1, 6] (shown in equation 3.2) can be used to define the plasma's resistive load. The resistivity (η) scales with the plasma's collisionality divided by density and is sensitive to the temperature and impurity content and insensitive to density. P_{OH} is determined from a known current profile j and resistivity when integrated over the plasma volume V. When an auxiliary heating method is applied to the plasma it can change the temperature.

The additional power source will cause the resistive load to vary due to variations in temperature and impurity content. This is shown on the left in figure 3.1 where temperature changes due to applied ICRF power are observed in the loop voltage. The higher temperature reduces the resistivity subsequently lowering necessary voltage needed to drive the same current. The addition of other auxiliary power reduces the ohmic contribution and changes plasma's power balance.

$$P_{OH} = \int \eta j^2 dV \qquad (3.2)$$

LHCD reduces the need for inductive ohmic power by both imparting momentum and asymmetrically modifying the collisionality of the plasma. As shown in figure 3.1, the effect of LHCD on the loop voltage is more pronounced with less power in comparison to ICRF power. The wave-generated fast electron asymmetry in velocity replaces the inductive current with a high degree of efficiency. The fast electron population also collisionally slows on the thermal population acting as bulk heating source. In all cases with auxiliary power, plasma changes influence other input power sources. Thus, each power source and the interplay between them must be taken into account in the power balance.

Understanding the Lower Hybrid power deposition requires characterizing each contribution to the power balance in equation 3.3. The stored energy and ohmic power independently influence the power loss channels, further complicating this analysis. A steady-state plasma with ohmic and Lower Hybrid power cannot be used to separate the contributions to the measured conductive loss and radiative loss. If the Lower Hybrid power is actuated as an independent variable, then the power deposition can be correlated to changes in the other parameters. The causal relationship of LHCD in reduc-

Figure 3.2: The plasma does not occupy the entirety of the available vacuum, with power escaping from inside and outside the separatrix (shown in green) to the wall. In this analysis, the control volume is considered the vacuum vessel interior (shown in blue). Calculations of P_{tot} will be defined using the vacuum vessel interior due to the known effects on the SOL by high density LHRF. The power loss will be characterized in two ways, through emission of radiation (shown in purple) and from the conduction of power to the divertor (shown in yellow). The power inputs (induction and LHRF) are not shown in this figure.
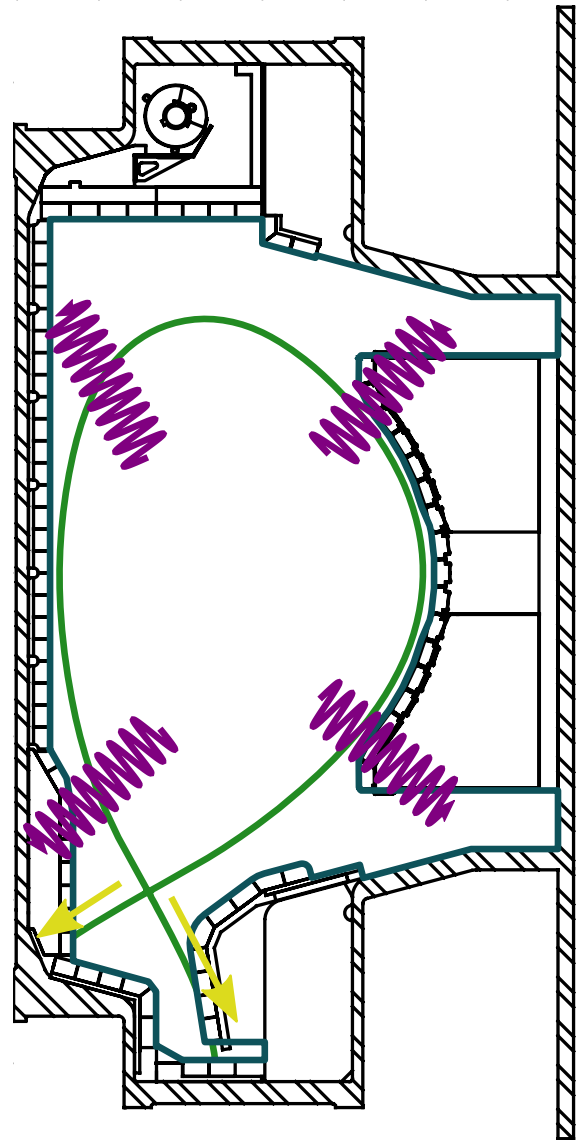
ing the inductive ohmic power requires treating changes in P_{OH} as a dependent variable.

The inverse problem of using the plasma to understand a power source requires reorienting the standard power balance equation. This is illustrated in equation 3.3 where instead of deducing changes solely in the stored energy ($\frac{\partial W}{\partial t}$), Lower Hybrid power deposition is deduces from changes in stored energy, the radiated power P_{rad}, the ohmic power P_{OH}, or the conducted power P_{cond}. This equation drops fusion alpha particle heating which is negligible on Alcator C-Mod in a plasma with only LHRF auxiliary power.

$$P_{LH} = \frac{\partial W}{\partial t} - P_{OH} + P_{cond} + P_{rad} \tag{3.3}$$

LHRF at low efficiency influences the SOL[7, 8, 9, 10] making it ambiguous what fraction of the LHRF power is deposited inside the LCFS. Because of this, the control volume is expanded to the entirety of the interior of the vacuum vessel as shown in figure 3.2. The total power P_{tot} is defined relative to this control volume with all inputs and losses passing through a solid surface. The escaping conducted and radiated power will intercept a solid surface and is considered lost.

Conducted power measurements are made in the divertor, as most field lines in the near SOL intercept surfaces in that vicinity. The radiated power is emitted from all plasma regions and is measured at various locations at differing wavelengths and time resolutions. While LHRF is meant to drive fast electrons, the loss of current drive requires examining all plasma regions and populations for signs of LHRF power absorption. Each of these populations influence the power losses thereby allowing efficiency loss characterization.

The LHRF plasma power flow can be isolated using the defined power balance equation with the larger control volume. In all cases it is required that the LHCD power be changed in order to compare two different power balance states. This can be accomplished either in similar discharges with different LHRF powers or using time-variation in the radiofrequency power. Natural variation discharge-to-discharge makes time variation the most precise method for understanding LHRF deposition. The effect of core absorption with time variation of power is best understood by evolving the plasma from one steady-state to another.

Comparing two Lower Hybrid power steady-states, the difference (ΔP_{LH}) will be reflected in changes in the other power sources. The total input power into the tokamak $P_{tot} = P_{LH} + P_{OH}$ will differ between the two cases depending on the LHCD's efficiency in replacing ohmic power. In the case that LHCD replaces ohmic power with the same efficiency, P_{tot} should be the same between both cases. As the current drive becomes more inefficient, the total power into the control volume will increase.

The change in P_{tot} between two steady states causes observable changes in the loss mechanisms (ΔP_{rad} and ΔP_{cond}). Shown in figure 3.3, ΔP_{LH} is reflected in differences of P_{OH}, P_{rad}, and P_{cond}. The current drive power replacing P_{OH} does not change P_{tot} and is hidden, though it eventually is lost from the plasma.

The evolution from LHCD efficiently producing current to the case of complete inefficiency will produce a range of ΔP_{tot}. This range in ΔP_{tot} is bounded by the value ΔP_{LH}, making ΔP_{LH} an important fiducial in efficiency-loss characterization. The fraction of power lost to each mechanism can be determined by normalizing the other power sources and sinks to ΔP_{LH}. This metric will be used to define the LHCD efficiency in the loss of current drive.

Figure 3.3: The deposition of auxiliary power feeds back on other sources. An example set of power balances is shown with two situations $P_{tot,1}$ and $P_{tot,2}$. In $P_{tot,1}$ the power is supplied fully by the ohmic drive (denoted by a small green bar), and is lost via radiation and conduction. In $P_{tot,2}$ the LHCD (shown by the red bar) is added which replaces some ohmic power (a reduction in the green bar). The changes in the conduction and radiation will sum to less than the combination of the auxiliary power and the previous power balance. Even though all of the LHRF power is eventually lost, LHCD changes P_{OH} therby reducing its contribution. When taken from this perspective, the input LHRF power can be conducted, can be radiated or can replace other input power sources.
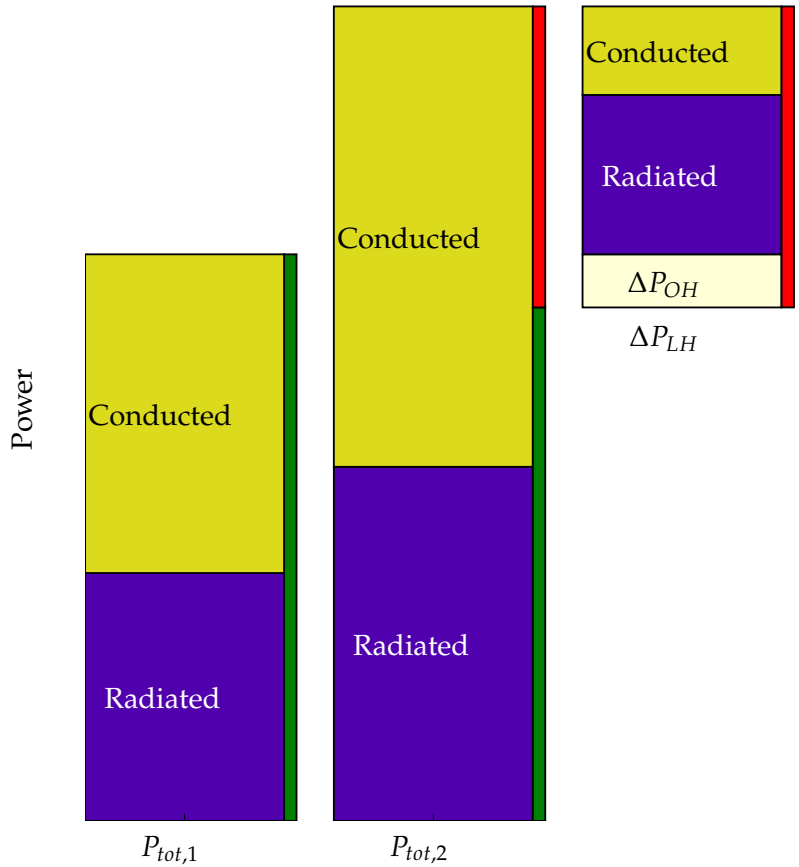
Understanding efficiency loss through power absorption changes begins by observing changes in the core ($\frac{\partial W}{\partial t}$). The core parameters' evolution during LHRF power change can be used to isolate LHRF's effect on the bulk core plasma (as opposed to the fast electron tail). Power absorption in the bulk without driving current can decrease the current drive efficiency. The most straightforward approach in characterizing radiofrequency power core absorption is to use a step in power. The plasma's step-response to instantaneous changes in LHRF power will evolve to another steady-state removing stored energy changes from the power balance. In this way, the changes in core absorption and in the overall power balance are easily evaluated. Multiple step-responses in a single plasma lead to the commonly-used technique of radiofrequency power modulation.

Principles of power modulation in tokamak plasmas

An instantaneous change in radiofrequency power from one level to another will lead to an evolution in the plasma conditions. This evolution, known as a step-response, can be used to understand radiofrequency wave damping. The magnitude and time response can be used to localize the power absorption with the process controlled by

the plasma's heat transport characteristics. The derived deposition's accuracy can be improved when done sequentially (*i.e.* modulating between levels).

Auxiliary power modulation in tokamaks has been used extensively to determine the radial deposition power profiles. It has been used to great effect in characterizing core plasma heating through changes in core plasma pressure. Modulation can also be used to understand fast particles dynamics using specifically designed diagnostics. In addition, the applied power can be used to determine the plasma's convective and diffusive characteristics. In these situations the proper modulation characteristics are dictated by the natural processes under observation.

The bulk plasma re-equilibrates with a power change on the order of the energy confinement time (τ_E). While this is generally the case for core-deposited power, the most physically accurate description of the time response depends on the deposition location. Core deposited power can be modeled using a cylindrical approximation of power balance assuming a thermal particle distribution shown in equation 3.4. The radial transport of local energy for population j ($\varepsilon_j = \frac{3}{2}n_j T_j$) is dictated by diffusion (using diffusion coefficient D) and convection (with radial convection velocity $\vec{v}$), with various source (P_{in}) and sink (P_{loss}) terms.

$$\frac{\partial \varepsilon_j}{\partial t} = \nabla \cdot (D\nabla\varepsilon_j + \vec{v}\varepsilon_j)) + \sum_k P_{in,k} - \sum_k P_{loss,k} \tag{3.4}$$

Assuming that the deposited power is observed as a temperature change, the deposition profile can be analytically determined in time and space. For example, in figure 3.4, the response time increases significantly with increasing distance from the heat source. This cylindrical toy model of a step response is an accurate representation of the dynamics expected with core deposition.

A Heaviside step function in temperature at a $\rho = .5$ represents the heating in this example. The temperature time history at each radius contains a different response to the heat source. The edge response is limited by the edge boundary condition, where the change in temperature at the boundary is zero. This indicates that edge losses can reduce the temperature response near the edge.

Different plasma temperature measurements can observe core-deposited power in the bulk of the plasma distribution. This has been measured using electron cyclotron emission (ECE)[11, 12] and Thomson scattering (TS)[13, 14] diagnostics at multiple locations over the course of the modulation. The radius of fastest response is the radius of deposition for a well-localized source. The rise time and magnitude at other radii depend on the plasma's convection and diffusion.
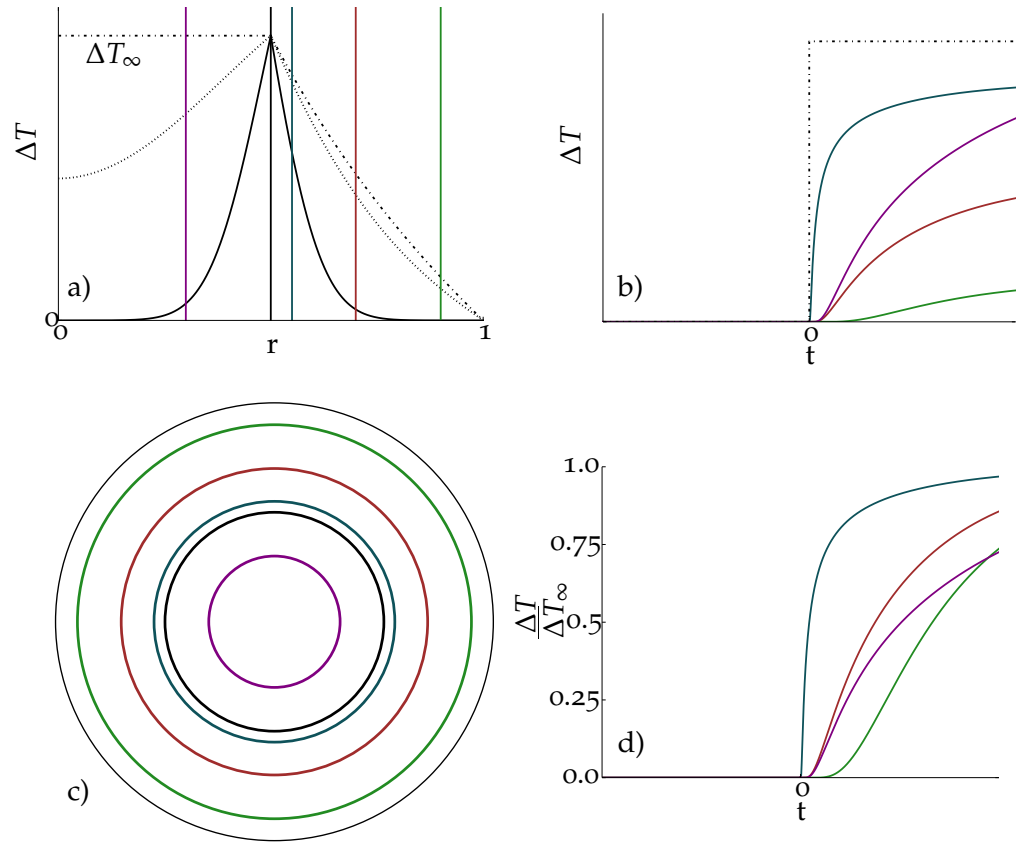
Figure 3.4: Cylindrical model of heat diffusion using an annular point source at $\rho = .5$. The heat source fixes the temperature at that location starting at t=0, which causes a variable heat source in time. The step response radial profile in a) shows the initial profile, two time-delayed profiles and the steady-state solution (T_∞). The measured time responses at radii of .3.,.55,.7 and .9 are shown in b) and d) where d) is normalized to the steady-state solution. The rise in T at $\rho = .5$ is shown in b) by the dotted line. These locations of temperature measurement are matched on plots a) and c). The measurements farther from the heat source are delayed in time, highlighted in the difference in green and blue. The location of a heat source can be deduced using the time response at a specific location and a known diffusion coefficient.

The source, convection and diffusion characteristics with different source and loss terms also dictate transport and radial density of fast particles generated in response to power modulation. These values differ from plasma's the bulk properties (*i.e.* the slowing down time and formation time for fast electrons are different from bulk heating), necessitating the use of a different modulation in power and period. The modulation period τ_{mod} dictates the analytical method needed to characterize deposition. Figure 3.5 shows the rise time of the core plasma stored energy as described by the simplified formula described in equation 3.5. The input power $\sum P_{in}$ is represented by a square wave with a 50% duty cycle. The ratio of modulation period

to energy confinement time (τ_{mod}/τ_E) strongly dictates the plasma response's nature.

$$\frac{\partial W}{\partial t} = \sum P_{in} - \frac{W}{\tau_E} \qquad (3.5)$$

In the case that $\tau_{mod} > \tau_E$, it is imperative that the modulation timescale be long enough to fully capture the plasma dynamics of interest. As discussed in the previous section, power balance calculations can be simplified if the initial and final stored energies are at equilibrium. This allows for separate modulations to be treated individually and independently. Fourier analysis can then be used to recover important radiofrequency power damping and transport characteristics. Modulation experiments also require that the diagnostics of interest acquire sufficient data to yield the necessary results. Lower bounds of the modulation period are set by the timescales of plasma hysteresis and measurement Nyquist frequency.

A secondary approach, break-in-slope analysis, relies on fast modulation with a shorter modulation period than the confinement time ($\tau_{mod} < \tau_E$). The variation in the background plasma and other power sources (*i.e.* ohmic power) is assumed to be minimal during modulation. The power balance equation can be linearized due to the fast parameter changes leading to a straight-forward interpretation of temperature and density changes into damping profiles. However, this method cannot be used for understanding LHRF core deposition due to the intrinsic link between Lower Hybrid current drive, ohmic power, and the plasma current. The modulation period must exceed the transport timescales and be comparable to the inductive timescales to characterize the impact of LHCD on the ohmic power.

Tokamak plasmas naturally contain some level of variation in their parameters due to factors like impurity injections or magnetohydrodynamic (MHD) modes. Consequentially, the stored energy constantly ebbs and flows, changing core profiles and associated power losses. The fast modulation power level change concentrates the important changes around a specific time. Long modulation periods unnecessarily waste time, as far-removed measurements have minimal residual effects from the power change. At long times, the plasma's natural variation will lead to a different plasma character than at the instantaneous power change. The modulation period must be needs only several confinement times in order to properly characterize the plasma.

The natural fluctuations in stored energy and power sources also set a lower bound the modulation's magnitude. To determine a significant plasma response, the modulated power must be a non-negligible fraction of the total power. The applied power must exceed this noise level for it to be properly isolated.
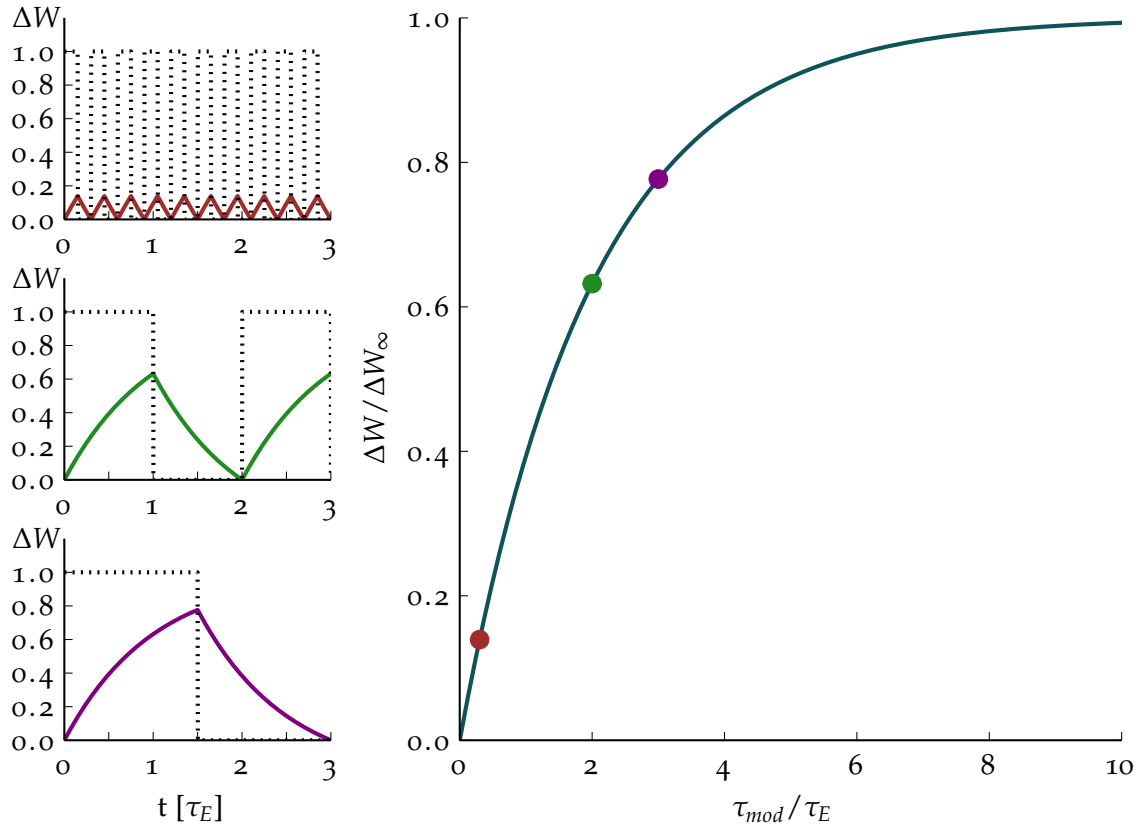
Figure 3.5: The ratio of the modulation period to the energy confinement time (τ_{mod}/τ_E) dictates the applicable power deposition analysis. Fast modulation times ($\tau_{mod}/\tau_E \ll 1$) cause reduced changes in the stored energy with a nearly linear rise and fall (exhibited in red). This is optimal for break-in-slope analysis. Longer modulation periods ($\tau_{mod}/\tau_E > 1$) approach steady state ($\Delta W = \Delta W_\infty$) and are effective for fourier-analysis and equilibrium-related analysis (shown in green and purple). The expected variability in the stored energy due to natural processes leads to an effective finite saturation time. This time is optimal for data return as longer periods are likely to be impacted by noise near saturation.

Historical precedent for radiofrequency power modulation

Perturbative analysis used in power modulation relies on fast-switching, high power auxiliary power sources. The first published use of a fast power perturbation in a plasma experiment occurred on the FM-1 spherator[15]. It determined the thermal conductivity via the increment and time delay in electron temperature to applied power as measured by a Langmuir probe. As diagnostic characterization improved and auxiliary power sources with fast activation became common its use in tokamak plasma physics became ubiquitous. Modulation was used to understand three tokamak plasma attributes: heat transport, fast particle transport, and auxiliary power deposition.

Initial theoretical treatments of power perturbations focused on changes in the core plasma electron temperature. Work by Barbato and Giannella[16] and others[12, 17, 18], determined mathematical

bases for evaluating the heat transport characteristics. Similar work exists in analyzing sawtooth heat-fronts[19], which contains many of the same attributes. The inclusion of electron density perturbations significantly improved the capability for numerical accuracy in this analysis, and was applied in characterizing heat transport and power deposition in the core plasma.

The determination of heat transport with modulation has focused on electron cyclotron radiofrequency power (ECRH) due to the very small radial extent of its power deposition. The small-wavelength radiation's vacuum propagation and deposition is straight-forward in most plasma conditions. This localized source is well known and can be treated like a delta function in radial space. This has been used effectively in most machines with ECRH (including DIII-D[20], TCV[21], DITE[22], T-10[23], RTP[24] and ASDEX[25]). Most cases utilize measurements of ECE due to its high radial and time resolution ($\ll \tau_E$)[26, 27], yielding sufficient data for this analysis. These results have effectively determined the background and perturbed electron heat diffusivity χ_e[28].

The auxiliary power's radial deposition profiles have been experimentally calculated using modulated ICRF[29], ECRH and NBI[30, 31]. Fast modulations tend to use break-in-slope analysis[32, 33], while slower modulation utilized Fourier-analysis[34]. Measurements of the electron and ion responses have required further analysis, as the decoupling of species (*e.g* ions slowing on electrons, etc.) causes a finite time delay. This analysis has advanced the understanding of wave propagation and damping of certain fusion-relevant waves within tokamak plasmas.

Several auxiliary power sources also create significant non-thermal populations. Modulation of ICRF and NBI have made great advances in characterizing the slowing-down and diffusion of fast ions[35]. However, characterizing non-thermal populations requires specific fast particle measurements. Work on C-Mod and elsewhere has utilized FIDA[36], FILD[37] and neutral particle analyzers to determine the fast ion populations[38]. LHCD modulation has utilized hard X-ray cameras to measure high energy bremsstrahlung from fast electrons.

LHCD modulation has focused on characterizing the produced fast-electron population. Fast electron populations cause high energy bremsstrahlung (hard X-rays) emission through collisions. Work on C-Mod[39] and elsewhere [40, 41, 42] yielded measurements of the fast electrons' slowing, diffusive, and convective character using Abel-inverted hard X-ray profiles. The X-ray measurement is not one-to-one with the electron population, introducing ambiguity in these calculations. The variation in measured diffusion coefficients and slowing-down times has implications on fast-electron edge loss as discussed in Chapter 5.

In this work, Lower Hybrid wave power modulation is instead utilized to calculate power absorption in the bulk ions and electrons at high density. The fast-electron population loss requires observing these other populations; specifically the core and edge are independently analyzed to fully characterize the power balance. Observation of power in other populations (and their location) is indicative of the mechanism causing the current drive loss.

EXPERIMENTAL SETUP

Methodology

While previous Alcator C-Mod experiments (discussed in Chapter 1) found that the current drive efficiency loss correlated strongly with $\bar{n}_e$; other parameters also influence the driven current. For example, higher plasma currents and smaller inner gaps (the closest distance between the inner wall and the separatrix) improve the current drive efficiency. These known current drive dependencies must be controlled to prevent them from influencing the interpreted power balance.

Unexpected and untested covariances can also influence the current drive efficiency and impact data interpretation. This is especially important in cases where it is critical to understand subtle effects or significant noise is expected. The experimental approach must avoid inadvertently influencing trends through uncontrolled variables (so-called unknown unknowns). Strict control of the plasma parameters are used both within a discharge and through the experiment to minimize these effects.

Previous Alcator C-Mod experiments have used density ramps during a discharge for characterizing the current drive loss[7, 43, 44]. The evolving conditions induced by large gas puffs in the SOL eventually lead to changes in the core plasma. Particle confinement and diffusion leads to finite delays (similar to the heat propagation in the previous section). This can lead to hysteresis (when compared to the independent variable $\bar{n}_e$), especially in fast particle populations. The evolution of parameters also makes power balance characterization difficult, as estimates of core energy in LHCD plasmas are known to be erroneous. Thus, in this experiment the density during flat-top was changed shot to shot instead of using a density ramp. Instead the LHRF power was changed in time to generate the necessary dataset.

In this study, plasma shape, current, density and magnetic field were fixed in time in order to minimize the impact of hysteresis from modulation to modulation and to avoid introducing errors. Results showed that while some natural variation in the $\bar{n}_e$ occurred, the small impact was useful, filling in the range density and the large number of modulations combined into a large dataset.
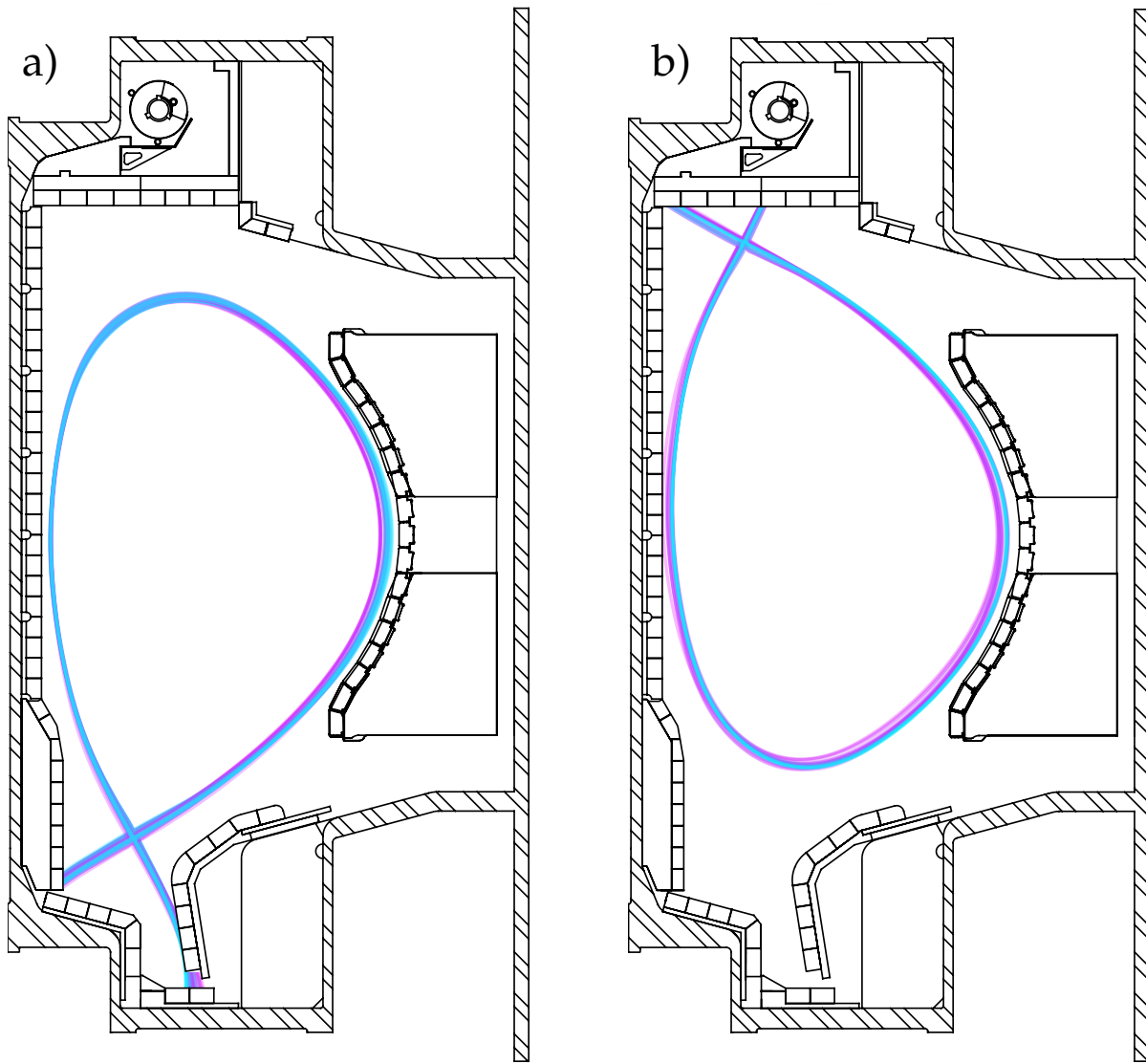
Figure 3.6: a) The plasma separatrix for 43 lower single null discharges during the pulse at 1.0 seconds. Each plasma LCFS is colored according to the $\bar{n}_e$ at that time. Lower densities are in blue with higher densities in purple. The outer plasma shape at high density is farther from the limiter to maximize power coupling. Variation in plasma shape from discharge to discharge is due to variability in control and reconstruction. The plasma strike points vary within the size of a tile (2.5 cm) and are purposefully chosen to maximize SOL data coverage. b) The plasma separatrix for 26 upper single null discharges during the pulse at .8 seconds. The shape was optimized for core analysis with Thomson scattering and for maximal LHRF coupling. The color scheme is the same as in a). In both cases, LHCD efficiency versus $\bar{n}_e$ is properly isolated with minimal variation in other plasma parameters.

Each chosen plasma had a distinct $\bar{n}_e$ to fill the range from full to negligible current drive. For the chosen plasma current (700kA) the density range was limited by the plasma control system and wall outgassing at low density ($\bar{n}_e = 6.5 \cdot 10^{19}$ [m^{-3}]). This dataset was also limited by H-modes induced by LHRF in forward field, limiting the range of $\bar{n}_e$ to be less than $1.3 \cdot 10^{20}$ [m^{-3}]. Understanding core deposition in 800kA discharges required increasing the upper range of densities to $1.5 \cdot 10^{20}$ [m^{-3}]. The variation in density, as is described

Figure 3.7: The modulation period of LHRF power is 100ms for these experiments. This period is $\sim 3\tau_E$ ($\tau_E \sim 35$ ms) which allows for core deposited power of each modulation to approach equilibrium. The modulation power is ~ 450 kW, representing a $> 50\%$ addition to P_{tot} in cases where P_{OH} is unaffected by the LHRF modulation. This minimizes hysteresis modulation to modulation, and represents a sizable change in the power balance. In discharges used to analyze core dynamics the LHRF power was turned off, and in edge analysis it is at a minimal level (100 kW). This is due to limitation in the LHRF control system. The low power setting is a small fraction of the ohmic power ($P_{OH} \sim 700$ kW). The power switching time from low to high power is $< 10\mu$s, which is instantaneous as compared to the global plasma dynamics.
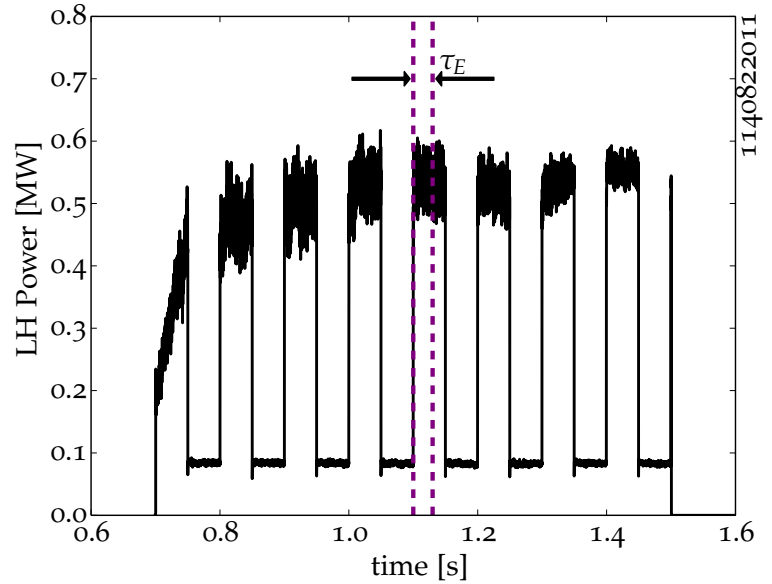
in detail in chapter 4 was on the order of $1 \cdot 10^{19}$ [m^{-3}], but was a function of the applied LHRF power at high density.

Subtle changes in the outer gap have previously been shown not to impact the LHCD density limit in other experiments. Variation in the outer plasma shape, as shown in figure 3.6, was allowed in order to maximize antenna coupling to the plasma. Other plasma parameters (*i.e* κ, δ) were kept constant to allow the most straightforward comparison of different plasma densities.

This method's strength lies in ensembling of the various discharges without a focus on any one plasma. Indeed, repetition and repeatability guarantees the validity of derived characteristics, and statistical error estimates are useful in cases where significant noise is expected. This is the case for power balance measurements in tokamak plasmas. Modulated, constant parameter plasmas provide the most precise method for determining the power balance across the current drive loss density range.

LHRF modulation parameters

Empirical predictions for the parameters of C-Mod plasmas set the LHRF modulation characteristics. The confinement time, ohmic power, influence of LHRF phasing and the current drive efficiency decay with density have all been previously characterized for the chosen plasma. The chosen LHRF modulation met the necessary requirements in the power magnitude and modulation time to analyze core and edge deposition.

A multi-parameter analysis of the current drive characteristics at low density ($\bar{n}_e < 1.0 \cdot 10^{20}$ [m^{-3}]) found that the deposition and effi-

ciency of LHCD correlated with the toroidal plasma current[44]. Unlike other tokamaks, the launched $n_\parallel$ was found to minimally change the radial damping profile or the current drive efficiency[7]. The chosen launcher phasing (90°) minimizes the reflected power (maximizing the injected power) achieving a launched $n_\parallel$ of 1.9. The results derived from this phasing are expected to represent the results for the typical range of launched $n_\parallel$ = 1.5-2.8.

The magnitude of LH power was constrained by the available system power and by the associated antenna coupling. This limited the modulation magnitude (ΔP_{LH}) to less than 500 kW in forward field in the lower single null. The modulation magnitude was higher for core deposition analysis in upper single null data (800 kW). Coupling in reversed field lower single null further limited ΔP_{LH} to 300 kW. The ΔP_{LH} applied in 700 kA and 800kA discharges which is > 50% of the 700 or 800 kW of ohmic power respectively. This significant power addition increases the likelihood that measurable changes caused by LHRF can be observed in the core and edge.

In the cases analyzed for core deposition, the LHRF power could be completely removed during the 'low power' modulation phase. The 'low power' phase in edge damping experiments was 100 kW due to LHRF control system changes[45]. This amount is a negligible fraction (< 15%) of the input ohmic power and minimally influences the plasma. Throughout the subsequent experiments, the LHRF change is characterized in the analysis.

The LHRF control system is capable of the necessary modulation dynamics. The rise and fall time of P_{LH} was less than 10μs, which is much shorter than C-Mod global plasma dynamic timescales. In the subsequent analysis, this power addition is idealized as a substantive, discontinuous source.

The LHRF square-wave modulation period was 100ms with a 50% duty cycle. Ohmic, L-mode, 700kA, lower-single-null discharges on Alcator C-Mod have energy confinement times near 30 ms. The modulation period was chosen to maximize the number of power steps per discharge while allowing for equilibration and proper diagnostic acquisition (for diagnostics with Nyquist frequencies near 100Hz). These analysis methods assume that the plasma evolves to a level where variation in the different power measurements is dominant. An example time-trace of the forward LHRF power is shown in figure 3.7, which meets these necessary requirements.

This experiment was designed to limit the number of independent variables that influence current drive efficiency. Constant plasmas with modulation precisely isolates the plasma response in a statistically meaningful way. Thus, a modulation period and power was chosen to meet requisite time and power qualities for power balance calculations. This methodology determines the location and magni-

tude of LHRF power deposition, which can then be used to understand LHCD density limit.

ANALYSIS OF CORE LHRF POWER DEPOSITION

Influence of fast electrons on T_e, n_e measurements

The non-thermal tail of electrons generated by LHCD can distort core electron temperature measurements[46]. These measurements usually assume a Maxwellian electron distribution for core conditions[47]. As the plasma deviates from this assumption, the interpreted results become increasingly incorrect[48]. The high-energy, asymmetric electron plateau can erroneously increase the interpreted T_e and can prevent the analysis of bulk core conditions. Understanding the sensitivity of diagnostics to fast electrons is important in their use for characterizing plasmas with LHCD. The measurements used to characterize core conditions must be minimally impacted by the fast electron tail.

Most modulation experiments for power balance utilize electron cyclotron emission (ECE) diagnostics for core temperature analysis due to their their high spatial and temporal resolution. The observable radiation emission due to the the electron motion is some harmonic of the cyclotron frequency (as is shown in equation 3.6) and is dependent on the electron velocity (through the relativistic mass increase dictated by γ). Cyclotron emission of interest can be reabsorbed by the plasma, leading to a blackbody-like emitted intensity (approximately proportional to T_e).

$$\omega_{ce} = \frac{qB}{\gamma m_e} \tag{3.6}$$

In Alcator C-Mod, radiation from the X-mode second harmonic of ω_{ce} is measured and analyzed to describe core T_e[11, 49, 50]. High energy electrons emit radiation at a lower frequency known as down-shifted emission. ECE from fast electrons of the same harmonic is reabsorbed in the plasma. This light must travel through the blackbody thermal layer that emits and reabsorbs the power. This light can be measured if it does not traverse this region of plasma. Higher harmonic ECE from fast electrons (such as the third or fourth harmonic) can downshift into the bulk second harmonic frequency range[51]. This additional radiation source cannot be separated from the bulk emission and thus will add to the overall intensity.

A fast electron emitting radiation at harmonic m_2 can be misinterpreted as a lower harmonic emission m_1. An electron at major radius R_2 with kinetic energy E will generate the same frequency radiation as a cold electron at radius R_1 as given in equation 3.7. This equation

assumes the tokamak magnetic field is dominated by the toroidal field, which is $\propto 1/R$.

$$E = m_e c^2 \left(\frac{m_2 R_1}{m_1 R_2} - 1 \right) \tag{3.7}$$

Discounting the poloidal magnetic field's influence, the downshift matching condition is independent of the magnetic field of the equilibrium and the range of observable energies is proportional to the electron rest mass. The range of energies and radii which can add to the thermal blackbody emission is generally limited by the aspect ratio. The conditions of second harmonic X-mode emission on Alcator C-Mod are shown in figure 3.8. Observations of ECE from locations near the core ($R \sim .62$ [m]) can also measure emission from other electrons with energies from zero to $m_e c^2 / 2$ of the third harmonic.

Figure 3.8: Downshifted ECE emission from high energy electrons will be generated at a greater major radius and will be observed as additional intensity on C-Mod. This will cause the calculated T_e to be systematically incorrect. Shown on right is the relation between the non-thermal emission observed at one radius emitted from another as defined a function of energy. The nonthermal contribution to the observed emission for a given radius ($R_{observed}$, in meters) is an integral over the viewing path to the thermal emission radius. The integral over $R_{emitted}$ convolves energy and radius (absorbed emission in gray). This dependency as described in equation 3.7 is shown for the 3rd harmonic (blue) and 4th harmonic (green) in 100 keV increments. The interplay of energy and radius prevents the removal of the non-thermal contribution from the interpretation of the signal intensity.
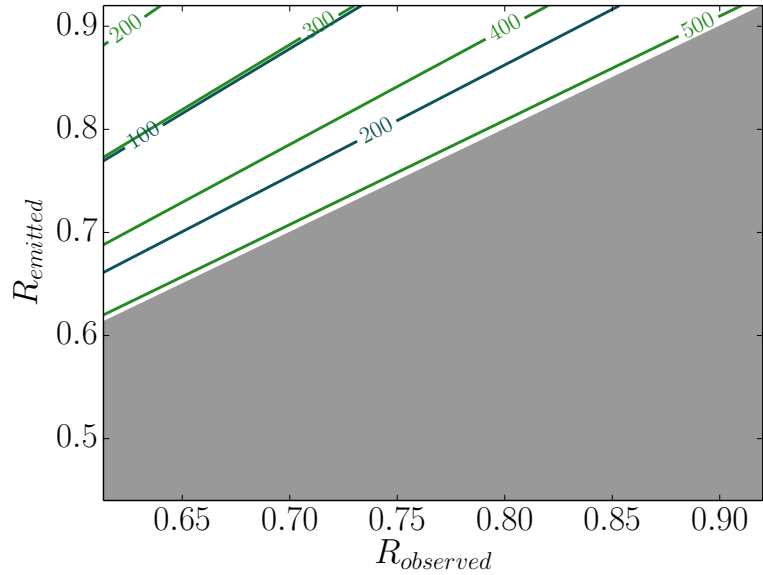
The frequency-downshifted power enhances the total emission at lower frequencies. This contribution means that T_e values will be incorrectly high. The interplay of energy and radius necessary to contribute to the intensity for the cyclotron frequency at R_1 makes the inversion and removal of the non-thermal portion extremely difficult. Because thermal electron modulation analysis using ECE is influenced by the tail distribution, it is subsequently not used for core T_e analysis in this experiment.

SOL-measuring channels of second harmonic X-mode have insufficiently long optical depths to meet the necessary blackbody condition. In principle, first harmonic emission from the high field side should

Figure 3.9: The intensity of nonthermal emission from downshifted second harmonic X-mode ECE exceeds the intensity of core second harmonic emission. The measured frequency at $B_T = 5.4$T corresponds to thermal emission edge plasma ($R = .93$ [m]). The electron temperature is found to become unphysical for edge thermal electrons during the application of LHCD. The measured value corresponds to a 10-15 keV blackbody emission. The long optical depth in the SOL means that the measured intensity is dominated by core nonthermal radiation. This value of nonthermal ECE exceeds the core emission (which is approximately 2keV). It is unknown if the change in core temperature is due to increased blackbody emission or from nonthermal contributions. The measurements shown here were made using a grating polychromator at $7.5 \cdot 10^{20}$ [m^{-3}]. The intensity from the edge channels provide a measurement of the fast-electron population in Alcator C-Mod.
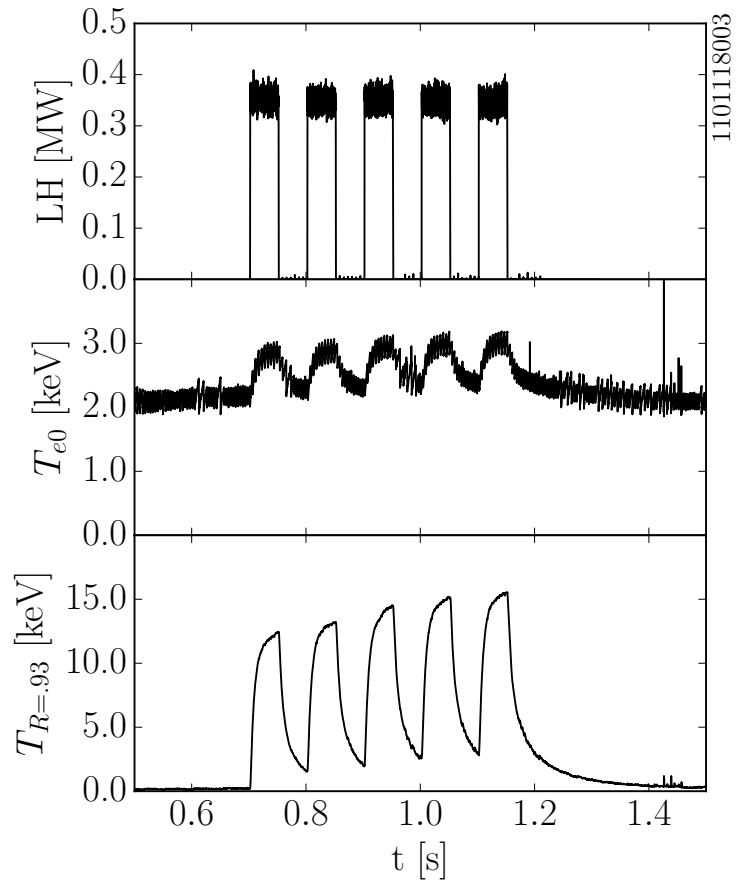
dominate the measurement. However, first harmonic emission is reflected by the right hand upper hybrid X-mode cutoff layer which prevents the measurement of the first harmonic thermal emission. Instead the measured radiation is dominated by the downshifted non-thermal second harmonic X-mode emission when present. These edge channels are used to roughly approximate the non-thermal population in the core, as thermal emission from the SOL is controlled by local dynamics of the temperature. Parallel heat conduction along open field lines limits the temperatures to less than 100eV, and as a consequence weakly emits radiation at ECE frequencies. This is shown experimentally in figure 3.9.

On Alcator C-Mod, the Thomson scattering (TS) diagnostic is also used to determine core T_e values[13, 14]. The light of a 1064nm laser travels vertically at a specific radius (R = .69 [m]) and is scattered radially. The incident $\hat{i}$ and scattered $\hat{s}$ directions are constrained to the poloidal plane with the light polarization $\hat{e}$ in the toroidal direction. The scattered emissivity $\frac{d^3P}{d\Omega_S dv_S d\vec{r}}$, including relativistic corrections for the Alcator C-Mod TS geometry[52], is defined in equation 3.8.

The light scattering direction $\vec{k} = \hat{s} - \hat{i}$ is similarly constrained to the poloidal plane. Consequently, the Alcator C-Mod system measures the frequency spread (v) caused by the electron distribution in the poloidal plane; this is symmetrized due to the orbital motion

(commonly denoted as $v_\perp$ and $v_\perp = v_k$). The relativistic depolariza-
tion ($|1 - \frac{1-\hat{s}\cdot\hat{i}}{(1-\beta_i)(1-\beta_s)}\beta_e^2|$) and velocity correction ($1 - \beta^2$) are both less
than one for all non-zero velocities ($\beta = v/c$).

$$\frac{d^3P}{d\Omega_S dv_s d\vec{r}} = 2\pi r_e^2 \langle S_i \rangle \frac{\omega_s^2}{\omega_i^2} \int \left|1 - \frac{1-\hat{s}\cdot\hat{i}}{(1-\beta_i)(1-\beta_s)}\beta_e^2\right|(1-\beta^2)\frac{f(v,v_k)}{k}d^2v \tag{3.8}$$

The scattered emissivity's linear dependence on the electron distri-
bution function ($f(v,v_k) = f_0 + f_1$) can be used to separate the non-
thermal contribution P_1 from the Gaussian contribution P_0 shown in
equation 3.9. The fast electron density (n_f) is significantly smaller
that of the thermal bulk (n_s), leading to an immeasurable change
in the scattered intensity and measured density (the zeroth moment,
$n_e = n_s + n_f \approx n_s$).

$$\frac{d^3P}{d\Omega_S dv_s d\vec{r}} = \frac{d^3P_0}{d\Omega_S dv_s d\vec{r}} + \frac{d^3P_1}{d\Omega_S dv_s d\vec{r}} \tag{3.9}$$

Temperature measurements are dictated by the scattered light fre-
quency distribution. While the limited number of experimental mea-
surements in wavelength (4) require the use of a non-linear Gaussian
fit, theoretically the temperature can be determined from the second
moment of the scattered spectrum. The character of the scattered spec-
trum's second moment in frequency can be used to understand the
fast electrons' effect on TS temperature measurements.

The contribution of P_0 to the second moment is approximately
Gaussian for temperatures below 10 keV. The second moment can be
approximately described when it is assumed that the average electron
velocity flow in $v_\perp$ is zero, the thermal electron density represents the
total electron density n_e, and the second moment of the fast electron
density is σ_f^2. The second moment of $\frac{d^3P}{d\Omega_S dv_s d\vec{r}}$ in frequency is described
in equation 3.10.

$$\frac{\int v_s^2 \frac{d^3P}{d\Omega_S dv_s d\vec{r}}dv_s}{\int \frac{d^3P}{d\Omega_S dv_s d\vec{r}}dv_s} \approx \frac{T_e}{m_e}^2 + \frac{n_f}{n_e}\sigma_f^2 \tag{3.10}$$

This simplification yields several simple conclusions. First, the fast
electrons' contribution to the second moment scales with the fast elec-
tron population ($n_f/n_e \ll 1$). Second, σ_f is the fast electron second
moment in $v_\perp$ space (due to the C-Mod TS system geometry) and will
not measure the important LHCD parallel velocity plateau. Third,
the plateau of high parallel velocities serves to reduce the fast elec-
tron contribution. Relativistic effects in scattering electrons reduce

the measured light causing 3.10 to overestimate the fast-electron contribution. As a result of these effects, fast electrons will minimally impact measurement of the thermal T_e using TS on Alcator C-Mod.

Core power deposition analysis will neglect results from ECE and focus on measurements from TS. The neutron emission's nature can characterize the LHRF effect on ions. Changes in density will use TS and interferometers. In tandem, these factors can determine LHRF's effect at high density on bulk core conditions.

LHRF impact on core T_e at high density

The analysis of core heat flow begins with the electron temperature characterization. The electron temperature was measured across the plasma using a multiple-point Thomson Scattering system[5, 13, 14]. Each TS measurement was acquired at a specific phase of the modulation so that several modulations could be combined. The ensemble of five modulations per discharge was averaged, reducing the variance in the calculated temperatures.

The rate of acquisition of the TS system allowed for six separate ensemble-averaged profiles (three during the LHRF 'on' period and three during the ohmic period). Due to the low time resolution, the six profiles are insufficient for anything more than the most basic Fourier analysis (< 30 Hz); thus the LHRF deposition analysis is qualitative in nature. However, this is sufficient in describing power balance changes caused by LHRF.

The ensemble averaged TS data and associated errors were used with Gaussian process regression (GPR)[53] to generate high resolution smooth temperature profiles[54]. This method allows for the TS data variance to be interpreted into a radially-varying profile error (using the maximum a posteriori probability (MAP) estimate of both the profile and error). This data was also used to quantify and estimate the change in electron temperatures by LHRF power.

In high efficiency LHCD discharges, the temperature profile change depends on the applied LHCD power. The plasma's radial redistribution of current will lead to changes in the ohmic power profile (thereby changing the profile of T_e). LHCD's influence on the magnetic shear (q) changes core MHD behavior and has been observed to create core internal transport barriers[55]. LHCD does not directly heat of bulk electrons but can heat the thermal distribution through the slowing down of fast electrons which occurs on different timescales from the thermal electrons. Each of these effects from LHCD influences the electron temperature profile and are less straightforward compared to other heating sources.

When low density plasmas with low power modulated LHCD (350 kW) were analyzed, they showed a subtle change in the core temperature. Specifically as highlighted in figure 3.10, the electron tempera-
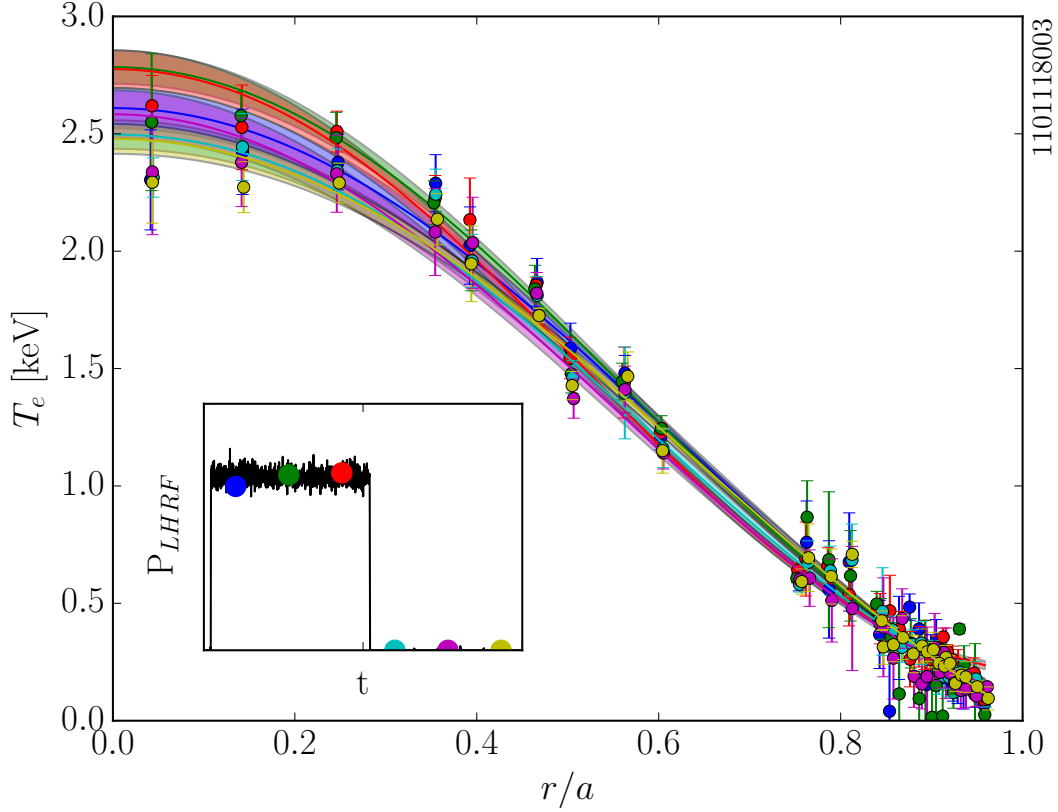
Figure 3.10: Five LHRF modulations from a single discharge were combined at various phases and ensemble-averaged (shown by colored points in inset). The 350kW of applied LHRF power in this 800kA ($P_{OH} = 800$kW) discharge caused a ~ 250 kW decrease in the inductive current ($\bar{n}_e = 7.5 \cdot 10^{19}$ [m^{-3}]). The ensemble-averaged points and associated errors are used with Gaussian process regression to estimate electron temperature profiles. The profiles (with similar color scheme) are MAP estimates with shown σ error bars. While differences with and without LHRF near mid-radius and outward ($r/a > .4$) are not observed, points inside the inversion radius show an increase in temperature. This evident both in the fit and in the TS points in comparing the 'on' phase (red, blue and green) to the 'off' phase (cyan, magenta and yellow). The rise in $T_e \sim 200$ eV, close to the error in the generated profiles.

ture rises in the core by < 400eV for $\rho < .3$. This exceeds the fitted profiles' σ error bar, suggesting that the observed dynamics are outside the variability associated with statistical fluctuations and fitting errors. The temperature increase for $\rho < .3$ highlights core plasma changes can possibly be observed even at lower LHCD power levels ($\Delta P_{LHRF}/P_{tot} = 350/800$ or 43%), where changes in the MHD behavior can improve confinement. This result gives confidence that core changes due to LHRF at high density will be observed with reasonable accuracy.

Using the same procedure, the electron temperature profile was evaluated for similar plasmas at higher densities. The applied LHRF power was 800 kW, nearly doubling P_{tot} due to the low current drive efficiency. Shown in figure 3.11 this large increase in P_{tot} changes T_e
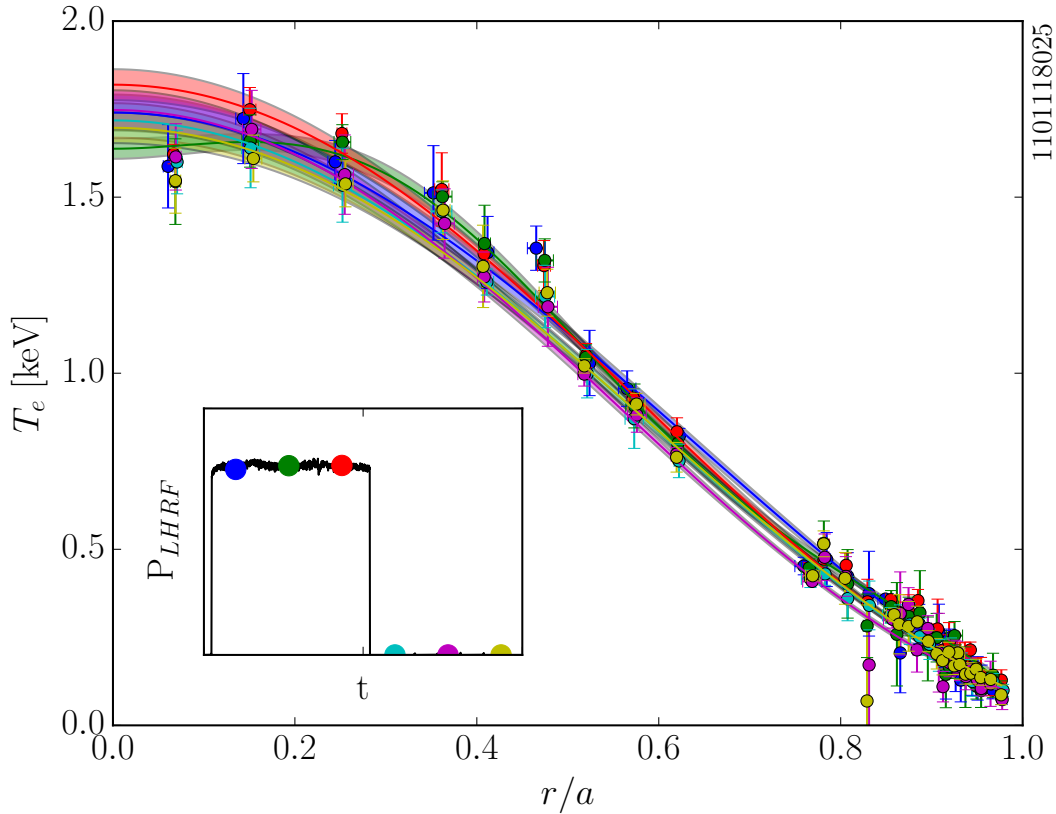
Figure 3.11: Five LHRF modulations from a single discharge were combined at various phases and ensemble-averaged (shown by colored points in inset). In this discharge ($\bar{n}_e = 1.35 \cdot 10^{20}$ [m^{-3}]), the modulation of LHRF power was 800kW. With little to no current drive, this doubles P_{tot} in the plasma (I_p is 800 kA). The MAP estimate profiles both in the fit and in the TS points in comparing the 'on' phase (red, blue and green) to the 'off' phase (cyan, magenta and yellow) show little to no change within the error bars from measurement to measurement. This suggests that a negligible amount of power is deposited in the core plasma in cases without current drive.

by less than 150 eV. Peak values of T_e were $\sim$ 1.7 keV, meaning that T_e varied by less than 10%. This insignificant change in T_e is less than the span of the profile σ error. It is possible that this difference is due to natural variability in the T_e profile.

The negligible change in T_e with the significant change in P_{tot} indicates LHRF's reduced core deposition at high density. The transition from full current drive to negligible current drive is marked by a reduced effect on T_e. The low LHCD efficiency minimally changes in the electron velocity distribution. This suggests that there is no core damping of LHRF on electrons. However, in lower density cases the T_e changes from LHRF are mostly masked by ohmic heating power reductions. The influence of LHRF power in the core of low density plasmas changes the loop voltage, and subsequently is observed in the core plasma for $\rho < .3$.

In the extreme case of immeasurable current drive, the temperature profile is invariant (as measured by Thomson scattering). While some

fast increase in temperature is observed in ECE measurements, it corresponds to a T_e change of less than 100 eV. These measurements are both small and possibly nonthermal, existing below the Thomson Scattering measurement-derived profile variance. In this circumstance, the LHRF waves do not damp on any core electron population. Other locations and populations must also be investigated for this power absorption, requiring the characterization of the core ion population.

The power balance depends on the stored energy and by extension the plasma pressure. While small changes in the electron temperature at high density indicates the lack of core LHRF absorption, changes in the stored energy can still occur. Density changes must also be investigated, as they too can also affect the power balance through the plasma pressure. The following sections describe the effect of LHRF on core electron density and on the ion population.

LHRF impact on core ions at high density

Changes to the core electron temperature indicate little to no deposition of LHRF power at high density. While LHRF waves are unlikely to damp on ions, changes to the core ion and impurity populations could possibly occur[56] at high density. Measurements of core soft X-rays[57] and neutron emission[58] can qualitatively describe the impact of LHRF at high density.

Shown in equation 3.11, the fusion reactivity is nonlinearly dependent on the ion temperature (with T_i in keV). Small ion temperature changes can greatly increase the reactivity with the reaction rate scaling with n_i^2.

$$\langle \sigma v \rangle_{DD} \approx 2.33 \cdot 10^{-8} T_i^{-2/3} e^{-18.76 T_i^{-1/3}} [\mathrm{m^3 s^{-1}}] \tag{3.11}$$

LHRF's impact on the ion population can be determined from this sensitive measure of the ion population. The neutron rate measurement in these plasmas is at the noise floor of the diagnostic. Shown in figure 3.12 is a smoothed time-trace of the total neutron emission. A small modulation in the neutron rate is observed with LHRF.

The exceedingly low total neutron emission makes the zero baseline (therefore the magnitude) questionable. However, the slow and small modulation of the neutron indicates either a change in the ion population, or a very small change in ion temperature. The minimal impact of LHRF on electron temperature would suggest that the small change in neutron rate occurs due to a change in the ion inventory in the plasma.

A similar modulation is also observed in the core soft X-ray emission as measured by the XTOMO system[57]. The soft X-ray emission is a function of the electron temperature and impurity content of the

Figure 3.12: A weak rise in neutron rate is observed with applied LHRF at high density (low efficiency). The rise and fall is similar to an observed response in soft X-ray emission (SXR). The brightness of the core viewing chord is shown. The strong dependence on fusion reactivity on ion temperature for low temperatures ($T_i < 5$ keV) suggests the rise in neutron rate is due to a similar rise in ion density, rather than temperature. The change in impurity X-ray emission also suggests a change in impurity density as there is minimal variation in T_e. The neutron rate of 10^{11} of these plasmas are significantly below the neutron rates of high-performance plasmas, which can achieve values of 10^{14} neutrons per second.
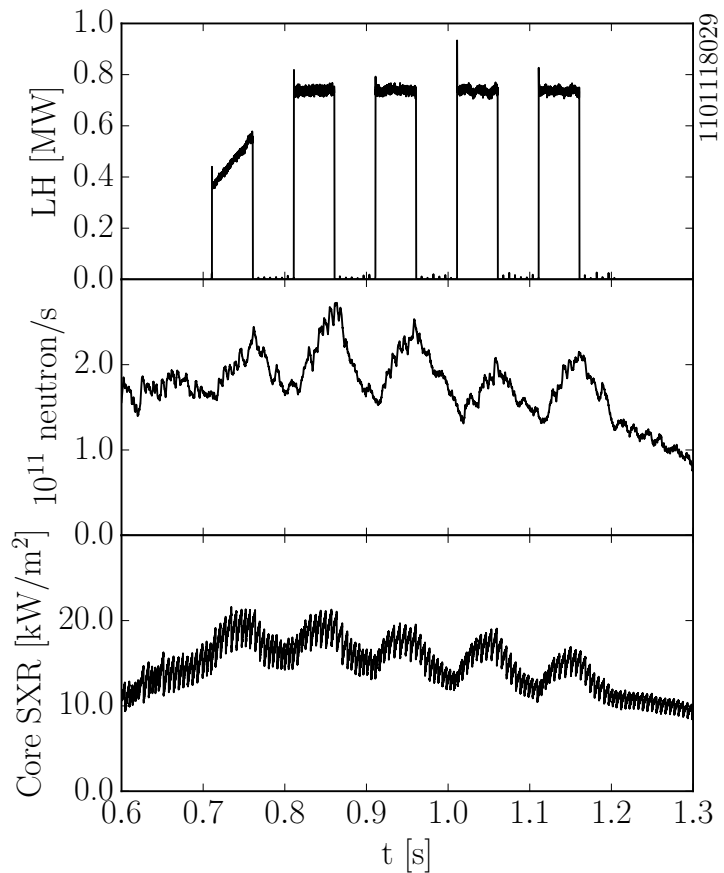
plasma. Minimal variation in T_e at high density indicates that rise in the impurity emission comes from a change in impurity density. The change in the neutron rate and the soft X-ray emission are due to increases in the ion and impurity inventories in the plasma. This motivates the analysis of core electron density profiles.

LHRF impact on core n_e at high density

While little to no variation in T_e is observed at high density with LHRF, improvements in particle confinement can also increase the stored energy. If the energy per particle is constant, a change in the overall inventory will proportionally change the stored energy. As a consequence, electron density profile changes (and the electron pressure) can influence the LHRF power balance. Unlike neutral beam injection which directly fuels the core, higher densities from auxiliary power must come from changes in transport involving edge sources.

Line-averaged density measurements performed using a two-color interferometer[59] show an increase in density with the application of low efficiency LHRF. This density modulation is shown in figure 3.13, responding on the global particle confinement time. This increase and decrease in line averaged density re-equilibrates $\sim$ 50 ms after the

Figure 3.13: The application of LHRF at high density causes a rise in the electron density as measured with a two-color interferometer (on bottom with $\bar{n}_e$) and Thomson scattering system (in middle with n_{e0}). The rise in density is 10% of the background and is dictated by the core particle confinement dynamics. This effect is only observed in cases with minimal current drive. The variation in the Thomson Scattering measured on-axis density makes deducing the 10% variation difficult. The individual modulations can be ensemble-averaged to improve resolution.
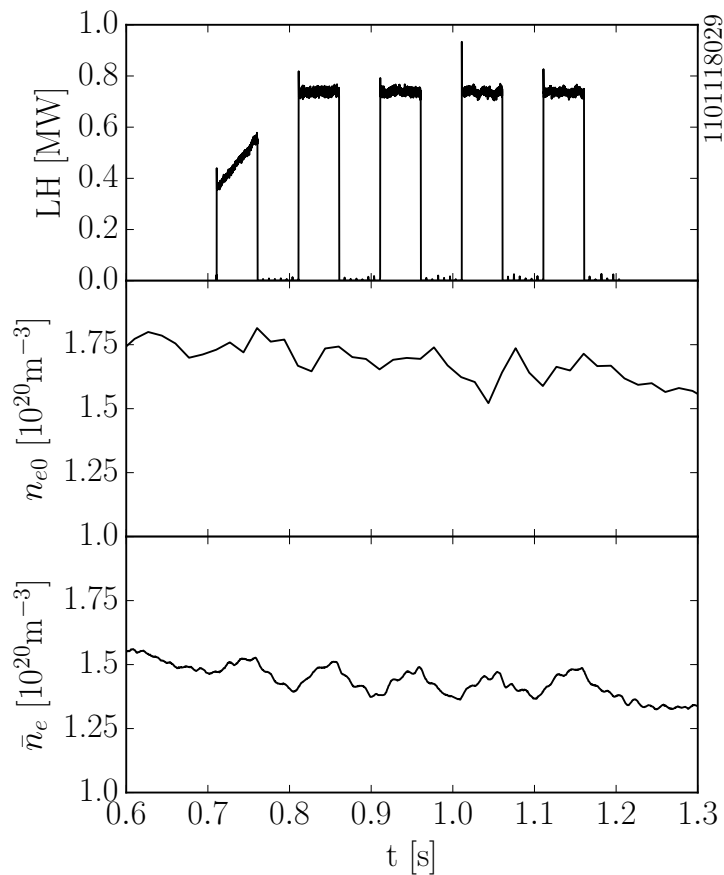
change in LHRF power. The increase in $\bar{n}_e$ correlates with the LHRF power and with the background density. Increasing inefficiency and increasing LHRF power enhance the change in $\bar{n}_e$. In cases with negligible current drive with > 500 kW LHRF, the observed increase in $\bar{n}_e$ is approximately 10%.

This rise in line-averaged density directly correlates with high density LHRF, a faster changes in LHRF power can also be observed on $\bar{n}_e$. In these cases, LHRF power losses due to arcing or high reflection coefficients can be observed in the line-averaged density. The core density will immediately decrease with LHRF power loss at the same rate observed in the rise with LHRF power. LHRF power changes the edge fueling causing the density rise at timescales of the global particle confinement time.

TS profiles can be used to determine any modifications to direct core fueling. The change in the density profile is first examined in low-density plasmas with efficient current drive. Shown in figure 3.14, no discernible change in electron density profile occurs with LHCD at low density. Most measurements of the six profiles overlap, with no systematic difference between the 'on' and 'off' average data points. The various smoothed profiles overlap within error bars across the plasma radius. A correction had to be applied due to variation in the laser energy (an applied 12.8% increase), but was distributed amongst
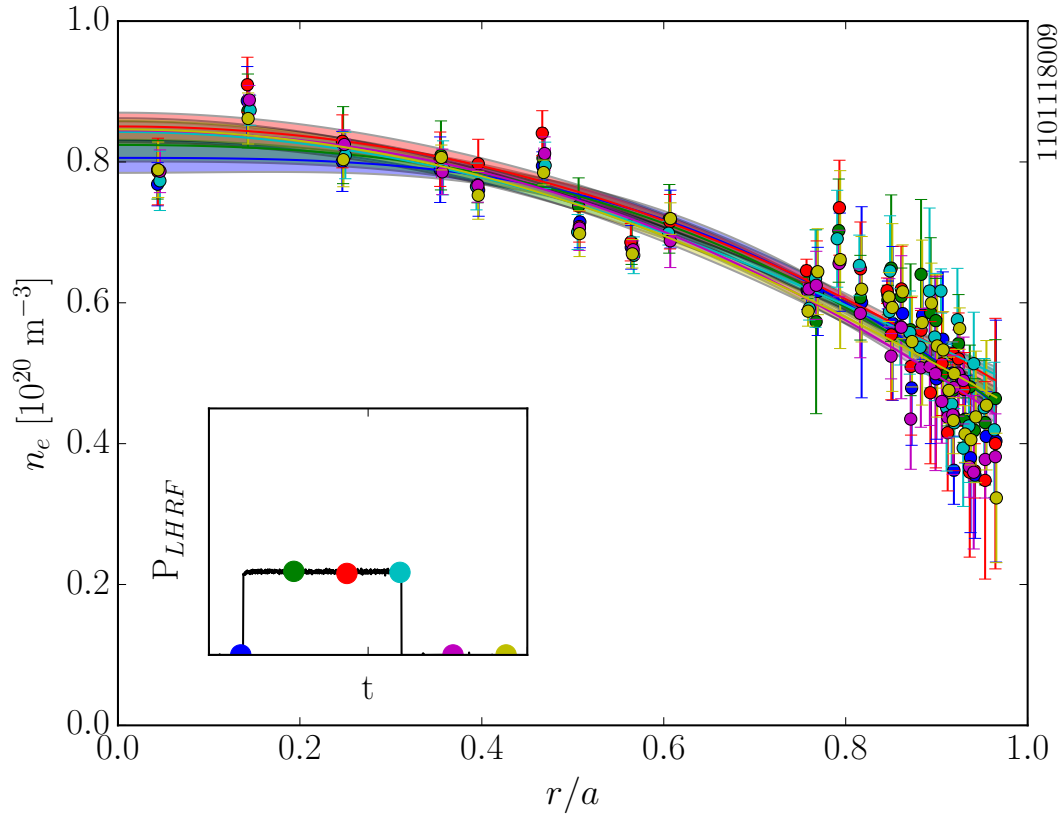
Figure 3.14: Five LHRF modulations from a single discharge were combined at various phases and ensemble-averaged (shown by colored points in inset). In this discharge ($\bar{n}_e = 7.5 \cdot 10^{19}$ [m^{-3}]), the modulation of LHRF power was 350kW. The measured density had to be corrected in some points due to a variation in the laser energy (12.8% variation in the energy). The difference in profiles is within error bars of one another (with the density correction). The overall particle confinement does not change with LHCD in L-mode plasmas (in cases that still have sawtoothing behavior).

the two periods (one phase in the 'off', and two in the 'on'). For this reason, the absolute density is approximate, but the conclusions about relative change in n_e are unaffected.

The TS data and line-averaged density increase minimally by efficient LHCD power. The transition to low current drive efficiency and its effect on the core can be bracketed by the case of immeasurable current drive. Six profiles from a high LHRF power, high density, negligible current drive discharge are shown in figure 3.15. In this instance, changes due to LHRF were observed in the measured electron density radial profile.

A small but systematic edge density increase can be observed in the measurements occurring for $\rho > .7$. This increase occurs in the profiles during the 'on' phase of LHRF. While there is significant noise in the individual measurements near the edge, there is also a consistent increase point to point. This is further reflected in the smoothed profiles, showing a near $\sim 10\%$ increase from $0.9 \cdot 10^{20}$ to $1.0 \cdot 10^{20}$
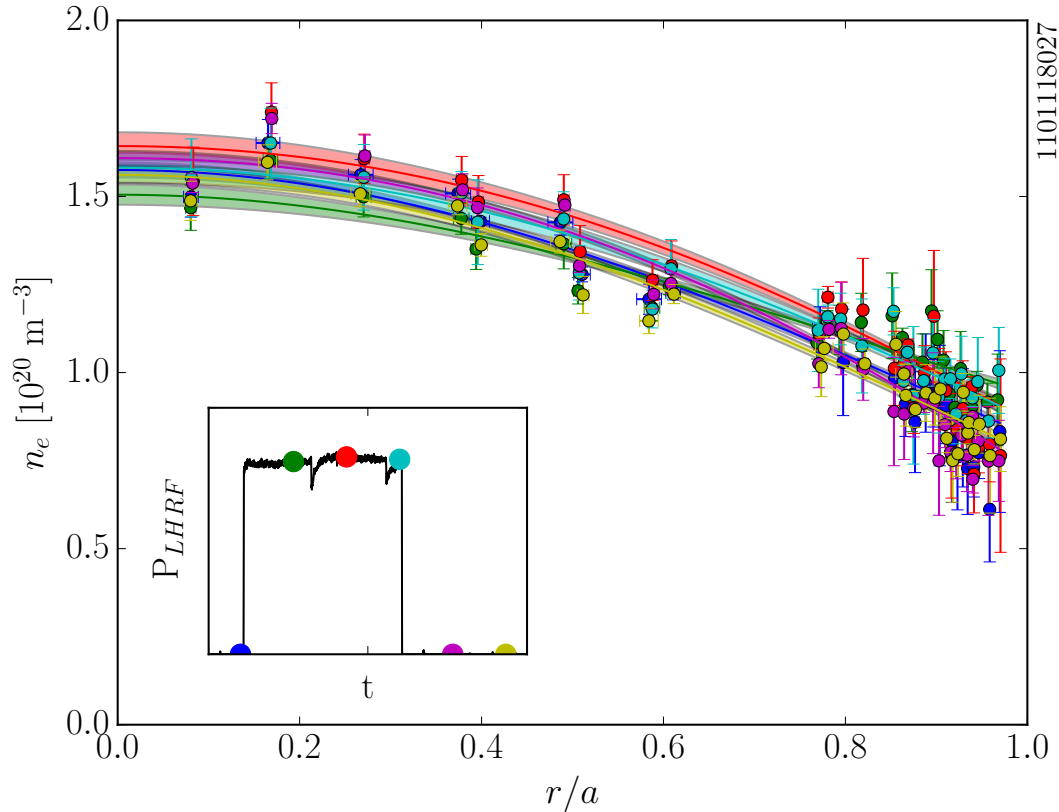
Figure 3.15: Five LHRF modulations from a single discharge were combined at various phases and ensemble-averaged (shown by colored points in inset). In this discharge ($\bar{n}_e = 1.3 \cdot 10^{19}$ [m^{-3}]), the modulation of LHRF power was 800kW with very little current drive. The measured density had to be corrected at some phases due to a variation in the laser energy (12.8% variation in the energy). When corrected, a rise in density for $\rho > .7$ occurs during the 'on' phase (green, red and cyan) of LHRF power. Core density is higher for red,cyan and magenta which suggests that density rise and fall is delayed into the core on the order of the particle confinement time. This trend is observable in the fitted profile and in the measured points (in general). The rise in density corresponds to the change in density observed with interferometry and is noted to begin at the periphery of the plasma. This enhanced confinement of particles leads to a $\sim 10\%$ enhancement in electron stored energy.

[m^{-3}]. This substantive change is outside of the determined σ error, suggesting this is a true effect.

The core density for $\rho < .6$ shows evidence of a delay as core profiles do not exactly match along 'on' and 'off' phases. The profile in the earliest phase of the 'on' period is at a low density. Similarly, the earliest phase of the 'off' phase has a high density. This is consistent with an edge particle source as a finite delay is expected for inward convective and diffusive particle transport.

This result matches the conclusion drawn from the time response in $\bar{n}_e$. An edge particle source would dictate plasma changes beginning with the edge and would have a finite delay in the core. Edge fueling would slowly change the plasma density, but would begin to rise and fall immediately with a change in LHRF power. The line-averaged

density immediately changes with LHRF power, but re-equilibrates on the global particle confinement time.

Assuming that current drive loss does not impact the core ion population, the LHRF does not deposit power instantaneously in the core plasma. However, the observed particle inventory increase leads to a change in the core stored energy. Quasi-neutrality dictates that a similar rise in ion density must occur with the electron density. With the minimal change in T_e, the core stored energy is a function of the LHRF-induced edge particle source. In the extreme case without current drive the increase in stored energy is similar to the density rise of nearly 10%. The particle confinement time dictates both the slow rise in the core density and change in the stored energy. This rigorous analysis shows that the LHCD pulse leads to a negligible instantaneous increase in T_e at high $\bar{n}_e$, which would be expected for core damping. Rather there is a slow 10% evolution in density, stored energy and neutrons which are consistent rather with a modification to the boundary plasma fueling.

This result allows for $\frac{\partial W}{\partial t}$ to be neglected on short timescales in the extreme case of immeasurable current drive. The observed edge particle source and associated negligible change in the core focuses the power balance to the edge. This limiting case dictates that the large increase in P_{tot} must be matched by a change in P_{loss}. Analysis of the loss mechanisms will determine the edge's effect on LHRF absorption at high density. These core results verify that the fast electrons losses are matched by an equal lack of absorption in the core thermal ions or electrons. The extensive analysis of the core species simplifies the power balance and motivates further study of the edge and SOL plasma for LHRF deposition.

EDGE DEPOSITION OF LHRF POWER

Instantaneous edge response

Conclusions from the core plasma analysis require significant boundary changes in order to satisfy power and particle balances. The only observable core plasma change with negligible current drive is a small and slow increase in stored energy. The stored energy rises due to a larger total particle inventory which necessitates modifications to the edge particle source. Deposited LHRF power in cases without current drive also require significant edge losses in order to satisfy power balance. Observed experimental measurements of the SOL must meet the necessary particle and power losses suggested by core plasma dynamics.

As highlighted in figure 3.4, the coupling of energy and particles between two locations is greater with a smaller separation. Core-deposited power is observed as edge losses at timescales on the order
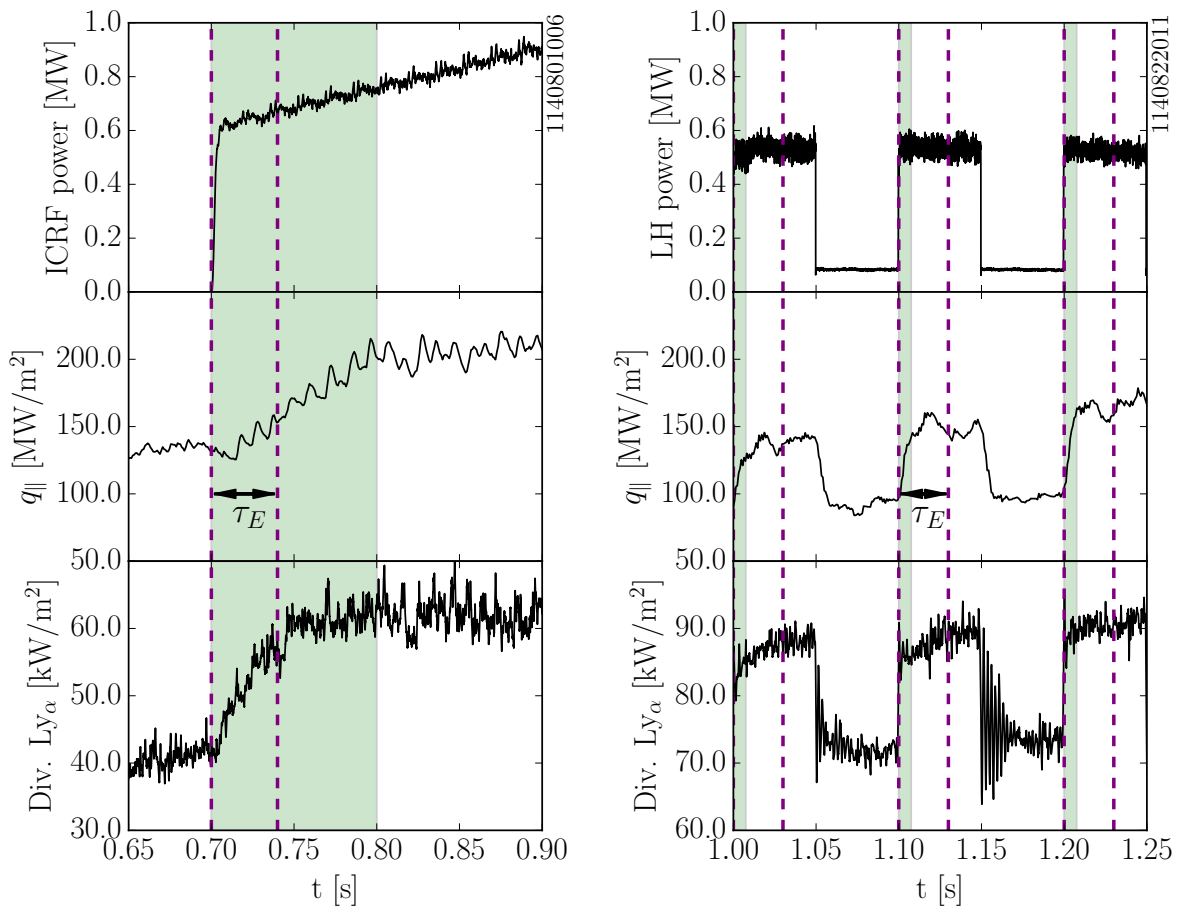
Figure 3.16: Edge radiation and conducted power respond promptly to applied LHRF power at high density. On left is a typical edge response time to applied ICRF power which damps in the core plasma. This corresponds to the energy confinement timescales, typically ~ 30ms on Alcator C-Mod. However, applied LHRF power is observed nearly instantaneously in radiation and conduction much shorter than the energy confinement time, shown on right. The rise time of the strike point heat flux is shown in green, as measured by a surface thermocouple. The increase in divertor Ly_α emission occurs in less than a millisecond.

of τ_E. Edge-deposited power must diffuse significantly shorter distances to be lost and as a consequence the response time is substantially shorter. Measurements of the strike point heat flux ($q_\parallel$) and the hydrogen Ly_α light show a nearly instantaneous response to LHRF power. This clearly indicates that the power of the LH waves is being directly deposited into the boundary plasma at high density, consistent with the lack of any instantaneous core response.

The fast response in the edge is shown in figure 3.17. The magnitude of the strike point parallel heat flux response increases with electron density (given by $\bar{n}_e$). Similarly, an increase in the Ly_α emission also occurs with increasing $\bar{n}_e$. In both cases the magnitude changes with a similar rise times.

The strike point heat flux measurement is made using a specially-designed surface thermocouple[60]. It directly measures the deposited power onto the divertor surface at timescales relevant for C-Mod op-
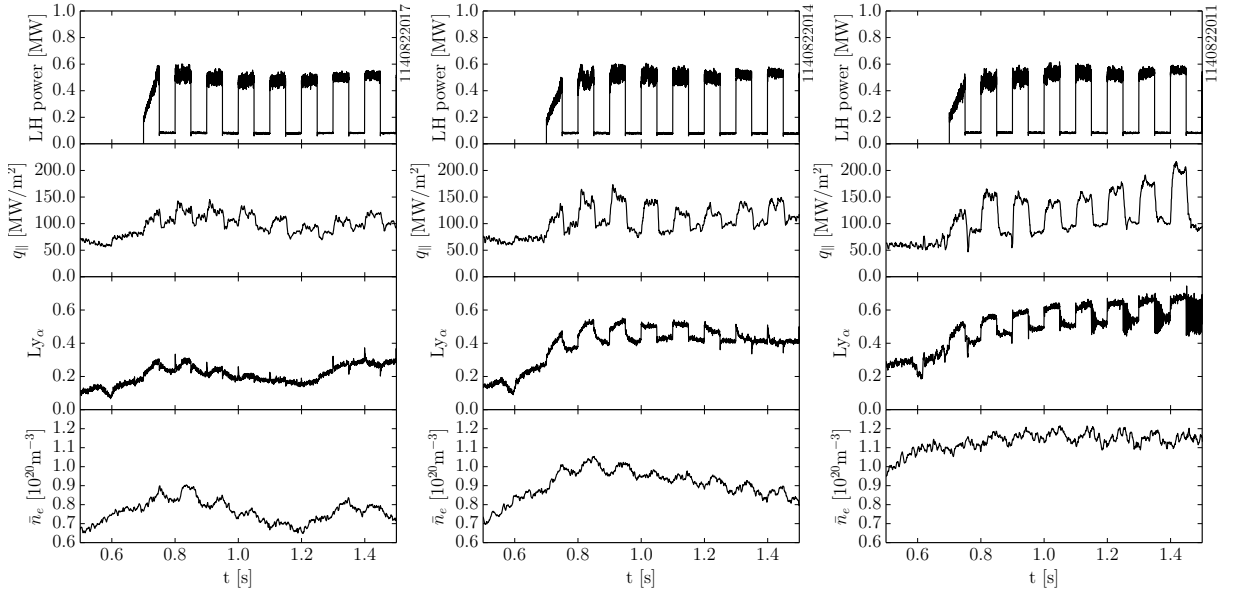
Figure 3.17: Three plasmas at different densities increasing from left to right. The response of the divertor plasma to Lower Hybrid wave power is observed in conduction (strike-point $q_\parallel$ and radiation (Ly_α)). The magnitude increases with density, while the time response is nearly instantaneous. The Ly_α measurement is from the lower divertor in a lower single null plasma. The rise in heat flux and radiation coming from increased total power because of the minimal change in the ohmic power (*e.g.* P_{tot} is a function of density). Fast oscillations in the Ly_α observed in the highest density case are due to oscillations in the divertor neutral pressure.

eration. The outer divertor strike point was placed on one surface thermocouple (within the capabilities of EFIT and the C-Mod control system). The time necessary for the change in heat flux is on the order of the measurement time resolution, $\sim 1ms$.

Measurement of the divertor Ly_α emission (as described in Chapter 2) represents changes in the edge radiation. It is closely related to ionization and can also be used as a proxy for SOL fueling changes. The increase in Ly_α also occurs at the diagnostic time resolution limit which is less than a millisecond. Similar responses to LHRF are also seen in other edge light measurements (such as in H_α and TS backgrounds).

The increasing losses due to edge conduction and edge radiation can be simply quantified due to the instantaneous nature of the edge loss. Instead of using breaking-slope or Fourier decomposition techniques, the subtraction of the two states (with and without LHRF) can separate the LHRF influence from the background shown in equation 3.12. The measured changes calculated from the subtraction are normalized to the step in LHRF power.

$$\Delta P / \Delta P_{LH} = \frac{P_2 - P_1}{P_{LH,2} - P_{LH,1}} \tag{3.12}$$

Figure 3.18: The change in the outer strike heat flux rises with line-averaged density as measured by a surface thermocouple. This change in $q_\parallel$ is normalized to the LHRF modulation power magnitude and increases with density. This trend (shown by a linear fit in red) occurs with the transition from the sheath-limited regime to the high-recycling regime. This is shown by the T_e as measured by a toroidally offset Langmuir probe. An increasing amount of LH power is being observed as conduction near the outer strike point with the decreasing of LHCD efficiency.
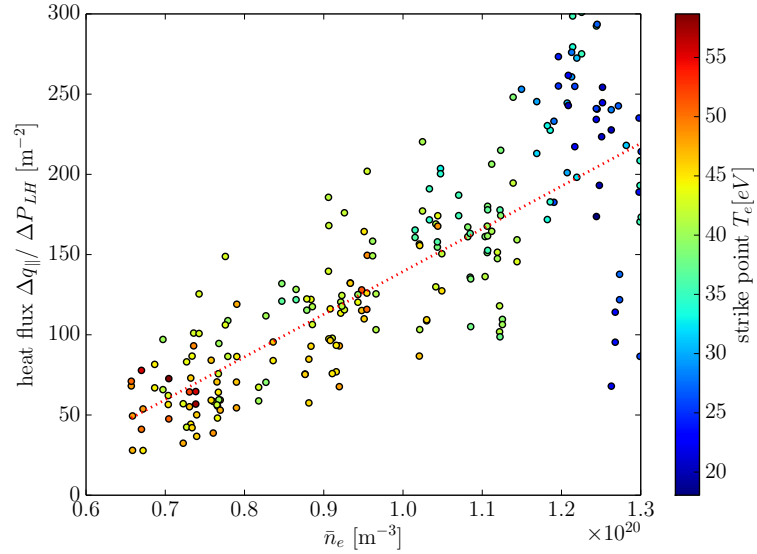
The normalized power $\Delta P/\Delta P_{LH}$ defines the LHRF power fraction that is observed in a particular mechanism. Fractional calculations assume that the measured parameters change linearly with the step in LHRF power. Trends in this metric define the relative importance across the loss of efficiency in current drive and can then be used to derive edge LHRF deposition characteristics.

Figure 3.18 was generated using the subtraction analysis with LHRF modulation steps of 450kW and 200kW. The change in outer strike point parallel heat flux is normalized to the step LHRF power. The figure highlights the heat flux's linear response to LHRF power. While some scatter is observed in the data about a linear trend with $\bar{n}_e$, there is no systematic difference between the two sets of measurements.

The rise in the outer strike point parallel heat flux occurs during the transition from a sheath-limited to conduction-limited SOL. The electron temperature dropped across the range of density as measured by a toroidally offset Langmuir probe. Edge effects due to LHRF increase linearly with decreasing LHRF efficiency indicating that LHRF increasingly interact with the edge. This result motivates further study of the characteristics observed during the transition to negligible current drive, discussed in the following chapter.

The fast response in the edge validates the edge deposition expected from the core analysis. The immediate reaction in conduction and radiation proves the edge absorption of LHRF power. Fractional loss calculations are simplified by the prompt edge response, allowing for LHRF power isolation through subtraction. These calculations quantify the edge deposition to determine its importance to current drive loss. The following sections determine modulation in P_{rad}, P_{cond} and P_{OH} in order to follow the LHRF power flow.

Edge-deposited conducted power

Measurements of the total conducted power were made using Langmuir probes[5] and IR thermography[61]. The inner and outer divertors were treated separately due to their physical separation and difference in plasma conditions, ΔP_{cond} is defined in equation 3.13. In lower single null forward field plasmas, the background conducted power is predominantly observed on the outer divertor. The modulation isolates the edge LHRF contribution allowing for the quantification and comparison to other power losses.

$$\Delta P_{cond} = \Delta P_{cond,inner} + \Delta P_{cond,outer} \tag{3.13}$$

The Langmuir probe-derived heat flux assumes a conservative sheath heat flux transmission coefficient (γ, where $q_\parallel = \gamma j_\parallel T_e$) of 7. Each array of probes is localized to a specific toroidal angle with a $< 5°$ toroidal spread. The interpolated toroidally symmetric heat flux profile (*i.e.* in the $\hat{R}$ direction) is integrated along the divertor surface. The assumed toroidal axisymmetry is counter to other results with LHRF on C-Mod[62] and other tokamaks[63, 64, 65] where edge power loss has been local to specific nearby surfaces. The following chapter discusses this assumption's validity.

A fast (300 fps) IR camera is also used to determine the heat flux to the outer divertor. Blackbody emission from the associated divertor temperature rise is translated into heat fluxes and into the integrated conducted power. The separate heat flux measurements derived from different physical principles provides confidence in the calculated total conducted heat to the outer divertor. Shown in figure 3.19, the modulation in the strike-point parallel heat flux is also observed in the integrated conducted power both in the Langmuir probes and by IR thermography.

The instantaneous conducted power increase with applied LHRF at high density is also observed in Langmuir probe and infrared measurements of the conducted power. The similarity in the derived total conducted heat suggests that the power loss is thermal in nature (which is addressed in chapters 4 and 5). At the same $\bar{n}_e$ and step in P_{LH}, variability in measurements of 100kW or greater exist for each of the calculated conducted powers. The conducted power difference is not systematic and varies shot to shot for both the modulation and ohmic periods of the discharge. This difference also leads to 20% variation in the conducted power loss fraction. The power balance analysis must be achieved in a statistically rigorous manner due to the observed scatter in values. Nonetheless one can see that at high density approximately 50%-70% of the LH power instantaneously appears as conducted power at the active divertor surfaces. This alone indicates very localized damping of LH wave power deposition in

Figure 3.19: The conducted power loss fraction of LHRF is found to be ~ 50% in this high density example. Calculation of the conducted loss fraction assumes toroidal symmetry of the measured heat flux and is integrated about the divertor plate surface. Measurements from both Langmuir probes and from infrared thermography instantaneously respond to LHRF power. Differences in the calculated fraction highlight the difficulty of the measurement, but are within 20% of one another.
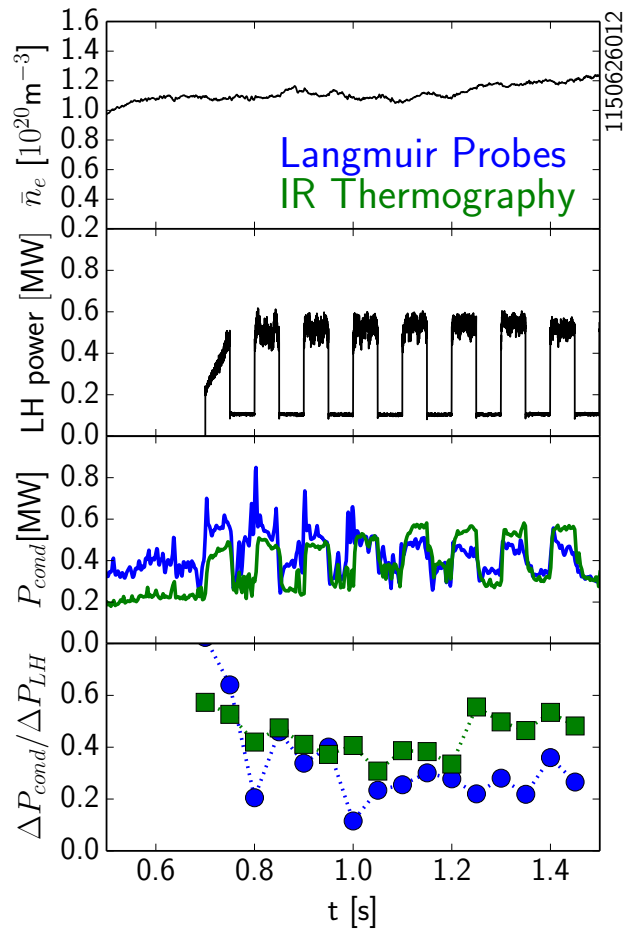
the boundary plasma. IR thermography is the best direct method for determining the deposited heat and is subsequently used in the following analysis.

In figure 3.19, the observed outer divertor conducted power fraction represents 50% of the LHRF power. This is evident in the outer divertor conducted power time-traces as measured by IR thermography and the Langmuir probes. For these plasma conditions (5.4T, 700kA, $\bar{n}_e \sim 1.1 \cdot 10^{20}$ [m^{-3}] and LSN), the sizable change in P_{cond} indicates that at least half of the LHRF power is not driving current and is instead directly depositing power in the boundary plasma. This example plasma discharge proves edge deposition's importance in the loss of LHCD.

Measurements of the conducted power to the inner divertor are significantly smaller with a reduced LHRF response. It is likely that the in/out distribution of edge-loss LHRF power follows similar characteristics to edge power loss observed with core deposition. In figure 3.20, the conducted power modulation does not exceed 10 kW. The measured ohmic conducted power is also small, measured below 100kW for the entire tested plasma density range.

Figure 3.20: The conducted heat measured on the inner divertor is small in forward field LSN plasmas. The example plasma shows ~ 5 kW of modulated LHRF power, which is approximately 50 times less than the LHRF conducted heat on the outer divertor. The modulation of inner divertor conducted power decreases with density and is intermittent is forward field. The observed LHRF power conducted to the inner divertor is typically less than 20 kW. For calculations of power balance in forward field, this contribution is neglected as variability in other losses are much greater.
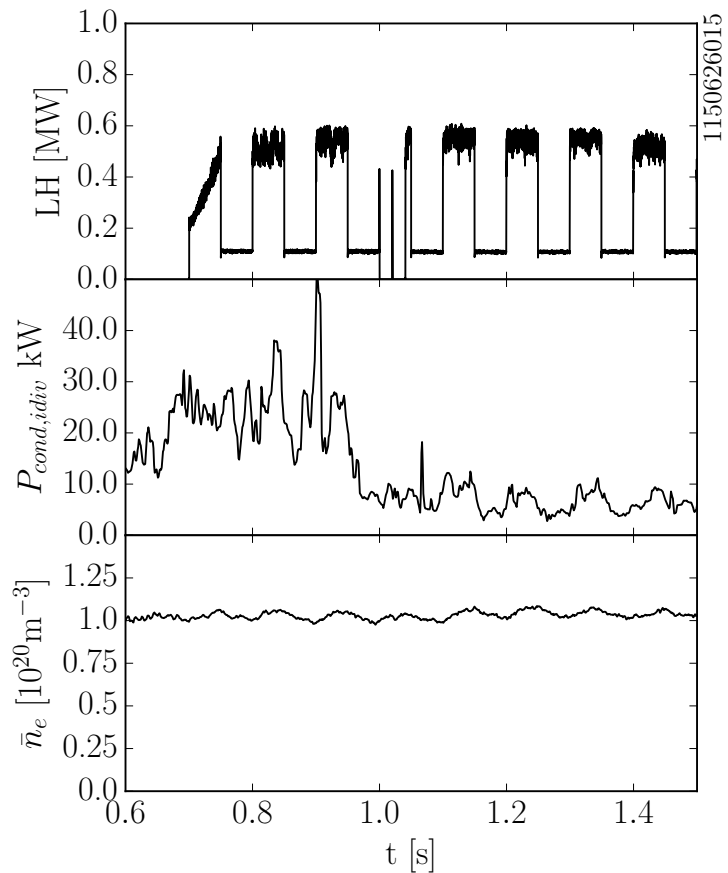
The inner divertor's conducted power modulation due to LHRF is intermittent in forward field plasmas. Just as in figure 3.20, in most cases modulation intermittently observed and are therefore not reliable. As a consequence of the possible field-direction dependence of the conducted power's in/out symmetry, the LHRF waves' power balance will be shown in forward field plasmas. This is due to the larger data set, better outer divertor diagnostic coverage and higher steps in LH power from improved coupling.

The observed inner divertor modulations decreased with line-averaged density countering to the observed trends on the outer divertor. It is likely that with increasing $\bar{n}_e$, the inner wall's high-recycling conditions reduces the conducted LHRF power. Variation in the measured power conducted to the outer divertor exceeds the entire modulation in conducted power on the inner wall. The inner wall contribution to the LHRF power balance is neglected due to the small contribution and irregular nature of the observable modulation.

A trend in the outer divertor conducted power fraction was generated from the integrated power as measured by IR thermography. The linear fit was generated from the ensemble of modulations from six discharges across the density span. The fraction of LHRF power conducted to the outer divertor increases with lower LHCD efficiency, shown in figure 3.21. The trend in the conducted power from 20% to

Figure 3.21: The fraction of LHRF power instantaneously lost as outer divertor conducted heat increases with increasing $\bar{n}_e$. This trend was measured by infrared (IR) thermography. Conduction losses increase with $\bar{n}_e$ and decreasing LHCD efficiency. This trend is derived from forward-field LSN plasmas on 1150626 with sufficiently accurate IR data. Measurements with little or no response to LHRF are neglected in order to remove false negatives. This impacts the lower bound of the trend, as changes $< 10\%$ or 50kW are noise dominated. The high density cases show upwards of 60-70% of LHRF power conducted to the outer divertor. This trend does not extend past $\bar{n}_e = 1.3 \cdot 10^{20}$ [m^{-3}] due to transitions to H-mode and the influence of high-recycling. This effect is described in Chapter 4.
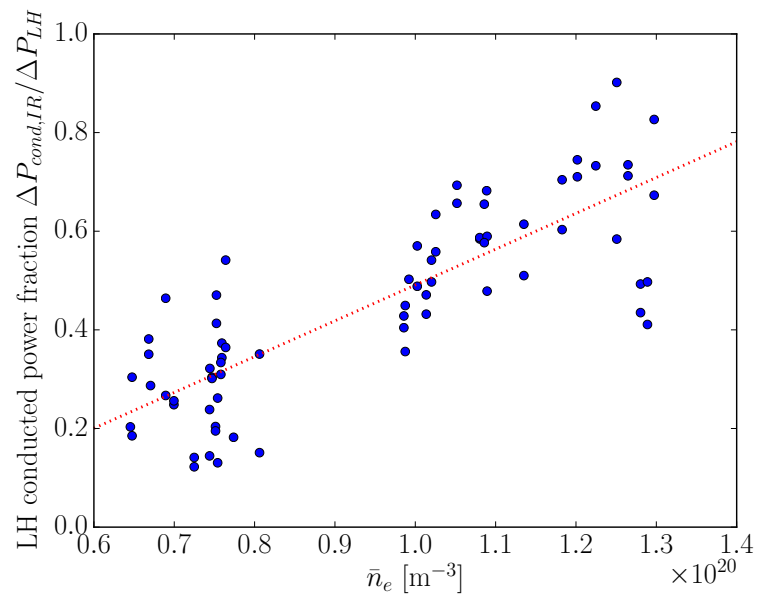
70% was fit using linear regression, yielding parameters described in table 3.2. The linear fit best matches the observed trends with $\bar{n}_e$ in the total conducted heat and in the strike point heat flux onto the outer divertor.

The conducted loss measurements below 20% were difficult to determine due to instrumental noise. This calls into question the validity of edge losses for low plasma densities. However, the edge loss trend is corroborated by the qualitative interpretation of the outer strike point heat flux as measured separately by the surface thermocouples. The instantaneous LHRF power edge loss via conduction is observed even at the lowest densities with efficient current drive (shown on far left in figure 3.17). This proves that edge loss mechanism occurs at all densities and that only the degree of importance is strongly correlated with $\bar{n}_e$.

Many modulations were combined to yield conducted power trends. The edge losses observed in conduction became dominant with the loss of current drive. This proves LHRF edge absorption at high density reduces the current drive efficiency. However, radiated power must also be evaluated for power balance, as it represents another possible loss mechanism. In the next section, radiative edge losses are evaluated for the power balance completion.

Radiated power

Radiation constitutes the other large edge loss mechanism on Alcator C-Mod. The immediate change in edge radiation indicates that radiative loss is also important for the LHRF power balance. This loss,

as shown in the measurement of Ly_α in figure 3.17 becomes increasingly important with $\bar{n}_e$. Multiple foil bolometer systems integrated radiation from Ly_α and other wavelengths. Two systems of absolutely calibrated foil bolometers observed LHRF modulation at high density.

The two bolometers systems each measure different aspects of the radiated power. A wide-viewing single foil bolometer integrates the emissivity across a large fraction of the vacuum vessel[66]. Viewing limitations reduce the observation of the outer leg of the divertor plasma. The second system uses an array of foil bolometers to determine the midplane radiation's radial profile[67]. This can be integrated over the plasma volume to yield the power from core radiation.

Core soft X-ray emission measurements (shown in figure 3.12) indicates a slow rise in the core radiation as the core density increases. This loss via core radiation can influence the LHRF power balance calculation and must also be independently characterized. The foil bolometers' slow time response makes separation of the prompt edge radiation from the core rise difficult. However, similar diode-based systems with similar views can better characterize the radiated power's rapid time response.

Figure 3.22: The fraction of LHRF power observed as core plasma radiation is small. This component of P_{rad} corresponds to the increase in core particle inventory in the main ion, electron and impurity populations. Core P_{rad} is generated from radial profiles of radiated power which are measured by a pinhole array of bolometers at the midplane. This fraction is $< 10\%$ of the LHRF power. A trend is not shown due as this contribution saturates near 10%, similar to the change in observed core density.
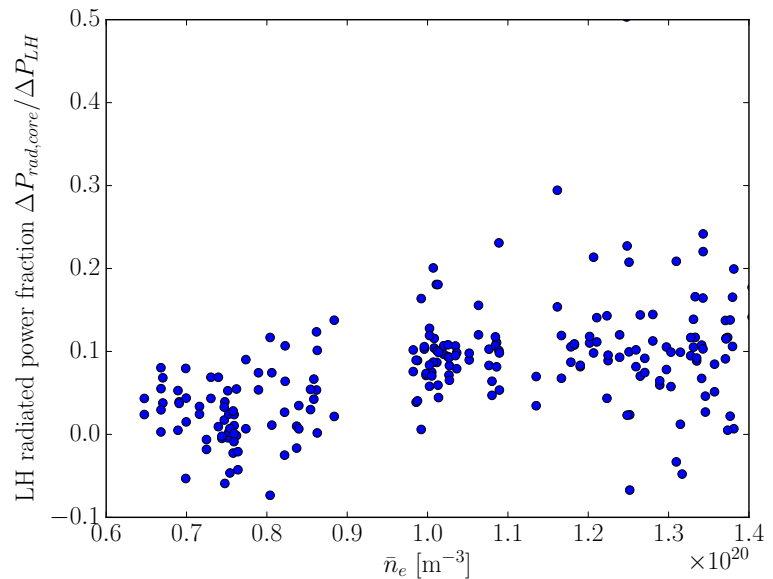
While the single foil bolometer system estimates the total radiated power, these two measurements' differences can give some idea of the divertor radiated power. The trends in the two measured radiated powers are given in figures 3.22 and 3.23. In both cases the change in radiated power is minimal at low density and increases with decreasing LHCD efficiency.

The modulation in core radiated power fraction approaches 10% in cases with negligible current drive. This low value is near the diagnostic's resolvable limit. However, the 10% fraction roughly matches

the fractional core density change determined by $\bar{n}_e$ (which is also $\sim$ 10%). The core radiation change is expected for similar core temperature and Z_{eff} plasma conditions.

The total radiated power as calculated by the '2π' bolometer shows an increase from nearly 0 to 30% of the LHRF power observed as radiation. The trend in LHRF radiated power fraction is given in table 3.2, with a lower R^2 value (in comparison to the trend in conducted power). The measurements contain similar variability as observed in the outer divertor conducted power, with a reduced range in radiated power fraction which causes the lower R^2 value.

Combining the two trends suggests that $\sim$ 20% of the LHRF power is observed as edge radiation. This loss correlates with current drive loss and matches the qualitative Ly_α observations. If the prompt conduction losses are included then at least 70% of ΔP_{LH} appears promptly in the boundary rather than the core, which causes all high-density LHRF power to be observed in the edge. This also matches the expectation derived from the core Thomson Scattering results.

Figure 3.23: The change in radiated power ΔP_{rad} increases with increasing electron density as measured by the 2π foil bolometer. The wide spread in data highlights the variability of the calculated radiated loss fraction of LHRF power ($\sim$ 10%). A least-squares linear trend shown in red for a dataset of > 300 independent values. This measurement does not include the radiated power from the outer strike point due to limitations in the view. The increasing observation of modulation in P_{rad} highlights the edge loss of LHRF. This data represents the combination of 2 rundays with the same LSN, 5.4T, 700kA equilibrium (1140822 and 1150626).
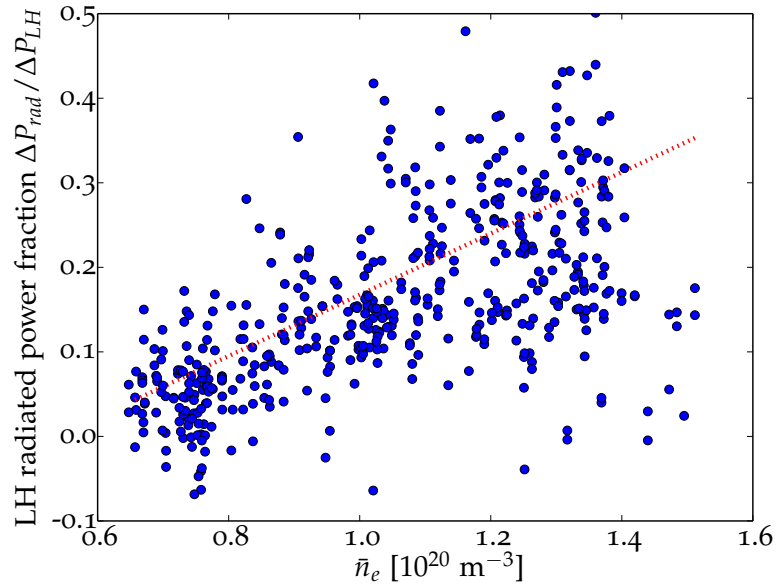
The power fraction observed as radiation is likely to increase beyond the tested density range as divertor detachment becomes more probable. In this case, very little conducted power is observed on the divertor. The transition of SOL regimes (*i.e.* the transition to high-recycling) also affects the distribution of edge losses in conduction and radiation. The large natural variance in the measured power losses makes any significant determination of this change difficult. Effects related to the interplay of radiation and divertor conduction are observed with LHRF, and are discussed in the following chapter.

Power balance

The capability of LHRF in driving current can be roughly estimated by using EFIT [68]. While some error can be expected in cases with significant current drive, the deposited ohmic power estimation improves at high density. Due to the modulation period, the time history of P_{OH} is derived from a set of EFIT reconstructions every millisecond (EFIT01). Unlike previous experiments which used density-ramps that change core temperature conditions, the modulation method can extract a trend in $\Delta P_{OH}/\Delta P_{LH}$ versus $\bar{n}_e$.

In the general plasma power balance, ohmic power represents an input. In the case of LHRF wave power balance, ΔP_{OH} is a 'loss' term, as ΔP_{LH} reduces P_{OH}. This difference can be observed in the ΔP_{tot} trend. As current drive becomes more inefficient, the LHRF wave power increases the total power within the vessel because the ohmic power is not reduced by LHRF.

Figure 3.24: The loss of current drive can be observed in the change in the total power into the C-Mod vessel (ΔP_{tot}). In cases with high efficiency current drive, the change in P_{tot} is approximately zero. ΔP_{tot} increases with the background density as the population of fast electrons degrades. This trend in ΔP_{tot} (and by extension P_{OH}) indicates the loss of current drive. At the highest densities where current drive is minimal, $\Delta P_{tot}/\Delta P_{LH}$ approaches unity. Variation in the ohmic power influences the power balance, highlighting the difficulty of the Lower Hybrid power balance calculation. This trend is highlighted by a linear fit in red, with data above $1.35 \cdot 10^{20}$ neglected due to change in confinement (high density data from H-mode which is neglected).
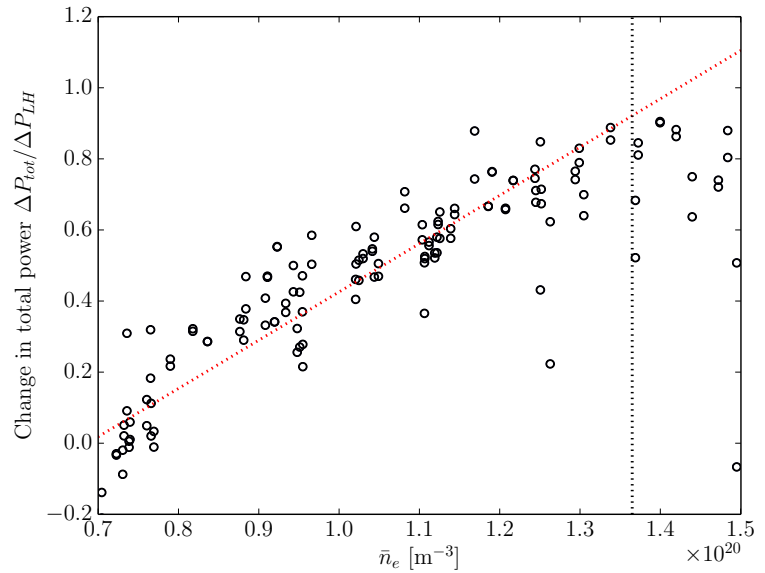
Shown in figure 3.24, the total power into the vessel increases with density as calculated by the EFIT-generated ΔP_{OH}. The nearly linear rise in this parameter at the lowest densities suggests that the current drive loss is linear with $\bar{n}_e$. At high densities, little to no LHRF power into the plasma drives current. With the calculation of ΔP_{tot} and ΔP_{OH}, the LHRF power balance can be completed.

The measurements of the current drive fraction ΔP_{OH} and P_{tot} each contain similar variability to the other power balance terms. However, the trend spans the physically allowable range of values from near zero change in ΔP_{tot} at low density to near unity at the highest densities. A fit in ΔP_{OH} is given in table 3.2, showing a $\sim 10\%$ error with a high R^2 value.

The ohmic and LHRF power balances are shown in figure 3.25 and table 3.1 for a forward field plasma with little current drive. A majority of the power is observed conducted to the outer divertor. The small contributions of certain sources (such as core radiation and inner divertor conduction) are on the order of the dominant losses' error. For the power balance of LHRF waves, these small contributions are neglected.

Loss	Ohmic %	LHRF %
ΔP_{OH}	-	20
$P_{cond,outer}$	43	56
$P_{cond,inner}$	7	1
$P_{rad,outer}$	10	4
$P_{rad,inner}$	25	13
$P_{rad,core}$	15	6

Table 3.1: Observed power balance of a discharge with significant edge absorption of Lower Hybrid power ($\bar{n}_e = 1.15 \cdot 10^{20}$ [m^{-3}], $B_T = 5.4$T, $I_p = 700$kA, forward field). The isolated net Lower Hybrid power generates a small fraction of the total current at this density, with edge absorbed power resembling the ohmic power loss. Errors on each measurement is of the order of $\sim 4\%$ for the Ohmic power balance per measurement, and $\sim 6\%$ for the Lower Hybrid power balance.

The precision in the edge loss measurements limit the fractional resolution of edge losses. For a given modulation of 450 kW, 5% of ΔP_{LH} is 22.5 kW, a value below the 50 kW reliable resolving capability of some power loss measurements. Power balance calculations can be improved using greater steps in LHRF power and can made more difficult with smaller steps in power. Future tests using LHRF power modulation for the edge loss current drive on C-Mod and other tokamaks requires the maximum power for the best resolving capability. The example highlights the importance of fractional measurement variance in the power balance's precision.

The trends in ΔP_{tot}, ΔP_{rad} and ΔP_{cond} each corresponds to the current drive loss via prompt edge absorption with increasing $\bar{n}_e$. Each measurement is independent and can be combined to generate a trend in power balance versus $\bar{n}_e$. These trends are shown in figure 3.26 and associated table 3.2. The three trends were created from the data of a single runday, as to remove any systematic biases that could develop from other operational days.

The calculated value of ΔP_{LH} is anomalously high by $\sim 15\%$. However, this discrepancy is likely due to the combination of a systematic and random error. Difficulties in measuring the ohmic power and conducted power with significant current drive likely cause the $\sim 15\%$ discrepancy in the power balance at low density. The error in this calculation is approximately $\sim 12\%$, which is generated through the
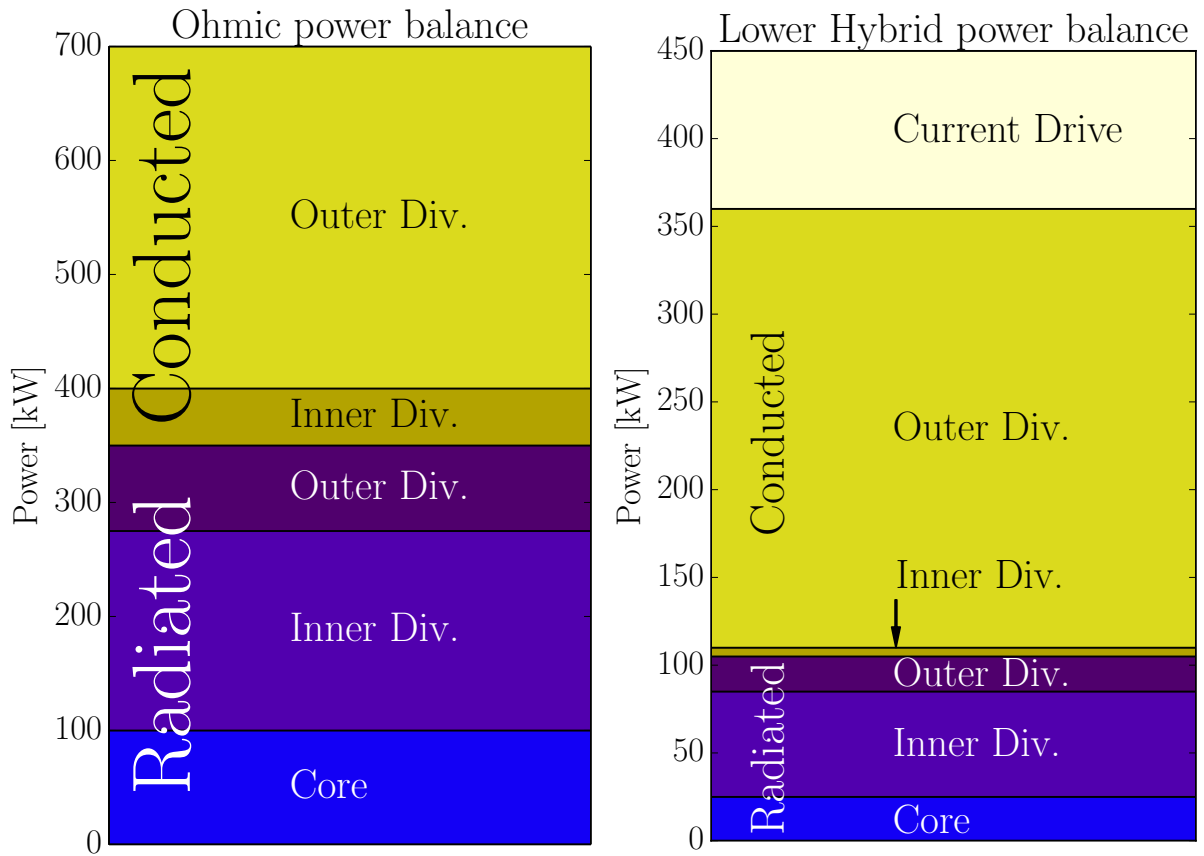
Figure 3.25: The power balance of ohmic Alcator C-Mod plasmas and the influence of ΔP_{LH} have been calculated. On left is an example ohmic power balance at $\bar{n}_e = 1.15 \cdot 10^{20}$ m^{-3} where a significant fraction of power is conducted to the outer divertor. The error in each loss mechanism calculation is ± 25kW. Similarly on right is the extracted loss channels of ΔP_{LH} with similar calculation errors. This induces an error of at least 10% with the dominant loss mechanism being the conduction to the outer divertor. A small fraction of LHRF power continues to drive current and accounts for 10% of I_p. This example is a snapshot of the power balance of Lower Hybrid power. The distribution of losses in radiation, conduction and location is dependent on $\bar{n}_e$ and I_p and will change accordingly. (data from 1150626012 at 1.2s, significant variability can be observed at the same conditions).

sum in quadrature of various fits. This is on the order of this discrepancy assuming that the error in each fit is independent.

The combination of the three independent trends into a complete and accurate power balance ($\Delta P_{LH} \sim 1$) indicates that current drive loss is promptly found in the boundary plasma. This is true across the range at which the current drive efficiency drops. The linear reduction in ohmic power due to LHRF is observed as conducted and radiated power. This would indicate that the current drive loss is due to a mechanism that parasitically absorbs power near the periphery.

While previous trends observe minimal current drive and hard X-rays for $\bar{n}_e \sim 1.2 \cdot 10^{20}$ [m^{-3}], a small $< 20\%$ fraction of power still drives current. This current drive is sufficiently small that global power balance is unable to properly resolve its effect on the ohmic
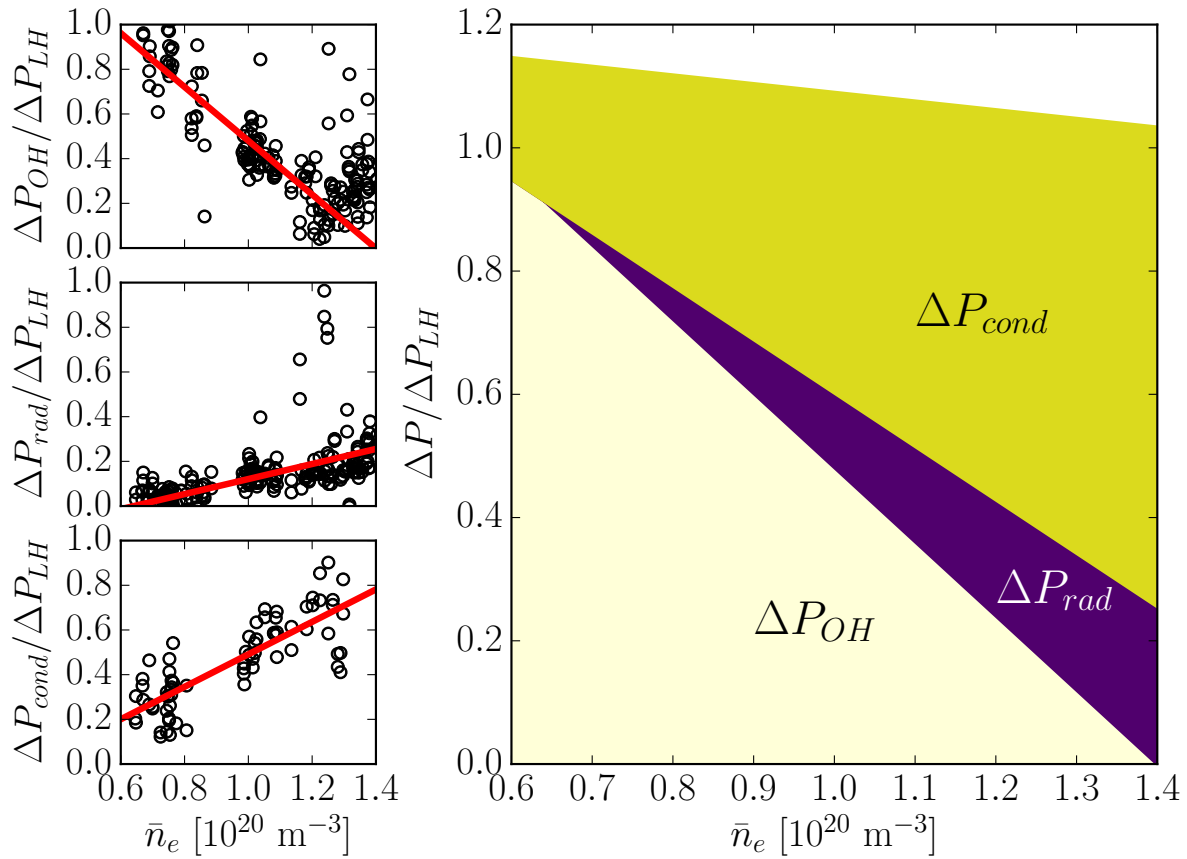
Figure 3.26: The power balance of LHRF waves in 700kA, forward field 5.4 T discharges is verified for the range of density of current drive loss. Each contribution is measured independently with its own linear trend. The ohmic contribution is generated from EFIT, the radiated contribution from a wide-viewing bolometer and the conducted power using IR thermography. Each trend and associated data is shown as a fraction of LHRF power on left. The combination of the three trends is within 15% of the total LHRF power (ΔP_{LH}) and is shown on right. This is within the variability of the combined trends, giving validity to parasitic edge deposition of LHRF power causing the loss of current drive efficiency. This data is generated from the 1150626 runday.

power. This contribution to the plasma current replaces less than 15% of the ohmic drive at 700kA for modest LHRF powers ($\sim$ 500 kW). This minuscule amount of current ($<$ 100 kA) is difficult to discern in V_{loop} changes. The further deterioration of current drive makes LHCD in H-modes ($\bar{n}_e > 1.4 \cdot 10^{20}$ [m^{-3}]) impossible.

A parasitic edge loss mechanism observed at low densities that increases in magnitude matches the power balance and associated effects of LHRF. The edge's fast response is observed at all densities and at various magnitudes. The current current drive loss must similarly exist at all densities to some degree. This power balance allows for this and other derived characteristics to be used in finding the cause of the loss of current drive efficiency.

Table 3.2: Linear fits of the data shown in figure 3.26 highlight the variability in deriving the power balance of LHRF waves in Alcator C-Mod. This data is valid for $\bar{n}_e = 6 \cdot 10^{19}$ - $1.3 \cdot 10^{20}$ [m^{-3}] forward-field, LSN discharges at 5.4T and 700kA. This comprises the density range where current drive is lost for this equilibrium. The errors in the parameters span $\sim 15\%$, which is 60kW for $\Delta P_{LH} = 400kW$. This impacts the goodness of fit, which is evident in the smaller P_{rad} trend. The total power balance generated from the combination of each trend is within 15% of the expected total across the density range. This is less than the expected error assuming that errors of each measurement are independent and add in quadrature. The dataset and linear regressions were generated from runday 1150626.

$f = A\bar{n}_e + B$	$\hat{A} \cdot 10^{-20}$ m^3	$\sigma_{\hat{A}}$	$\hat{B}$	$\sigma_{\hat{B}}$	R^2
$\Delta P_{OH}/\Delta P_{LH}$	-1.294	$\pm$.068	1.684	$\pm$.071	.708
$\Delta P_{rad}/\Delta P_{LH}$	.337	$\pm$.074	-.216	$\pm$.073	.416
$\Delta P_{cond}/\Delta P_{LH}$	.726	$\pm$.061	-.236	$\pm$.060	.661
$\Delta P/\Delta P_{LH}$	-.231	$\pm$.118	1.232	$\pm$.118	-

SUMMARY AND DISCUSSION

Radiofrequency power modulation has been used extensively for understanding both the plasma's heat transport and the deposition of power. This technique was used to understand the LHRF density limit through the characterization of the core and edge plasma. The set of constant-parameter plasmas allowed for reproducible, independent LHRF wave power balance calculations. Trends in the various power balance components versus $\bar{n}_e$ show the prompt increasing deposition of LHRF power in the edge plasma.

Only small increases in density could be resolved in the core plasma with the application of LHRF power with negligible current drive. Calculated using Thomson scattering, no statistically significant change in the core electron temperature was observed. Changes in the core electrons density subtly increased the core's stored energy with similar core ion population changes. The small variation in any core population to LHRF matches the reduced fast-electron population at high density. The insignificant change in the power balance and the edge density source could only be caused by a large deposition of LHRF power in the edge.

A corresponding instantaneous response was observed in edge diagnostics with the reduction in current drive efficiency. The fast response allowed for the simplification of LHRF power balance calculations through the use of subtraction. LHRF edge absorption, observed as conducted and radiated power, matched core driven current reductions. In conditions with negligible current drive, nearly all power was promptly observed in conduction and radiation.

From the independent core and edge measurements, power balance was reconstructed. Changes in P_{tot} due to decreasing LHCD efficiency were recovered in P_{rad} and P_{cond}. This was only possible through the

ensemble of many modulations due to the large scatter in the fractional loss data. With rigorous analysis, the power balance was shown to be correct within the expected errors of the independent fits.

In effect it is the magnitude of edge loss which dictates the current drive efficiency. The completed power balance across the range of density indicates that with the current drive loss an increasing fraction is absorbed in the edge. Linear trends are observed in each absorption mechanism with $\bar{n}_e$, increasing with $\bar{n}_e$ for radiation and conduction, and decreasing for current drive. This edge loss is a parasitic mechanism reducing the power available for current drive current drive and reducing core deposition.

The parasitic mechanism of edge loss is observable even at the lowest densities. It is likely that the cause of the loss of efficiency in LHCD with $\bar{n}_e$ is not a 'threshold' behavior, but one that increases in importance. The character of the instantaneous edge response increases in magnitude with $\bar{n}_e$ but does not change in time. These characteristics can now be used with the power balance to determine other attributes of the parasitic edge LHRF deposition.

Observing the edge particle source, radiated power and conducted power can determine the nature of the edge LHRF deposition. Poloidal and toroidal localization can be used to isolate a specific cause of the loss of current drive. Correlations of the LHRF edge deposition with SOL characteristics also inform on the cause of edge absorption. The next step in analysis is only possible through this rigorous LHRF power balance calculation.

BIBLIOGRAPHY

[1] L. Spitzer. *Physics of Fully Ionized Gases: Second Revised Edition*. Dover Books on Physics. Dover Publications, 1962.

[2] S. Shiraiwa, S. Baek, A. Dominguez, E. Marmar, R. Parker et al. Direct detection of lower hybrid wave using a reflectometer on Alcator C-Mod. *Review of Scientific Instruments*, 81(10), 2010.

[3] S. G. Baek, R. R. Parker, S. Shiraiwa, G. M. Wallace, P. T. Bonoli et al. Characterization of the onset of ion cyclotron parametric decay instability of lower hybrid waves in a diverted tokamak. *Physics of Plasmas*, 21(6):–, 2014.

[4] S. G. Baek, G. M. Wallace, T. Shinya, R. R. Parker, S. Shiraiwa et al. Measurements of the parallel wavenumber of lower hybrid waves in the scrape-off layer of a high-density tokamak. *Physics of Plasmas*, 23(5), 2016.

[5] N. P. Basse, A. Dominguez, E. M. Edlund, C. L. Fiore, R. S. Granetz et al. Diagnostic systems on Alcator C-Mod. *Fusion Science and Technology*, 51(3):476–507, April 2007.

[6] O. Sauter, C. Angioni and Y. R. Lin-Liu. Neoclassical conductivity and bootstrap current formulas for general axisymmetric equilibria and arbitrary collisionality regime. *Physics of Plasmas*, 6(7):2834–2839, 1999.

[7] G. M. Wallace, R. R. Parker, P. T. Bonoli, A. E. Hubbard, J. W. Hughes et al. Absorption of lower hybrid waves in the scrape off layer of a diverted tokamak. *Physics of Plasmas (1994-present)*, 17(8):–, 2010.

[8] G.M. Wallace, A.E. Hubbard, P.T. Bonoli, I.C. Faust, R.W. Harvey et al. Lower hybrid current drive at high density in Alcator C-Mod. *Nuclear Fusion*, 51(8):083032, 2011.

[9] J. L. Terry, M. L. Reinke, J. W. Hughes, B. LaBombard, C. Theiler et al. Improved confinement in high-density H-modes via modification of the plasma boundary with lower hybrid waves. *Physics of Plasmas*, 22(5):–, 2015.

[10] J.W. Hughes, A.E. Hubbard, G. Wallace, M. Greenwald, B. LaBombard et al. Modification of H-mode pedestal structure with lower hybrid waves on Alcator C-Mod. *Nuclear Fusion*, 50(6):064001, 2010.

[11] J. W. Heard, C. Watts, R. F. Gandy, P. E. Phillips, G. Cima et al. High resolution electron cyclotron emission temperature profile and fluctuation diagnostic for Alcator C-Mod. *Review of Scientific Instruments*, 70(1):1011–1013, 1999.

[12] Peter Joseph Larkin O'Shea. *Measurements of ICRF Power Deposition and Thermal Transport with an ECE Grating Polychromator on the Alcator C-Mod tokamak*. PhD thesis, Massachuetts Institute of Technology, March 1997.

[13] J. W. Hughes, D. Mossessian, K. Zhurovich, M. DeMaria, K. Jensen et al. Thomson scattering upgrades on Alcator C-Mod. *Review of Scientific Instruments*, 74(3):1667–1670, 2003.

[14] J. W. Hughes, D. A. Mossessian, A. E. Hubbard, E. S. Marmar, D. Johnson et al. High-resolution edge Thomson scattering measurements on the Alcator C-Mod tokamak. *Review of Scientific Instruments*, 72(1):1107–1110, 2001.

[15] S. Ejima, M. Okabayashi and J. Schmidt. Determination of the electron thermal conductivity across magnetic surfaces in the FM-1 Spherator. *Phys. Rev. Lett.*, 32:872–875, Apr 1974.

[16] E. Barbato and R. Giannella. A possible measure of the energy deposition profile in additional plasma heating experiments. *Physics Letters A*, 110(6):309 – 312, 1985.

[17] J O'Rourke. An analytic solution of the inhomogenous coupled diffusion problem. *Plasma Physics and Controlled Fusion*, 35(1):111, 1993.

[18] A. Jacchia, P. Mantica, F. De Luca and G. Gorini. Determination of diffusive and nondiffusive transport in modulation experiments in plasmas. *Physics of Fluids B*, 3(11):3033–3040, 1991.

[19] T. C. Luce, C. C. Petty and J. C. M. de Haas. Inward energy transport in tokamak plasmas. *Phys. Rev. Lett.*, 68:52–55, Jan 1992.

[20] G.L. Jahns, S.K. Wong, R. Prater, S.H. Lin and S. Ejima. Measurement of thermal transport by synchronous detection of modulated electron cyclotron heating in the doublet iii tokamak. *Nuclear Fusion*, 26(2):226, 1986.

[21] A Manini, J-M Moret, S Alberti, T P Goodman and M A Henderson. Modulated ECH power absorption measurements using a diamagnetic loop in the TCV tokamak. *Plasma Physics and Controlled Fusion*, 44(2):139, 2002.

[22] M. Cox, N. Deliyanakis, J. Hugill, D.C. Robinson, M. Ashraf et al. Thermal wave studies of electron transport using modulated ECRH. *Nuclear Fusion*, 33(11):1657, 1993.

[23] V F Andreev, Yu N Dnestrovskij, M V Ossipenko, K A Razumova and A V Sushkov. The ballistic jump of the total heat flux after ECRH switching on in the T-10 tokamak. *Plasma Physics and Controlled Fusion*, 46(2):319, 2004.

[24] G. Gorini, P. Mantica, G. M. D. Hogeweij, F. De Luca, A. Jacchia et al. Simultaneous propagation of heat waves induced by sawteeth and electron cyclotron heating power modulation in the RTP tokamak. *Phys. Rev. Lett.*, 71:2038–2041, Sep 1993.

[25] K K Kirov, F Leuterer, G V Pereverzev, F Ryter, W Suttrop et al. ECRH power deposition studies in ASDEX Upgrade. *Plasma Physics and Controlled Fusion*, 44(12):2583, 2002.

[26] V Erckmann and U Gasparino. Electron cyclotron resonance heating and current drive in toroidal fusion plasmas. *Plasma Physics and Controlled Fusion*, 36(12):1869, 1994.

[27] H.J. Hartfuss, H. Maassberg, M. Tutter, W VII-A Team and ECRH Group. Evaluation of the local heat conductivity coefficient by power-modulated electron cyclotron heating in the Wendelstein VII-A stellarator. *Nuclear Fusion*, 26(5):678, 1986.

[28] F Ryter, R Dux, P Mantica and T Tala. Perturbative studies of transport phenomena in fusion devices. *Plasma Physics and Controlled Fusion*, 52(12):124043, 2010.

[29] D.J. Gambier, M.P. Evrard, J. Adam, A. Becoulet, S. Corti et al. ICRF power deposition profile and determination of the electron thermal diffusivity by modulation experiments in JET. *Nuclear Fusion*, 30(1):23, 1990.

[30] B. A. Grierson, K. H. Burrell, B. Crowley, L. Grisham and J. T. Scoville. High speed measurements of neutral beam turn-on and impact of beam modulation on measurements of ion density. *Review of Scientific Instruments*, 85(10), 2014.

[31] P. Mantica, T. Tala, J. S. Ferreira, A. G. Peeters, A. Salmi et al. Perturbative studies of toroidal momentum transport using neutral beam injection modulation in the Joint European Torus: Experimental results, analysis methodology, and first principles modeling. *Physics of Plasmas*, 17(9), 2010.

[32] E A Lerche, D Van Eester and JET EFDA contributors. Improved break-in-slope analysis of the plasma energy response in tokamaks. *Plasma Physics and Controlled Fusion*, 50(3):035003, 2008.

[33] Y Lin, S J Wukitch, P T Bonoli, E Marmar, D Mossessian et al. Ion cyclotron range of frequencies mode conversion electron heating in deuterium–hydrogen plasmas in the Alcator C-Mod tokamak. *Plasma Physics and Controlled Fusion*, 45(6):1013, 2003.

[34] X.L. Zou, G. Giruzzi, J.F. Artaud, F. Bouquey, A. Clémençon et al. Electron heat transport and ECRH modulation experiments in Tore Supra tokamak. *Nuclear Fusion*, 43(11):1411, 2003.

[35] C. K. Phillips, M. G. Bell, R. Bell, N. Bretz, R. V. Budny et al. Ion cyclotron range of frequencies heating and current drive in deuterium–tritium plasmas. *Physics of Plasmas*, 2(6):2427–2434, 1995.

[36] B Geiger, M Garcia-Munoz, W W Heidbrink, R M McDermott, G Tardini et al. Fast-ion d-alpha measurements at asdex upgrade. *Plasma Physics and Controlled Fusion*, 53(6):065010, 2011.

[37] M. García-Muñoz, P. Martin, H.-U. Fahrbach, M. Gobbin, S. Günter et al. Ntm induced fast ion losses in asdex upgrade. *Nuclear Fusion*, 47(7):L10, 2007.

[38] Aaron Craig Bader. *Experimental measurements and numerical modeling of fast-ion distributions in the Alcator C-Mod Tokamak*. PhD thesis, Massachusetts Institute of Technology, February 2012.

[39] A. Schmidt, P. T. Bonoli, O. Meneghini, R. R. Parker, M. Porkolab et al. Investigation of lower hybrid physics through power modulation experiments on Alcator C-Mod. *Physics of Plasmas (1994-present)*, 18(5):–, 2011.

[40] Y Peysson. Transport of fast electrons during LHCD in TS, JET, and ASDEX. *Plasma Physics and Controlled Fusion*, 35(SB):B253, 1993.

[41] D. Moreau and the TORE SUPRA Team. Lower-hybrid current drive experiments in TORE SUPRA. *Physics of Fluids B*, 4(7):2165–2175, 1992.

[42] R. Bartiromo, E. Barbato, L. Gabellieri, A. Spaziani, A.A. Tuccillo et al. Fast electron confinement during lower hybrid experiments in ASDEX. *Nuclear Fusion*, 33(10):1483, 1993.

[43] G. M. Wallace, I. C. Faust, O. Meneghini, R. R. Parker, S. Shiraiwa et al. Lower hybrid current drive at high density in the multipass regime. *Physics of Plasmas*, 19(6):–, 2012.

[44] S.G. Baek, R.R. Parker, P.T. Bonoli, S. Shiraiwa, G.M. Wallace et al. High density LHRF experiments in alcator C-Mod and implications for reactor scale devices. *Nuclear Fusion*, 55(4):043009, 2015.

[45] G.M. Wallace, S. Shiraiwa, J. Hillairet, M. Preynas, W. Beck et al. Advances in lower hybrid current drive technology on Alcator C-Mod. *Nuclear Fusion*, 53(7):073012, 2013.

[46] P Gomez, J.L Ségui, G Giruzzi, P Froissard, Y Peysson et al. Lower hybrid dynamics by ECE spectra in Tore Supra. *Fusion Engineering and Design*, 53(1–4):169 – 175, 2001.

[47] Vladimir Krivenski. Electron cyclotron emission by non-Maxwellian bulk distribution functions. *Fusion Engineering and Design*, 53(1–4):23 – 33, 2001.

[48] I.H. Hutchinson. *Principles of Plasma Diagnostics*. Cambridge University Press, 2005.

[49] G. Taylor, B. LeBlanc, C. K. Phillips, G. Schilling, J. R. Wilson et al. Electron power deposition measurements during ion cyclotron range of frequency heating on c-mod. *AIP Conference Proceedings*, 485(1):490–493, 1999.

[50] A. Janos, M. McCarthy, E. Fredrickson, K. McGuire and G. Taylor. Operation of two grating polychromators on tftr and new observations of magnetohydrodynamic phenomena. *Review of Scientific Instruments*, 66(1):668–670, 1995.

[51] K. Kato and I. H. Hutchinson. Nonthermal electron velocity distribution measured by electron cyclotron emission in alcator c tokamak. *Phys. Rev. Lett.*, 56:340–343, Jan 1986.

[52] I H Hutchinson, B LaBombard, J A Goetz, B Lipschultz, G M McCracken et al. The effects of field reversal on the Alcator C-Mod divertor. *Plasma Physics and Controlled Fusion*, 37(12):1389, 1995.

[53] Carl Edward Rasmussen. Gaussian processes for machine learning. In *Gaussian processes for machine learning*. MIT Press, 2006.

[54] M.A. Chilenski, M. Greenwald, Y. Marzouk, N.T. Howard, A.E. White et al. Improved profile fitting and quantification of uncertainty in experimental measurements of impurity transport coefficients using Gaussian process regression. *Nuclear Fusion*, 55(2):023012, 2015.

[55] S. Shiraiwa, G. Baek, P.T. Bonoli, I.C. Faust, A.E. Hubbard et al. Progress towards steady-state regimes in Alcator C-Mod. *Nuclear Fusion*, 53(11):113028, 2013.

[56] J.J. Schuss, M. Porkolab, Y. Takase, D. Cope, S. Fairfax et al. Lower hybrid heating in the Alcator A tokamak. *Nuclear Fusion*, 21(4):427, 1981.

[57] R.S. Granetz and L. Wang. Design of the X-ray tomography system on Alcator C-Mod. In P.E. Stott, D.K. Akulina, G. Gorini and E. Sindoni, editors, *International School of Plasma Physics*, pages 425–437. Editrice Compositori Bologna, 1991.

[58] C. L. Fiore and R. L. Boivin. Performance of the neutron diagnostic system for Alcator C-Mod. *Review of Scientific Instruments*, 66(1):945–947, 1995.

[59] J. H. Irby, E. S. Marmar, E. Sevillano and S. M. Wolfe. Two-color interferometer system for Alcator C-MOD. *Review of Scientific Instruments*, 59(8):1568–1570, 1988.

[60] D. Brunner and B. LaBombard. Surface thermocouples for measurement of pulsed heat flux in the divertor of the Alcator C-Mod tokamak. *Review of Scientific Instruments*, 83(3):–, 2012.

[61] J. L. Terry, B. LaBombard, D. Brunner, J. Payne and G. A. Wurden. Divertor ir thermography on Alcator C-Mod. *Review of Scientific Instruments*, 81(10), 2010.

[62] C Lau, G R Hanson, B Labombard, Y Lin, O Meneghini et al. Effects of LH power on SOL density profiles and LH coupling on Alcator C-Mod. *Plasma Physics and Controlled Fusion*, 55(2):025008, 2013.

[63] Y. Liang, X. Z. Gong, K. F. Gan, E. Gauthier, L. Wang et al. Magnetic topology changes induced by lower hybrid waves and their profound effect on Edge-Localized Modes in the EAST tokamak. *Phys. Rev. Lett.*, 110:235002, Jun 2013.

[64] J.P. Gunn, V. Petržílka, A. Ekedahl, V. Fuchs, E. Gauthier et al. Measurement of lower hybrid hot spots using a retarding field analyzer in Tore Supra. *Journal of Nuclear Materials*, 390–391:904 – 906, 2009. Proceedings of the 18th International Conference on Plasma-Surface Interactions in Controlled Fusion Device.

[65] M. Goniche, J. Mailloux, Y. Demers, V. Fuchs, P. Jacquet et al. Strong toroidal asymmetries in power deposition on divertor and first wall components during LHCD on TdeV and Tore Supra. *Journal of Nuclear Materials*, 241:745 – 749, 1997.

[66] E. R. Müller and F. Mast. A new metal resistor bolometer for measuring vacuum ultraviolet and soft X-ray radiation. *Journal of Applied Physics*, 55(7):2635–2641, 1984.

[67] M. L. Reinke and I. H. Hutchinson. Two dimensional radiated power diagnostics on Alcator C-Mod. *Review of Scientific Instruments*, 79(10), 2008.

[68] L.L. Lao, H. St. John, R.D. Stambaugh, A.G. Kellman and W. Pfeiffer. Reconstruction of current profile parameters and plasma shapes in tokamaks. *Nuclear Fusion*, 25(11):1611, 1985.

ATTRIBUTES OF EDGE-DEPOSITED LHRF POWER

The completed power balance found an increasing fraction of the LHRF power absorbed in the edge with increasing $\bar{n}_e$. LHRF power absorption in the edge plasma is a parasitic mechanism which serves to reduce the power available for current drive at high density. The observed edge losses' attributes can be used to understand and determine the cause of edge deposition. Knowing the mechanism behind the current drive loss can improve current drive on C-Mod and other future high-performance, steady-state tokamaks.

The total LHRF power balance links the magnitude of edge LHRF absorption to the importance of observed edge characteristics. Increases in radiated and conducted power due to LHRF and their effects on the scrape-off-layer (SOL) can all be used to understand edge LHRF deposition. Other additional diagnostics on Alcator C-Mod can test previous assumptions necessary for power balance calculations such as toroidal symmetry. The combined synthesis of modulation, power balance, and measurements from other plasma diagnostics can be used to categorize the loss of current drive.

In this chapter, it is determined that ionization in the active divertor causes the expected edge particle source inferred from the slow core density evolution. Multiple corresponding measurements confirm that LHRF-induced ionization at high densities increases the SOL and core plasma densities. The B-port Lyman-alpha (BPLY) camera's wide view was key in making this determination. The observed ionization is important in implicating the active divertor plasma in the absorption of LHRF power in the edge.

Reversed-field discharges are used to change the SOL and divertor characteristics which provide further evidence to the nature of the edge power loss. Other modulation schemes can determine the upstream impact of LHRF in the SOL. Together, these effects are used to highlight the importance of the SOL's natural characteristics in LHRF absorption.

The preponderance of accumulated evidence supports collisional absorption near the active divertor as the dominant loss mechanism. While there is no direct method that presently exists to detect the collisional absorption in the active divertor, by elimination of other loss mechanisms this remains as the most likely explanation that is self-consistent with observed trends. Furthermore, the observed attributes are necessary but not sufficient conditions for proving collisional absorption as the cause for the loss of current drive. This implies that

future tokamaks must avoid LHRF propagation through divertor regions in order to guarantee high current drive efficiencies.

LHRF-INDUCED ACTIVE DIVERTOR IONIZATION

Divertor particle source

It was found that the core electron density rose in response to a fast rise in edge density ($.8 < \rho < .95$) with a slower global particle confinement time increase in the core particle inventory. This phenomenon is correlated with LHRF power's magnitude as higher steps in LHRF power causes larger changes in electron density. This particle source is an effect of the edge-deposited LHRF and can be used to understand its nature.

Using an X-mode SOL reflectometer [1], upstream density measurements were made in reversed field plasmas. Typical SOL density measurements using this reflectometer find that the electron density is rarefied in the region just in front of the launcher [2]. The SOL density profile measured in front of the launcher is dominated by the local ponderomotive effects induced by the high grill electric fields[3]. In this instance, the electron density was measured at the midplane along magnetic field lines not connected to the LHRF launcher in order to characterize the global character LHRF's influence. The measurement's fast time resolution can be used to understand the upstream SOL response to LHRF power.

Unlike the local effects near the launcher, an edge density increase is observed with LHRF at high $\bar{n}_e$. This effect is shown in figure 4.1, where density enhancement is seen across the SOL in phase with the LHRF power. Frequency sweep limitations force an upper bound in density; the measured regions are constrained to regions just outside the last closed flux surface (LCFS) for the tested span of $\bar{n}_e$. This causes the modulation around $R = .9$m observed in the figure.

The lack of a density reference point introduces systematic and random errors into the generated profiles. As such, ensemble averaging was used to improve the density profile's accuracy in a manner similar to the collection of TS data in chapter 3. The density data was combined into 6 profiles as shown in figure 4.2 each with 4ms time bins for 5 different modulations. Error bars were formulated from the variation in the profiles and does not reflect the other expected errors.

The increase in the density profile matches observed outward shifts in the ionization profiles as measured by a midplane Abel-inverted Ly$_\alpha$ pinhole camera. The shift in the Ly$_\alpha$ emissivity profile occurs on a sub-millisecond timescale similar to the response time of measurements used for power balance. Figure 4.3 provides an example of the emissivity shift to greater ρ. The greatest change in the Ly$_\alpha$ radial profile occurs near the separatrix.
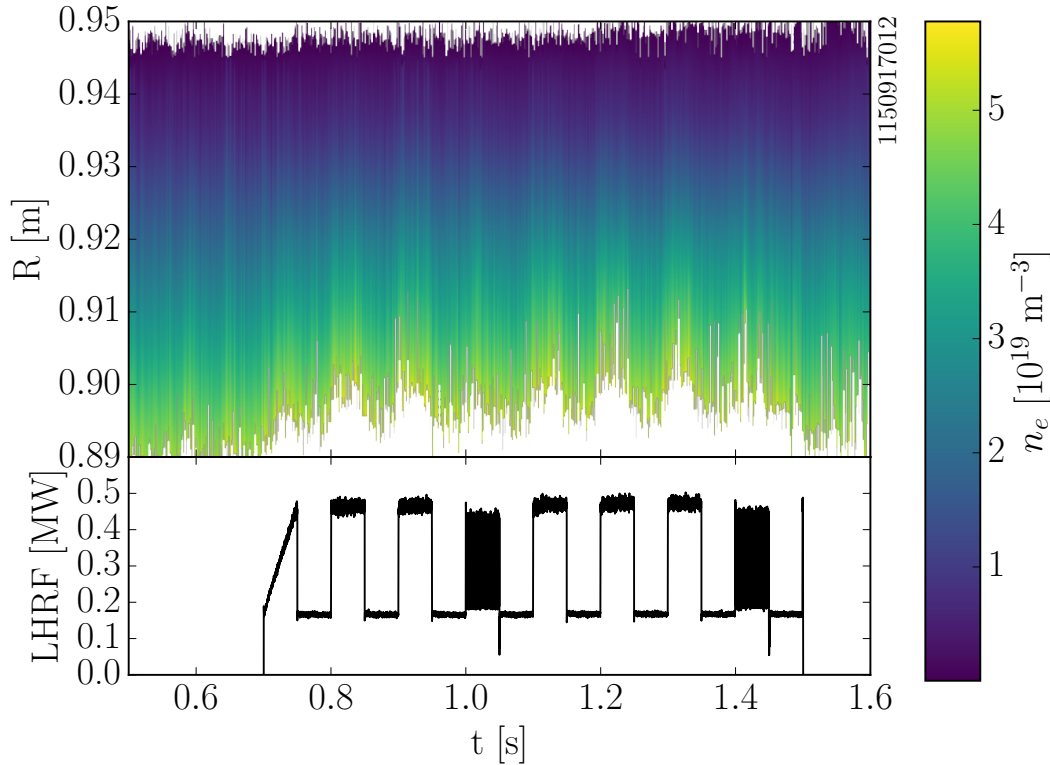
Figure 4.1: The upstream density of the SOL increases with applied LHRF power at low efficiencies. This measurement is made using a reflectometer on field lines not connected to the LHRF launcher. Unlike density profiles near the LHRF antenna, where ponderomotive effects cause a rarification of the density profile, an increase in upstream SOL electron density is observed. This increase in density in the SOL far from the launcher is due to an edge particle source. This rise in density occurs only at high $\bar{n}_e$, with this example being a $\bar{n}_e \sim 1.0 \cdot 10^{20}$ [m^{-3}], reverse-field LSN plasma. The fourth and eighth modulation have a secondary fast modulation which exhibits a reduced change in the upstream edge density.

A distinct rise of the upstream density occurred in less than 6ms after the LHRF power step. While this confirms that the particle source is local to the edge, it sets an upper bound on the upstream SOL's response time. The profile at 2ms is intermediate of the two equilibria, indicating that some evolution of the upstream conditions does occur. This finite response time in density would indicate that the density source is separated from the upstream density measurement. The difference in density between the two equilibria exists outside of their respective error bars, making the density rise a rigorous result.

A similar change in plasma density is also observed in certain cases at the divertor plate. In figure 4.4 a USN, forward-field plasma (with similar SOL conditions to a reverse-field LSN plasma) has a large, very prompt rise in density at the inner divertor plate with LHRF power. In this configuration the inner divertor is expected to be attached, where the electron temperature is 8 eV and does not vary with LHRF power. The density increase is faster than the standard
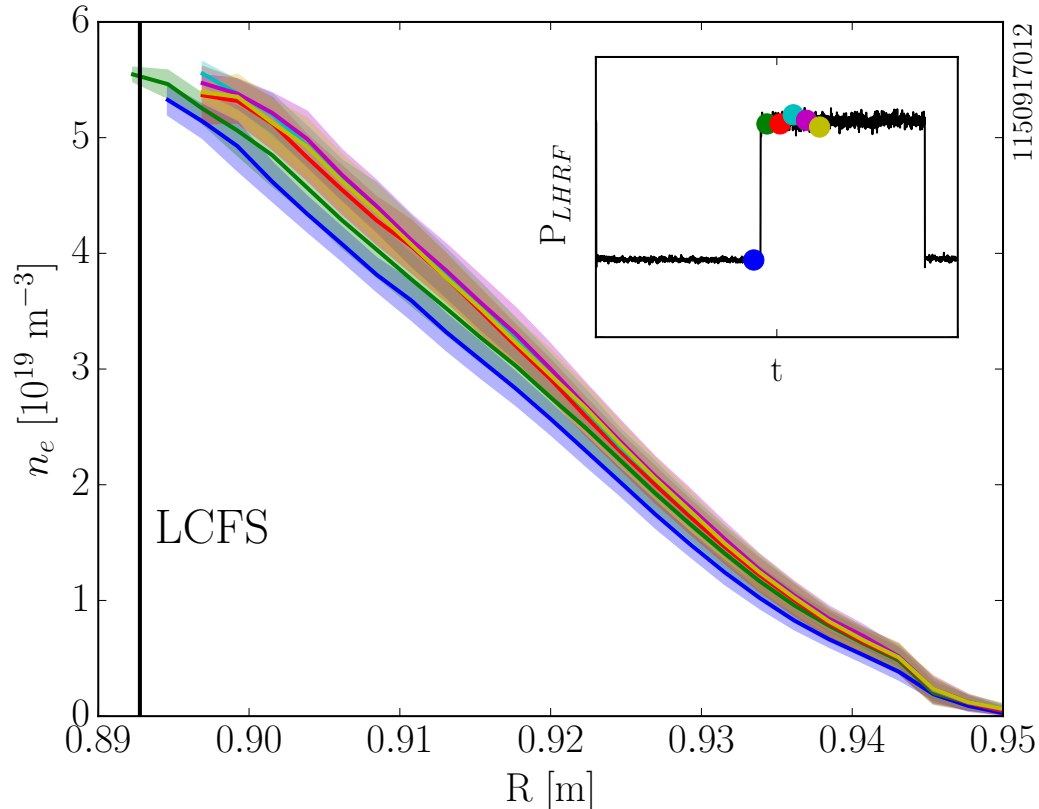
Figure 4.2: Several modulations from a single discharge (shown in figure 4.1 were combined to characterize the time history of the edge electron density. The density profiles were generated 2ms before, and 2,6,10,14 and 18 ms after the change in LHRF power. The midplane edge density profile rises to a new equilibrium within 4ms of the rise in LHRF power. The edge density ensemble was made using the full power modulations in reversed-field. The 700kA LSN plasma has the same equilibrium used for other experimentation.

Langmuir probe time resolution ($<$ 2ms). The edge particle source affects the entirety of the SOL.

In this example, the increased electron density highlights the significant effects of the edge particle source and the additional LHRF power. The modulation in the strike-point electron density is comparable to average core electron density. The electron temperature is invariant in this example but the outer divertor strike point electron temperature has been observed to change due to LHRF in forward-field LSN equilibria.

The overall change in SOL density does not indicate the edge density source's location. Rather, neutral pressure measurements at various locations[4] indicate that the active divertor is the source of density. An anti-correlated response is observed in the divertor neutral pressure with the LHRF modulation. The drop in neutral pressure matches increases in SOL density and divertor Ly_α (from figure 3.17).

This phenomenon at high density is shown in figure 4.5. A $\sim$ 30% change in the neutral pressure occurs with the step in applied LHRF

Figure 4.3: Example inverted radial profiles of Ly$_\alpha$ emission from the midplane (measured from K-port) shift outward with LHRF power. This shift in emission occurs with the application of LHRF at high density (with significant edge losses) and on the order of a millisecond. The outward shift indicates that changes to the SOL occur with applied LHRF.
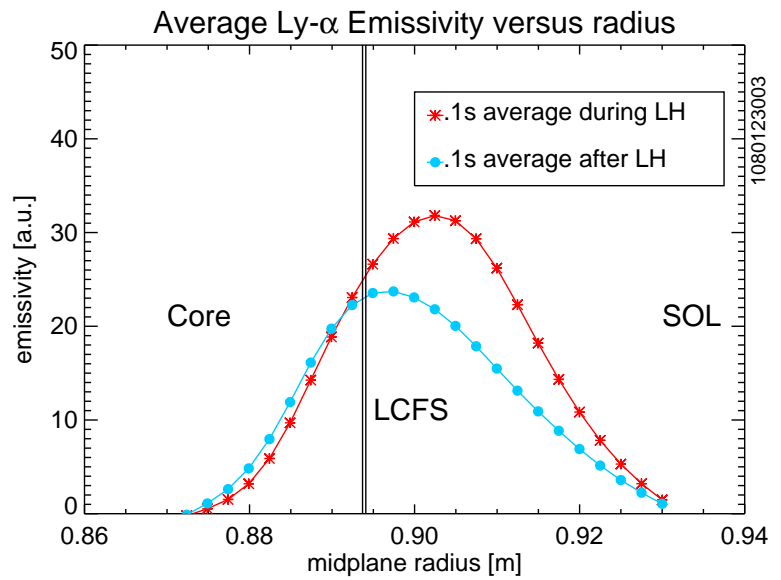
power. This reduction in neutral pressure occurs near the active divertor in both LSN and USN plasmas. In this LSN equilibrium the modulation is most pronounced in the active divertor.

The combined observations of the neutral pressure, electron density and Ly$_\alpha$ emission indicate that the LHRF power ionizes neutrals in the active divertor. This effect is seen in all plasma shapes as measured by the LHRF-induced change in Ly$_\alpha$ emission at low efficiency (example plasmas with USN, LSN, and DN configurations are given in figure 4.13). This ionization indicates that power is either absorbed in the divertor plasma or quickly flows into the divertor plasma.

The edge change caused by the LHRF power can induce H-modes at specific densities in LSN, forward-field plasmas (with $\bar{n}_e \sim 1.4 \cdot 10^{20}$ [m^{-3}]). This effect limits the range of useful data due to confinement changes which alters the core and edge plasma. The weak H-mode increases the particle confinement with a possible small core temperature change. The differences from the rest of the data set prevents its use in generating trends or deriving characteristics. In most circumstances, the removal of additional LHRF power at the end of the step causes the plasma to revert back into L-mode. This result matches observations from Terry, *et. al.*[5] that found improvements in H-mode confinement with low LHCD efficiency. The improvement in the H-mode confinement correlated with a reduced edge neutral pressure.

The active divertor ionization by LHRF power suggests that the divertor plays a key role in absorbing power. This particle source affects the SOL and core plasma at different timescales, further emphasizing LHRF's edge absorption. However, the LHRF absorption which causes the ionization can still occur upstream of the ionization source. Given that the parallel SOL heat transport is nearly instantaneous, the power can be deposited wherever along a SOL field line.
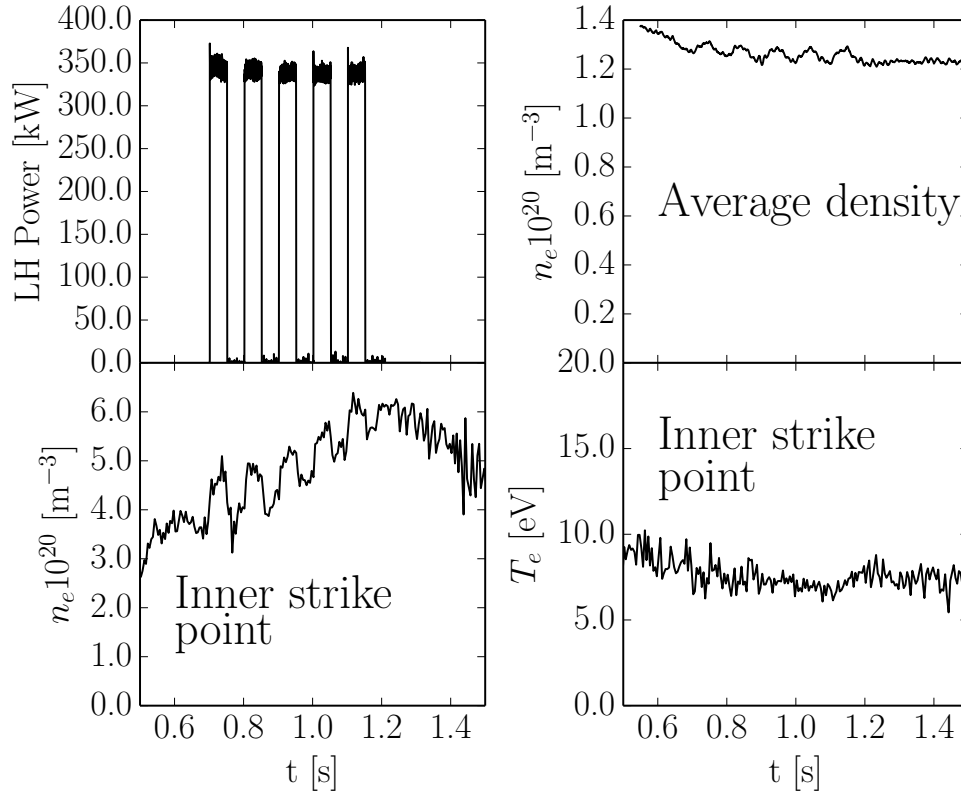
Figure 4.4: The inner divertor exhibits a strong rise in density with the application of LHRF power. This example is in a forward-field USN plasma where the inner divertor is typically attached because of the $\vec{B} \times \nabla|\vec{B}|$ is away from the active divertor. The electron temperature of the inner divertor is constant during the modulation. In lower single null, forward-field discharges an increase in the electron temperature occurs with LHRF on the outer divertor at high $\bar{n}_e$.

Differences in the upstream and target time responses are too short to be separated using the standard power balance plasma diagnostics. The SOL equilibration times sufficiently fast to require other methods for determining power absorption poloidal location.

The importance of various LHRF absorption mechanisms are dependent on the SOL plasma's background characteristics. Correlating LHRF-induced ionization with SOL conditions can yield useful information about the LHRF edge power absorption. Changes in the LHRF power balance and ionization with different SOL attributes lead to a different power flow. The field direction strongly impacts the nature of the inner and outer divertor plasmas[6, 7], these conditions impact the regions of greatest collisionality and possible PDI growth. The differences between forward and reversed field plasmas are investigated for their effect on edge LHRF absorption.

The absorption location's ambiguity in causing ionization requires other correlated measurements. Delay timing using fluctuation diagnostics could also find a more precise time delay in the heat flux and edge radiation. Unfortunately, divertor ionization is a necessary but

Figure 4.5: The application of LHRF at high $\bar{n}_e$ causes the active divertor neutral pressure to decrease as measured by a divertor gauge located between B and C ports. This effect matches results observed with the increased emission of divertor hydrogenic Ly_α. The edge particle source comes from ionization of the active divertor. The vertical line indicates a transition to H-mode caused by the increased P_{tot}. The H-mode induces a rapid density rise shown in the measured $\bar{n}_e$. This result highlights the importance of the active divertor in the absorption of LHRF power.
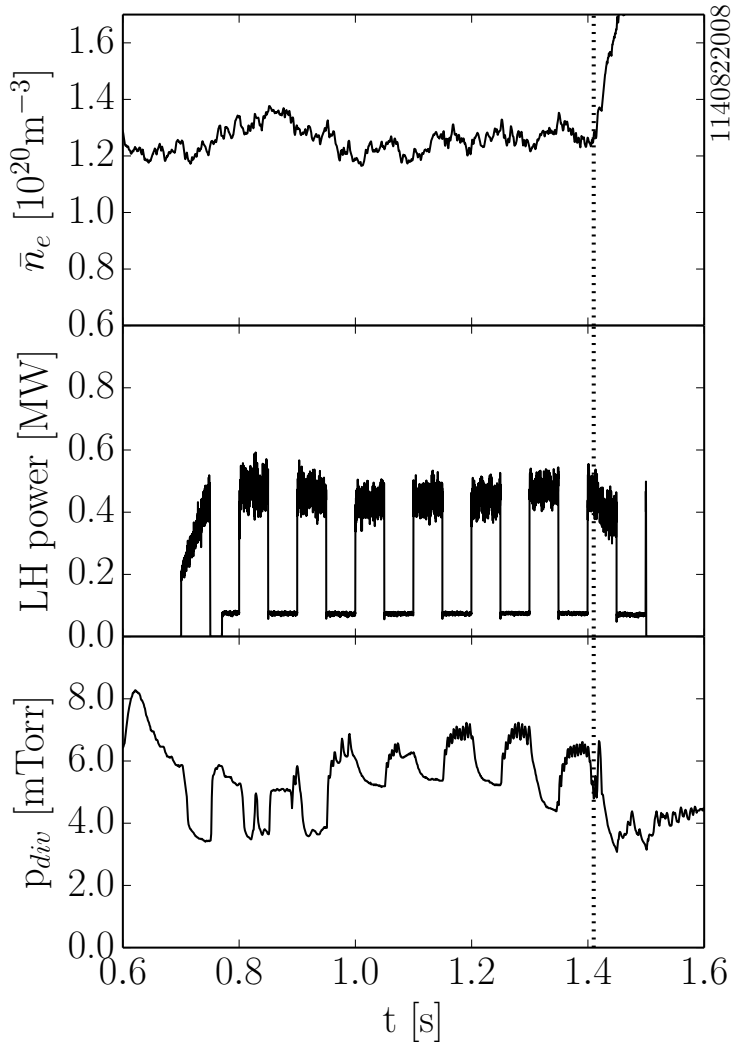
not sufficient condition for divertor LHRF deposition. The absorption's poloidal location is key for separating Landau damping effects from collisional absorption. The following sections attempt to determine the LHRF absorption location in the SOL.

Ionization oscillation at high $\bar{n}_e$

The change in conducted power and in ionization with applied LHRF is prone to rapid oscillations at specific values of $\bar{n}_e$. This was observed in the LSN, 700 kA, forward-field discharges with specific background neutral densities and Lower Hybrid powers. This becomes noticeable near cases where LHRF can induce H-modes with $\bar{n}_e \sim 1.3 \cdot 10^{20}$ [m^{-3}]. While the cause of this oscillation is an interesting physics topic in its own right[8, 9], it can in this case be used to understand LHRF's edge parasitic absorption. The ionization can be
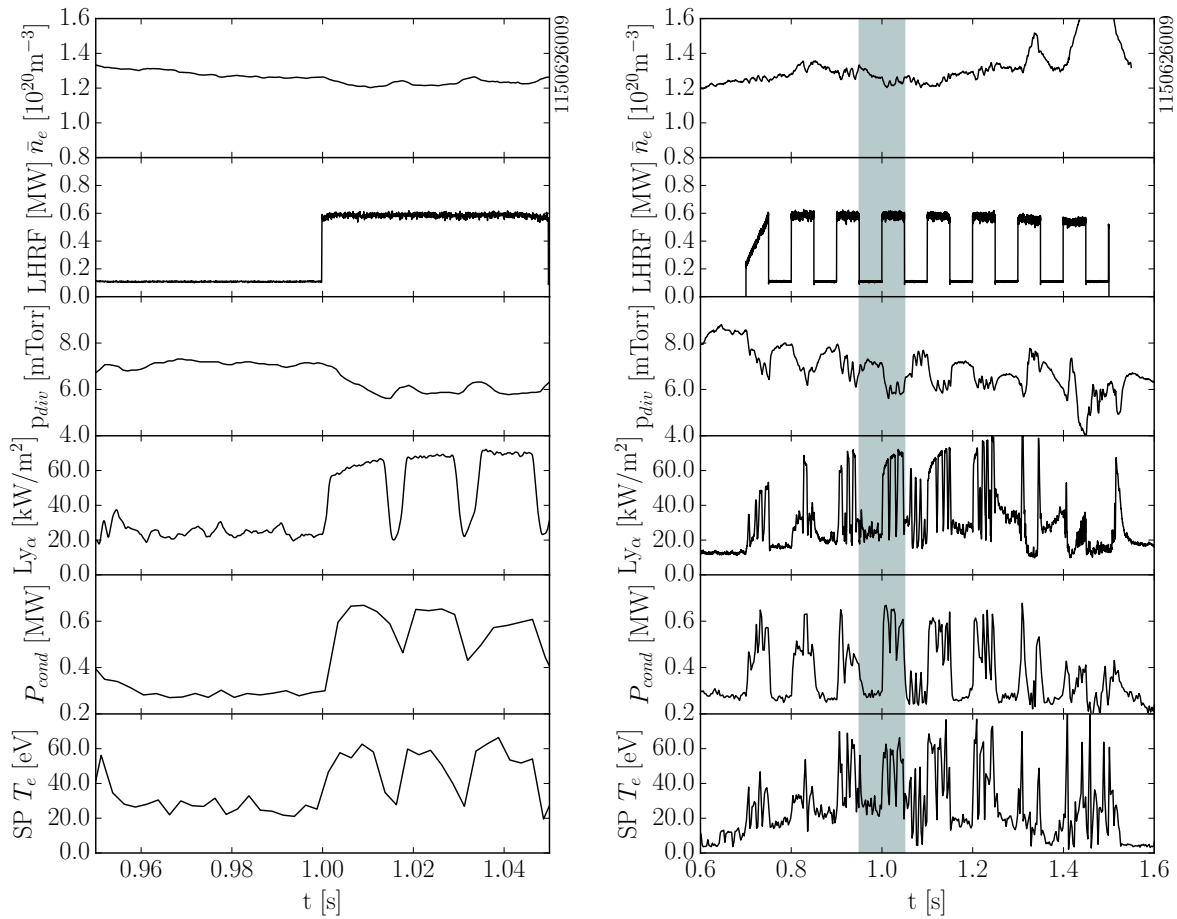
Figure 4.6: At specific $\bar{n}_e$ in the used equilibrium (700kA, forward-field, LSN) an oscillation is observed in the conducted power, neutral pressure, Ly$_\alpha$ and the strike point electron temperature. This effect occurs near at densities which can cause H-modes (at 1.3 and 1.4s in the figure). The oscillation can occur at low and high LHRF powers depending on the $\bar{n}_e$. The loss of conducted power, the reduced Ly$_\alpha$ emission and reduced strike point temperature is matched by an increased divertor neutral pressure.

correlated to changes in specific parameters enhanced or changed by LHRF power.

An example of the oscillation is shown in figure 4.6, a case where minimal current drive is found at high density. The rapid oscillations in conducted power, strike point temperature, and Ly$_\alpha$ emission are anti-correlated to the neutral pressure with applied LHRF power. During rapid oscillations the Ly$_\alpha$ emission can drop suddenly to levels consistent with those without LHRF. The conducted power drops by a substantial amount as does strike point T_e. Simultaneously the neutral pressure begins to increase. Interestingly, this is similar to the observed transitions to H-mode where the neutral pressure temporarily rises, then falls (seen both in figures 4.6 and 4.5).

The divertor strike point electron temperature correlates with the variation in the outer-divertor conducted power in this equilibrium. Radially farther out in the SOL, modulation in the divertor $\bar{n}_e$ oc-

curs in phase with the LHRF power. However, the greatest heat flux change due to LHRF occurs at the strike point, indicating that ΔT_e is the dominant contribution. This subject is best addressed in the SOL deposition's radial character, which is discussed in the following section.

The intermittent oscillation in LHRF power highlights the relation of the increased heat flux to the divertor plate to increases in Ly_α and strike point T_e. It proves that the conducted power to the outer divertor occurs in part due to a change in the electron temperature. This oscillation phenomenon is similar to other observed divertor oscillations that occur with changes in confinement. The oscillation is an indicator of the non-linear interaction of LHF power with the SOL evolution. LHRF power traversing through the SOL changes the SOL's nature and the path that the edge-deposited power takes is not as straight-forward as the power balance would dictate. The SOL loss and ionization's intermittent nature indicate that other phenomenon are at also at play influencing LHRF's edge absorption.

LOCALIZATION OF LHRF WAVE POWER

Toroidal symmetry

Total power balance calculations required an ansatz about the conducted power's toroidal location. Assuming that the profile represents toroidal character, the local radial profiles of heat flux are generated from measurements at specific toroidal locations and are integrated about the tokamak. The absolute radiated power is calibrated from discharges with highly toroidally-symmetric radiation emission.

Edge deposition toroidal symmetry is contrary to the edge-damping observations of most tokamak RF power sources [10, 11, 12, 13, 14]. Lower Hybrid grill-induced ionization is often observed at high powers and densities in front of the launcher (shown in figure 4.9). In most cases, the LHRF reverse $n_\parallel$ spectrum induces asymmetric edge absorption in tokamak plasmas. Hot-spots and field-line dependent ionization are observed on other tokamaks like Tore Supra[12] and NSTX[10]. Evaluating the degree of toroidal symmetry is key for understanding LHRF edge absorption on Alcator C-Mod.

The toroidal symmetry is evaluated using a set of diodes, cameras and Langmuir probes to varying degrees of resolution. Combined, these diagnostics can determine most observed asymmetries' nature and significance. Various diagnostic toroidal locations are shown in figure 4.7; a field line mapping from the LHRF antenna to the outer divertor is shown in gray (for the forward-field, LSN equilibrium). Several measurements are not along field lines which intercept the launcher, important for evaluating the symmetry. Each measurement independently verifies the LHRF power loss' degree of symmetry.
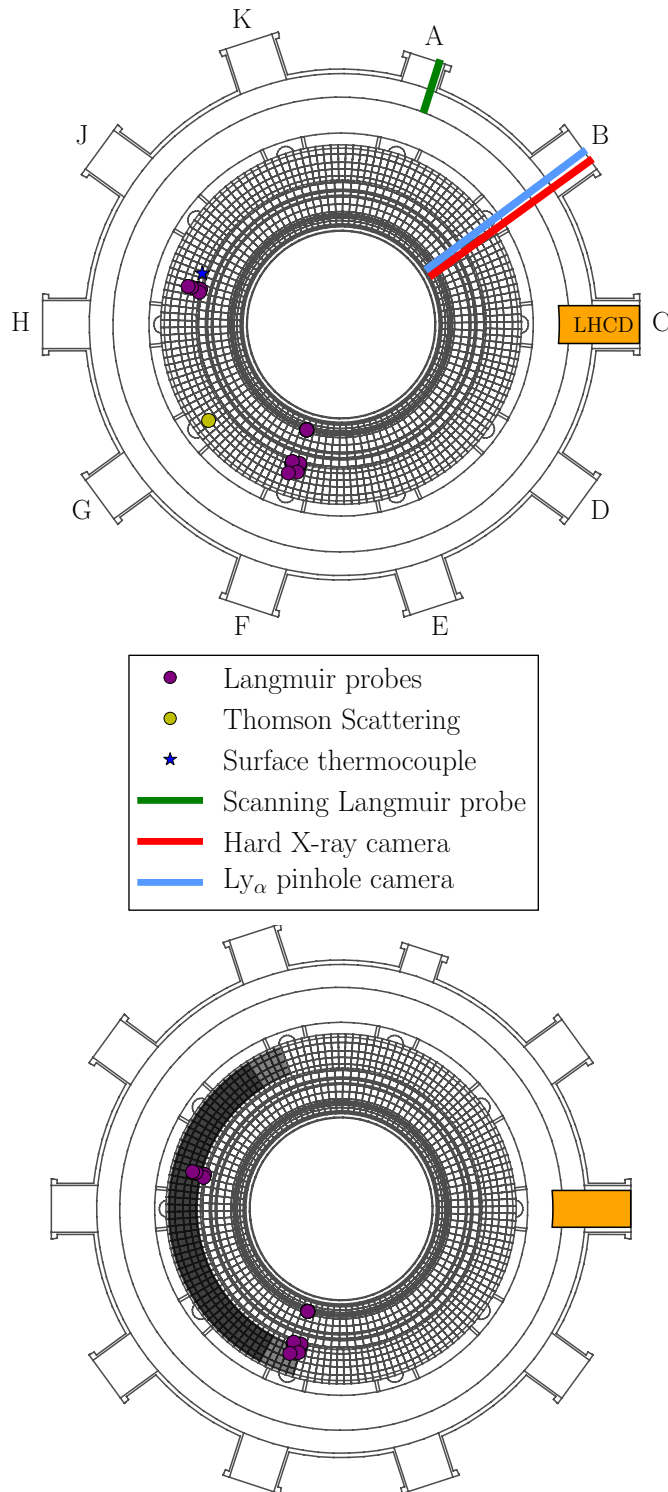
Figure 4.7: The toroidal positions of several diagnostics (both for the core and edge) show the toroidal offset from the LHRF launcher. The 10 ports are labeled, giving a rough representation of the toroidal offset by the port name. The port LHRF launcher is at zero degrees on right in orange at C-port. The mapping of the SOL in front of launcher to the divertor surface is shown in black, with partial overlap in gray. The field lines connected to the F-port divertor probes map to the very corner surface of the LHRF launcher at 700kA, while the J-port probes connect to field lines which pass in front of the full LHRF grill face. For calculations of toroidal symmetry, the DMBOLO views are shown on figure 4.8, and the camera locations are given by port name.

Figure 4.8: Measurement of radiated power during modulation at high density shown at four locations offset from LHRF launcher (defined by toroidal angle in degrees) at high density. All signals respond similarly, suggesting that the prompt radiation emission from the edge is highly toroidally symmetric. At low density, the rise time in all the signals follows core confinement time, suggesting changes in the core temperature. The view is a wide-angle poloidal view measuring all locations except the lower outer divertor leg with a narrow toroidal slice. These measurements represent the poloidal dynamics at a specific toroidal location.
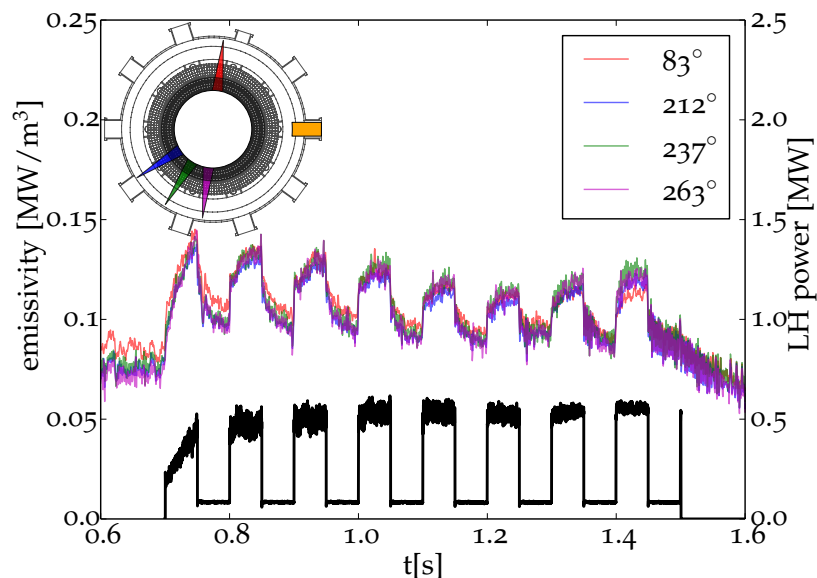
A set of toroidally-displaced AXUV diodes were designed and installed for analyzing disruptions [15]. Each diode measures a small toroidal slice of the plasma during modulated LHRF. Located about the torus, the diode's high time resolution showed similar characteristics to the measured radiated power. The diodes were cross-calibrated during the ohmic portion of the discharge and filtered for noise. It was found that at high $\bar{n}_e$, a similar rapid response was observed on each measurement.

Figure 4.8 shows an example of this symmetry where four of the six diodes were recorded. Toroidally offset from the launcher about C-Mod, each contained the fast rise observed in the edge visible and VUV light. In addition to the prompt change in radiation, a slow decay and rise occurs consistent with the evolution of the core plasma. The high time resolution, and low toroidal resolution indicate that the radiation induced by edge-absorbed LHRF is toroidally symmetric about the tokamak.

Wide-viewing visible cameras from F and G ports (located 216° and 252° offset from the launcher) captured lower time resolution images of the plasma; these cameras provide high spatial-resolution pictures of the plasma at < 100 Hz. The F-port camera images into the near-infrared (< 900 nm) at 90 fps. The G-port camera images in the visible at 60fps. In both cameras an increased emission of visible light occurs symmetrically near the inner divertor in forward-field discharges.

The view from G-port observes a highly symmetric and highly asymmetric component to the visible edge light, as highlighted in figures 4.9 and 4.11. An LHRF-induced asymmetric light component occurs near the LHRF launcher and a symmetric component occurs in the divertor. The increase in LHRF emission comes from the inner divertor as the emission expands through most of the inner divertor

Figure 4.9: Two wide camera views (from the WIDE2 camera at F-port) during the two phases of modulation in a high density discharge (1150626005). Instead of being gray scale images they are blue and red scaled, which are combined into the lowest composite image. The region of blue near the active divertor comes from a lack of red color which indicates that the red-scaled image is brighter in that location. There is an increased divertor brightness in the red image (the LH high power segment). The symmetry of this difference in blue indicates that the visible emission of light due to LHRF has a high degree of toroidal symmetry. Light emission from the LHRF launcher can be observed in the red image (on the right hand side of the center stack). This emission is not observed in the blue (LH off) segment.
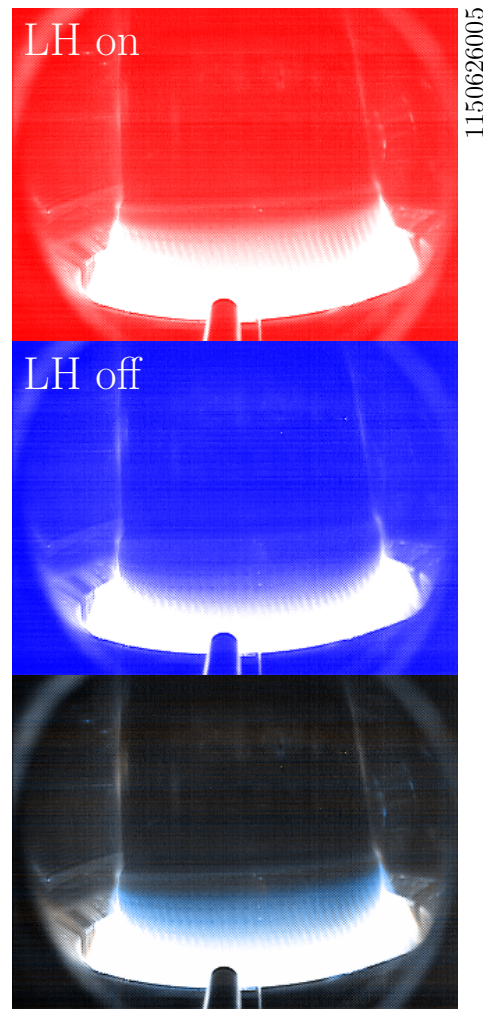
at high LHRF powers. The same effect is seen on the G-port camera with a wide emission belt wrapping around the inner divertor.

The absence of a large asymmetric component further confirms the LHRF-induced edge radiative losses' axisymmetric nature. Specifically, the previous power balance calculations provided by radiated power are more likely valid due to the observed symmetry. While this would imply that LHRF power is absorbed symmetrically in the edge, further confirmation can be extracted from the conducted power. The toroidal symmetry ansatz is vital to the total conducted power calculation. Multiple measurements of the total conducted power can inform on the degree of toroidal symmetry.

Diagnostic limitations reduce this comparison to a few cases. The probe arrays are prone to damage from specific high performance discharges and disruptions. This will lead to under-sampled heat flux profiles, that can distort the calculated total heat. The data from several rundays used different probe styles, making the comparison of total heats difficult. Measurements are only made from two locations near F-port and J-port, shown in figure 4.7. The J-port locations have

field lines which map to the LHRF launcher in the 700kA, LSN equi-
librium. The outer F-port probes map to the very corner of the LHRF
launcher. For these reasons, the conclusions about conducted power's
toroidal symmetry are less absolute compared to those of edge radia-
tive loss.

Figure 4.10: Measurements of the
conducted heat via arrays of Langmuir
probes were made at two toroidally
offset locations (J-port and F-port). An
ohmic cross-calibration between the
two conducted powers (causing a
numerical constant of 1.8) is applied
to the F-divertor calculated total heat.
The modulation behavior is similar
between the the two measurements is
similar with the applied calibration
factor. This would indicate that the
conducted loss from edge LHRF
deposition is symmetric. Data from
this run day used similar probes,
while data from other rundays had
differing styles of probes. Analysis of
these other rundays were inconclusive.
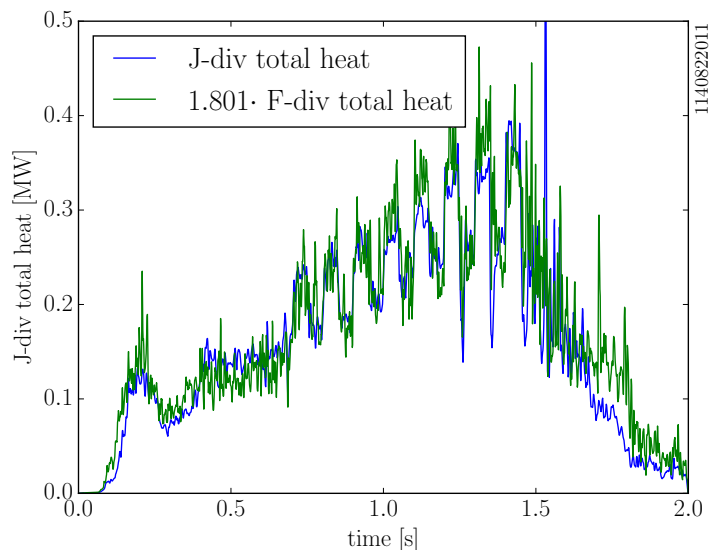
Shown in figure 4.10, the power loss' symmetry can be observed.
There is a systematic difference of ≈ 1.8 from one probe array to the
other that is determined from the ohmic phase of the discharges. This
factor is likely due to divertor segment alignment and shadowing. It
impacts absolute power balance, but does not affect conclusion that
the heat flux is toroidally symmetric. The two calculated total heats
depend on the current and equilibrium geometry causing the corre-
lation to be time-dependent and current dependent. Changes in this
value in time will introduce differences in the calculated total heat,
causing errors and bias in the degree of axisymmetry.

A small set of results from LSN found similar results with high
$\bar{n}_e$ discharges using a more complete set of Langmuir probes. These
discharges were similar to the example in 4.10 showing the robust-
ness of this result (from rundays 1100701 and 1100714). The key dur-
ing the modulation is the similarities in the change in divertor heat
with the step in LHRF power. In most, if not all cases, the measured
LHRF power at F-port is within 100kW (or $< 25\%$) of the J-port mea-
surement with LHRF at high $\bar{n}_e$. The two measurements suggest that
LHRF-induced conducted power increase is also axisymmetric.

The two locations severely limit the characterization of the toroidal
symmetry. Testing the symmetry over a range in currents is necessary
in order to change the Langmuir probe mapping away or closer to the
LHRF antenna. The example cases are limited to currents between
700-800 kA where the LHRF launcher mapping is shown in figure
4.7. However, the current drive efficiency and the edge absorption
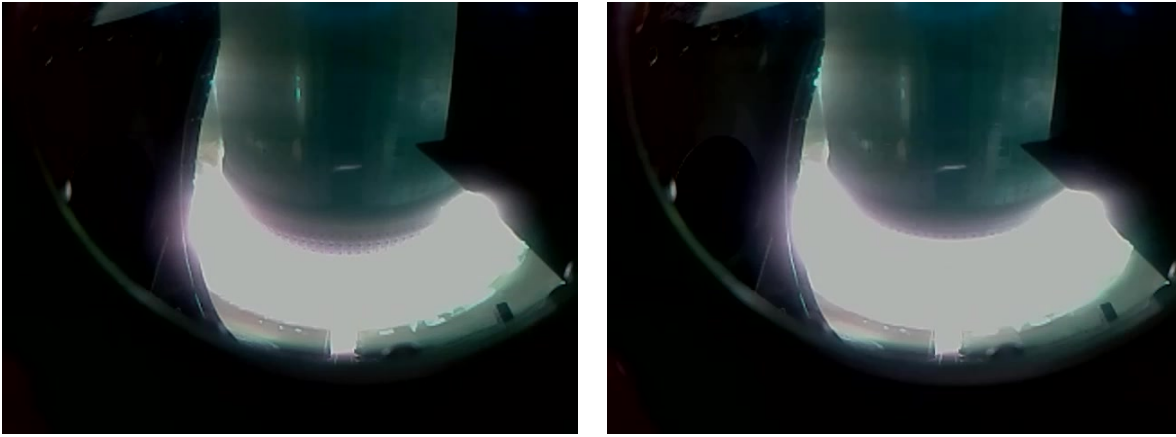
Figure 4.11: Downward-viewing visible and near-IR (< 900 nm) wide camera frames from G-port (WIDE3). There is a toroidally symmetric reduction in the active divertor light emission, as varying degrees of the inner divertor (known as the skirt) can be observed. The 'low' LHRF power is on left and 'high' LHRF power on right. This matches the observation from figure 4.9

are known to be strong functions of the plasma current. While further study of this axisymmetry is likely required, all measurements indicate a strong toroidal symmetric character in the edge-deposited LHRF observed as conducted power. Extended studies in changing how the LHRF launcher is mapped will balance the effects of more efficient current drive.

The edge-deposited LHRF power is observed to be significantly axisymmetric in both the radiated and conducted power. This would suggest that the parasitic power absorption is axisymmetric as parallel conduction is significantly faster than perpendicular transport. Deposition local to a specific toroidal position would appear as helical stripes on images[10, 14]. Toroidally symmetric edge losses can occur two ways: if the power is deposited just within the separatrix, or if the power is deposited in the SOL over long ray trajectories through the SOL. The LHRF wave absorption in the Alcator C-Mod core plasma is generally in the weak-damping regime due to the mostly low ($T_e(\rho = 0) < 4$ keV) core electron temperatures. The waves reflect from cut-off layers bouncing in and out through the SOL in a nearly stochastic manner (in the limit of many bounces known as the multiple-pass regime). Since both cases are likely, further research is necessary to determine the cause of the toroidally axisymmetric losses.

While very little of this power is observed in the core, it is not the immediate local absorption in the SOL which causes the edge losses. Unlike near-launcher effects, this LHRF wave absorption in the edge occurs after some interaction between the waves and the core plasma. This complicated phenomenon counters most other documented cases of edge-absorbed radiofrequency power. It indicates that the LHCD density limit is fundamentally different that the localized SOL interactions found at low density with efficient LHCD.

Deposition near the separatrix

The total conducted power onto the divertors are generated from the heat flux profiles along the divertor surfaces. In general, these profiles are dictated by the SOL cross-field diffusion characteristics and the magnitude of power crossing the separatrix. These profiles are peaked near the LCFS and monotonically decay with distance from the strike point. LHRF axisymmetric edge absorption requires that these assumptions be retested as losses of edge deposited power could trend differently than losses of core conducted power. In this case the radial heat flux profiles can be used to determine the LHRF power radial absorption profile.

Measurements of the LHRF conducted power were made using the divertor Langmuir probes[4] and IR thermography[16]. Ensemble averaging improved accuracy and characterized variability in the heat flux profile. The heat flux profile was mapped to the midplane using EFIT through the `eqtools` package. Unlike the calculations of the total heat (which uses the symmetric saturation current density $j_{sat,sym}$), these heat fluxes are parametrized by the parallel heat flux $q_\parallel$.

Figure 4.12: Heat flux profiles on the attached outer divertor surface as measured by Langmuir Probes (assuming $\gamma = 7$) and IR thermography during the two phases of modulation. The rise in measured parallel heat flux due to Lower Hybrid wave power is highest near the strike point (shown by the dashed line).
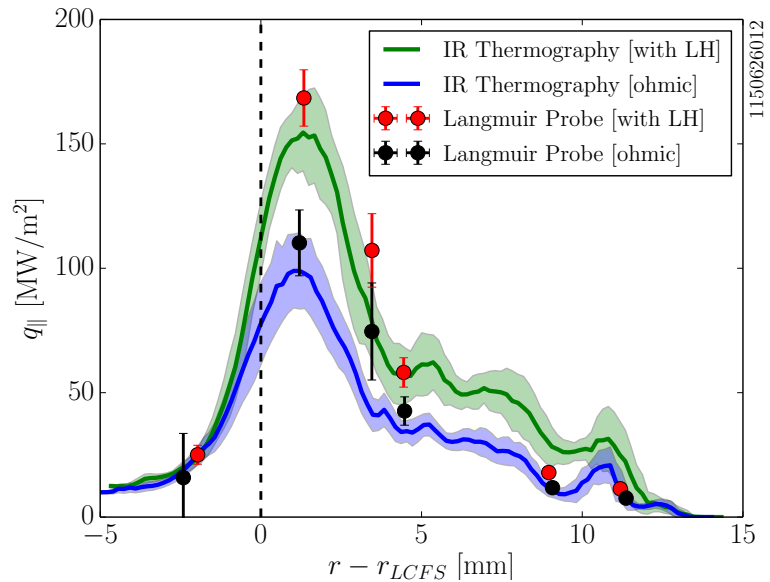
An example set of heat flux profiles is shown in figure 4.12 using the J-divertor Langmuir probes and IR thermography. The error bars represent the variation in the data points and do not reflect the measurement or fitting errors in the calculated heat flux. Both heat flux profiles show that the increase in heat flux due to edge-deposited LHRF is at its highest near the separatrix. In all cases, the change in the heat flux due to LHRF monotonically decreases with increasing R (outside the private flux region). However, this intensified heat flux from edge-deposited LHRF is observed across the profile and maintains a similar profile shape to the ohmic condition. Therefore, while

the LH power is clearly absorbed near the separatrix, it is not limited to that region.

While the far-SOL density increases with LHRF[17], the far-SOL effects are unimportant due the minimal radiation and heat flux increase in that region. In forward-field, LSN discharges, the LHRF edge absorption near the LCFS is dominated by a change in T_e at the outer divertor (as highlighted in figure 4.6). This change in T_e is the dominant contribution to the conducted heat. Farther out in the SOL the higher heat fluxes are caused by larger plasma densities. The power-starved, cold far-SOL plasmas are likely to ionize with additional power. However, from a power-balance perspective, the effects of the far-SOL are irrelevant for understanding LHRF wave edge absorption.

The heat-flux profiles' monotonic nature indicates that neither the far-SOL or mid-SOL dominates the power absorption. Thus, the LHRF edge-deposition mostly occurs near the separatrix. This power can influence the SOL ionization and heat flux profiles, but seems to be still influenced by the edge plasma's transport processes.

This new result proves the axisymmetric parasitic absorption of LHRF power is maximum near the LCFS. Some change in the heat flux occurs in some distance from the LCFS, indicating that deposition or transport of power occurs away from the LCFS. Those mechanisms which can induce LHRF wave edge absorption must cause maximal damping near the separatrix. This strongly limits the mechanistic interpretation of LHRF edge absorption and is discussed in the following section.

Importance of the active divertor

The addition of a divertor reduces the core plasma's impurity content, dramatically changing the edge plasma character. This feature has led to increased tokamak plasma performance and unlocked the potential of alternate confinement regimes[18, 19]. The current drive loss correlates with the addition of the divertor implying that it is significant in causing LHRF edge absorption. However, it is important to distinguish whether the edge absorption occurs *in* the divertor or due to changes in edge plasma *because* of the divertor. The LHRF edge-deposition's poloidal dependence can separate these two responses via differences in the divertor plasma conditions compared to the upstream SOL conditions. Determining the divertor plasma's importance in absorption can help further characterize the mechanism causing current drive loss.

In figure 4.13, the measurement of Ly_α across the plasma shows the greatest increase in the active divertor with applied LHRF. The fast increase in the divertor Ly_α emission (from two measurements 1ms apart) highlights both the LHRF-induced ionization processes
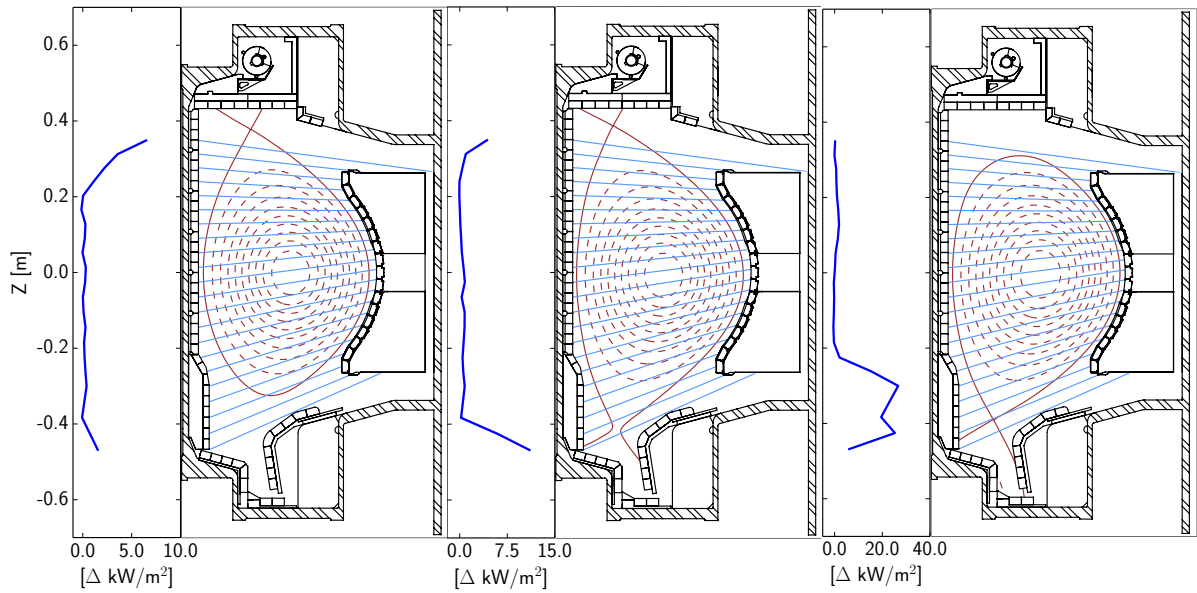
Figure 4.13: The equilibrium active divertor location dictates the location of Ly_α variation with LHRF at high $\bar{n}_e$. In the examples shown, three plasmas with three configurations (USN, DN and LSN) each have dominant contributions from the upper, both, and lower divertors respectively. The change in Ly_α comes from ionization in the divertor which indicates that the LHRF edge power loss is being observed in the active divertor.

and edge power deposition. This active-divertor dependence in emission is observed in all diverted plasma topologies (LSN, USN, and DN). Similar changes are also seen in neutral pressure measurements, where the dominant neutral pressure reduction in occurs near the active divertor. The power loss and ionization indicate that the LHRF power appears promptly in the active divertor.

However, the ionization increase from LHRF can be due to power conducted from another location in the SOL. Heat conduction and transport are extremely fast parallel to magnetic field lines. The upstream SOL plasma weakly loses power to surrounding volume, with a vast majority transported to the divertor. This makes upstream absorption nearly invisible to measurement. Instead, this power is observed as radiation and conduction in the cooler, denser divertor region. The ionization change is inconclusive in proving the deposition of power in the divertor plasma without higher time resolution, but still highlights its traversal to it. Determining the poloidal location will require other methods to find the direct power absorption.

One method for determining the poloidal deposition location exists in the more precise calculation of the edge loss time delay. Originally, the extremely short time delay was used for proving LHRF edge loss. These diagnostics are restricted to Nyquist frequencies of ~ 1 kHz due to data acquisition limitations and associated noise levels. Many of these diagnostics cannot sample at rates which can distinguish upstream from near-target LHRF SOL deposition. However, sufficient sampling rates are available on certain Alcator C-Mod fluctuation

diagnostics[20, 21] and in principle allow for this determination. A preliminary set of fast LHRF power modulations (at 3kHz and 10kHz) were included in the LHRF power for reversed field discharges. The outcome, though inconclusive, is discussed in the next section.

Divertor balance and reversed field effects

The LHRF edge absorption occurs with the addition of a divertor indicating that the loss of efficiency is is due to the SOL plasma's different characteristics. Modifying the SOL plasma can test the edge absorption and the subsequent edge losses associated with LHRF waves. For example, the LHCD efficiency depends on the plasma current[22] which correlates with reduced SOL widths[23]. The cross field density and temperature decay lengths scale with the Greenwald fraction[24], indicating the possible importance of edge collisionality in the SOL and the edge absorption of LHRF power. Other SOL alterations can be achieved through reversing the plasma current and can be used to understand edge LHRF absorption.

The SOL is strongly affected by the $\vec{B} \times \nabla|\vec{B}|$ direction versus null location (in the case of single null plasmas)[6, 7]. In forward field, the $\vec{B} \times \nabla|\vec{B}|$ direction points downward, and vice versa for reversed field. A forward-field USN plasma's SOL conditions are similar to those of a reversed-field LSN plasma. The in/out balance of conducted power loss and the threshold for detachment change depending on this relation.

In forward-field LSN plasmas (*i.e.* plasmas with the $\vec{B} \times \nabla|\vec{B}|$ direction toward the divertor), most of the conducted power is observed on the outer divertor. This is evident in the power balance given in chapter 3, where a much larger fraction ohmic power conducts to the outer divertor. The cold inner divertor tends to be in the high-recycling or detached regime with significant radiation (as can be observed in figures 4.9 and 4.11). The threshold for H-modes is reduced in this topology which limited the density range for this experiment. This restriction does not occur in reversed-field LSN plasmas as no LHRF-induced H-modes were observed.

Reversed-field LSN has the $\vec{B} \times \nabla|\vec{B}|$ direction away from the divertor, which changes many of the SOL plasma's characteristics. The conductive power loss tends to be balanced between the inner and outer divertors. Access to H-mode is more difficult and the emission of divertor radiation is reduced for the same conditions. The overall divertor plasma is less collisional than in forward-field.

This difference in field direction on the conducted power is highlighted in the example shown in figure 4.15. In this case, the inner and outer divertor LHRF conducted power are similar in magnitude. The total conducted power fraction combines to a substantive amount but varies widely due to the small modulation magnitude (300 kW).
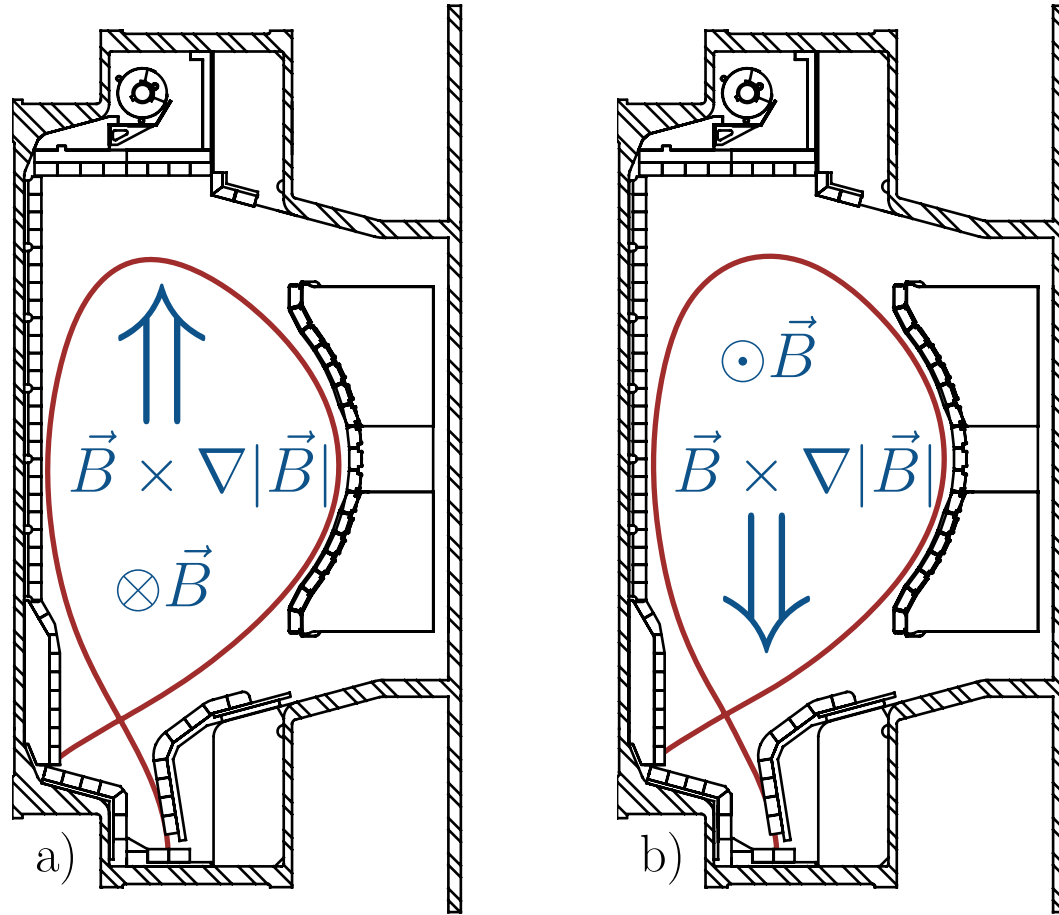
Figure 4.14: Alcator C-Mod is capable of operation with the magnetic field in the 'forward' and 'reversed' directions. Reverse-field plasmas, shown on left (a), have the current and magnetic field traveling counter-clockwise as viewed from above the tokamak. Forward-field plasmas (b), have the current and magnetic field traveling the opposite (clockwise) direction. The current and magnetic field directions are limited by engineering constraints. The direction of the $\vec{B} \times \nabla|\vec{B}|$ vector with respect to the null location strongly affects the nature of the SOL plasma, which can also impact core performance. This fact can be used to understand the edge absorption of LHRF power. The power balance calculations of the previous chapter were made in forward-field.

Errors on the order of 20% are likely and the rigorous completion of power balance in reversed-field requires more experimentation. However, even in this limited case, qualitative differences between forward and reversed field are still evident.

The in/out asymmetries in the SOL characteristics (*e.g.* heat flux, detachment, density and T_e) are also exhibited as enhanced differences in the radiative loss [6, 7, 25] and arise from drifts in the SOL. The asymmetry in conducted edge-deposited LHRF power is similar to core-deposited power, suggesting that the change in the SOL caused by LHRF happen to the thermal population. This effect also

Figure 4.15: The observed conducted power in reversed field on the inner and outer divertor are similar. Measurements were made using arrays of Langmuir probes on the inner and outer wall. The loss of power in the edge follows characteristic changes observed with the change in field. The lower ΔP_{LH} makes characterization of the conducted power loss fraction difficult. A secondary fast modulation can be observed during the high LHRF power phase on the fourth and eighth modulation.
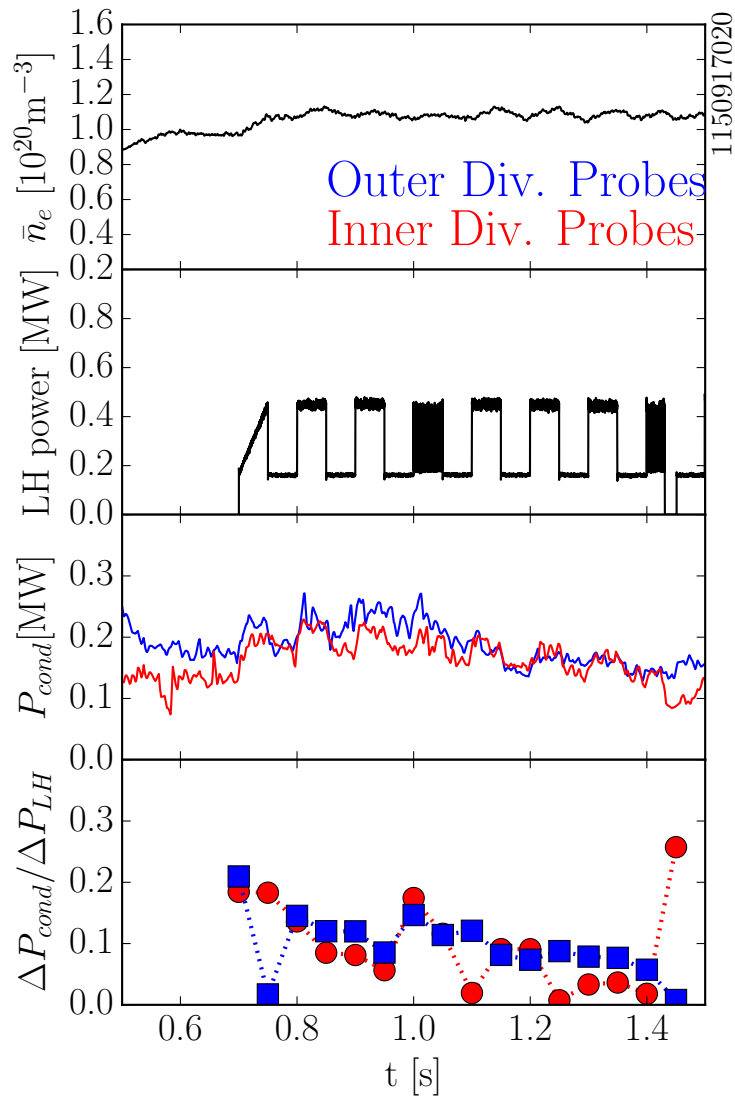
changes the in/out radiation asymmetry in forward-field plasmas as shown in figure 4.16.

The application of LHRF power enhances the radiation from the cooler inner divertor in forward-field discharges. The ratio of two bolometric divertor measurements (one of the inner divertor and one of the outer divertor) is used as a metric for the in/out radiation balance. LHRF enhances the asymmetry in divertor radiation (shown as this ratio in figure 4.16) increasing with higher densities. As the outer divertor electron temperature approaches 10 eV (at $\bar{n}_e > 1.25 \cdot 10^{20}$ [m^{-3}]), the asymmetry weakens. The recycling on the outer-divertor increases the radiative power loss. Divertor-viewing visible radiation measurements highlight the LHRF-enhanced radiation asymmetry in forward field.

This divertor radiation asymmetry is likely correlated with the ionization induced by the edge-absorbed LHRF. The observed LHRF-

Figure 4.16: The observed in/out asymmetry of radiative emission is enhanced by applied Lower Hybrid wave power at high density. The ratio of measurements from a divertor viewing AXUV pinhole bolometer is given for the ohmic and high power LHRF periods. The asymmetry in forward field lower single null discharges is due to the high recycling of the inner divertor which occurs at a lower density than the outer divertor. The ratio is higher with applied LHRF due to enhanced emission from the inner divertor leg. The emission becomes more symmetrical as the SOL transitions to high-recycling with densities near 1.25×10^{20} [m^{-3}].
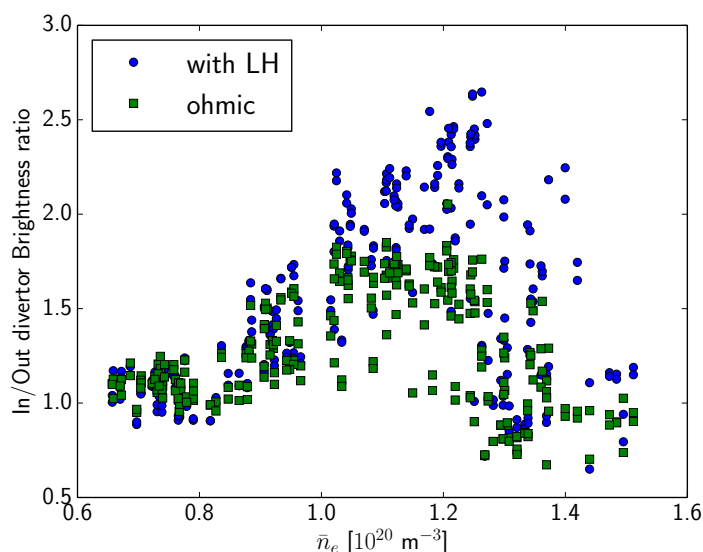
induced thermoelectric currents [17, 26] match the higher inner divertor plasma densities with higher outer divertor plasma electron temperatures. Also, the LHRF radiation power loss fraction in forward field is due to the cold inner divertor plasma. In reversed field, the symmetrization of SOL characteristics requires a higher average plasma density to cause significant radiation at the inner leg. The emitted radiation will come from both divertors, likely leading to more overall radiative loss. This is observed in trends of the radiated power loss in reversed field shown in figure 4.17.

The onset of significant radiative power losses for edge-deposited LHRF occurs at a higher density (at $\bar{n}_e > 1.05 \cdot 10^{20}$ [m^{-3}]). However, the power loss fraction increases with $\bar{n}_e$ at a higher-rate illustrated by the trend in green, recovering a similar loss fraction with the complete loss of current drive. This result supports the hypothesis that the changes in the divertor character impact the LHRF loss channels. The alteration in radiative LHRF power loss versus $\bar{n}_e$ is caused by the reversing of the magnetic field.

While the power balance in reversed field was not fully completed, its differences from the forward field LHRF loss attributes can be qualitatively analyzed. The changes in in/out radiation and conduction balance typically observed with field-reversal are also seen in the edge-deposited LHRF. The similarities between the two edge losses would suggest that in each case the power is carried by a population which is influenced by the SOL drifts (*i.e.* the thermal electron population). In forward field, LSN plasmas, the LHRF power enhances the asymmetry with higher densities and radiation in the inner divertor plasma and higher temperatures in the outer divertor plasma. This is the necessary conditions to induce the thermoelectric currents previously observed with the LHCD density limit[26]. The enhanced asymmetries indicate that the edge-deposited LHRF power is located

Figure 4.17: Fraction of Lower Hybrid wave power lost as radiation. Data shown in green is 'reverse field', with forward field data in gray. The radiated loss rises at a higher density than in forward field. This result follows changes in recycling and radiation observed with the change in field.
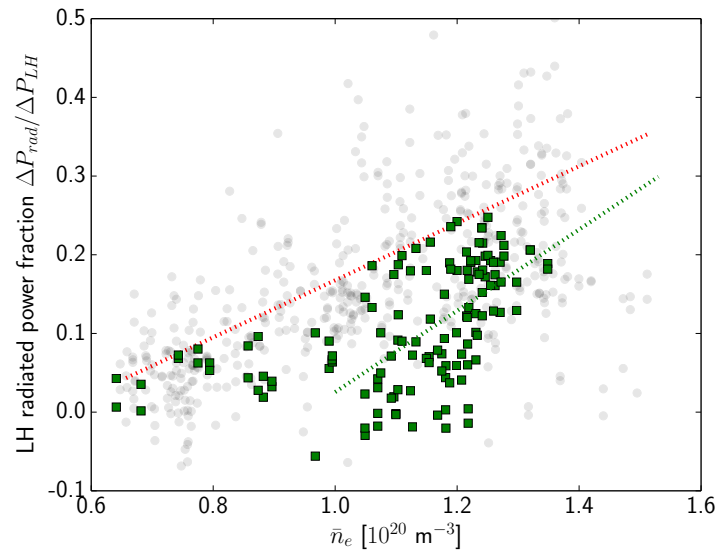
differently from core power which diffuses into the SOL. These results motivate future work to quantitatively deduce power loss' field-direction dependence through the completing power balance in reversed field.

MECHANISTIC INTERPRETATION OF EDGE DEPOSITION

Epithermal tails and electron Landau damping

The wave power absorption via electron Landau damping is strongly influenced by the $n_\parallel$ and the plasma's electron temperature. With strong absorption occurring at $3v_{th}$ as a rule-of thumb, damping can occur in the edge for LHRF waves with $n_\parallel$ greater than 10 (assuming $T_e \sim 100$ eV). Processes that strongly upshift the LHRF wave $n_\parallel$ can cause significant damping near or inside the LCFS. This can create an epithermal electron population that locally heats the plasma.

Epithermal electrons just inside the separatrix are poorly confined and are capable of causing the observed toroidal symmetry and immediate LHRF SOL power loss. Additionally, edge absorption just inside the LCFS will minimally change the core temperature due to this poor confinement. This power will follow the typical SOL transport characteristics due to the electron's relatively low energies and rapid thermalization. Furthermore, the damping strength increases with T_e, making wave absorption just inside the LCFS more likely. The LHRF wave edge Landau damping generates the necessary absorption characteristics.

However, the loss of ~ 1 keV electrons to the SOL will change the plasma sheath's nature and, consequently, will change the interpretation of the plasma at the divertor target. Pioneering work by Stangeby[27, 28] rederived the sheath conditions for epithermal distri-

Figure 4.18: Two idealized profiles of the sheath potential along a magnetic field line. Parallel losses dictates the development of a potential which changes with the character of the plasma. Ions are accelerated through the sheath from potential V_s to V_{fl} and shields electrons from the surface. High electron temperatures and fast electrons cause larger floating potentials V_{fl}. This is shown by the differences in the blue and green sheaths (ΔV_{fl}). ℓ is the distance along the magnetic field line.
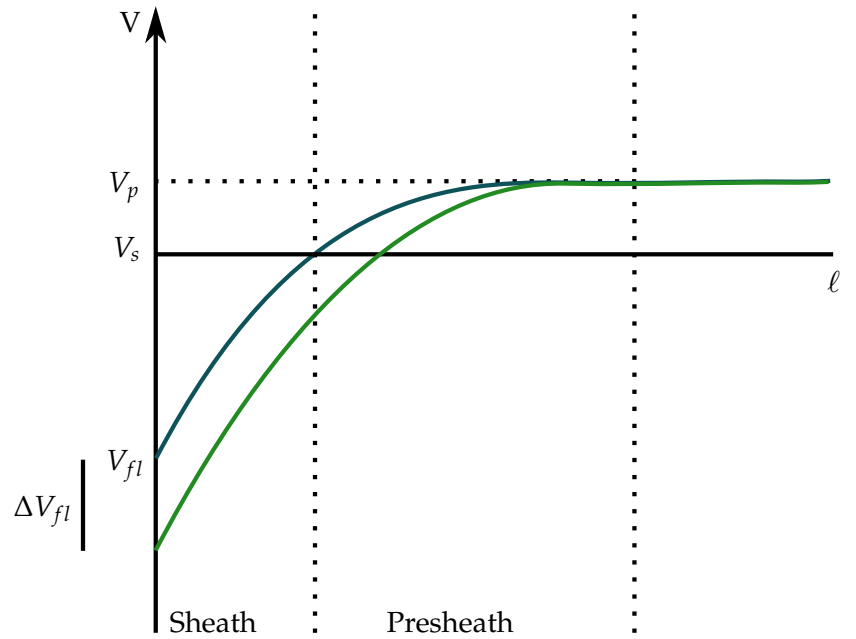
butions parameterized as secondary higher-temperature Maxwellians. These distributions are known to exist in cases with sufficiently short connection lengths where electrons with energies greater than 100eV appear collisionless (*i.e.* they travel unhindered to the divertor surface). This is likely the case for electron Landau damping heated electrons near or just inside the separatrix.

The additional high energy component increases the sheath potential in order to recover ambipolarity. The floating potential depends on several parameters including the ratio of the two population densities at the pre-sheath $f_n = n_{ef}/n_{es}$ (where n_{ef} is the 'fast' population density, and n_{es} is the 'slow' population density). It is also a sensitive function of f_T, the ratio of the two population temperatures, T_{ef}/T_{es}. Corrections to the sound speed with the secondary population are given in equation 4.1, with f defined in equation 4.2.

$$c_s = \sqrt{\frac{T_i + f T_e}{m_i}} \tag{4.1}$$

$$f = f_t \frac{1 + f_n}{f_t + f_n} \tag{4.2}$$

The floating potential is defined from the voltage necessary to yield a net zero current and achieved by balancing electron and ion fluxes. V_{fl} can be derived from this balance which is given in equation 4.3. The change in floating potential (ΔV_{fl}) due to fast electrons can also be derived from this equation in a second condition with possible

non thermals. The two V_{fl} measurements given by equation 4.3 can derive ΔV_{fl} assuming one case has $n_{ef} = 0$.

$$\frac{n_{es}}{4} c_{es} e^{eV_{fl}/T_e} + \frac{n_{ef}}{4} c_{ef} f_T^{1/2} f_n e^{eV_{fl}/(T_e f_T)} = \frac{1}{2} n_i c_s \tag{4.3}$$

A representation of the fast electron influence on the sheath is given by figure 4.18. The addition of a high-energy population causes a lower value V_{fl} which reduces the electron flux. V_{fl} is defined relative to the plasma potential V_p, but the fluxes are defined with respect to the presheath V_s.

Figure 4.19: V_{fl}/T_e has been theoretically shown to be a good metric for non-thermals in the sheath of a divertor plasma. The application of modulated LHRF is not observed in this metric, even though modulations in T_e and V_{fl} occur. This would suggest that the LHRF-induced increase in T_e and $q_\parallel$ is thermal in nature. However, this metric is only useful in cases with significant epithermal distributions (high energy electrons in the SOL are treated in chapter 5).
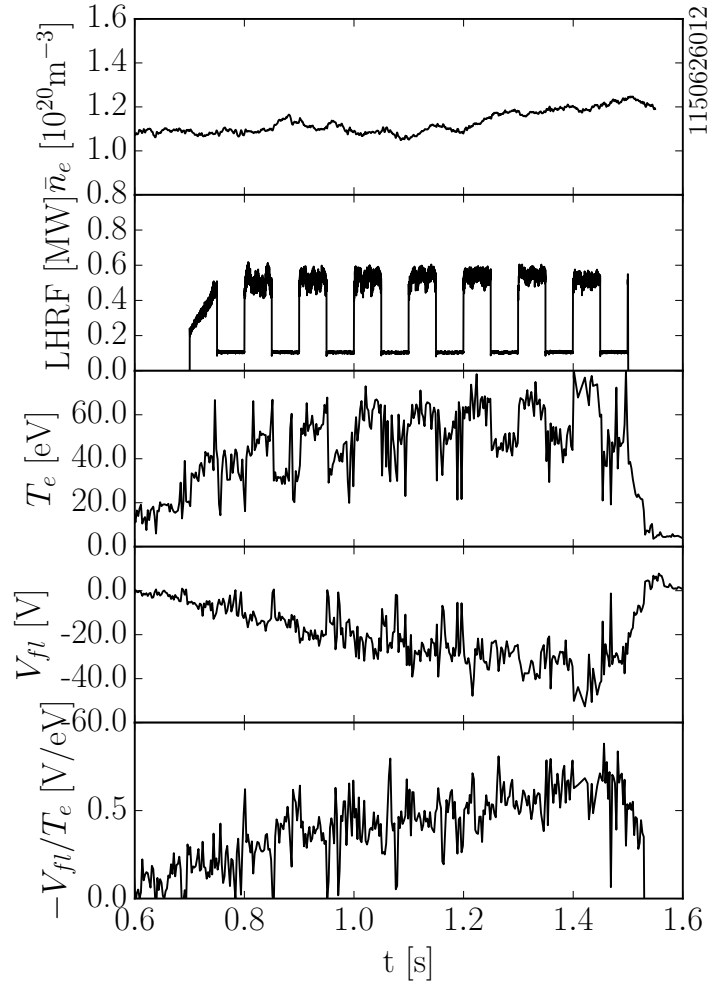
As reflected in the work by Stangeby, the change in the floating potential by a non-thermal population can be characterized by the ratio of the floating potential to the electron temperature, V_{fl}/T_e. This parameter is sensitive to the ratios f_n and f_T; small values of these ratios capable of changing V_{fl}/T_e by many orders of magnitude[28, 29]. This ratio is theoretically fixed for a purely Maxwellian plasma; however, experimentally this value varies. An epithermal population

caused by LHRF should induce some in-phase, immediate change in this ratio (some ΔV_{fl}). The immediate step in heat flux should lead to some substantive ΔV_{fl} in the case of epithermal electrons.

An example at high $\bar{n}_e$ is given in figure 4.19, where some modulation exists in T_e and V_f. Significant noise exists in the data, but the V_{fl}/T_e ratio is clearly not modulating with LHRF power. The temperature and floating potential at the strike point are measured by an innovative rail probe at F-port. Similar characteristics are observed on the standard proud Langmuir probes on Alcator C-Mod. This lack of a modulation indicates one of two conclusions, either that the increase in temperature at the strike-point is thermal or the non-thermal electron population minimally changes the sheath (*i.e.* a small but very high energy population). This matches the results and conclusions from Ochoukov[30] on Alcator C-Mod which found that the edge changes in electron temperature from LHRF to be thermal in nature. The similarity in conducted power measured by IR thermography and Langmuir probes also suggests the thermal population absorbs this power. However, the possibility of an extremely non-thermal population motivates the characterization of high-energy electrons in the SOL and is investigated in chapter 5.

The electron Landau damping inside the LCFS should be similar to the edge loss of ohmic power in the case that the electrons thermalize. Electrons which gain energy through Landau damping must thermalize to be observable on diagnostics which measure bulk thermal parameters (*e.g.* Langmuir probes, H_α emission). Theoretically, upstream diagnostics that view the edge should observe LHRF power modulation with minimal delay.

A fast modulation at 3kHz and 10kHz of 300kW was applied to the LHRF power in reversed-field, 700kA, LSN plasmas. Measurements using fluctuation diagnostics with Nyquist frequencies > 1 MHz were taken during this period across a $\bar{n}_e$ range. A scanning mirror Langmuir probe[20] measured T_e, n_e and V_f during the fast-modulation in the SOL along field lines not connected to the LHRF launcher.

The only discernible fluctuation which matched the imposed fast modulation occurred in measurements which observe reverse-$n_\parallel$ edge damping. This power exists near field lines connected to the launcher, which in reversed-field LSN travel counter-clockwise into the lower divertor. Analysis of gas-puff imaging[16] at B-port found a finite delay which corresponds to the thermal flow of electrons from the launcher. Specific channels of the two-color-interferometer[31] at H-port and magnetics between B and C ports also observed the waves. No other measurements observed the fluctuation. This indicates the absence of deposition in core plasma.

An example spectrogram from the scanning mirror Langmuir probe is given in figure 4.20. The modulation applied at 10kHz does not ex-

Figure 4.20: A spectrogram of the A-port scanning probe floating potential at high $\bar{n}_e$. It does not measure an imposed 10 kHz LHRF amplitude modulation which occurs from 1.0-1.05 seconds and 1.4-1.45 seconds. Only diagnostics which measure along field lines connected to the LHRF launcher observe the 10kHz signal (Gas Puff Imaging, certain interferometer channels and certain magnetics). This is likely due to localized damping of reverse $n_\parallel$ waves in this 700kA, LSN, reversed-field plasma which travel into the divertor past those diagnostics.
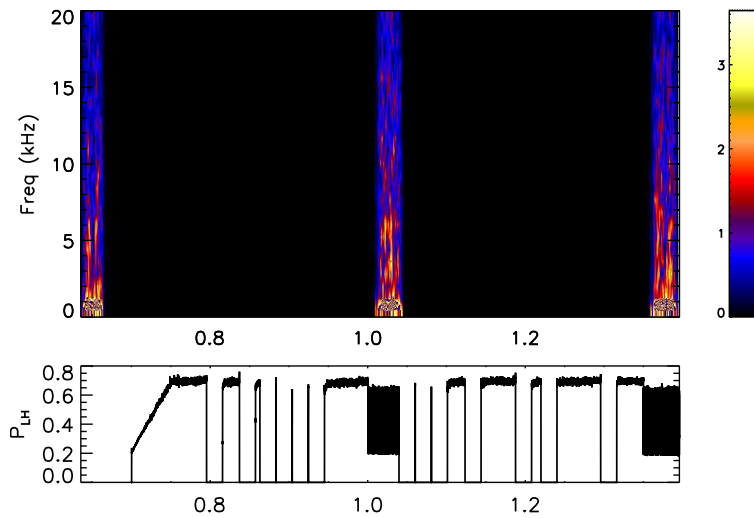
ist at the fundamental or harmonic frequencies as a fluctuation in potential. A coherence analysis between the LHRF power and the Langmuir probe measurements (T_e,n_e) are similarly inconclusive. None of the fluctuations were definitely observed in the SOL or inside the LCFS.

This lack of observation is a necessary but not sufficient condition in disproving the high $n_\parallel$ electron Landau damping of waves just inside the LCFS. However, several strict criteria exist for electron Landau damping to cause the LHCD density limit. First, the deposited power must thermalize inside the LCFS. As shown in figure 4.21, electrons $\sim 3v_{th}$ have electron-ion momentum collision mean-free-paths $\lambda_{mom,ei}$ on the order of the Alcator C-Mod SOL connection length or longer. Electrons which absorb power from Landau damping are not collisional enough to thermalize along the length of the C-Mod SOL. While some small fraction of $\sim 500eV$-1keV electrons may be generated, a sufficiently large population is needed to recover the observed heat fluxes. The nature of the heat flux requires that the waves damp and the electron thermalize just inside the LCFS. Second, $n_\parallel$ must exceed 10 to damp near the LCFS at $100-300eV$ temperatures but not exceed 17 to prevent open-field line damping. Third, the edge absorption from Landau damping must occur at low densities to observe the low density edge deposition. Fourth, the similar LCFS densities and temperatures to limited plasmas in L-mode require that the change in the wave causing Landau damping must occur in the SOL and must be dependent on I_p. These observations make it less likely that edge electron Landau damping is responsible for the LHCD density limit.

In addition, no sign of the LHRF waves damping just inside the LCFS with a secondary fast modulation. Thus, more extensive experimentation with high-frequency LHRF power modulation is necessary at other locations previously untested (*e.g* the divertor or inner wall). The direct observation of high frequency damping along field-lines

Figure 4.21: The slowing-down mean free path ($\lambda_{mom} = \nu_{ei}(v)v$) of low energy electrons generated by Landau damping show that λ_{mom} is longer than the Alcator C-Mod SOL conditions. The velocity of the electron is assumed to be $2.5v_{th}$, and is plotted versus SOL T_e and n_e. The contours are in meters with 10m contour in red signifying the typical parallel field-line length of the C-Mod SOL. SOL parameters of the modulation experiments near the LCFS are shown in gray. Electron Landau damping in the SOL will create electrons which will be nonthermal at the divertor targets.
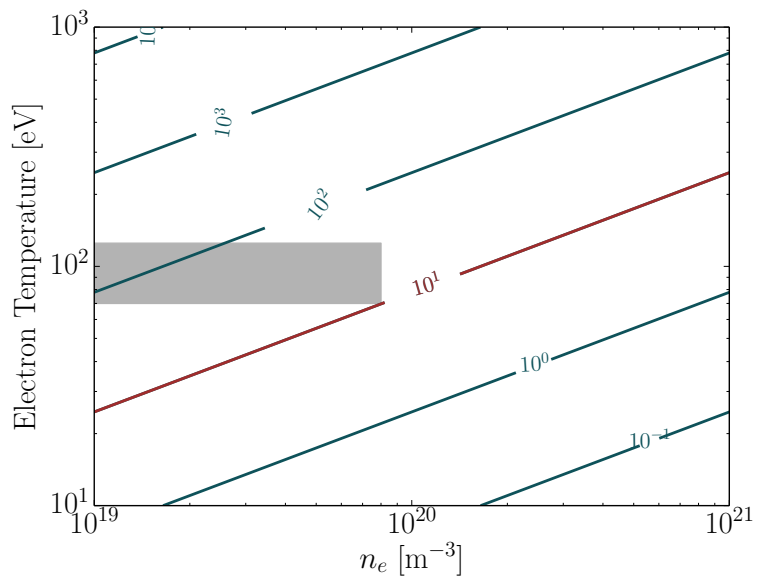
not connected to the LHRF launcher would concretely determine the importance of edge LHRF Landau damping.

Collisional absorption

Unlike the poloidally symmetric power loss expected for edge electron Landau damping, collisional damping occurs in the plasma's collision regions. In the case of a diverted discharge, the maximum collisionality exists in the divertor plasma near the strike point (due to $\nu_{ei} \propto Z_{eff} n_e T_e^{-3/2}$). The divertor plasma wave absorption on Alcator C-Mod represents a possible RF power loss mechanism that may be important for future tokamaks.

The electron velocity distribution change due to collisional power absorption is thermal. The absorption strength is approximately proportional to the $e^{v^2} v^{-3}$ and to the collision frequency. These attributes match the edge deposition's observed thermal nature. LHRF wave absorption via collisions most likely occurs in the divertor as the collisionality along the field line increases with proximity to the target. Using the two-point model, the collisionality at the target ($\nu_{ei,t}$) scales as n_u^6 where n_u is the upstream density (derived from dependencies of n_t and T_t[32]).

As the upstream density rises (represented by $\bar{n}_e$) the divertor neutral pressure and density also increase significantly. This causes the divertor temperatures to decrease and the collisionality to also rise significantly. Increasing collisionalities are exhibited by the transition to the high-recycling regime and the onset of detachment. The upper bound of the tested density range represents the transition from the sheath-limited regime to the high-recycling regime. The doubling of the core density (at 700kA) across current drive loss' density range

represents a 64 times increase in the target plasma collisionality. The significant current drive loss correlates with marked change in SOL collisionality.

Figure 4.22: The application of LHRF modulation in H-mode plasmas is limited to a very small number of circumstances ($<$ 8 cases). In each, the strike point heat flux and conducted power is reduced with the transition to H-mode. This is accompanied with an increase in the stored energy and radiation emission from the core plasma. The divertor Ly_α increase is concentrated in the lowest parts of the divertor. Other examples including H-modes are shown in figures 4.5 and 4.6.
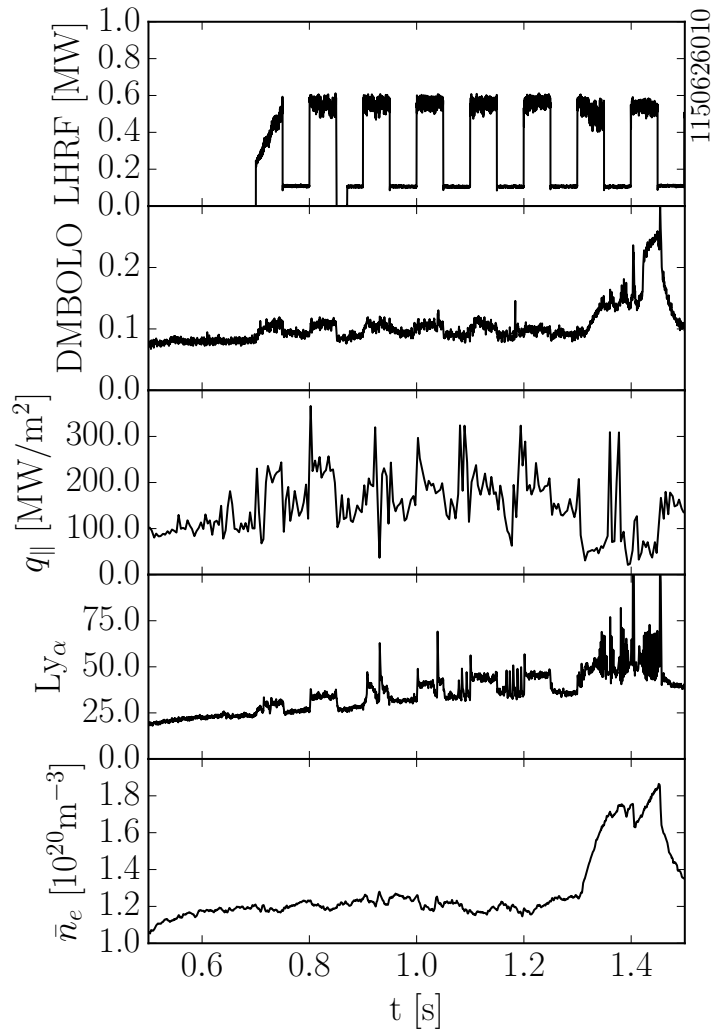
H-modes are generated by edge-deposited LHRF through some un-characterized change in the plasma. Example H-modes can be observed in figures 4.5, 4.6 and 4.22. The H-mode can be used to help deduce the poloidal location of edge LHRF deposition. The significant difference in diffusion parallel and perpendicular to the field lines can be used in conjunction with the increasing stored energy of the H-mode.

LHRF power deposited in the SOL will predominantly stay on open field lines. If the edge losses are reduced during the transition to H-mode, LHRF power is flowing into the plasma and increasing the stored energy. The diffusion characteristics of the SOL would signal that collisional absorption is not the cause of the LHCD density limit. If the edge losses stays relatively constant during the change in stored

energy, then collisional absorption may be the cause to the LHRF edge absorption.

Without proper power balance calculations during the H-modes, it is impossible to tell if changes in the power balance occur due to increases in radiation or from change in ohmic power. A plethora of mechanisms can increase the stored energy by changing any of the sources or sinks. Further experimentation with the onset of H-modes is needed to test this hypothesis. Proper power balance during and after H-mode onset with a statistically rigorous sample size could be used to determine the deposition location and can shed light on the importance of collisional absorption for LHRF waves.

Collisional absorption simply meets the necessary criteria for the LHCD density limit. First, it exists at low density, as the $k_{\perp I} \propto \omega_{pe} \nu_{ei} n_{\parallel} / 2c\omega$. Second, it is absorbed in the plasma thermally and promptly in the SOL likely near the most collisional regions (*i.e.* possibly the inner strike point). Third, it is likely to ionize the active divertor without directly changing the core plasma, and could cause enhanced asymmetries if asymmetric collisionality exits in the divertor. Fourth, collisional regions do not regularly occur in limited plasmas and are strongly correlated with I_p. It is likely that collisional absorption is the cause of the LHCD density limit.

SUMMARY AND DISCUSSION

LHRF wave power balance was used to derive further characteristics of the parasitic edge absorption at high density. Most of the discovered attributes correlate with divertor plasma collisionality; these attributes highlight the importance of the highly-collisional plasma caused by the addition of a plasma null.

The LHRF power edge loss was shown to be toroidally axisymmetric as observed by toroidally separated total heats, broad-spectrum radiation, and visible light measurements. This result contradicts most other observed edge losses caused by radiofrequency power. The radial heat flux profiles indicate that edge absorption must occur near the LCFS. Two possibilities exist which can cause symmetric loss near the LCFS. Collisional absorption of LHRF waves which traverse the SOL multiple times are capable of absorbing in the small but highly collisional strike point region, appearing to be toroidally symmetric. Electron Landau damping just inside the LCFS can also cause the observed characteristics in edge losses.

This parasitic LHRF edge power absorption can quickly ionize the divertor and change the upstream density profiles. The ionization change in the divertor correlates with the generation of H-modes. Oscillations in the conducted power, divertor electron temperature, and ionization indicate that the higher electron temperatures cause ionization.

Floating potential and electron temperature analyses at the outer strike point reflect previous analyses that show the edge loss' thermal nature. In/out asymmetries which drive thermoelectric currents are enhanced by LHRF, and are affected by field reversal. This indicates that edge epithermal populations induced by LHRF are small. Fluctuation measurements also show no sign of LHRF damping just inside the LCFS. These characteristics indicate that edge electron Landau damping can cause the LHCD density limit in very specific cases, and is therefore unlikely.

However, the same modulation scheme was used in a similar reversed-field equilibrium for a similar density range. These plasmas with different SOL conditions found the same edge LHRF power loss distributed similarly to the core-deposited power edge loss. The edge absorbed LHRF power was conducted in similar amounts to the inner and outer divertors. LHRF was incapable of causing H-modes and the onset LHRF-induced divertor radiation occurred at higher density. This result mirrors the LHRF power deposition just inside the LCFS, and indicates its thermal nature.

Addition of a divertor changes the SOL and causes the LHRF density limit. The cold divertor plasma generated by the increased connection lengths is correlated with the LHRF edge parasitic absorption. The greatest amount of LHRF-induced ionization, radiation and conduction comes from the most collisional portions of the plasma. Unlike Landau damping induced by PDI, the current drive loss is not a threshold mechanism. The edge losses and collisions in the divertor occur even at low density. This correlation with collisionality suggests that future LHRF systems must limit wave propagation through collisional regions.

Minimizing propagation through collisional regions is important due to the use of detachment in future high-performance tokamaks. Long distance coupling through the SOL[33] can also lead to edge absorption, possibly even on the first SOL traversal. Asymmetric edge ionization by radiofrequency systems highlights this possibility. The dichotomy of attributes needed for divertor power handling and for steady-state plasmas makes avoiding this effect a priority.

Further study and experimentation is necessary to separate the importance of these two mechanisms. The derived characteristics do not effectively prove one over the other, but indicate a more likely cause. However, the key in separating the two mechanisms is in the edge absorption's poloidal dependence. Precise time-delay experiments or H-mode threshold experiments using divertor and other fluctuation diagnostics can help answer this question.

BIBLIOGRAPHY

[1] C. Lau, G. Hanson, Y. Lin, J. Wilgen, S. Wukitch et al. First results of the SOL reflectometer on Alcator C-Mod. *Review of Scientific Instruments*, 83(10):–, 2012.

[2] C Lau, G R Hanson, B Labombard, Y Lin, O Meneghini et al. Effects of LH power on SOL density profiles and LH coupling on Alcator C-Mod. *Plasma Physics and Controlled Fusion*, 55(2):025008, 2013.

[3] Orso (Orso-Maria Cornelio) Meneghini. *Full-wave modeling of lower hybrid waves on Alcator C-Mod*. PhD thesis, Massachusetts Institute of Technology, February 2012.

[4] N. P. Basse, A. Dominguez, E. M. Edlund, C. L. Fiore, R. S. Granetz et al. Diagnostic systems on Alcator C-Mod. *Fusion Science and Technology*, 51(3):476–507, April 2007.

[5] J. L. Terry, M. L. Reinke, J. W. Hughes, B. LaBombard, C. Theiler et al. Improved confinement in high-density H-modes via modification of the plasma boundary with lower hybrid waves. *Physics of Plasmas*, 22(5):–, 2015.

[6] I H Hutchinson, B LaBombard, J A Goetz, B Lipschultz, G M McCracken et al. The effects of field reversal on the Alcator C-Mod divertor. *Plasma Physics and Controlled Fusion*, 37(12):1389, 1995.

[7] B. Labombard, J.A. Goetz, I. Hutchinson, D. Jablonski, J. Kesner et al. Experimental investigation of transport phenomena in the scrape-off layer and divertor. *Journal of Nuclear Materials*, 241–243:149 – 166, 1997.

[8] M. Z. Tokar. Self-sustained oscillations in a plasma-wall system with strongly inhomogeneous diffusion of charged particles. *Phys. Rev. Lett.*, 95:265002, Dec 2005.

[9] A. Loarte, R. D. Monk, A. S. Kukushkin, E. Righi, D. J. Campbell et al. Self-sustained divertor plasma oscillations in the JET tokamak. *Phys. Rev. Lett.*, 83:3657–3660, Nov 1999.

[10] R. J. Perkins, J. C. Hosea, G. J. Kramer, J.-W. Ahn, R. E. Bell et al. High-harmonic fast-wave power flow along magnetic field lines in the scrape-off layer of NSTX. *Phys. Rev. Lett.*, 109:045001, Jul 2012.

[11] Greg Wallace. *Behavior of Lower Hybrid Waves in the Scrape Off Layer of a Diverted Tokamak*. PhD thesis, Massachusetts Institute of Technology, February 2010.

[12] M. Goniche, J. Mailloux, Y. Demers, V. Fuchs, P. Jacquet et al. Strong toroidal asymmetries in power deposition on divertor and first wall components during LHCD on TdeV and Tore Supra. *Journal of Nuclear Materials*, 241:745 – 749, 1997.

[13] The ASDEX Team, T.E. Evans, J. Neuhauser, F. Leuterer and E.R. Müller. Characteristics of toroidal energy deposition asymmetries in ASDEX. *Journal of Nuclear Materials*, 176:202 – 207, 1990.

[14] Y. Liang, X. Z. Gong, K. F. Gan, E. Gauthier, L. Wang et al. Magnetic topology changes induced by lower hybrid waves and their profound effect on Edge-Localized Modes in the EAST tokamak. *Phys. Rev. Lett.*, 110:235002, Jun 2013.

[15] G.M. Olynyk, R.S. Granetz, M.L. Reinke, D.G. Whyte, T. Golfinopoulos et al. Rapid shutdown experiments with one and two gas jets on Alcator C-Mod. *Nuclear Fusion*, 53(9):092001, 2013.

[16] J. L. Terry, B. LaBombard, D. Brunner, J. Payne and G. A. Wurden. Divertor ir thermography on Alcator C-Mod. *Review of Scientific Instruments*, 81(10), 2010.

[17] G.M. Wallace, A.E. Hubbard, P.T. Bonoli, I.C. Faust, R.W. Harvey et al. Lower hybrid current drive at high density in Alcator C-Mod. *Nuclear Fusion*, 51(8):083032, 2011.

[18] M. Greenwald, R.L. Boivin, F. Bombarda, P.T. Bonoli, C.L. Fiore et al. H mode confinement in Alcator C-Mod. *Nuclear Fusion*, 37(6):793, 1997.

[19] D.G. Whyte, A.E. Hubbard, J.W. Hughes, B. Lipschultz, J.E. Rice et al. I-mode: an H-mode energy confinement regime with L-mode particle transport in Alcator C-Mod. *Nuclear Fusion*, 50(10):105005, 2010.

[20] B. LaBombard and L. Lyons. Mirror langmuir probe: A technique for real-time measurement of magnetized plasma conditions using a single Langmuir electrode. *Review of Scientific Instruments*, 78(7), 2007.

[21] J. L. Terry, S. J. Zweben, K. Hallatschek, B. LaBombard, R. J. Maqueda et al. Observations of the turbulence in the scrape-off-layer of Alcator C-Mod and comparisons with simulation. *Physics of Plasmas*, 10(5):1739–1747, 2003.

[22] S.G. Baek, R.R. Parker, P.T. Bonoli, S. Shiraiwa, G.M. Wallace et al. High density LHRF experiments in alcator C-Mod and implications for reactor scale devices. *Nuclear Fusion*, 55(4):043009, 2015.

[23] T. Eich, B. Sieglin, A. Scarabosio, W. Fundamenski, R. J. Goldston et al. Inter-ELM power decay length for JET and ASDEX upgrade: Measurement and comparison with heuristic drift-based model. *Phys. Rev. Lett.*, 107:215001, Nov 2011.

[24] B. LaBombard, J. W. Hughes, N. Smick, A. Graf, K. Marr et al. Critical gradients and plasma flows in the edge plasma of Alcator C-Mod. *Physics of Plasmas*, 15(5), 2008.

[25] P.C. Stangeby. *The Plasma Boundary of Magnetic Fusion Devices*. Series in Plasma Physics and Fluid Dynamics. Taylor & Francis, 2000.

[26] G. M. Wallace, R. R. Parker, P. T. Bonoli, A. E. Hubbard, J. W. Hughes et al. Absorption of lower hybrid waves in the scrape off layer of a diverted tokamak. *Physics of Plasmas (1994-present)*, 17(8):–, 2010.

[27] Peter C Stangeby. Langmuir-, and bolometer-probe interpretation for plasmas with two electron components. *Journal of Nuclear Materials*, 128–129:969 – 973, 1984.

[28] P C Stangeby. A problem in the interpretation of tokamak langmuir probes when a fast electron component is present. *Plasma Physics and Controlled Fusion*, 37(9):1031, 1995.

[29] D. Tskhakaya, S. Kuhn, V. Petržilka and R. Khanal. Effects of energetic electrons on magnetized electrostatic plasma sheaths. *Physics of Plasmas*, 9(6):2486–2496, 2002.

[30] R. Ochoukov, D. G. Whyte, I. Faust, B. LaBombard, B. Lipschultz et al. Experimental investigation of RF sheath rectification in ICRF and LH heated plasmas on Alcator C-Mod. In *RADIO FREQUENCY POWER IN PLASMAS: Proceedings of the 19th Topical Conference*, volume 1406, pages 207–210, 2011.

[31] C. P. Kasten, A. E. White and J. H. Irby. A new fast two-color interferometer at Alcator C-Mod for turbulence measurements and comparison with phase contrast imaging. *Physics of Plasmas*, 21(4), 2014.

[32] C S Pitcher and P C Stangeby. Experimental divertor physics. *Plasma Physics and Controlled Fusion*, 39(6):779, 1997.

[33] A. Ekedahl, G. Granucci, J. Mailloux, Y. Baranov, S.K. Erents et al. Long distance coupling of lower hybrid waves in JET plasmas with edge and core transport barriers. *Nuclear Fusion*, 45(5):351, 2005.

CHARACTERIZATION OF EDGE FAST ELECTRON LOSSES

It has been proposed that the diffusion of fast-electrons into the SOL could cause the loss of current drive efficiency on Alcator C-Mod[1]. Plasma current is lost when the passing fast electrons responsible for current drive impact solid surfaces. The low collisionality of these electrons results in high current drive efficiency but also leads to immediate loss on open field lines. A non-thermal population can impact the interpretation of Langmuir probes and distort the measured power in the divertor[2, 3]. Characterizing the loss of LHCD-generated fast electrons is important for the quantification of power balance and investigating the physics behind current drive loss.

Strong up/down asymmetries in the emission of hard X-rays are observed in diverted discharges on Alcator C-Mod[4]. Line-integrated hard X-ray count rates from the active divertor can be several times higher than chords viewing the opposite divertor. This asymmetry is not strongly observed in the core, but as evidenced by figure 5.1, it is pronounced for chords that view the periphery. Theories suggest this is due to trapped fast electrons in the SOL or enhanced fast electron confinement near the plasma X-point[1].The divertor has some effect in generating high energy bremsstrahlung, which is likely caused by the interaction of the edge with a fast electron population.

These results highlight the edge plasma's significance in using LHCD for future experiments. Experiments on other tokamaks have measured fast electron losses near the strike point of diverted plasmas[6]. These electrons' diffusion will lead to fast-electrons in the SOL, which could impact the heat flux and change the divertor's power-handling characteristics. This edge loss could be important for future tokamaks which use low field side launched LHCD, as they are likely to have significant edge fast electron populations due to high edge electron temperatures[7]. Alcator C-Mod is suited to investigate this effect and its implications for future steady-state devices.

This chapter estimates the edge fast electron losses in Alcator C-Mod through measurements of thick-target bremsstrahlung. A new plasma shape was developed to see the inner strike point with the Hard X-ray Camera (HXR) allowing quantification of the thick-target bremsstrahlung. `Win X-ray`, an electron-microscope analysis code, is used to estimate the fast electron flux from this measure of thick-target bremsstrahlung[8]. The strike point X-ray intensity was found to decrease as current drive efficiency decreased (*e.g.* with increasing $\bar{n}_e$). This analysis proves that loss of current drive efficiency is

Figure 5.1: Significant X-ray emission can be observed from the plasma near the active divertor in diverted discharges. This asymmetry, measured by the Alcator C-Mod hard X-ray camera[5], can exceed the core measured brightness. The separatrix is shown, with an overlay of the chord views. The brightness of each viewing chord is shown at the Z location of the chord at the inner wall, with the color of the profile matching to the LCFS color of the plasma. For shot 1101104012, the hard X-ray brightness profile is shown at 1.1s, and at .758s for 1080312016. Both of the shown discharges are in forward field, which can affect the observation of thick-target bremsstrahlung from the inner wall.
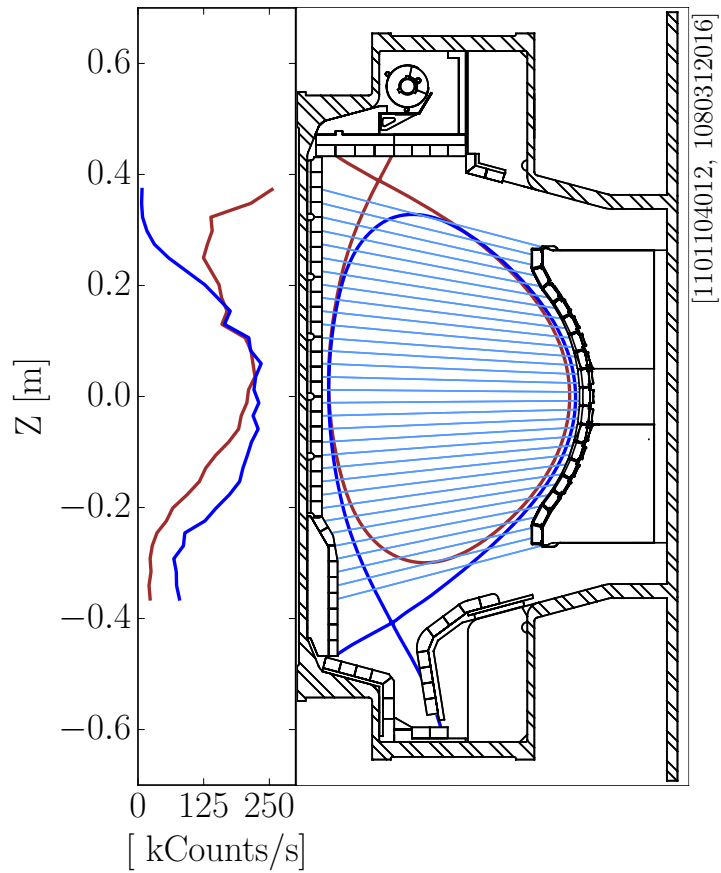
not caused by edge fast electron losses. Additionally, this chapter describes a framework for determining the importance and subsequent impact of fast-electrons from LHCD in the SOL.

IMPACT OF FAST-ELECTRONS ON THE EDGE PLASMA

Model of edge fast-electron losses

The radial profiles of electron temperature and density strongly influence wave damping in the plasma. The wave's upshift evolution is set by the initial condition of the location and $n_\parallel$ at launch. This sets the influence of the temperature, density, and magnetic field on the propagation of the wave and dictates the nature of absorption. Current devices contain temperature profiles which lend to upshift and damping near mid-radius when launched from the outer midplane. However, the electron temperatures on many current tokamaks are low in comparison to those expected for steady state fusion reactors.

Future devices will likely have significant edge pedestal electron temperatures leading to electron Landau damping near the edge. Estimates for ITER find the pedestal to be nearly 5keV, greater than many peak core temperatures in Alcator C-Mod[9]. Some reactor designs include pedestals upwards of 8keV with significant densities possibly

limiting accessibility. The necessary upshift required is minimal when launching from the low-field side, allowing for current drive to occur near the edge at $\rho \sim .9$[7]. Understanding the effect of fast electrons generated and confined so close to the LCFS could be necessary for future tokamaks.

While the deposition location may be different, the non-thermal electron population of electrons for these devices will follow the same physical effects as those observed on current tokamaks. Analysis of core fast-electrons in C-Mod and other tokamaks can be used to describe the dynamics of the fast-electrons near the edge in C-Mod and predict dynamics in future devices. These electrons' low collisionality will also be observed at the expected densities and temperatures. This suggests convection and diffusion can describe the transport of fast electrons.

The fast electron population (at a density given by n_f) can be described with a convective-diffusive equation with a slowing-down loss term as described in 5.1.

$$\frac{\partial n}{\partial t} = \nabla \cdot (D \nabla n) - \nabla \cdot (\vec{v} n) - \frac{n}{\tau_s} + S \qquad (5.1)$$

For steady state plasmas with minimal convection ($|\vec{v}| = 0$), the equation can be nondimensionalized. Assuming a tokamak plasma with minor radius of a (characteristic length scale), the combination of a,D and τ_s combine to the nondimensional parameter $\zeta = \frac{a}{\sqrt{\tau_s D}}$. This requires characterizing the slowing down time τ_s and diffusion coefficient D for fast electrons. The values for D and τ_s have been experimentally and theoretically treated for electrons with energy greater than 20 keV. ζ for current and future tokamaks can be estimated from these values.

The slowing-down time τ_s (the time for the fast-electron to thermalize) depends on the background electron density and velocity[10]. As shown in figure 5.2, the slowing down time for ~ 100keV electrons is in the range of 3ms for densities near $1 \cdot 10^{20}$ [m^{-3}]. Future reactors will have significant edge densities with edge conditions similar to the core of Alcator C-Mod. The experimental values of τ_s and D observed on C-Mod can be extrapolated for future devices. Theoretical predictions are also similar to experimentally determined values observed on C-Mod and elsewhere. These results find that most tokamaks will have fast-electron slowdown times on the order of milliseconds.

While the value of the diffusion coefficient D has been characterized on a number of tokamaks, its actual value is more ambiguous. Previous work on Alcator C-Mod has found the diffusivity of fast electrons to be in the range of $.005 - .01$ m^{2}s^{-1}. Other C-Mod thesis work found higher diffusivities were needed to properly match

Figure 5.2: Theoretical prediction of the fast-electron slowdown time τ_s as a function of electron energy and background density [10]. Contour labels are in milliseconds, showing that for most tokamaks that the slowdown time is on the order of 1-10ms.
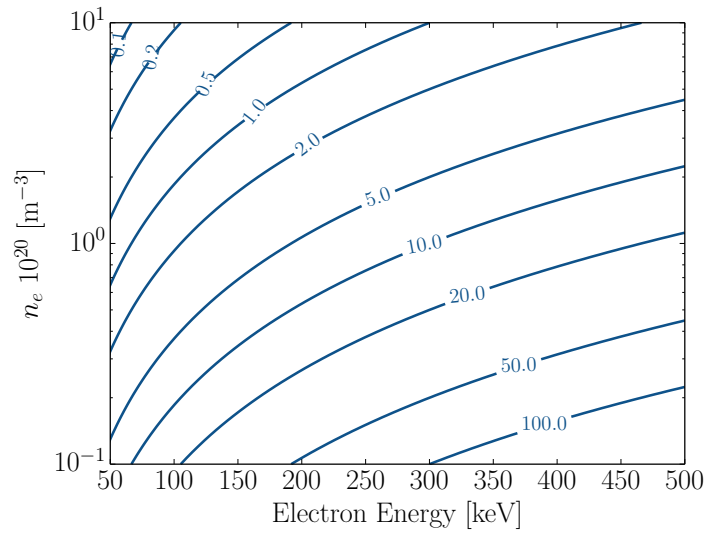
hard X-ray brightness profiles[1]. However, other authors consider this procedure to be possibly misleading [11]. A wide range of expected values for D have been observed experimentally, giving some freedom in numerical modeling. Because dependencies of D on other parameters have not been well-characterized, it is the largest source of variability in ζ.

$$n = \nabla_\rho \cdot \left(\frac{1}{\zeta^2} \nabla_\rho n \right) + S\tau_s \tag{5.2}$$

Equation 5.2 assumes τ_s is invariant across the profile. When integrated across the plasma volume V, this equation can be used to understand the sources and sinks of the Lower Hybrid power. For a source S and surface area A, the fraction of the source particles lost to the SOL can be defined as the parameter f_L. f_L can be related to theoretical treatment of fast-electron diffusive losses described by a fast-electron confinement time τ_D detailed in Chapter 1.

$$f_L = \left(1 - \zeta^2 \frac{\int_V n dV}{\int_A \frac{\partial n}{\partial \rho}\big|_{\rho=1} dA} \right)^{-1} \approx \left(1 + \frac{\tau_D}{\tau_s} \right)^{-1} \tag{5.3}$$

This model can characterize the edge particle loss of fast electrons. Fast electrons are a necessary but not sufficient condition for current drive, and their edge loss is representative of inefficiency in current drive. In the case that the current per particle and current drive efficiency are known, this can be converted into a power fraction. The particle edge loss fraction and the power edge loss fraction are both derived from f_L. The parameters of C-Mod and ITER are used in a cylindrical model with a δ-function source at radius ρ.

Table 5.1: Projected SOL fast-electron loss fraction for current and future tokamaks for a given a, τ_s and D. The model assumes source is represented by a δ-function at prescribed ρ in cylindrical coordinates. *Note:* except for C-Mod all other tokamak values are projected.

Tokamak	τ_s [ms]	D [m^{2}s^{-1}]	ζ	$f_L(\rho = .8)$	$f_L(\rho = .95)$
C-Mod[4]	3	.005	56.8	$1.04 \cdot 10^{-5}$	.057
EAST[12]	5	.8	8.54	.162	.636
EAST[13]	10	.3	9.86	.124	.596
ITER	5	.005	400.	$< 10^{-8}$	$< 10^{-8}$
ITER ramp-up [14]	5	1.0	28.2	.00318	.238

Figure 5.3: Contour plot of the particle edge loss fraction as a function of the deposition location and ζ (the non-dimensional diffusion slowing down number) using a cylindrical representation. The lack of definitive numbers for the diffusion coefficient for many tokamaks [11] leaves ambiguity in projected values of ζ. Future devices are likely to have 1% to 10% of particles to be lost via the SOL when deposition occurs near ρ of .9 to .95. However, this model does not include likely scalings of D with $|\vec{B}|$ or I_p that other results suggest [4].
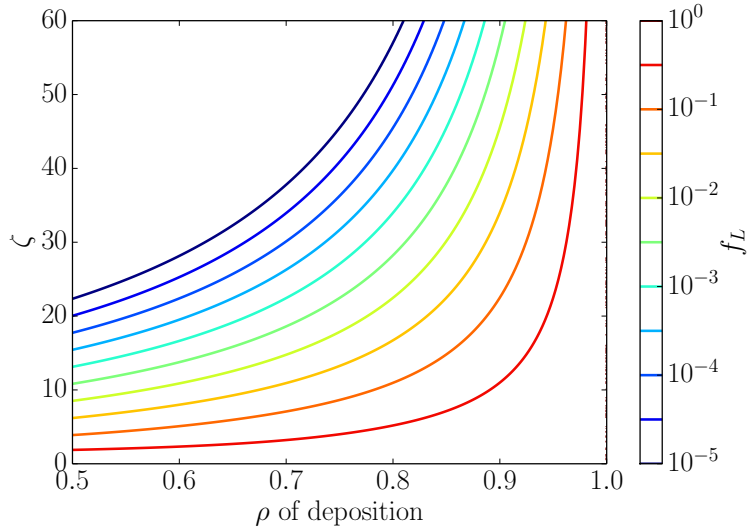
This model predicts that the loss of fast-electrons to the SOL on Alcator C-Mod is insignificant for LHCD deposition with $\rho < .9$ as Landau damping strongly factors high temperature regions of the plasma. Most Lower Hybrid deposition models find the majority of power is deposited for $\rho < .9$. The generated current is roughly proportional to the fast-electron population, suggesting a minimal impact on current drive efficiency. The edge plasma's fast response to LHCD power requires that the damping of LH wave power occur near the edge. The significant power loss to edge loss on Alcator C-Mod also requires significant damping for $\rho > .95$. Characterizing the population of fast-electrons in the SOL can determine the importance of SOL diffusive loss on the current drive efficiency.

For devices such as ITER, edge losses require damping at the very periphery ($\rho > .99$) in order to be important. The large minor radii of these devices significantly increases the distance necessary to reach open field lines. As is shown through the projected ITER values, the substantial size necessary for tokamak reactors makes this analysis unnecessary. However, this analysis assumes that the diffusivity is similar to the measured C-Mod values. Better projections for values

of D (solving for the dependencies on B, $\bar{n}_e$, aspect ratio, etc.) would substantially improve confidence in this expectation.

LHCD systems on current devices which lead to significant deposition at $\rho \sim .9$ could lose a sizable fraction of fast electrons into the SOL. When these electrons make it into the SOL they can affect the particle and power balance. This edge loss will impact the current drive efficiency and will also have an associated effect on divertor-conducted power. Devices with high edge electron temperatures increase the likelihood of this possibility.

Interaction of fast electrons with the SOL

Future tokamaks require the use of detachment to minimize heat flux to the divertor surfaces[15]. The neutral barrier sustained by recombination and high collisionality dissipate the energy to the larger inner surface of the tokamak via isotropic radiation. However, this is only effective for particles which favorably interact with the cold plasma and neutrals located in the divertor. For fast-electrons, the detachment efficacy for reducing the flux depends on their characteristic strength of interaction with neutrals and the SOL plasma. It is particularly important to characterize these effects in cases for LHCD with significant edge losses.

The high efficiency of LHCD is partly due to the low collisionality exhibited by high-energy electrons. This counters the very low temperatures and subsequent high collisionalities expected in a detached divertor plasma. The slowing-down time for fast electrons (shown in figure 5.2) is much longer than the residence time in the SOL. Only in circumstances with nearly full perpendicular motion ($\mu < 10^{-3}$) does the electron sufficiently reside in the SOL. This analysis does not take into account variation in the magnetic field which leads to particle trapping. The plasma in the SOL does not significantly interact with the passing fast population, and the plasma does not impede their travel to the target.

Fast electrons will freely travel to the divertor plates leading to possible changes in the sheath (in attached plasmas). Previous theoretical calculations of this effect on the sheath used a model of a secondary Maxwellian with higher T_e. With sufficient fast electron fractions, the secondary electron distribution was found to dramatically influence the floating potential, heat flux, and particle fluxes to the target[2, 3, 16]. However, the fast particles from LHCD are not very Maxwellian in nature and often are limited to velocities greater than $3v_{th}$. The high energy (> 10 keV) LHCD electrons can only be blocked by extremely high sheath potentials which typically only shield out low energy thermal electrons. The secondary Maxwellian still is concentrated at a low-energy bulk blocked by the sheath potential. The paradigm of this model is insufficient to describe the scenario of edge

Figure 5.4: The length of time for an electron to travel 100m is shown as a function of the pitch angle μ and electron energy. The residence time is shown for μ of 1, .1, .01, and .001. In nearly all circumstances (for $\mu > 10^{-3}$) the residence time is shorter than the slowdown time (given in figure 5.2). Passing fast-electrons generated by LHCD (*i.e.* $\mu > .1$) are unlikely to interact with the plasma before hitting a solid surface while in the SOL. This analysis does not include the impact of trapping, which will increase residence times when $\mu \sim 0$.
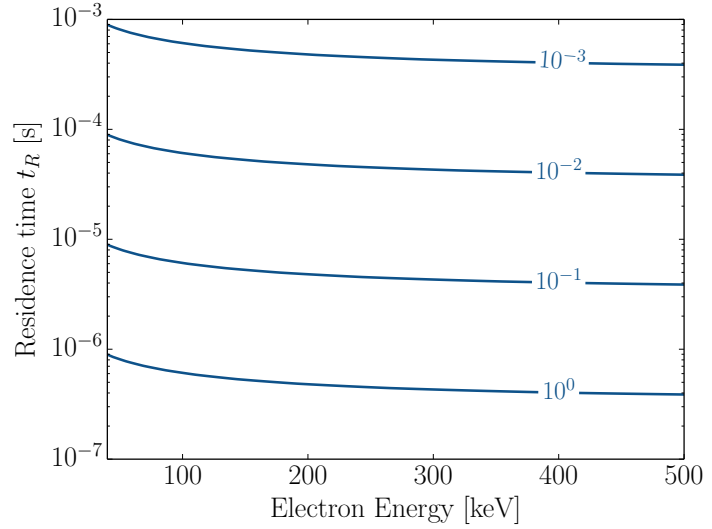
loss fast electrons, given the unrealistic characteristics that could possibly be observed.

The impact of a small, nearly isothermal, high-energy fast electron flow can better represent LHCD electrons' effect on the sheath. An electron population with density n_{efs} at the sheath edge will lead to a density through the sheath described in equation 5.4. Unlike thermal electrons or cold ions which rarefy when close to a solid surface, the sheath slightly slows the fast electrons, thus densifying them. This densification depends on the initial energy at the sheath entrance E; the potential of the sheath V varies from the value at the sheath entrance V_s. The sheath potential and the effect of fast electrons is shown in the previous chapter in figure 4.18. The change in potential from the core plasma to the sheath entrance is small compared to the electron energy, or the approximate energy leaving the confined plasma.

$$n_{ef} = n_{efs}\sqrt{\frac{E}{E - e(V_s - V)}} = n_e f_n \sqrt{\frac{E}{E - e(V_s - V)}} \qquad (5.4)$$

When this fast-electron distribution is combined into Poisson's equation and Taylor expanded about the sheath entrance, a new Bohm criterion can be derived. This solution can be parameterized using the same nomenclature describing in the two-Maxwellian solution given in chapter 4. The fast electron density and energy are given as ratios to the slow population f_n and f_t. A single-energy source which is greater than the sheath potential yields $f_t = -2E/T_e$; this value is used in the sound speed given in equation 4.1. However, fT_e must be positive for a physically meaningful solution. The negative value of f_t comes from the slowing of the fast electrons, but f still remains positive for the values expected in tokamak sheaths ($f_n \ll |f_t|$).

The correction to f (defined in equation 4.2) for $f_t = 10^3, f_n = 10^{-3}$ is .1%, and for most circumstances f is proportional to $1 + f_n$ ($f_t/f_n \gg 1$). Sheath potential is still dictated by the low velocity components of the ion and electron distributions. High-energy electrons minimally impact the sheath, and the sheath changes them insignificantly in turn. Variation in the divertors particle and energy fluxes will be subtle with the addition of fast electrons in the target plasma.

Ambipolar diffusion dictates that the increase in electron flux due to fast electrons will lead to an increase in ion flux. Due to minimal changes in the sheath, this increase in electron flux is balanced by a higher collected ion density. The equation 5.5 gives the change in the floating potential due to fast electrons in cases with the same ion flux and electron temperatures. The change in floating potential ΔV_{fl} will be negative in circumstances with populations of fast electrons.

$$\frac{e\Delta V_{fl}}{T_e} = \ln\left((1+f_n)(1-\frac{|j_f|}{|j_{sat}|})\right) \approx f_n - \frac{|j_f|}{|j_{sat}|} = f_n\left(1 - \frac{2\sqrt{2}}{1+f_n}\sqrt{\frac{m_i}{m_e}}\sqrt{\frac{E}{T_i+T_e}}\right)$$

(5.5)

The addition of high energy electrons is expected to yield minimal changes in the sheath and the thermal electron distribution. However, noticeable changes to the floating potential are possible depending on the flux of fast electrons. The inability for either the sheath or plasma to affect the fast electrons derives from their high energy. This lack of interaction will lead to divertor power measurements to be underestimated by typical Langmuir probes.

In an attached regime, LHCD fast electrons flow through the SOL and impact the divertor. The high energy of each particle means a much smaller particle flux is necessary to generate similar heat fluxes to the thermal plasma. While the thermal heat conduction to the divertor has been mitigated experimentally through the use of detachment, the utility of detachment for fast electrons must be evaluated. Detachment depends on ion-neutral friction and radiative power loss which controls the ion flux. The electron flux is controlled via the combined influence of low temperature and ambipolar diffusion. The small fraction of high energy electrons is unaffected by the sheath or background plasma. For detachment to be effective for these electrons, they must be favorably controlled by electron-neutral collisions.

This process can be understood by comparing the cross-sections for interaction at high energies. In MARFE conditions (similar to detachment), measures of the neutral density are nearly 10^{17} to 10^{18} m^{-3}. The mean free path ($\lambda_{mfp} = (n\sigma)^{-1}$) for fast electrons ($> 1$keV) is greater than 100m. As shown in figure 5.5, the observed cross-sections are below 10^{-19} m^2 across the entire energy range. The interaction dis-

tance is much greater than the field line length through the divertor in most tokamaks.

Figure 5.5: The interaction of fast-electrons with the background neutrals are minimal. The trends in the total collision cross-section for electron impact on molecular Hydrogen[17], ionization cross section for atomic Hydrogen[18] and the electron excitation from the ground state of atomic Hydrogen[19] show that there is likely two orders of magnitude decrease in the cross section at energies > 10 keV. For neutral densities of 10^{20} [m^{-3}], the mean free path is likely > 50 m for electrons with energies above 10 keV.
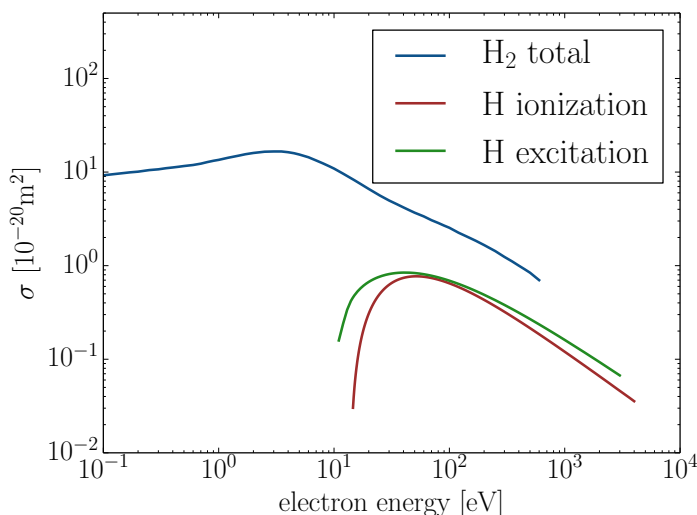
This fast electron-neutral interaction length has been observed experimentally with pellet injection and LHCD[20]. Cyrogenic pellets injected during the application of LHCD observed a rapid degradation in the pellet penetration depth. This weak penetration was due not to the overall additional heat flux provided by the fast electrons, but due to volumetric heating of the pellet by the fast electrons. This effect underscores the weak interaction of these high-energy electrons with neutrals as volumetric heating can only come from long mean-free-path interactions. This experimentally verifies the theoretical impossibility of reducing heat flux through fast electron-neutral interactions.

The fast electrons which escape into the SOL cannot be stopped by the plasma or neutrals located in the edge. The vast majority of this energy will be deposited in the divertor close to the strike point. A small particle flux can deposit significant power due to the high energy per particle of the LHCD fast electrons. However, this effect is significant only when deposition is near the edge with certain diffusion and slowing characteristics. While edge loss effects for future tokamaks are more likely due to higher edge electron temperatures, the larger physical size reduces this possibility.

The previous theoretical analysis suggests that edge losses of fast-electrons are minimal and unimportant for C-Mod and future devices for affecting the thermal plasma of the edge and divertor. However, the experimental characterization of fast-electron edge losses will prove the thermal or epithermal nature of the LHCD edge loss on Alcator C-Mod. This effect cannot be measured with typical edge diagnostics as previously shown by the impact on the sheath, SOL plasma, and neutrals. Through the measure of high energy X-rays generated by thick-target bremsstrahlung, it is possible to character-

ize this loss mechanism. The trend in SOL thick-target bremsstrahlung versus current drive efficiency dictates the importance of fast electron edge loss in the LHCD density limit.

DETERMINATION OF ELECTRON FLUXES FROM THICK-TARGET BREMSSTRAHLUNG

Observation of thick-target bremsstrahlung in tokamaks

The photons generated by the acceleration of electrons (usually due to collisions with other charge particles) is known as bremsstrahlung. Theoretical treatments given by Bethe-Heitler-Elwert[21, 22] formula (for electron-ion collisions) and Haug formula[23] (for electron-electron collisions) describe the emitted photons' anisotropic energy spectrum and cross section probability. These formulas have been used to forward-model the emission of hard X-rays for optically thin media such as tokamak plasmas.

The complicated expressions of bremsstrahlung emission can be reduced to several simple conclusions. First, energy conservation dictates that only high energy electrons are capable of inducing hard X-rays in tokamaks. Hard X-ray bremsstrahlung in tokamaks is indicative of high energy electrons which in turn describes the effects of LHCD. The hard X-ray emission can be used as a proxy for the fast-electrons.

Secondly, the intensity of bremsstrahlung is proportional to the electron population and the background ion density. The significantly higher number densities of solids (10^{28} [m^{-3}] for molybdenum versus 10^{20} [m^{-3}] for tokamak plasmas) causes bremsstrahlung emission from solids to be orders of magnitude higher for the same electron population. The high Z of molybdenum and other metallic wall materials are highly efficient in X-ray generation (in comparison to Deuterium). While the emission spectrum is broad for monoenergetic electron beams, the intensity can give an electron population estimate. Smaller electron populations can be observed in higher density materials (for the same flux), making hard X-ray bremsstrahlung from solids a much more sensitive indicator of fast electrons.

However, due to various factors, the interaction of fast electrons with solids is more complicated. For one, the emitted bremsstrahlung X-rays can be attenuated by the high-density material of the solid. The high probability of multiple scattering events for a single electron can lead to electron's diffusive movement in the solid. Along with bremsstrahlung, collisions of high energy particles with high Z atoms can excite electrons, emitting characteristic high energy X-rays at specific energies. Combined, these aspects lead to a large, high-probability, complicated phenomenon which can be observed in the cameras used to measure the core plasma bremsstrahlung emission.
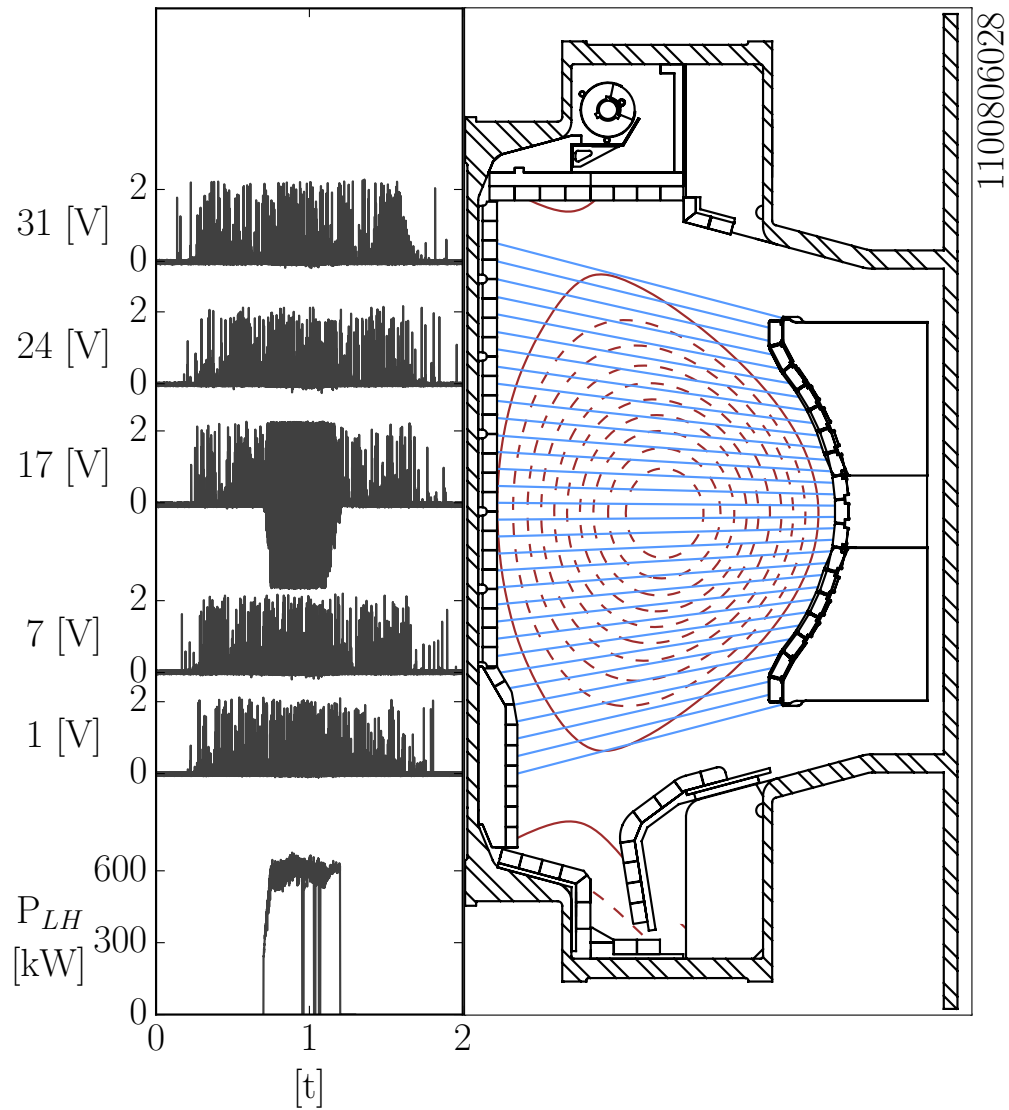
Figure 5.6: Inner wall limited plasmas with LHCD often impact the operation of the HXR camera. Shown on left are several raw pulse voltage time traces placed vertically close to the viewing sightline vertical position (Channels 1,7,17,24, and 31). Each vertical line is a representative pulse, which comes off of a baseline value (near 0 Volts). This data is converted into count rates off of the measured pulses. The count rate increases during LHCD (power trace shown at the bottom-left). Measurements near the limiting point (shown by channel 17) shows 'blindness' during the LH pulse due to extremely high X-ray fluxes. This causes the baseline to move to very large negative voltages and removes the ability to discern pulses. Other chords near the limiting point face similar issues (channels 14-19). This effect is due to fast electron escaping into the SOL and creating thick-target bremsstrahlung through collisions with the Molybdenum wall.

The bremsstrahlung from solids is generally known as thick-target bremsstrahlung due to the solid's strong stopping power for electrons. This phenomenon occurs in tokamaks when fast electrons interact with solid materials at the plasma edge. The Molybdenum Alcator C-Mod first wall is an ideal material for inducing thick-target bremsstrahlung due to its high density and high Z. The effect has

been observed on Alcator C-Mod in the use of LHCD in inner-wall-limited plasmas.

Thick-target bremsstrahlung easily propagates through the plasma and can be observed with X-ray cameras designed for observing the bremsstrahlung emission from the core plasma. The Alcator C-Mod hard X-ray (HXR) camera[5] integrates the X-ray emission along 32 chords through the plasma and terminates on the inner wall. Thick-target bremsstrahlung can overwhelm Alcator C-Mod hard X-ray camera (HXR) central channels in inner-wall-limited plasmas (where the plasma intercepts the inner wall near the midplane), as shown by figure 5.6. This experimental result shows that the hard X-ray emission from thick-target effects can be more significant than plasma bremsstrahlung. Indeed, LHCD-induced thick-target bremsstrahlung can saturate measurements of core fast electrons.

Detectors are blinded for chords which view near the strike point due to the additional thick-target bremsstrahlung. The utility of the HXR for cases in inner wall limited discharges is limited to the regions outside the central core of the plasma. Similar effects have been observed on other tokamaks like Tore Supra and JT-60U near the inner wall limiting point and strike-point respectively. However, thick-target bremsstrahlung was rarely observed in those tokamaks, thus minimally changing their HXR cameras utility but highlighting the existence of fast electrons in other tokamaks' edges.

The interaction of unconfined fast electrons with solids is significant on the Alcator C-Mod in cases with current drive. The saturation of the HXR camera suggests a measurable diffusion of fast-electrons to the occurring in all IWL plasmas; this could also be important in diverted topologies. The inner wall emission can be used to understand SOL fast electrons. Procedures used for forward-modeling the bremsstrahlung emission can be inverted to roughly deduce the character of the unconfined fast electrons in the SOL. This capability can determine diffusive loss's significance to the current drive efficiency loss in high density diverted plasmas on Alcator C-Mod.

Win X-ray and pinhole optics for thick-target bremsstrahlung

The interplay of attenuation and electron scattering by solids can alter the thick-target bremsstrahlung X-ray spectrum. X-rays emitted in the solid are exponentially attenuated to fractions described by the material's stopping power and the emission depth. The scattering of electrons in the solid is a random process leading to the depth of emission, energy and associated attenuation of the photon to also be random. Unlike plasma bremsstrahlung which occurs in single independent electron encounters, several photons can be emitted from multiple related collisions in solids. The serial dependence of pho-

ton emission prevents the first principles calculation of thick-target bremsstrahlung spectra, requiring the use of numerical modeling.

Electron scanning microscopes also observe high-energy electrons impinging on solid surfaces. A program named `Win X-ray`[8] models electron impact effects on solids in these devices. It uses a Monte-Carlo procedure to model electron collisions and the associated X-ray emissivity while the attenuation of the X-rays is determined analytically. The measured X-rays can be generated from bremsstrahlung and atomic excitation. The ensemble of individual representative X-rays are combined to generate the expected X-ray spectrum for large sample sizes.

Figure 5.7: 200 trajectories of 60 keV electrons simulated with the `Win X-ray` code in solid molybdenum. Red trajectories represent electrons which reflect out of the solid where blue trajectories fully deposit energy within the material. Significant variation in the paths highlight the high number of collisions for each electron in the first 10μm of the material.
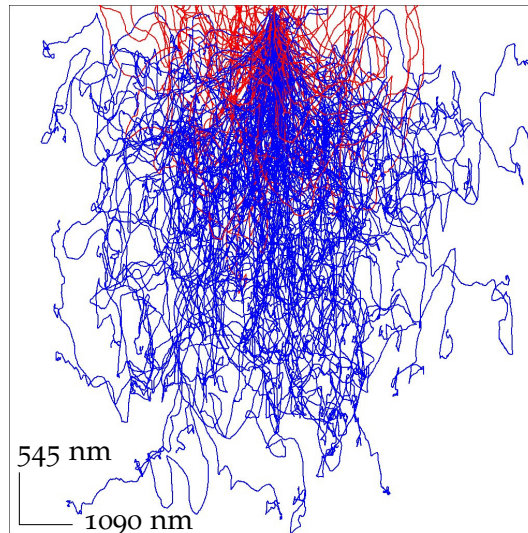
The emission spectrum determined from `Win X-ray` is defined as $C(E, I_B, \Omega | E_i, \hat{r}, \hat{r}')$. It is a function of several parameters, the foremost being the initial electron energy E_i, beam current I_B, and the solid angle of the detector Ω. The beam incidence direction $\hat{r}$ and detector to beam impact direction $\hat{r}'$ also affect the spectrum but are fully specified on C-Mod. E_i is specified in `Win X-ray` as a single value which contrasts the spectrum of electron energies observed with LHCD, and must be set *a priori*.

Normalizing the spectral intensity $C(E, I_B, \Omega | E_i, \hat{r}, \hat{r}')$ to the beam current I_B determines the X-ray fluence per electron. The intensity of X-ray emission is inherently linear to I_B due to the low probability of beam electrons changing the solid or interacting with other beam electrons (*i.e.* each electron can be treated separately). The viewing geometry can be specified with an expected solid angle Ω, which can also be used to normalize the spectrum per unit steradian (assuming minimal change in $\hat{r}'$ across the measuring solid angle). Together, this

creates the important parameter $C(E|E_i, \hat{r}, \hat{r}')$ defined in equation 5.6 which converts fluences of X-rays into a total number of fast electrons.

$$C(E|E_i, \hat{r}, \hat{r}') = \frac{C(E, I_B, \Omega | E_i, \hat{r}, \hat{r}')}{I_B \Omega} \tag{5.6}$$

The *a priori* determination of E_i serves as a limitation and requires $C(E'|E_i, \hat{r}, \hat{r}')$ to be evaluated at various E_i for a number of electron energies. The range of $C(E|E_i, \hat{r}, \hat{r}')$ sets bounds to the measured electron particle and heat flux. The calculated flux at a specific energy provides an "average" response. The determined bounds will likely provide order-of-magnitude accuracy, sufficient for understanding the order-of-magnitude of fast-electron particle and heat fluxes in the Alcator C-Mod SOL.

Figure 5.8: The spectrum of X-rays ($C(E|E_i, \hat{r}, \hat{r}')$) from molybdenum for a monoenergetic beam of electrons from 20-70keV in 5keV increments. The excited X-rays from molybdenum are below the low energy threshold of the HXR. All measured HXR X-ray counts come from bremsstrahlung events, which become increasingly important with E_i, the inital electron beam energy. *K* shell X-rays do not occur for low energy (20keV) electrons, and the bremsstrahlung emission is very exponential in character.
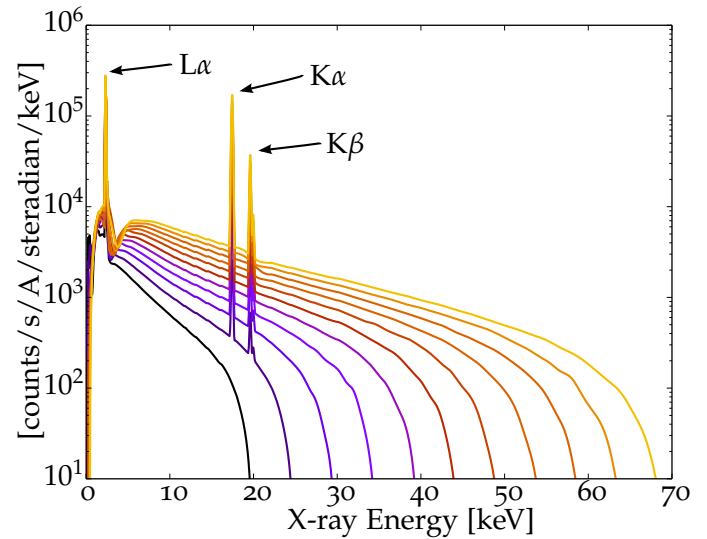
The material properties are important in dictating attenuation, scattering, and X-ray production. The first wall material on C-Mod, molybdenum, can be covered in a $< 1\mu$m thick boron layer. The boron has a low stopping power for photons with energies greater than 10keV and is very thin (a 1μm thick boron layer attenuates $< 10^{-6}$ of the X-ray intensity). Consequently, the boron has little impact on the hard X-ray emission spectrum. The solid molybdenum is a high Z, high number density, refractory metal which is a favorable target for hard X-ray emission. The simulations used to calculate the fast electron fluxes assume solid molybdenum at standard pressure and temperature.

Geometry is also important for calculating the X-ray spectrum due to the variation in electron scattering and attenuation path lengths. The different layers relative thicknesses, beam intercept angle, and detector measurement angle are all inputs to the code. Off-normal incidence of the electron beam (given by $\hat{r}$) brings the initial bremsstrahlung emission closer to the surface. This reduces the attenuation due to a

shorter path length, thereby increasing the overall intensity. The beam incidence for passing electrons is the magnetic field strike angle onto the divertor (the inner wall). $\hat{r}$ can be determined *a priori* through the use of EFIT-derived values at the strike point and can be manually set in `Win X-ray`. $\hat{r}'$ is determined from the the geometry of the HXR, which is a known and calibrated quantity. Geometric aspects of the X-ray generation in the expected spectrum are known, and accounted for.

`Win X-ray` solves for thick-target X-ray intensity through the use of Monte-Carlo methods. With the proper geometry, materials, and normalization, the data can be used to interpret measured hard X-ray intensities in terms of fast-electron currents. However, the measurement of hard X-rays in tokamaks differs from the point source emission observed in scanning electron microscopes. Instead of a thin beam measured by a large detector at a set distance, tokamaks have diffuse electrons with very defined viewing geometries (that use pinhole optics). The electrons creating X-rays on the inner wall surface must be within the detector's view and are weighted by the solid angle subtended by the detector (which varies across the view). This ambiguity is best treated by determining the average across the view, which can be properly integrated about the torus. This is possible through the use of fundamental characteristics intrinsic to pinhole optics, requiring further interpretation for understanding thick-target hard x-ray count rates.

Pinhole optics limit the volumetric view of a detector allowing for it to be parametrized as a line of sight with a small angular divergence and a small cross-sectional area. The étendue ε, as described in chapter 2, represents this angular divergence and cross-sectional area and is a constant along the line of sight. The measured count rate spectrum of detector X-rays (or intensity spectrum, $\frac{dI(E)}{dE}$) can be converted into an flux of X-rays by dividing by the étendue. The étendue determines the interplay of viewing area and solid angle, which is useful in removing the ambiguity of the size and solid angle at the inner wall. This allows for a more straight-forward interpretation of the thick-target bremsstrahlung as the flux of photons can be used to describe an average electron flux $\bar{j}_f$ within the view.

$$\bar{j}_f = \int \frac{\frac{dI(E)}{dE}}{\varepsilon C(E|E_i, \hat{r}, \hat{r}') T(E)} dE \tag{5.7}$$

Equation 5.7 shows that for an invariant spectral shape, the intensity is linearly related to the electron flux. $T(E)$ is the detector efficiency and window transmission factor, which is important for low energy (< 40 keV) X-rays. $\bar{j}_f$ will be solved for a number of E_i, from which a range of electron fluxes can be determined. The change in

Figure 5.9: The X-rays emitted inside the vacuum vessel must pass through a 1mm aluminum window to be measured with the HXR. Some fraction of the emitted X-rays are attenuated, with the probability dependent on the X-ray energy. 316L stainless steel pieces of varying thicknesses are added infront of the window as attenuators in order to reduce the HXR count rate. This reduces the measured pileup on the CdZnTe hard X-ray detectors. The non-linear filter function complicates interpretation of the observed X-ray energy spectrum. This is important in the low energies, as the X-ray spectrum is weighted to lower energies. Proper comparisons of different discharges requires the use of same thicknesses of attenuators.
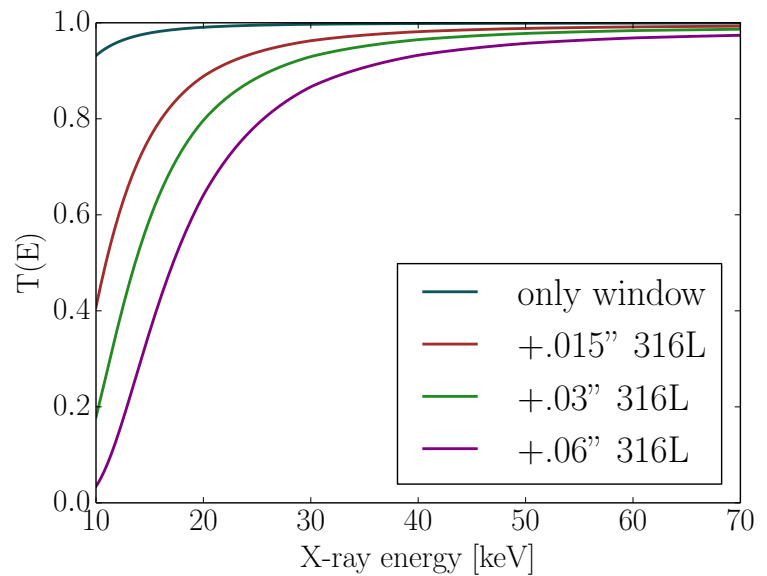
spectral shape and intensity represents changes in the fast electron population.

The combined use of `Win X-ray` and the HXR pinhole camera can determine a range of possible fast electron current densities to the wall. Both the impact on the sheath (and its ability to be observed) and the fast-electron heat flux can be estimated from this procedure. This result can inform on the accuracy of Langmuir probes in determining the density and temperatures at the target. The trends in $\bar{j}_f$ can determine the impact of fast electron edge loss on current drive loss in Alcator C-Mod.

EXPERIMENTAL SETUP

Creation of a high inner-strike-point discharge

The passing fast electrons in the SOL generated by LHCD stream along magnetic field lines without collision, leading to their impact in the divertor near the last closed flux surface. As shown in figure 5.6, the limiting point near the inner wall midplane degrades the HXR camera operation. Thick-target bremsstrahlung in Alcator C-Mod diverted plasmas can be measured when the inner strike point is in view of the Hard X-ray camera. The measurement of thick-target bremsstrahlung can then be analyzed with the previously defined analysis.

A specific diverted plasma shape was developed with a high inner strike point which could be observed with the HXR. This lower Single null (LSN) plasma was chosen due to the array of Langmuir probes located on the lower divertor inner wall. Most diverted LSN plasmas on Alcator C-Mod have the inner strike point on the inner wall's

Figure 5.10: The movement of the inner strike point was necessary for observation of thick-target bremsstrahlung with HXR. The strike point was translated upward four tiles from the common lowest-inner-wall-tile position (for LSN plasmas), shown by the red arrow. The thick-target optimized separatrix is in green, with a typical plasma separatrix shown in red (from previous LHCD modulation experiments), derived from EFIT calculations. Instrumentation available at this location (Langmuir probes, tile thermocouples) improves the characterization of heat fluxes expected from LHCD plasmas. The high strike point with regular upper triangularity was achieved with a smaller elongation ($\kappa = 1.47$ versus 1.57 with normal strike point position), and an inward movement of the X-point.
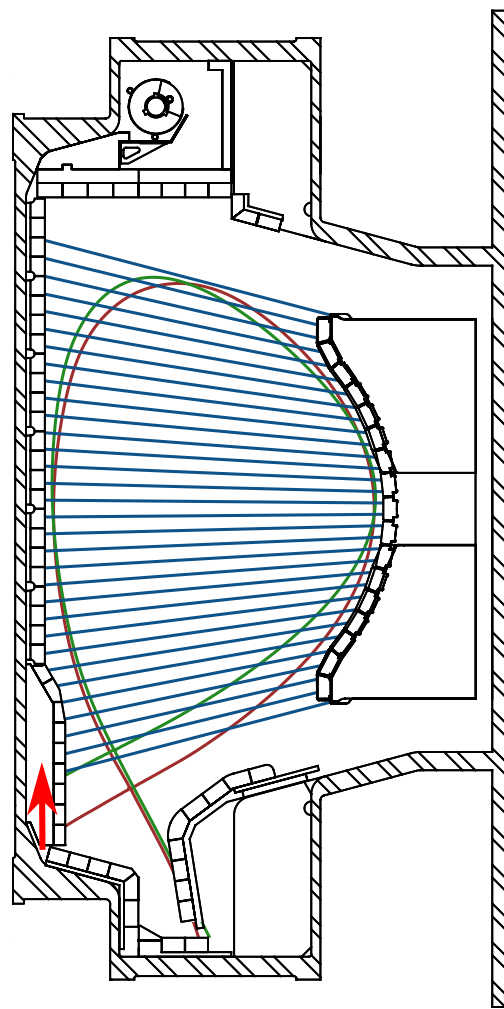
lowest tile. This location is optimal for plasma performance and for control with the poloidal field coils located nearby.

The high strike point as shown in figure 5.10 is located on the fourth tile, near control limits using the poloidal field coils. Compared to standard plasma shapes the high strike-point plasma has a reduced elongation, slight shift upward, and a slight radially inward X-point position with the inner strike point shown in detail in figure 5.11. The outer strike point is located close to the outer strike point of other LHCD modulation experiments and, as a consequence, the outer divertor leg is very long. The equilibrium used gives good measure of both the inner and outer strike points with an extensive diagnostic set matching capabilities used in other modulation experiments.

Langmuir probes[24] can determine the position of the inner strike point to a distance of half of a tile (approximately 1cm). The spot size and total view of the HXR can be seen in figure 5.12 for the developed plasma shape. Each HXR camera chord in the lower divertor measures the height of one tile as the Chord 1 views the inner strike

Figure 5.11: Position of the inner strike point provided by Langmuir probe measurements on the inner wall. This data independently verifies that the strike point location is in the expected viewing region of Chord 1. Locations of the probes are shown as circles, with the profile of density shown as an interpolated color mapped positionally to the inner wall. Limitation in the probe separation makes the strike point location known to within ~ 1cm.
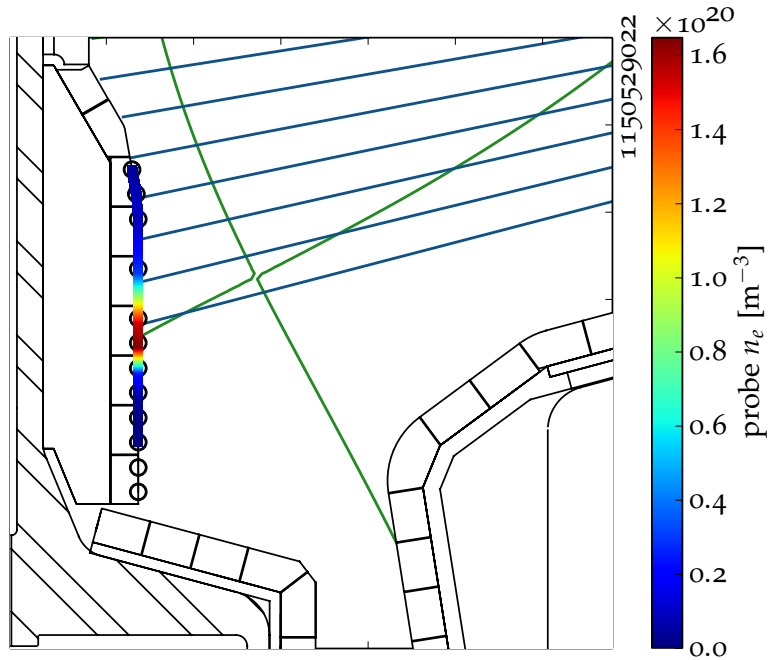
point. The comparison of the EFIT reconstruction, Langmuir probe pressure profile, and HXR thick-target emission gives confidence that the HXR observes the strike point on the fourth tile from the bottom. Chord 1 only views through the SOL of the plasma which removes any possibility of viewing confined fast electrons (unless they are deeply trapped). This allows for the core X-ray emission to be compared to the SOL thick-target emission.

The HXR camera can measure the entirety of the inner divertor plasma due to the low elongation and high X-point. Previously observed asymmetries with hard X-ray emission were only partially characterized as the extent of the asymmetry into the divertor was unknown. The contribution of thick-target bremsstrahlung on measured HXR from the active divertor can be deduced from the inner strike-point view. Chord 1 can in time separate the thick-target loss from the plasma emission and help determine the observed asymmetry's nature.

Implications of an LHCD-induced electron asymmetry on inner divertor thick-target bremsstrahlung

As a consequence of the SOL's minimal effect on fast electrons, the passing population in the SOL can be described by a single distribution. The two divertors completely absorb this population near the strike points, one divertor measuring the co-current distribution and the other the counter-current distribution. The asymmetry of the electron distribution in the core plasma which carries current will also lead to an asymmetry in the distribution of fast electrons which diffuse into the SOL. It can then be expected that an asymmetry in X-ray
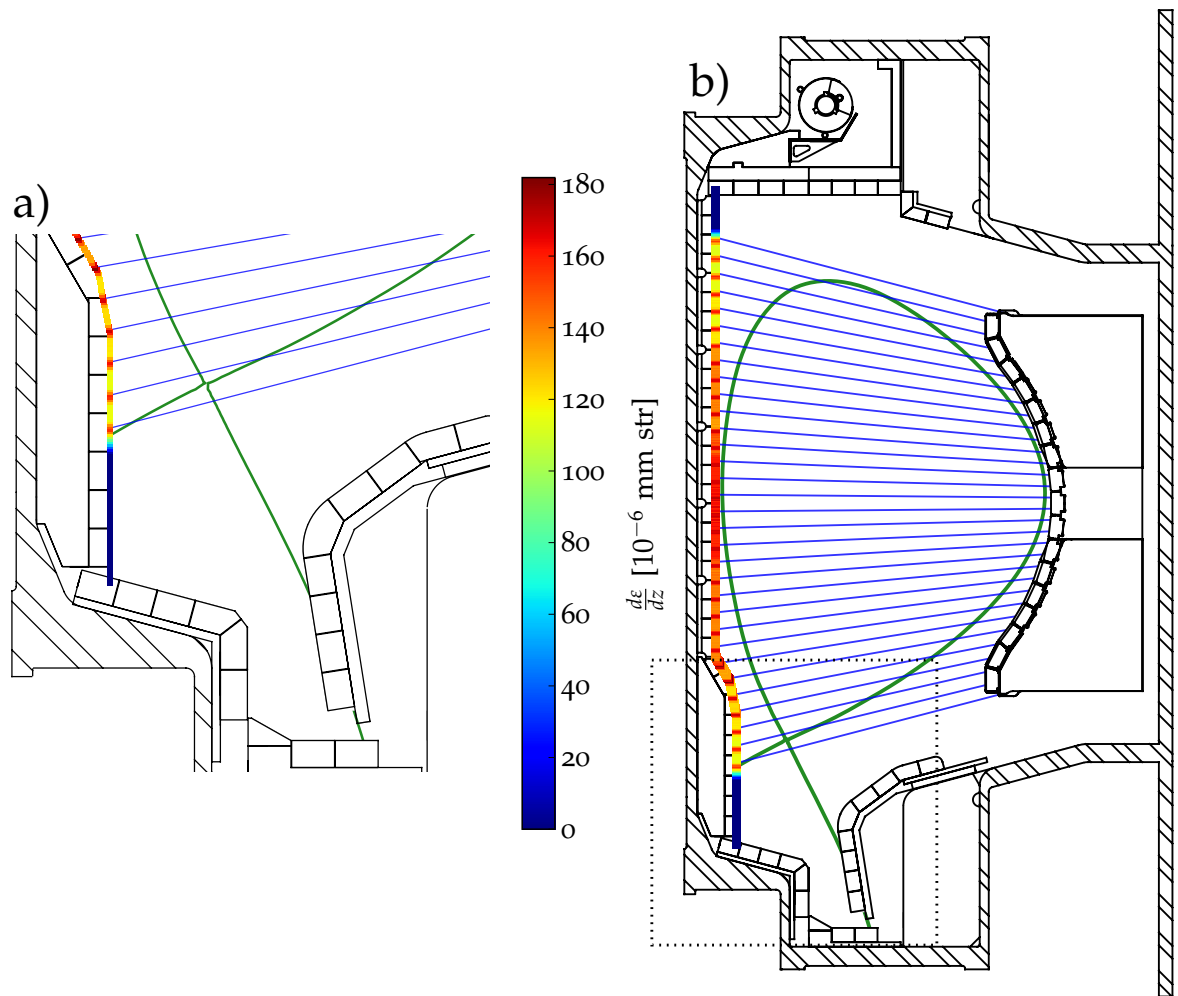
Figure 5.12: Each of the 32 chords of the HXR pinhole camera intercept the inner wall of C-Mod. Chord 1 views the lower divertor with each successive chord numbered vertically to 32 at the upper divertor. Figure a) shows the inner strike point (separatrix in green) can be observed with the chord 1 of the HXR (chords in blue). The color of the inner wall is the differential etendue (in the z direction) between the surface and diode. The profile of étendue contains a high spatial frequency component (due to the individual diodes), and a low spatial frequency component (due to the diode fan/ pinhole geometry). Figure b) highlights the wide view of the inner wall provided by the HXR. Chord 32 exclusively measures from the SOL which characterizes the bremsstrahlung from the SOL plasma. The region of figure a) is outlined on figure b) in dotted line.

production will be observed on the inner and outer divertors due to LHCD fast electrons. The measured inner strike point thick-target bremsstrahlung will only provide information on half of the SOL fast-electron population.

The inner divertor only measures the electrons which travel in one direction and depending on the current direction either measures the co- or counter-current electrons. The magnetic field's helicity and direction determines which divertor measures which portion of the passing distribution. On Alcator C-Mod, the design's physical constraints limit $\vec{B} \parallel \vec{I}_P$ leading to the inner divertor absorbing co-current electrons in reverse field and counter-current electrons in forward field (in LSN plasmas). The electron plateau formed by Lower Hy-
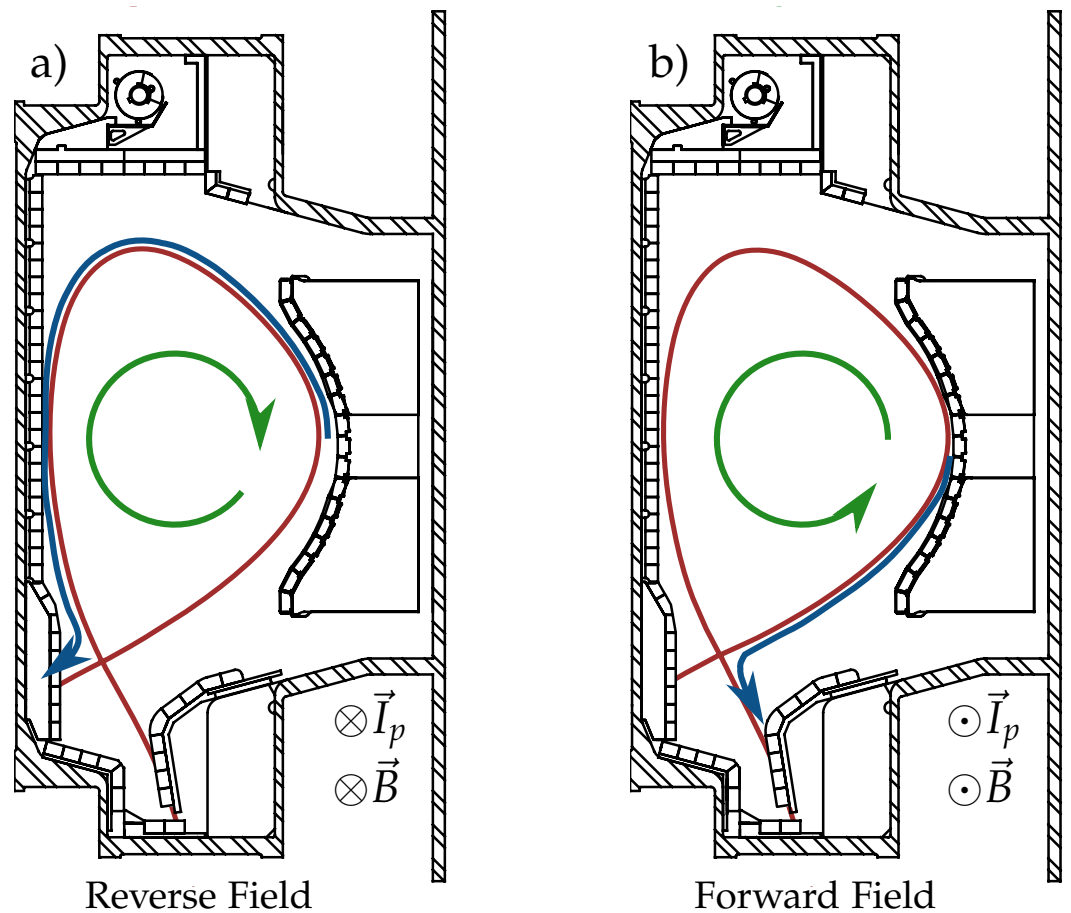
Figure 5.13: The asymmetry in fast-electrons generated by LHCD influences which divertor plate is impacted large electron fluxes. The diffusion of current-generating fast electrons will create a larger population with velocity in the direction opposite of I_p in the SOL (opposite of $\vec{B}_p$, shown in green). The helical nature of the magnetic field is the same for forward and reverse field ($\vec{B} \parallel \vec{I}_p$) by design in Alcator C-Mod. Illustrated in the figure, electrons which escape at the midplane which were generated with $\vec{v} \parallel \vec{n}_\parallel$ will have a more favored divertor (shown in blue). The electrons which are observed in the forward field inner divertor are likely generated by reverse-$n_\parallel$ Landau damping.

brid waves travels opposite of I_p, as shown in figure 5.13. Thus, a larger population of fast electrons should be expected on the outer divertor in forward field and on the inner divertor in reverse field.

In order to fully describe the population, measuring the loss of fast electrons requires using the same plasma shape in forward and reverse field. While differences in the SOL character are expected with field reversal, this does not impact the SOL fast electrons. Density and temperature changes in the core plasma (*i.e.* changes the confinement) can impact the damping of LHCD waves which in turn can change the LHCD fast electron edge losses. While this likely only plays a minor role, the SOL losses must be compared by using the core x-ray emission as the fiducial. The core emission will represent the core fast electron population and can be used to roughly observe f_L.

OBSERVATION OF FAST ELECTRONS IN THE C-MOD SOL

Hard X-ray bremsstrahlung from the core and strike point was measured using the HXR in both forward and reverse field in the FY15 campaign. In each case a range of densities was tested using multiple plasmas with the designed equilibrium and with steady densities (a process similar to the modulation scheme presented in Chapter 3). Significant hard X-ray emission was observed at the inner strike point at low densities in both field directions. The range of densities tested allowed for several conclusions about the edge loss fast-electrons to be derived.

The core emission in forward and reverse field followed previously observed trends that exhibited an exponential dependence in the HXR emission versus $\bar{n}_e$. This matched observations in many separate experiments on Alcator C-Mod (which had strong dependencies of HXR emission on I_p and $\bar{n}_e$). The modulation scheme was used to separate the effects of LHCD power from the background. Diversions from this trend in the thick-target emission define the importance of edge diffusion in the efficiency loss.

Figure 5.14: The fast electrons flowing opposite of the electron current (as measured in a forward field plasma given in figure 5.12) create significant bremsstrahlung on the inner wall. This emission is nearly 5 times greater than the peak core emission in this $\bar{n}_e \sim 9 \cdot 10^{19}$ m^{-3} plasma. Thick-target bremsstrahlung is predominantly observed near the strike point on Chord 1, with a much smaller fraction observed on Chord 2.
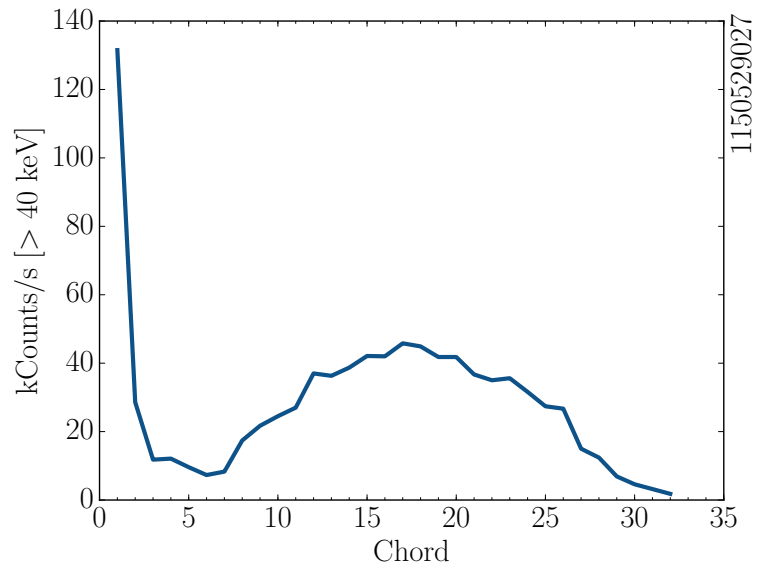
The thick-target bremsstrahlung emission from the inner strike point was in all cases greater than any other individual chord viewing the core plasma. In forward field, this edge emission was 5 times greater than the peak core emission. However, the strike point emission in reverse field was significantly more intense than in forward field. Shown in figure 5.14 and figure 5.15, the thick-target emission attributed to counter-current traveling fast electrons is significantly more intense than from co-current fast electrons. The hard X-ray count rate observed from the reverse field strike point is generally 5 to 10 times higher than the forward field strike point for the same

plasma conditions. This leads to the strike point emission to be 25 to 50 times greater than the peak core emission in reverse field.

The asymmetry in the electron distribution needed for current drive leads a larger population of counter-current traveling electrons (these electrons are the driven plasma current by LHCD). Given that a fast electron's diffusion is equally likely for those traveling co- and counter-current, it is expected that a larger number of electrons in the reverse field will diffuse into the SOL. The observed difference in thick-target bremsstrahlung for forward and reverse field validates that LHCD creates a larger number of electrons which travel opposite of the I_p direction thus creating current drive (assuming that the fast electron confinement and energy distributions are similar between field directions). This gives confidence that the hard X-rays measured on Chord 1 (the chord viewing the strike point), are dominated by thick-target emission. The HXR can be used to understand the SOL fast-electron losses and related core dynamics.

Figure 5.15: The emission of thick-target bremsstrahlung in reverse field is significantly higher compared to forward field. The ratio of peak core emission to edge emission is a factor of 10-30, which is higher than the factor of 5 observed in forward field. Limitations in the dynamic range (in count rate) of the HXR makes measuring both the core and edge emission very difficult at statistically significant levels.
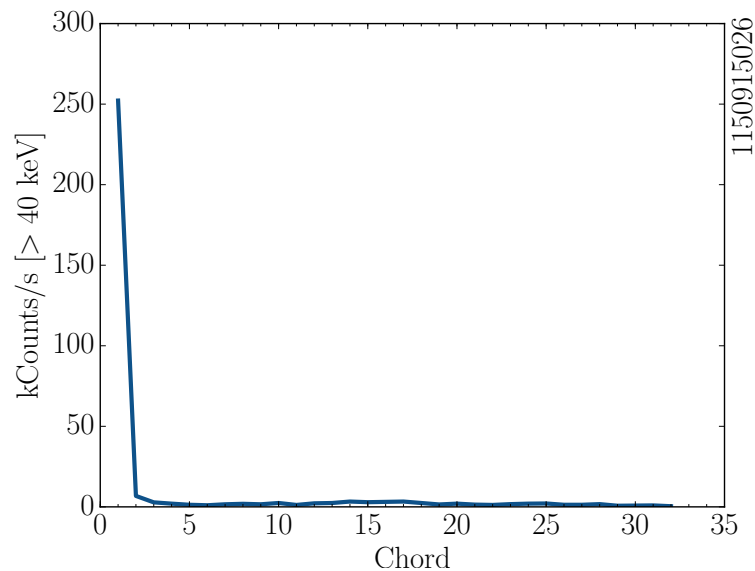
If the loss of current drive is due to an increase in edge deposition or enhanced edge diffusion, then the magnitude of thick-target emission should be correlated with current drive efficiency. The core X-ray emission is used as a proxy for the current drive efficiency and as a benchmark for trends in the strike point emission. In the extreme case that all of the current drive fast electrons diffused into the SOL, the edge HXR emission should be anti-correlated with the core emission. At the highest densities, all the fast electrons would be observed in the SOL, unable to drive current.

However, because the formation of the core plateau of electrons is a non-linear process, it is also possible that changes in the edge loss of fast-electrons would manifest in the electrons' energy distribution. Those electrons lost to edge diffusion reflect the change in the core populations. The loss of fast electrons to the edge could

shift to a different distribution as the plateau cannot be sustained in the core. Changes in the electron distribution would also modify the bremsstrahlung spectrum and would be identified as a change in the X-ray energy spectrum rather than in the X-ray count rate. Both the magnitude and spectrum of X-rays are useful in understanding electron distribution changes.

Evolution of core and edge HXR emission with $\bar{n}_e$

The significant separation between the core and edge emission in count rate pushes the HXR camera to the limitations of its design. The dynamic range of the HXR camera is set by the pile-up threshold and limits in the statistical variation. The HXR's lower limit is around $5 \cdot 10^3$ counts/s for a 1 ms time bin which leads to around 5 measured counts. The upper limit is set by the time response of the detector and pulse-shaping (which for the HXR is near $2.5 \cdot 10^5$ counts/s). This two order of magnitude dynamic range limits the span of measurable thick-target electron fluxes and can be observed in the trends versus density.

Figure 5.16: The emission of thick-target bremsstrahlung at the inner divertor strike point is proportional to the core bremsstrahlung emission across the range of current drive loss. The electrons traveling opposite of $n_\parallel$ in the SOL are observed on Chord 1 in forward field, which decrease with $\bar{n}_e$. The decreasing population of fast electrons in the SOL indicated that the impact of these electrons near the edge diminishes with increasing density. Channel 1 represents the thick target bremsstrahlung, while the sum of channels 2-32 represent the free electron bremsstrahlung.
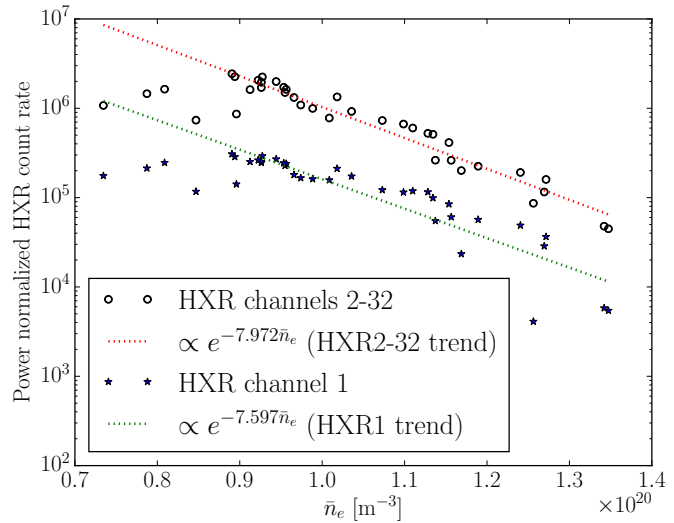
These issues led to two different experimental densities of HXR data in forward and reverse field. The reverse field data was limited to densities $> 1.0 \cdot 10^{20}$ [m^{-3}] with its significantly higher SOL/core count rate ratio. In contrast, the forward field data was measurable across the current drive range for densities $> 0.7 \cdot 10^{20}$ [m^{-3}]. While this discrepancy could be corrected with attenuators placed in front of the HXR pinhole (with varying thicknesses of 316L stainless steel), this would significantly complicate the interpretation of the diagnostic. The attenuation of photons is energy dependent, introducing an ambiguity into the HXR interpretation (which cannot be deconvolved due to detector-induced energy broadening). Changes in the energy distribution in the attenuated energy range would manifest in the

magnitude of emission. However, even with these limitations the data from these two ranges overlap slightly. This allows for a direction comparison in the density range with the greatest efficiency decrease (around $1 \cdot 10^{20}$ [m^{-3}] at 800 kA).

The reverse field data set is skewed due to limitations in available LHCD power and in the HXR dynamic range. The derived trends likely underestimate the exponential coefficient in both the core and edge. Even at minimal forward LHRF powers (300 kW) the SOL fast-electrons were capable of exceeding the pile-up count rate limit (at $1 \cdot 10^{20}$ [m^{-3}]). The low LHRF powers were insufficient to create significant core HXR emission profiles, with the trends at high density representing the lower limit on count rates. In both cases, it served to "flatten" the trends in density, and highlights the difficulty of properly measuring HXR emission from the edge and core simultaneously. However, the total core emission at $\bar{n}_e$ of $1 \cdot 10^{20}$ [m^{-3}] shows order-of-magnitude similarity in forward and reverse field. This provides confidence that the LHRF damping in both field directions is similar and thus can be compared (which matches previous experimental observations on Alcator C-Mod).

Figure 5.17: The observed X-ray count rate of thick-target bremsstrahlung is an order of magnitude greater in reversed field than in forward field shown in figure 5.17. The density range where Chord 1 properly measures count-rates of thick-target bremsstrahlung begins in the region where current drive is relatively inefficient ($\bar{n}_e = 1 \cdot 10^{20}$ [m^{-3}]). The monotonic drop in thick-target emission in reverse field is due to a smaller LHCD fast electron population in the SOL at higher densities. This suggests that edge losses are not the cause of the LHCD efficiency loss at high density. The limitations in the HXR capabilities make the comparison of core versus edge HXR emission difficult. At low density, the thick-target emission of the HXR is above the pile-up threshold. At high density, the emission of X-rays from the core is statistically insignificant (at the noise floor).
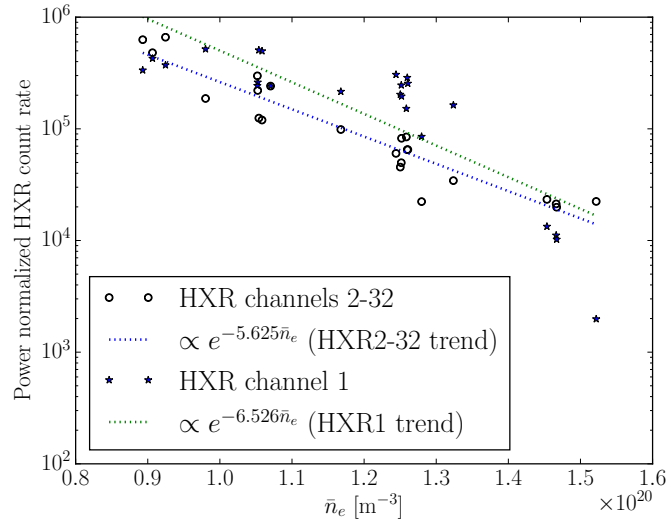
The HXR emission exponentially decreases with increasing plasma density in both forward and reverse field plasmas shown in figure 5.16 and 5.17. This exponential dependence of the measured thick-target bremsstrahlung on density matches the exponential trend in core emission. However, the rate of decrease with density is slightly weaker in comparison to the core emission. These results match those previously observed in the comparison of normalized HXR profiles on Alcator C-Mod.

However, the emission from the strike-point monotonically decreases with increasing density. The lower count rate means the electron pop-

ulation which diffuses into the SOL decreases with increasing density. A reduction in the edge emission would either come from a reduced core fast-electron population or from weaker edge diffusion. The smaller core population (exhibited by the reduction of core HXR emission) leads to the substantive change in the strike point thick-target bremsstrahlung.

This argument can be understood through the theoretical derivation of f_L. The core bremsstrahlung emission is roughly proportional to $\int_V Z_{eff} n_e n_f dV$. The thick target bremsstrahlung emission from edge fast electrons is proportional to SOL fast electron flux, which is proportional to $\int_A D \frac{\partial n_f}{\partial r}|_{r=a} dA$. Unlike the core emission, the edge emission occurs from collisions with an unchanging solid surface. The ratio of these two bremsstrahlung sources (defined as g) is similar to equation 5.3 if the following average is used (shown in equation 5.8) and the slowing down time τ_s is known. g is defined as the core bremsstrahlung emission (roughly measured on chords 2-32) divided by the thick-target inner wall emission (as measured on chord 1).

$$\langle Z_{eff} n_e \rangle = \frac{\int_V Z_{eff} n_e n_f dV}{\int_V n_f dV} \tag{5.8}$$

In order to fully define g, we define β as the ratio of necessary coefficients for absolutely calculating this ratio without n_e dependence. β varies with many parameters including the fast electron energy distribution. In this case the distribution is assumed to vary minimally across the range of density (shown by measurements of T_{ph} in figures 5.20 and 5.21), and β is assumed to be similar for low and high density. β, f_L and $\langle Z_{eff} n_e \rangle$ can then be related to g, and the change in f_L can be roughly estimated. This is defined in equation 5.9.

$$g \approx \beta \frac{\int_V Z_{eff} n_e n_f dV}{\int_A D \frac{\partial n_f}{\partial r}|_{r=a} dA} = \beta \langle Z_{eff} n_e \rangle \tau_s (f_L^{-1} - 1) \tag{5.9}$$

The change in the edge fraction from low to high density can be characterized by the respective values of g. The low density edge loss fraction is defined as f_{L1}, and the high density (no current drive) case as f_{L2}. The change in the edge loss is defined in equation 5.10.

$$\frac{f_{L1}}{f_{L2}} = 1 + (1 - f_{L1})\left(\frac{g_2 \tau_{s1} \langle Z_{eff} n_e \rangle_1}{g_1 \tau_{s2} \langle Z_{eff} n_e \rangle_2} - 1\right) \approx 1 + (1 - f_{L1})\left(\frac{g_2 Z_{eff1}}{g_1 Z_{eff2}} - 1\right) \tag{5.10}$$

For low density conditions (i.e. $\bar{n}_e < 9 \cdot 10^{19}$ [m^{-3}]), g_1 is ~ 10 in forward field, and ~ 5 in reverse field. The value of g_2 at high

density varies from ~ 3 to ~ 1.5 for forward and reverse field respectively. Shown in figure 5.18, the observed core profiles of HXR brightness changes minimally with increasing density, thus the ratio $\langle Z_{eff} n_e \rangle_1 / \langle Z_{eff} n_e \rangle_2 \approx Z_{eff1} \bar{n}_{e1} / Z_{eff2} \bar{n}_{e2}$. The ratio of $Z_{eff1}/Z_{eff2} = 1$ which is the most conservative value that can be used, though values of 2-5 are also observed. The fast-electron slowing down time scales inversely with the collision frequency which simplifies the slowing down time ratio $\tau_{s1}/\tau_{s2} \approx \bar{n}_{e2}/\bar{n}_{e1}$.

In the limit that $f_{L1} \ll 1$, the fast electron edge fraction is expected to change by less than an order of magnitude across the range of density. In the case that $f_{L1} \approx 1$, the edge loss changes minimally. The intermediate range of f_{L1} (for values greater than .1) could cause a substantial change in the edge loss thereby causing the density limit. However, the direct conduction of power to the divertor at low density is thermal in nature and is less than 20% of the LHRF power (shown in chapter 3). Theoretical expectations of f_L at low density (shown in table 5.1) do not exceed .1 for deposition inside of $\rho = .95$ which suggests that f_{L1} is less than .1.

While the relative emission (edge versus core) from thick-target bremsstrahlung increases with density, the change in the core population dominates the density dependence of the thick-target emission. The increase in the relative emission is less than an order of magnitude across the tested span in density. While the importance of thick-target emission becomes more important at higher densities, this small change is unlikely to cause the multiple order of magnitude variation in the LHCD efficiency.

Hysteresis effects on trends in HXR up/down asymmetries

As observed in the edge trends versus $\bar{n}_e$, other studies found that the active divertor emission near the X-point becomes more prominent with increasing density, becoming a factor of two to three larger (in a normalized profile) at high density. The HXR emission core profile's shape was invariant with density, except at extremely high densities where the profile was flat with nearly zero measured X-ray emission. This result was most prominent in the lower-single-null data. However, it is unclear whether this effect is due to greater emission from the core plasma or from background thick-target emission. Analysis in the high strike point plasmas implicate hysteresis effects associated with the density rise in enhancing this effect.

The asymmetry shown in previous analyses of LSN plasmas was determined from density ramps. In these cases, a 25% change in density occurred over the span of 50ms, the edge densities across this range not exceeding $1 \cdot 10^{20}$ [m^{-3}]. Theoretical slowing-down times of the electrons measured with the HXR (as shown in figure 5.2) exceeded 2 ms in all cases, and are comparable to the density rise time.

Figure 5.18: The normalized profiles of the core X-ray emission (Chords 2-32) are shown at 3 different densities. The profiles are similar (with some statistical variation) except for the strike-point viewing chord (Chord 1).The previously observed importance of the active divertor at high density is specific to the strike point (thick-target viewing). The prominence of X-rays in the periphery of other plasmas could be due to hysteresis effects of the experimental design. The density ramp of those discharges may be too fast in time to 'quench' the edge fast-electron/runaway population which can be observed as thick-target bremsstrahlung. This can distort the spatial distribution of hard X-rays.
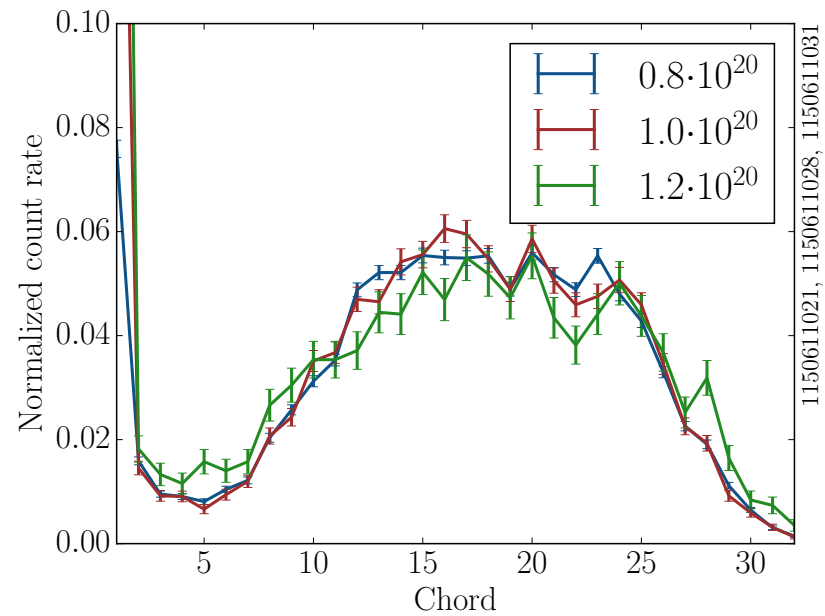

If a small population of high-energy electrons exists before the density ramp, they can still diffuse into the SOL at higher densities due to their significant slowing-down times. These electrons travel through the SOL and collide with the inner wall, resulting in an artificially enhanced asymmetry at the higher density.

Normalized HXR profiles were generated using the low-elongation shape shown in figure 5.18 in forward field (at the same plasma current). Minimal change in the asymmetry was observed across all core channels (*i.e.* all but Chord 1), shown by three different constant density plasmas. At the highest densities, low count rates caused significant variation in the profile shape (as can be observed in the increasing size of the σ error bars). The strike point thick-target emission became more prominent with higher densities (which follows the observed trends versus $\bar{n}_e$). While this data shows that the density ramp is responsible for the profile change in HXR, it does not prove that edge thick-target emission causes the increasing prominence of asymmetry.

The edge fast-electron population's hysteresis and its associated thick-target emission can be seen in low-density modulated plasmas. Shown in figure 5.19, a small amount of LHCD power (100 kW) can seed a slow change of HXR emission during the course of the plasma discharge. Superimposed on this chord is a modulation of the HXR count rate on the timescale of the modulated LH power; this is also observed, at a slightly different level, on a chord viewing the other side of the plasma. Similar to the expected hysteresis during fast density transients, the two temporally distinct features could also be caused by a normal core population of fast electrons with a small higher-energy component. The small high-energy component responds on very long timescales by minimally interacting with the low density

Figure 5.19: Bremsstrahlung near the strike point displays two different timescale effects dependent the background density and the modulating LHCD. Modulations 1,3 and 4 can be distinctly seen on the upper (Chord 30) and lower (Chord 2) views. The change in the HXR count rate is of the same order of magnitude following the modulation timescales on both chords. However, the active divertor channel observes an increasing 'background' of X-rays which trends inversely with density during the application of LHCD. This effect is more important the closer to the strike point the chord views. It is theorized that this is due to a very small population of higher energy electrons striking the divertor on field lines farther out in the SOL.
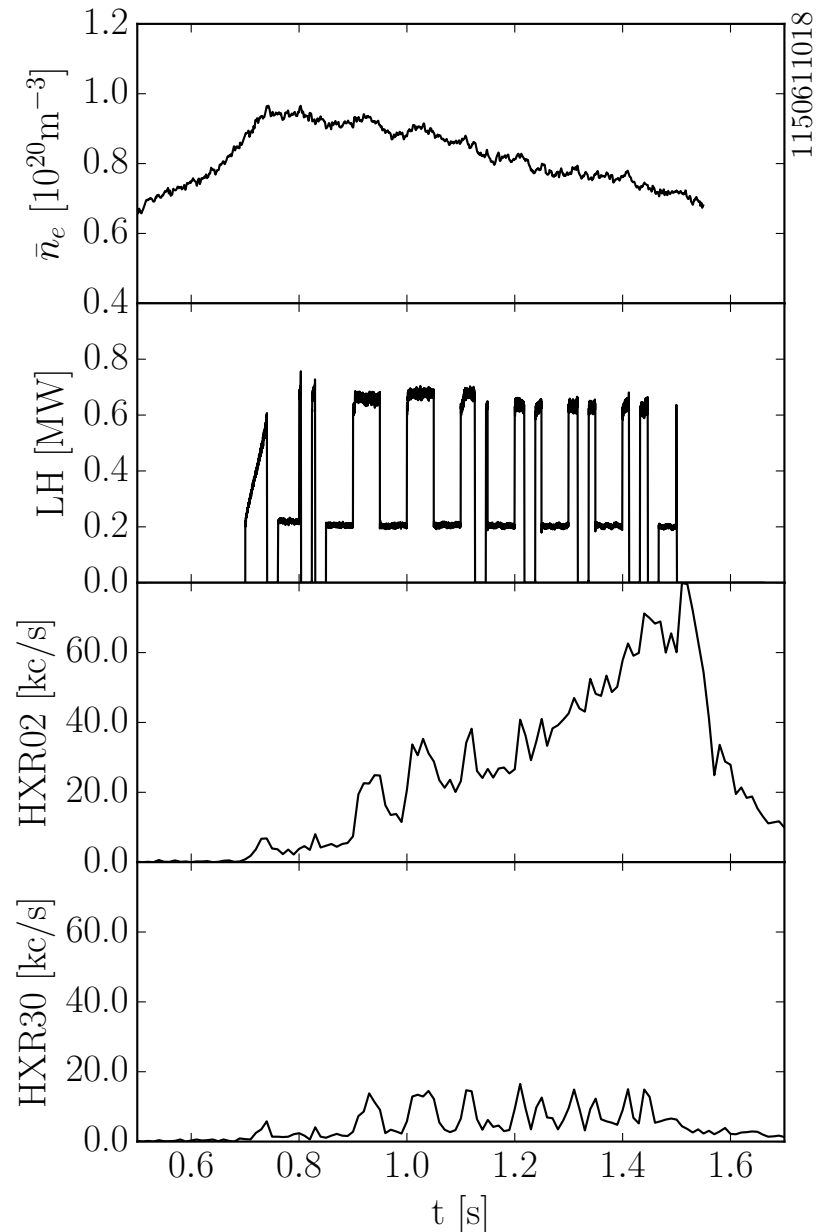
edge plasma but can be immediately observed upon collision with the divertor. The high probability of X-ray emission for thick-target bremsstrahlung can significantly weight measured profiles even in the case of small electron populations.

The initial asymmetry has been investigated using ray-tracing models. The enhanced path length through the plasma exhibited near the active X-point increases the observed chord count-rate. The asymmetry was reproduced with GENRAY/CQL3D using a full 2D conduction-limited SOL model of Alcator C-Mod.

If the electron distribution which induces thick-target bremsstrahlung is different from the core LHCD-driven electrons, the energy spectrum of emitted X-rays should also be different. Comparing the strike-

point energy spectrum with the core can hint at differences in electron distributions. Characterizing the changes in the X-ray energy spectrum provides a possible window in the energy dynamics of edge losses. The energy dynamics can confirm this theorized trend and thus help characterize the SOL's fast electron energy distribution.

Thick-target and core bremsstrahlung energy spectra

The higher count rate from reverse field thick-target bremsstrahlung can be attributed to the LHCD-induced core fast-electron asymmetry. While the electron energy distributions in each direction and their respective diffusion rates are likely to be different, the asymmetry is predominantly due to the difference in population. The energy spectrum of bremsstrahlung X-rays can test the similarity in energy distribution between forward and reverse field. In principle, the energy discrimination capability of the HXR can be used to validate this theory and characterize any energy dependencies in the edge loss.

Physical effects of the hard X-ray emission and its measurement make this characterization difficult. First, the distribution of thick-target X-ray energies (highlighted by figure 5.8) is nearly exponential for a given electron energy. This exponential's coefficient weakly varies with the initial electron energy, making it difficult to determine a spectrum of energies. Second, the detector response function leads to a significant spread in the measured X-ray energies (FWHM > 20 keV on the C-Mod HXR camera). This leads the observed X-ray spectrum to possibly be non-unique. Attempts to use this require additional assumptions or simple metrics in order to determine the electron distribution's attributes.

The ambiguity and difficulty caused by these effects has been noted previously in the analysis of other hard X-ray cameras and cannot be verified in this analysis. These effects diminish HXR's capability to determine changes in the bremsstrahlung spectra. However, large discrepancies between the X-ray spectra from the thick-target bremsstrahlung will definitively disprove the assumptions in the differences between forward and reverse field. Experimental hard X-ray spectra tend to be exponential in nature, and are characterized with an effective temperature T_{ph} known as the photon temperature, as described in equation 5.11.

$$\frac{dI(E)}{dE} \propto \frac{1}{E} e^{-E/T_{ph}} \tag{5.11}$$

Observing trends in T_{ph} and its error can describe macroscopic changes in the spectrum. Increases in the value of T_{ph} suggest an increase in higher energy fast electrons. Significant changes in the error describes deviation from the exponential spectral shape. T_{ph} has

Figure 5.20: The photon temperature (T_{ph}) is similar between core and thick-target measuring chords. T_{ph} is an exponential fit of the energy distribution of X-ray counts. The similar error bars and values of T_{ph} in the core and edge means that the energy spectrum are very similar (as measured by the detector). Due to the limitations in the HXR camera, this result is not a sufficient condition in proving the similarity of fast-electron distributions in the core and edge.
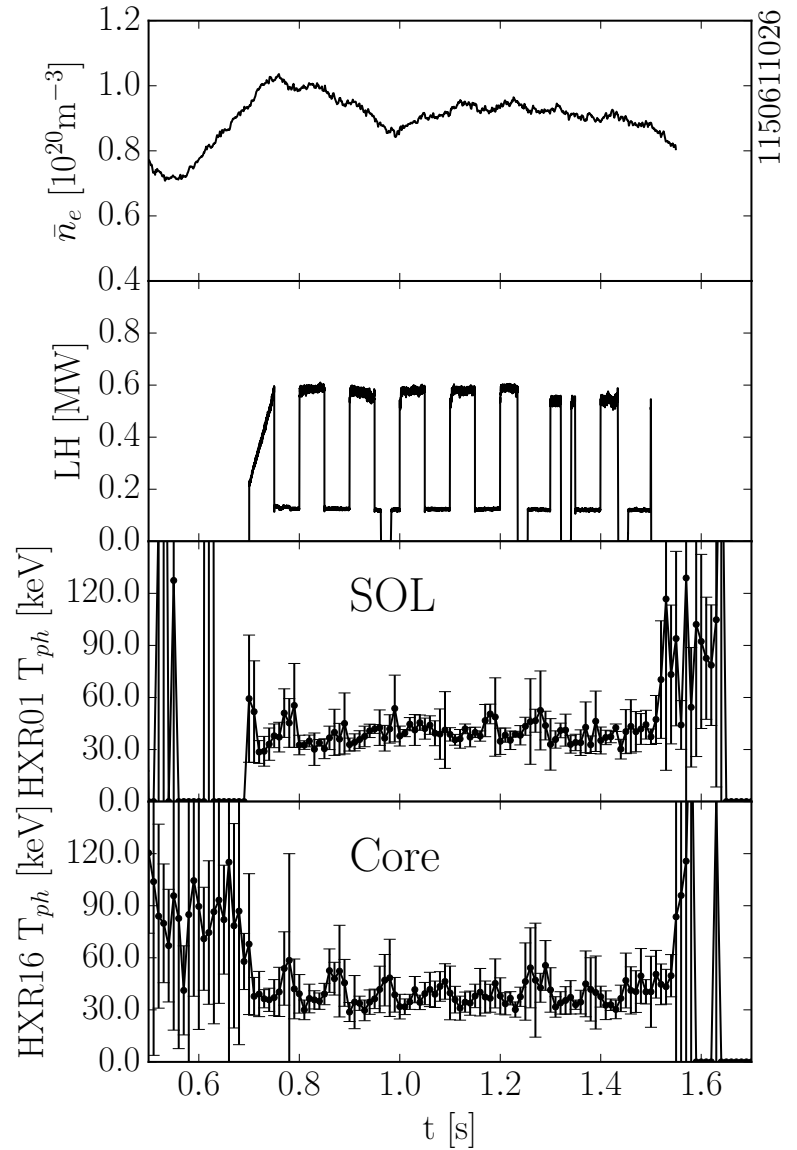
been used on a range of tokamaks with LHCD systems to reduce the higher dimensional data. This parameter is a simplified metric for describing changes in the core fast electrons and edge in time.

The photon temperature and associated error was calculated in each time bin based on the count rate energy spectrum. The fit of T_{ph} is strongly correlated with the overall count rate, as greater variability in the spectrum is observed with a lower count total causing. This is generally seen as a higher value of T_{ph} with an equivalently high error. In low count rates the the calculated error in T_{ph} approaches the value of T_{ph}, sometimes exceeding 80keV. However, at sufficiently high count rates T_{ph} was found to fall within the range of 30-40 keV in nearly all circumstances in forward field.

The spectra of X-rays were compared in discharges which have sufficient count rates in the core and at the strike point. Shown in figure

Figure 5.21: Comparsions of the edge and core T_{ph} show similar values. Due to the extremely large thick-target X-ray fluxes, the corresponding core emission is weak. This weak emission causes significant error in the determined T_{ph} and is subsequently difficult to determine. The count rate in the edge allows for proper calculation of T_{ph}, but the corresponding core count rate is too low to properly generate a measurement of the photon temperature.
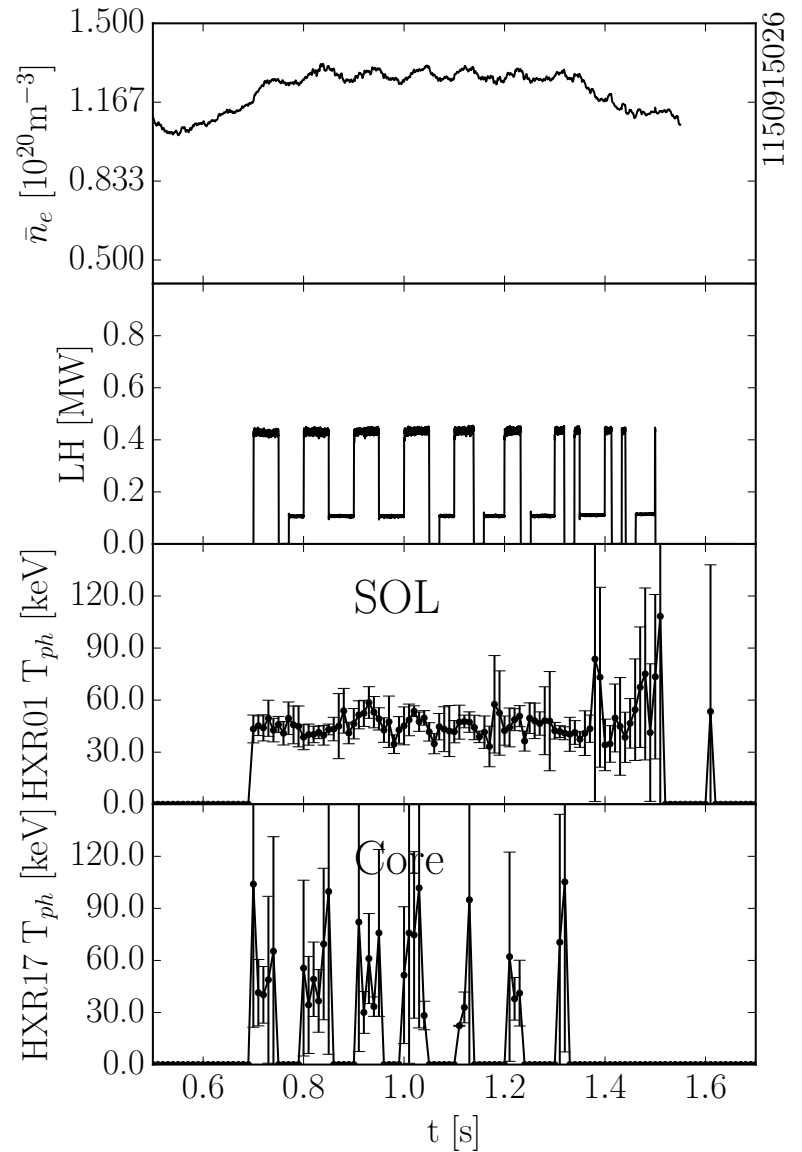
5.20 the T_{ph} of a core viewing chord is compared to the strike point. It shows that both spectra have similar exponentials with values of T_{ph} which are in the range of 30-40 keV. The similarity in T_{ph} is observed in all circumstances with sufficient count rates. In forward field T_{ph} fluctuates in correspondence to the fitted error and is only observed to contain time dependent structure near the low count rate condition.

The significant difference in count rate between the core and edge in reverse field makes the comparison of energy spectra extremely difficult. However, the measured thick-target spectrum can be easily compared to the forward field data. The core T_{ph} rises in the low power portion of the modulation due to the very low count rates observed, causing possibly erroneous structure in the time history of

T_{ph}. However, the measured T_{ph} is similar to the forward field distribution suggesting similarity between the electron distributions.

As was previously mentioned, the unquantified systematic errors in the measured X-ray spectrum leads to systematic errors in the calculated T_{ph}. Due to this effect, the sensitivity of T_{ph} to changes in the electron distribution is effectively unknown for C-Mod through measurements of the HXR (though attempts at forward modeling this dependency have been made). As a consequence, T_{ph} and the associated photon energy spectra are the same and not useful in understanding the fast-electron distribution. Regardless, the equivalent values of T_{ph} in the core and edge for forward and reverse field are a necessary but not sufficient condition in proving the similarity in the distribution of edge lost fast electrons and core electrons.

Little variation is observed in the X-ray energy spectra in various locations in the plasma. The trends in edge thick-target emission cannot be discerned from core emission through differences in the energy spectrum. The similarity in the spectra does not disprove similarity in the electron energy distribution. Calculations of thick-target bremsstrahlung are required at many energies, which can significantly change the efficiency of X-ray emission.

Quantification of fast electron edge losses using Win X-ray

As shown in the previous section, the strike-point bremsstrahlung emission becomes a slightly more pronounced feature of the HXR profile with increasing densities. This result suggests that the edge becomes increasingly important at lower current drive efficiencies. However, thick-target emission is more efficient in X-ray production for a given electron flux. The direct comparison of the magnitude of X-ray intensities will improperly weight the importance of strike point emission. Generating an accurate value of the SOL fast electrons from the X-ray intensity requires a different method than is used for the core. The results using Win X-ray will give a quantity and a level of importance to the edge loss in the LHCD density limit.

The data from Win X-ray shown in figure 5.8 are used with the HXR experimental data to determine the magnitude of fast-electrons. The modeled spectra from a range of monoenergetic electron beams (50 to 70 keV) were used to give a bounded value to the electron fluxes to the inner wall in a low-density discharge ($.7 \cdot 10^{20}[\mathrm{m}^{-3}]$). Equation 5.7 which uses Win X-ray spectrum is integrated from across the energy range of the HXR with the observed count-rate spectrum (> 20 keV). The transmission factor is assumed to be 1 (no attenuation of the photons by the vacuum window).

The chosen low density plasma is representative of the lower bound of the high strike-point discharge density range. This shot has significant current drive and the highest edge X-ray intensity in forward

field. The highest edge X-ray count rates were observed at the lowest densities. The following calculation makes use of the upper bound on the observable HXR count rate ($2.5 \cdot 10^5$ counts/s). This is in an attempt to set a quantitative upper bound on the measurable SOL electrons.

When combined together, several trends are observable based on the energy chosen for the SOL electrons. Results showed that the interpreted current densities (fluxes) became larger for lower energy electrons. This is due to the efficiency of X-ray production scaling with the electron energy. This would suggest looking at even lower electron energies (< 40 keV) for the possibility they contain significant electron fluxes.

Figure 5.22: The fast electron flux calculated from the measured thick-target bremsstrahlung on Chord 1 with data from `Win X-ray` versus time. This is a low density plasma ($\bar{n}_e = .7 \cdot 10^{20} [\mathrm{m}^{-3}]$) forward field discharge. While the predicted flux of particles increases for lower electron energies and spans an order of magnitude, the heat flux ($q = E_i j_f$) does not exceed 50 kW/m^2. This is a small value in comparison to the expected thermal heat flux, suggesting that the total heat through the edge from fast electrons is small.
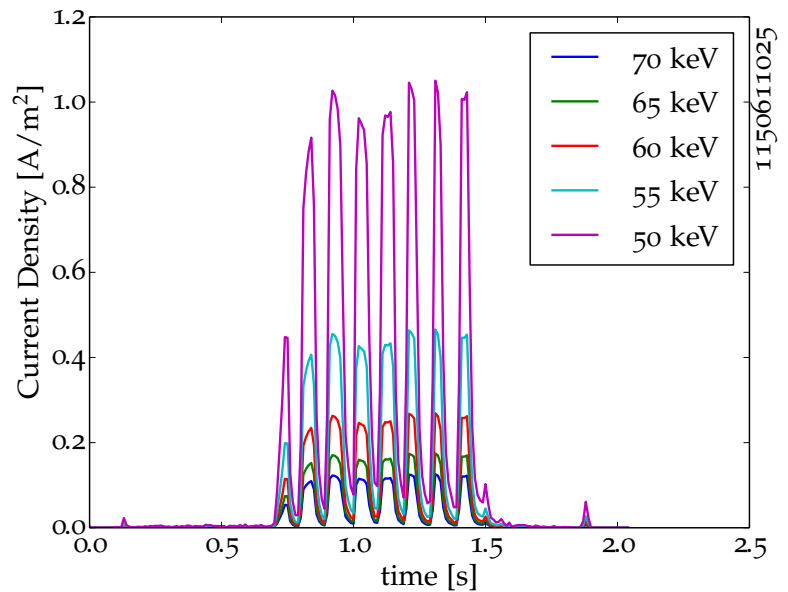
However, the X-ray spectrum requires that higher energy electrons greater than 70keV must exist for energy conservation. While physically impossible, the lower (50 keV) bound at low density is likely representative of the highest possible SOL fast electron fluxes. Even in this case, 1A/m^2 of fast electrons is at least 3 orders of magnitude less than the measured ground current densities with Langmuir probes (> 1 kA/m^2). The change in the observed floating potential (given by equation 5.5) will be negligible, as the ratio of j_f to j_{sat} is at minimum $1/1000$.

A rough estimate of the observed heat flux can be calculated by taking the current density and multiplying by the energy per particle ($q = E_i j_f$. This assumes that the electron distribution is monoenergetic and moving only towards the target plate. In this case, the electron heat fluxes are approximately 50 kW/m^2, which is significantly lower than the background heat flux (> 1 MW/m^2). At the strike point the heat flux is likely to be extremely thermal in character.

The calculated value of heat flux and current density are averaged over the view of the HXR chord. The width of the fast-electron SOL

scale-length (assuming an exponential/ diffusion-dictated profile) is much smaller than the SOL width. This is due to the significant drop off in X-ray emission on chords 2 and 3. It is likely that the small flux occurs over a small area meaning that the total current of fast electrons is very small.

The similarity in the X-ray energy distributions makes calculations in other conditions (*i.e.* different densities or reverse field) proportional to the calculated result. This result suggests that the reverse field spectrum (those electrons which carry the LHCD current) likely has upwards of 100s of kA/m^2 of current density at low densities (due to the count rate exceeding the HXR measurement range). This current density translates to a current of less than 10 kA to the inner wall due to fast electrons. Even at those levels, the effect on the SOL's measured parameters of the SOL will be minimal. At the highest densities in the reverse field plasmas the previous result shows minimal and decreasing population of SOL fast electrons. This completely rules out fast electrons streaming to the divertor plate to be a significant power loss mechanism at high densities.

The intensity of X-rays for a given electron flux is higher for thick-target bremsstrahlung due to the density of solid molybdenum. The large discrepancy in particle density and in Z from the molybdenum surface to the Deuterium plasma makes the wall significantly more sensitive to high energy electrons. The quantitative analysis enabled by `Win X-ray` shows that a population with .1 % of the total fast electron population colliding with the wall can cause significant X-ray emission. The features induced by thick-target emission strongly weight the profile, and can easily overwhelm the core emission of bremsstrahlung.

Future tokamaks which have high Z divertors (*i.e.* tungsten) will likely generate significant X-ray fluxes from even small populations of fast-electrons in the SOL. Great care must be taken in designing hard X-ray cameras which have functional viewing dumps. Cameras which view the outer midplane (radial cameras) rather than the inner wall (poloidal cameras) are unlikely to see limiting points or strike points. Radial views also benefit from the higher X-ray fluxes expected from the bremsstrahlung of the passing fast electrons' small-angle scattering. Future hard X-ray camera designs should focus on radial, rather than poloidal measurements.

SUMMARY AND DISCUSSION

The creation of a non-thermal tail of electrons using LHCD leads to the possibility of fast-electrons in the SOL of tokamak plasmas. The population of fast electrons observed in the SOL is dependent on where they are created, their diffusivity and their slowing down times. The loss of current carrying electrons to the edge represents a

process which can reduce current drive efficiency. In most tokamaks the electrons will thermalize before diffusing into the edge plasma, leading to minimal edge loss. However, there is the possibility that deposition of LHCD very close to the edge can induce significant edge losses. This nearly collisionless beam of high energy particles can possibly induce significant heat fluxes near the strike point.

In order to test the importance of edge fast-electron losses on Alcator C-Mod, a specially designed discharge was developed. The low elongation and high inner strike point of the plasma was measured with with the HXR camera. The generation of thick-target bremsstrahlung from the inner strike point was compared to the core emission of hard X-rays in both field directions. The high Z wall (molybdenum) is extremely efficient at X-ray generation, leading to a very sensitive measure of unconfined fast electrons.

Several steady-state plasmas with LHCD modulation were used to create a density scan. The hard X-ray emission from core and edge reduced exponentially with rising $\bar{n}_e$ in forward and reverse field. However, the exponential decay with the density of strike point emitted X-rays was slightly weaker than that of the core. The increasing prominence of the edge suggests that edge loss plays an increasing role at higher densities. However, the monotonically decreasing trend in edge emission suggests a reduced edge population at high densities. This would suggest that edge loss of fast-electrons is not the cause of the LHCD density limit.

Differences in the forward and reversed field emission of strike-point hard X-rays highlight the asymmetry in LHCD electrons. Observations of these populations find no difference in the X-ray energy spectra reinforcing this theory. Trends in the observed strike-point emission implicates edge emission in causing the increasing HXR asymmetry observed at higher plasma densities. The magnitude of the fast-electrons required to generate this asymmetry can describe the importance of edge loss at high density.

The strike-point emission was quantitatively bounded using the `Win X-ray` code. This code is designed to calculate the X-ray spectrum from a known electron beam in scanning electron microscopes. Data from `Win X-ray` finds the flux of fast-electrons necessary to generate the observed emission is less than $10A/m^2$. This current density carries a heat flux less than 500 kW/m^2, a small fraction ($< 1\%$) of the observed heat flux. With the applied LHRF representing a 50% change in the total input power, the edge loss of fast-electrons is a small fraction of the changing conducted heat flux. This quantitative measure of the edge fast electron population finds that fast-electron edge loss is not the definitive cause of the LHCD density limit.

A small population of edge electrons is capable of influencing HXR measurements and is difficult to discern from core emission. The small flux of electrons at high density minimally impacts the elec-

tron distributions of the SOL. Comparisons of the total conducted heat with IR thermography[25] and Langmuir probes[24] are similar within their respective errors. This suggests that the parasitic edge loss of LHCD occurs in a thermal-like process.

This work suggests that future HXR designs must take great care in minimizing thick-target emission within the view. The observed edge emission and its increased importance to density was found to be a red herring. However, this result highlights the importance of characterizing the thermal nature of the parasitic edge loss.

[1] Orso (Orso-Maria Cornelio) Meneghini. *Full-wave modeling of lower hybrid waves on Alcator C-Mod*. PhD thesis, Massachusetts Institute of Technology, February 2012.

[2] Peter C Stangeby. Langmuir-, and bolometer-probe interpretation for plasmas with two electron components. *Journal of Nuclear Materials*, 128–129:969 – 973, 1984.

[3] P C Stangeby. A problem in the interpretation of tokamak langmuir probes when a fast electron component is present. *Plasma Physics and Controlled Fusion*, 37(9):1031, 1995.

[4] A. Schmidt, P. T. Bonoli, O. Meneghini, R. R. Parker, M. Porkolab et al. Investigation of lower hybrid physics through power modulation experiments on Alcator C-Mod. *Physics of Plasmas (1994-present)*, 18(5):–, 2011.

[5] J. Liptac, R. Parker, V. Tang, Y. Peysson and J. Decker. Hard x-ray diagnostic for lower hybrid experiments on Alcator C-Mod. *Review of Scientific Instruments*, 77(10):–, 2006.

[6] K. Ushigusa, T. Kondoh, O. Naito, Y. Ikeda, S. Ide et al. Direct loss of energetic electrons during lower hybrid current drive in JT-60U. *Nuclear Fusion*, 32(11):1977, 1992.

[7] G. M. Wallace, S. G. Baek, P. T. Bonoli, I. C. Faust, B. L. LaBombard et al. High field side launch of RF waves: A new approach to reactor actuators. *AIP Conference Proceedings*, 1689(1), 2015.

[8] Raynald Gauvin, Eric Lifshin, Hendrix Demers, Paula Horny and Helen Campbell. Win X-ray: A new monte carlo program that computes X-ray spectra obtained with a scanning electron microscope. *Microscopy and Microanalysis*, 12:49–64, 2 2006.

[9] E.J. Doyle, W.A. Houlberg, Y. Kamada, V. Mukhovatov, T.H. Osborne et al. Chapter 2: Plasma confinement and transport. *Nuclear Fusion*, 47(6):S18, 2007.

[10] K. Hizanidis and A. Bers. Steady-state rf-current drive theory based upon the relativistic Fokker–Planck equation with quasilinear diffusion. *Physics of Fluids*, 27(11):2669–2675, 1984.

[11] Y Peysson. Transport of fast electrons during LHCD in TS, JET, and ASDEX. *Plasma Physics and Controlled Fusion*, 35(SB):B253, 1993.

[12] Xianmei Zhang, Yanhui Wang, Limin Yu, Xin Shen and Jianbin Wang. Effects of the radial dependence of the fast electron diffusion coefficient on the current driven by lower-hybrid waves in tokamak. *Physics of Plasmas*, 19(7), 2012.

[13] C Yang, P T Bonoli, J C Wright, B J Ding, R Parker et al. Modelling of the east lower-hybrid current drive experiment using GENRAY/CQL3D and TORLH/CQL3D. *Plasma Physics and Controlled Fusion*, 56(12):125003, 2014.

[14] S H Kim, J F Artaud, V Basiuk, A Bécoulet, V Dokuka et al. Lower hybrid assisted plasma current ramp-up in ITER. *Plasma Physics and Controlled Fusion*, 51(6):065020, 2009.

[15] T. Eich, A.W. Leonard, R.A. Pitts, W. Fundamenski, R.J. Goldston et al. Scaling of the tokamak near the scrape-off layer H-mode power width and implications for ITER. *Nuclear Fusion*, 53(9):093031, 2013.

[16] D. Tskhakaya, S. Kuhn, V. Petržilka and R. Khanal. Effects of energetic electrons on magnetized electrostatic plasma sheaths. *Physics of Plasmas*, 9(6):2486–2496, 2002.

[17] Jung-Sik Yoon, Mi-Young Song, Jeong-Min Han, Sung Ha Hwang, Won-Seok Chang et al. Cross sections for electron collisions with hydrogen molecules. *Journal of Physical and Chemical Reference Data*, 37(2):913–931, 2008.

[18] Yong-Ki Kim and M. Eugene Rudd. Binary-encounter-dipole model for electron-impact ionization. *Phys. Rev. A*, 50:3954–3967, Nov 1994.

[19] P. M. Stone, Y.K. Kim and J. P. Desclaux. Electron-impact cross sections for dipole- and spin-allowed excitations of hydrogen, helium, and lithium. *Journal of Research of the National Institute of Standards and Technology*, 107(4):327–337, July 2002.

[20] A. Géraud, J. Bucalossi, T. Loarer, B. Pégourié, C. Grisolia et al. Pellet fuelling in tore supra long discharges. *Journal of Nuclear Materials*, 337–339:485 – 489, 2005. PSI-16.

[21] H. Bethe and W. Heitler. On the stopping of fast particles and on the creation of positive electrons. *Proceedings of the Royal Society of London A: Mathematical, Physical and Engineering Sciences*, 146(856):83–112, 1934.

[22] Gerhard Elwert and Eberhard Haug. Calculation of bremsstrahlung cross sections with sommerfeld-maue eigenfunctions. *Phys. Rev.*, 183:90–105, Jul 1969.

[23] E. Haug. Bremsstrahlung and pair production in the field of free electrons. *Zeitschrift für Naturforschung A*, 30(9):1099–1113, September 1975.

[24] N. P. Basse, A. Dominguez, E. M. Edlund, C. L. Fiore, R. S. Granetz et al. Diagnostic systems on Alcator C-Mod. *Fusion Science and Technology*, 51(3):476–507, April 2007.

[25] J. L. Terry, B. LaBombard, D. Brunner, J. Payne and G. A. Wurden. Divertor ir thermography on Alcator C-Mod. *Review of Scientific Instruments*, 81(10), 2010.

CONCLUSIONS & FUTURE WORK

In this thesis the unexpected loss of current drive at high density on Alcator C-Mod was investigated using power modulation. Previous experimental work suggests that edge losses are responsible for the reduced current drive efficiency. This work completed the LHRF power balance, proved edge losses in causing the loss of current drive, and derived further attributes at high $\bar{n}_e$. The loss of LHRF is observed to have the following empirical characteristics with new results in bold:

- A loss of current drive is exhibited in diverted plasmas at high densities which contrasts the significant current drive in similar limited plasmas[1, 2].

- The fast electron population decreases exponentially with increasing $\bar{n}_e$. This is measured via non-thermal ECE emission and hard X-ray bremsstrahlung[1, 2].

- Thermoelectric currents are generated by LHRF in the edge with the loss of current drive[1, 2].

- Core HXR brightness profiles do not change in shape, but in magnitude with increasing $\bar{n}_e$[3].

- Ion-cyclotron quasi-mode PDI is observed with the onset of the LHCD density limit[4, 5].

- The loss of current drive correlates with the plasma current. Higher currents maintain current drive to higher densities[6].

- LHRF power in H-modes causes changes in the pedestal E_r-well which can modify pedestal characteristics[7, 8].

- **LHRF absorption is not observed in any core population, thermal or fast.**(Chapter 3) The stored energy of the core plasma only changes due to an increased edge particle source. No measurable change in core temperatures were observed (within the precision of the diagnostics).

- **Prompt edge losses balance the loss of power to current drive.** (Chapter 3) The fast response in edge radiation and conduction prove with a completed power balance that the edge absorption of LHRF power is a competitive mechanism to current drive.

- **Edge losses occur at low densities with efficient current drive.** (Chapter 3) A small prompt response is observed in the conducted power at low density, which suggests that the loss of current drive is not a 'threshold' behavior.

- **Edge power losses of LHRF power are toroidally symmetric.** (Chapter 4) Changes in edge radiation with diodes and cameras occur symmetrically about the torus. Measurements of the conducted power suggests a similar conclusion.

- **Edge losses of LHRF power occur near the separatrix.** (Chapter 4) Profiles of the conducted power by Langmuir probes and IR thermography have a maximum change in the heat flux near the LCFS with applied LHRF power. Deposition of power must occur near the LCFS.

- **Edge losses appear in the thermal plasma distribution in the SOL.** (Chapter 4) The balance of LHRF conducted and radiated power to the inner and outer divertor are influenced by field reversal. Measurements of the LHRF total heat from IR thermography and Langmuir probes are similar, indicating thermal assumptions in Langmuir probe theory still hold. Measurements of V_{fl}/T_e also change minimally, suggesting thermal SOL distributions.

- **Edge-deposited LHRF instantly enhances ionization in the active divertor** (Chapter 4) Measurements of the Ly_α emission show a large change in brightness in the active divertor in all diverted topologies. This is matched by changes in the neutral pressure and edge density, which acts as the particle source for the observed core density rise.

- **Edge-deposited LHRF can induce H-modes.** (Chapter 4) At specific conditions, the additional LHRF power can trigger H-modes in specific diverted plasmas.

- **The LHRF density limit is not due to fast-electron edge losses.** (Chapter 5) Observation of the inner strike-point in both field directions show decreasing thick-target X-ray emission with $\bar{n}_e$. Order-of-magnitude calculations of the X-ray flux suggest that this emission comes from a small $< 10\,\mathrm{A/m^2}$ flux. Fast electron transport to the edge changes minimally with $\bar{n}_e$.

This evidence can be used to categorize the mechanism behind the loss of current drive. While it does not definitively prove a specific mechanism, all of the results are quantitatively and qualitatively consistent with collisional damping of LHRF waves. The characteristics of edge absorption highlight the importance of edge collisionality in LHCD. The loss of current drive on Alcator C-Mod is a cautionary

tale of the effects of collisionality. Future tokamaks must avoid LHRF wave propagation through regions of high collisiality for use in current drive.

Finally, the path towards proving collisional absorption in the divertor is described. Further work on the power balance with H-modes can find if the power is absorbed just inside the LCFS, or in the divertor. Time-delay studies with better time precision can be used to separate upstream from downstream changes, which can also address this ambiguity.

CONCLUSIONS

Parasitic edge absorption of LHRF power

Previous results had conjectured that the response the in the edge plasma and lack of core fast electrons indicated edge absorption. In this work, the edge absorption of LHRF waves at high density was proven through modulation power balance. This LHRF power balance contains errors typical in other power balance calculations, with a difference in P_{tot} of less than $\sim 20\%$ across the range in density. However, for increasing $\bar{n}_e$ it is definitely shown that current drive (via ΔP_{OH}) is replaced by larger edge losses. These edge losses balance the loss of core absorption.

This calculation required the synthesis of different measurements at multiple locations to verify assumptions in the power balance, specifically the toroidal symmetry of loss. The fast edge response to LHRF power and its extensive influence was widely observed, understating the large change in P_{tot} by modulated LHRF power. The results of Hughes[7] and Terry[8] are a by-product of this significant change in the SOL, leading to the observed modification of ionization and H-mode characteristics. The edge LHRF deposition can be simplified to an efficient actuator of P_{SOL} due to the thermal nature of the observed power.

These losses occur at a small but measurable level at low density indicating that the loss of current drive is not a threshold mechanism. Edge ionization and its effect on the particle inventory can be observed even at the lowest densities. Increases in the strike point heat flux also occur promptly in the divertor. Some edge absorption exists due to the high $n_\parallel$ reverse LHRF spectrum, but the launched waves are asymmetrically damped along field lines near the antenna. This has been characterized to contain a small fraction of the power, some of which causes ionization in front of the grill[1, 9] but the $n_\parallel$ for maximal damping would occur inside the LCFS (reverse spectrum $n_\parallel$ peak is near 10). The lack of a threshold to the LHCD density limit was theorized from a different HXR analysis[10]. Prompt edge losses

exist at low density and increase in magnitude with increasing $\bar{n}_e$ proving that no threshold is observed.

Edge LHRF power loss follows typical in/out asymmetries observed in low edge collisionality/ sheath-limited regimes ($L/\lambda_{ee} < 15$, where L is the field line length and λ_{ee} is the mean-free-path for electron-electron collisions). In forward field, the inner divertor plasma has a low temperature and high density with more intense radiation. The outer divertor plasma is higher temperature and lower density, with plasma flows from on divertor to another possibly coupled by a thermoelectric current. LHRF power application enhances these attributes with higher outer divertor temperatures, higher inner divertor densities, increased thermoelectric currents, and larger in/out radiation asymmetries. Observations of thermoelectric currents with LHRF power at high densities is an indicator of this enhanced SOL asymmetry and is verified by the path of conducted and radiated power.

The completed power balance motivated the analysis of various plasma diagnostics. Changes in plasma attributes due to edge absorbed LHRF were correlated with a fraction of power loss and given a relative importance. The large number of plasma diagnostics spread about the tokamak recording various attributes yielded multiple conclusions which were used to determine a mechanism for the edge loss. The evidence suggests that the SOL collisionality is key in causing the LHCD density limit on Alcator C-Mod.

Evidence correlates with SOL collisionality

The toroidal symmetry and strike-point loss of edge deposited LHRF power indicates that localized SOL effects (especially in the far SOL) are unimportant in the loss of current drive. Two possible conclusions can be derived from this result when combined with the nearly instantaneous response of the edge. The deposition of power must occur very close to the LCFS, either just inside or just outside this boundary. Each of these cases has an associated dominant mechanism for wave absorption.

First, high $n_\parallel$ Landau damping could occur on electrons at the LCFS (with $T_e \sim 100$ eV). This requires values of $n_\parallel$ greater than 17 to be generated in the SOL either at that location or farther out radially. The damping of power should create an epithermal 'bump' in the electron velocity distribution. These electrons are unlikely to generate a current due to their low velocities and cannot asymmetrically modify the resistivity due to the minimal change in their collisionality. When lost to the SOL, electrons with energies greater than > 900 eV have momentum mean-free paths similar or longer than the SOL field-line length in Alcator C-Mod. This should lead to some non-thermal contribution to the distribution of electron energies at the divertor plate.

However, measurements of X-ray emission from high-strike point discharges limit this absorption to the electron population with energies less than 3 keV.

Indicators of non-thermals are not observed symmetrically in the SOL and deposition inside the LCFS was not found. The measurement of the heat flux by Langmuir probes assumes a thermal distribution of electrons and ions but their measurements are still similar to the heat fluxes calculated from IR thermography and fast thermocouples. Also, the ratio of the floating potential to electron temperature changes with non-thermal distributions[11, 12] but was not observed in the divertor with LHRF power. An increase in the electron temperature at the edge ($.8 < \rho < .95$) was not observed with LHRF to the precision of the available diagnostics. The changes in $n_\parallel$ would need to occur in cases with good drive where power in ion-cyclotron quasi-mode PDI is low. Finally, fast modulation of LHRF power at 3-10 kHz is not in the core plasma where deposition inside the LCFS would be expected.

For edge Landau damping to cause meet the necessary thermal conditions, power must either be absorbed by thermal electrons (necessitating higher values of $n_\parallel$), damp inside the LCFS or have a shorter collision mean free path than estimated. The creation of thermal electrons in the SOL would require higher $n_\parallel$ values that would seem to violate the $\sim 3v_{th}$ damping condition or violate the deposition location evidence. This odd circumstance is only possible if the waves are absorbed as they are created, as they cannot propagate and thus is highly unlikely.

Damping just inside the LCFS can properly thermalize the particles, but sets strict limitations on the absorbed $n_\parallel$. It cannot absorb in the SOL (for $T_e < 100eV$) and cannot absorb far from the LCFS (for $T_e > 300$ eV), this translates to $17 < n_\parallel < 30$. Observations of very prompt changes in the SOL upstream far from the launcher are not observed.

The slowing down distance on Alcator C-Mod for $3v_{th}$ electrons are on the order or greatly exceed the SOL connection length. The absence of these effects are necessary conditions for disproving edge Landau damping as cause for the LHCD density limit. However, this does not disprove the existence of significant absorption caused by this mechanism. These attributes only make it more unlikely.

Collisional absorption meets most, if not all of the evidence listed at the beginning of this chapter. First, the wave absorption can meet the necessary symmetrization and strike-point localization constraints. The collisionality is highest near the strike point and the strike point detaches first to detach at high densities. Wave damping is expected to be weak in the core with many reflections in the SOL. A large number of passes through the SOL can lead to toroidal symmetrization. Toroidal symmetrization by collisional absorption can be caused by a low-probability single pass with significant damping or by many

high-probability traversals with weak damping. A collisional zone exists in the high density, low temperature divertor plasma and can lead to large absorption in a single pass. However, this region is small and distant from the core plasma. Either of these cases can become dominant when the average absorption per pass through the edge plasma exceeds the core absorption. Collisional absorption represents a parasitic mechanism.

Collisional absorption leads to the thermal attributes of LHRF edge losses. The field-direction dependence, enhanced asymmetry, thermal nature of the conducted power, and increase in ionization all suggest thermal absorption. The absorption of power via collisions is approximately proportional to v^{-3}, meaning a large fraction is absorbed in low-energy thermal bulk of the electron distribution. The changes in the thermal plasma by LHRF power are dictated by the SOL characteristics typically observed in ohmic plasmas.

Collisionality of tokamak SOLs increases with the addition of a divertor when compared to a limited discharge[13]. The LHCD efficiency's plasma current dependence also mirrors trends in the SOL with higher plasma currents. Higher plasma currents have been rigorously shown to create smaller SOL widths[14, 15] and lead to lower SOL collisionalities. The collisionality of the SOL scales with the Greenwald fraction, similarly to the trends in current drive loss.

Finally, low density edge losses can also be expected with collisional absorption. Collisional absorption is dictated by $k_{\perp I}$ and scales with $\omega_{pe} \nu_{ei} n_{\parallel} / 2c\omega$ for typical SOL parameters. The finite value of $k_{\perp I}$ at all collisionalities can lead to finite absorption at low densities. Together, these results indicate that collisional absorption does not have a threshold-like nature, only a changing importance.

These attributes advocate for collisional absorption as the dominant absorption mechanism in the edge. However, this is a circumstantial set of evidence which does not prove, but suggests one mechanism over another. Measurements which unequivocally prove or disprove edge Landau damping or collisional absorption are difficult. High $n_{\parallel}$ absorption affects the same electrons as collisional absorption. Without high accuracy measurements of the electron distribution function, other attributes must be found. Additional characteristics to separate these two mechanisms can be found based off of the evidence and are described in the future work.

Irrelevance of fast electron edge losses

Langmuir probes are sensitive to the fast electron content in the SOL[11, 12]. A population of fast electrons as small as a .1% can cause a doubling in the sheath potential[16]. The trends in particle flux, density and temperature derived from Langmuir probes can be misinterpreted under the influence of fast electrons. The edge loss of fast

electrons can also be a substantial loss mechanism and has been observed on other tokamaks as discussed in chapter 1.

A simple theoretical model of the edge loss was generated from the balance of diffusion and slowing down processes. Edge losses are only substantial for LHRF deposition $> .95\rho$ on Alcator C-Mod with experimental diffusion coefficient values determined by Schmidt, *et. al.*[3]. Extrapolation to future devices finds edge loss to be negligible, even with the expected edge electron pedestal temperatures. This work highlights the need for current and magnetic field dependencies for the fast-electron radial diffusivity.

Thick-target bremsstrahlung measurements were interpreted with a Monte-Carlo scanning electron microscope X-ray code (`Win X-ray`). The interpretation of the X-ray count rate found small currents of high energy electrons (for $E > 25$ keV) could generate the prominent strike point X-ray emission. High Z walls like molybdenum are ideal surfaces for X-ray generation and can make substantial backgrounds. Similarly, measurements of soft X-rays using the XTOMO system found no sign of the LHRF modulation (for $E > 3$ keV). As a consequence, the order-of-magnitude fast electron current was $\sim 10^{-6}$ times less than the thermal ion saturation current.

This small population can only account for a very small fraction of the power and was observed to decrease with increasing density. The fraction lost to the edge did not change substantially, which was expected to increase in the case that edge diffusion caused the LHCD density limit. These three methods using modeling, experiment and theory all suggest that edge losses on Alcator C-Mod are small and will be inconsequential on future steady-state devices. However, the large X-ray fluxes from minuscule fast electron populations will require future hard X-ray cameras to avoid viewing the strike point.

Implications for future LHRF systems

Similar regimes of L/λ_{ee} occur in the SOL of across various tokamaks (where L is the connection length, and λ_{ee} is the electron collision mean-free-path), yielding sheath-limited, high-recycling and detaching divertor conditions. However, the small C-Mod size is balanced by highly collisional divertor conditions. This is emphasized by the high heat and particle fluxes capable in Alcator C-Mod SOL. As was derived in Chapter 1, the scale length of absorption ($k_{\perp i}$) is proportional to $\omega_{pe}\nu_{ei}/c\omega$. Future tokamaks will likely have similar divertor conditions, LHRF frequencies, and SOL collisionalities as those observed on Alcator C-Mod.

The trends of edge losses with increasing collisionality indicates that collisional regions of the plasma must be avoided. This matches conclusions in previous theses[1, 17], which state that it is vital to maximize absorption on the first pass through the core plasma. It is

possible that the LHRF waves propagate through and interact with a collisional region before entering plasma. This can cause significant edge losses even with conditions leading to significant core absorption. The results of thesis dictate a stricter requirement for 'single-pass' absorption: LHRF waves must not travel through highly collisional regions. As an example, LHCD launching from the divertor could also significantly reduce the efficiency.

Even in future LHCD systems the initial propagation through the SOL must be evaluated. Designs which send waves through conditions similar to the Alcator C-Mod divertor plasma ($\bar{n}_e > 2 \cdot 10^{20}$ m^{-3}, $T_e < 10$ eV) must be considered with a high degree of caution. Long distance coupling needed for large devices[18] can lead to long traversals through the SOL before reaching the core plasma. In cases with weaker $k_{\perp i}$, the longer traversed distance can still lead to substantial absorption.

However, there are characteristics of future tokamaks which could be utilized to minimize parasitic edge losses. The use of alternate launching locations[19] in favorable SOL conditions[20] (*i.e.* high-field side launch in double null plasmas) can lead to improved core damping. PDI and collisional absorption depend on the launched frequency, higher frequency RF sources can reduce these effects. The trends in SOL heat flux widths which trend inversely with plasma current[14] indicate that future SOLs may also be 'thin' enough radially to avoid significant edge absorption. However, operation of future tokamaks will be near the Greenwald limit, which will lead to significant SOL collisionalities and wider far-SOL density and temperature widths[21]. Conditions on future tokamaks will require further experimentation to test edge LHRF absorption at these conditions, as is apparent by this work. The extremely complex nature of effects like PDI and collisional absorption need to be experimentally evaluated with the changing plasma conditions of high performance tokamaks. The parasitic edge loss of LHRF power on Alcator C-Mod accentuates the importance of tailoring the propagation of LHRF to minimize interaction with the edge plasma.

FUTURE WORK

Precise time delay determination in the SOL

The short time delay observed in multiple edge characteristics confirmed the edge deposition of LHRF power. However, measurement of these parameters were limited in time resolution which prevented the poloidal localization of the power. Power on a SOL field line will propagate to the divertor over a finite time. The time for thermal plasma to travel the length of a field line ($t_R \sim \sqrt{m_i L^2 / T_e}$), is less than a millisecond with $t_R \sim 200 \mu$s for a 5m long, 10 eV SOL. Only fluctu-

ation measurements with Nyquist frequencies of 100 kHz or greater can determine the poloidal location of deposition to the necessary precision. The differences in SOL when comparing wave damping inside and outside the LCFS can be separated from the differences in upstream from downstream plasma conditions.

While data from several measurements indicate the lack of upstream deposition, these are necessary but insufficient criteria for proving divertor deposition. The mirror Langmuir probe[21] does not observe fluctuating LHRF at the midplane, and a finite time delay is observed in the midplane density rise. These prove the absence of deposition, not the deposition itself. Edge LHRF absorption in the SOL with an extremely short time ($< 10\mu$s) delay would prove local deposition. The use of fast cameras[22] and mirror Langmuir probes[21] in the divertor can provide the necessary time resolution. These measurements must occur on field-lines not connected to the LHRF launcher to minimize asymmetric contributions. Observation of extremely short time delays would sufficiently prove collisional absorption as the edge absorption mechanism.

The confinement of particles and energy on open fields line are sufficiently weak that the deposition via collisional absorption would be on the order of the electron thermalization time. With collision frequencies $\sim$ 1MHz, delay from the finite absorption time is on the order of $\sim 10\mu$s, still allowing for the localization of power to occur in the SOL. The time for light to propagate 1 km is $\sim 3\mu$s; waves can propagate toroidally around the C-Mod plasma many times before generating a significant time delay. The deposition and propagation times are short enough to allow for this determination. The direct observation of deposition is necessary to fully prove a specific mechanism for the edge absorption of LHRF power.

H-mode power balance for core absorption

The significant difference in diffusion coefficients parallel and perpendicular to the magnetic field can also be used to separate the location of LHRF deposition. The SOL decay length on Alcator C-Mod dictates that $D_\perp \sim .1$ m^{2}s^{-1}[23], with $D_\parallel \sim L^2/t_R \sim Lv_s \sim 10^5$[13]. The significant difference in diffusion can be used to understand flow of edge-deposited LHRF power. As shown in chapter 4, the edge LHRF power can induce H-modes in certain circumstances. The higher core stored energy indicates a power flow into the plasma.

Power deposited in the SOL will predominantly flow along the field lines to the divertor surfaces. If the increase in stored energy occurs with a reduction in edge losses, then it is likely that the edge deposited power is increasing the stored energy. This would indicate that the power is not deposited on open field lines and that the LHCD density limit is not caused by collisional absorption. In the case that

the edge losses are maintained with the increasing stored energy of the H-mode, then the power flow in the SOL is the same indicating collisional absorption in the SOL. However, if the conditions of the SOL change dramatically with the onset of the H-mode, then it can affect the loss mechanism thereby rendering this argument moot.

Testing these hypotheses in a limited set of experiments should be possible and could definitely prove the cause of the LHCD density limit on Alcator C-Mod. However the results and evidence of this thesis indicates that the losses are strongly correlated with higher SOL collisionalities. Great care must be taken into the design and implementation of future LHRF systems to avoid the possible edge losses which appear in collisional regions of the plasma.

BIBLIOGRAPHY

[1] G. M. Wallace, R. R. Parker, P. T. Bonoli, A. E. Hubbard, J. W. Hughes et al. Absorption of lower hybrid waves in the scrape off layer of a diverted tokamak. *Physics of Plasmas (1994-present)*, 17(8):–, 2010.

[2] G.M. Wallace, A.E. Hubbard, P.T. Bonoli, I.C. Faust, R.W. Harvey et al. Lower hybrid current drive at high density in Alcator C-Mod. *Nuclear Fusion*, 51(8):083032, 2011.

[3] A. Schmidt, P. T. Bonoli, O. Meneghini, R. R. Parker, M. Porkolab et al. Investigation of lower hybrid physics through power modulation experiments on Alcator C-Mod. *Physics of Plasmas (1994-present)*, 18(5):–, 2011.

[4] S G Baek, R R Parker, S Shiraiwa, G M Wallace, P T Bonoli et al. Measurements of ion cyclotron parametric decay of lower hybrid waves at the high-field side of Alcator C-Mod. *Plasma Physics and Controlled Fusion*, 55(5):052001, 2013.

[5] S. G. Baek, R. R. Parker, S. Shiraiwa, G. M. Wallace, P. T. Bonoli et al. Characterization of the onset of ion cyclotron parametric decay instability of lower hybrid waves in a diverted tokamak. *Physics of Plasmas*, 21(6):–, 2014.

[6] S.G. Baek, R.R. Parker, P.T. Bonoli, S. Shiraiwa, G.M. Wallace et al. High density LHRF experiments in alcator C-Mod and implications for reactor scale devices. *Nuclear Fusion*, 55(4):043009, 2015.

[7] J.W. Hughes, A.E. Hubbard, G. Wallace, M. Greenwald, B. LaBombard et al. Modification of H-mode pedestal structure with lower hybrid waves on Alcator C-Mod. *Nuclear Fusion*, 50(6):064001, 2010.

[8] J. L. Terry, M. L. Reinke, J. W. Hughes, B. LaBombard, C. Theiler et al. Improved confinement in high-density H-modes via modification of the plasma boundary with lower hybrid waves. *Physics of Plasmas*, 22(5):–, 2015.

[9] C Lau, G R Hanson, B Labombard, Y Lin, O Meneghini et al. Effects of LH power on SOL density profiles and LH coupling on Alcator C-Mod. *Plasma Physics and Controlled Fusion*, 55(2):025008, 2013.

[10] Orso (Orso-Maria Cornelio) Meneghini. *Full-wave modeling of lower hybrid waves on Alcator C-Mod*. PhD thesis, Massachusetts Institute of Technology, February 2012.

[11] Peter C Stangeby. Langmuir-, and bolometer-probe interpretation for plasmas with two electron components. *Journal of Nuclear Materials*, 128–129:969 – 973, 1984.

[12] P C Stangeby. A problem in the interpretation of tokamak langmuir probes when a fast electron component is present. *Plasma Physics and Controlled Fusion*, 37(9):1031, 1995.

[13] P.C. Stangeby. *The Plasma Boundary of Magnetic Fusion Devices*. Series in Plasma Physics and Fluid Dynamics. Taylor & Francis, 2000.

[14] T. Eich, B. Sieglin, A. Scarabosio, W. Fundamenski, R. J. Goldston et al. Inter-ELM power decay length for JET and ASDEX upgrade: Measurement and comparison with heuristic drift-based model. *Phys. Rev. Lett.*, 107:215001, Nov 2011.

[15] B. LaBombard, J. W. Hughes, N. Smick, A. Graf, K. Marr et al. Critical gradients and plasma flows in the edge plasma of Alcator C-Mod. *Physics of Plasmas*, 15(5), 2008.

[16] D. Tskhakaya, S. Kuhn, V. Petržilka and R. Khanal. Effects of energetic electrons on magnetized electrostatic plasma sheaths. *Physics of Plasmas*, 9(6):2486–2496, 2002.

[17] Seung Gyou Baek. *Detection of lower hybrid waves at the plasma edge of a diverted tokamak*. PhD thesis, Massachusetts Institute of Technology, February 2014.

[18] A. Ekedahl, G. Granucci, J. Mailloux, Y. Baranov, S.K. Erents et al. Long distance coupling of lower hybrid waves in JET plasmas with edge and core transport barriers. *Nuclear Fusion*, 45(5):351, 2005.

[19] G. M. Wallace, S. Shiraiwa, S. G. Baek, P. T. Bonoli, A. D. Kanojia et al. A scoping study for high-field-side launch of lower hybrid waves on ADX MIT. *IEEE Transactions on Plasma Science*, PP(99):1–6, 2016.

[20] N. Smick, B. LaBombard and C.S. Pitcher. Plasma profiles and flows in the high-field side scrape-off layer in Alcator C-Mod. *Journal of Nuclear Materials*, 337–339:281 – 285, 2005. PSI-16.

[21] B. LaBombard and L. Lyons. Mirror langmuir probe: A technique for real-time measurement of magnetized plasma conditions using a single Langmuir electrode. *Review of Scientific Instruments*, 78(7), 2007.

[22] J. L. Terry, S. J. Zweben, K. Hallatschek, B. LaBombard, R. J. Maqueda et al. Observations of the turbulence in the scrape-off-layer of Alcator C-Mod and comparisons with simulation. *Physics of Plasmas*, 10(5):1739–1747, 2003.

[23] B. LaBombard, J. Goetz, C. Kurz, D. Jablonski, B. Lipschultz et al.
Scaling and transport analysis of divertor conditions on the Al-
cator C-Mod tokamak. *Physics of Plasmas*, 2(6):2242–2248, 1995.